Activity of Cs (K)-promoted Cu-MgO in the formation of oxygenates from CH_3OH/CO and CO/H_2

by

Shahin Goodarznia

B.Sc., Sharif University of Technology, 2005

A THESIS SUBMITTED IN PARTIAL FULFILLMENT OF

THE REQUIREMENTS FOR THE DEGREE OF

DOCTOR OF PHILOSOPHY

in

THE FACULTY OF GRADUATE STUDIES

(Chemical and Biological Engineering)

THE UNIVERSITY OF BRITISH COLUMBIA

(Vancouver)

September 2012

Abstract

The selective synthesis of C_2 oxygenates, especially ethanol, from C_1 species such as CH_3OH and synthesis gas (CO/H_2) is of interest as the demand for clean fuels, including biofuels, increases. However, over alkali-promoted Cu-ZnO catalysts the synthesis of C_2 oxygenates occurs with very low selectivity. Previous mechanistic studies suggest that the basic properties and the Cu properties of these catalysts are critical in determining the C_2 oxygenate selectivity. However, the possible synergistic effect of these catalyst properties on the selectivity of C_2 oxygenates is poorly understood. In the present study, Cu-MgO catalysts were investigated since MgO possesses noticeably higher basic properties compared to ZnO. Furthermore to address the knowledge gap in the literature with respect to a synergistic effect between catalyst basic properties and Cu properties on the synthesis of C_2 oxygenates from CH_3OH/CO, MgO, Cu-MgO and Cs (K)-promoted-Cu-MgO catalysts were prepared, characterized and tested at 101kPa and 498-523K. The catalysts had intrinsic basicities of 3.9 – 17.0 µmol $CO_2.m^{-2}$, SA_{Cu^0} of < 3 $m^2.g^{-1}$ and $SA_{Cu^{2+}}$ of < 2 $m^2.g^{-1}$. The results showed that methyl formate was the dominant C_2 oxygenate, while selectivity to ethanol and acetic acid was low (< 5 C-atom%). At SA_{Cu^0} (< 2 $m^2.g^{-1}$), there was an optimum basicity (9.5 µmol $CO_2.m^{-2}$) at which the selectivity to C_2 species and methyl formate reached a maximum. Also, at approximately constant specific basicity (384.5 – 415.9 µmol $CO_2.g^{-1}$), an increase in SA_{Cu^0}, led to an increase in methyl formate yield, whereas no correlation between $SA_{Cu^{2+}}$ and methyl formate yield was observed.

The 0.5wt%Cs-40wt%Cu-MgO catalyst showed the highest selectivity towards C_2 oxygenates at 101 kPa and was used for high pressure studies to investigate oxygenates synthesis from CO/H_2 at typical industrial conditions (6000-9000kPa and 558-598K). CH_3OH was the dominant produced oxygenate (>66 C-atom%). The reaction kinetics of CH_3OH was studied. The Cs-Cu-MgO catalyst was noticeably less active for the synthesis of oxygenates, compared to a conventional Cs-Cu-ZnO catalyst, which was caused by lower Cu dispersion and weaker Cu-metal oxide interaction in the Cs-Cu-MgO compared to Cs-Cu-ZnO, as well as poor electronic-conductivity and lack of hydrogenation-activity of MgO compared to ZnO.

Preface

This PhD thesis consists of five chapters. Version of Chapter 2 and Chapter 3 have been published in the literature. The PhD study was conducted by Shahin Goodarznia under the supervision of Professor Kevin Smith. Catalyst preparation, catalyst characterization, catalyst testing, kinetic moldering, Apsen simulations, as well as the literature review and the PhD thesis preparation were conducted by Shahin Goodarznia under the supervision of Professor Kevin Smith. The list of the publications corresponding to Chapter 2 and Chapter 3 are shown below:

1- S. Goodarznia and K.J. Smith (2010) Properties of alkali-promoted Cu-MgO catalysts and their activity for methanol decomposition and C_2-oxygenate formation, Journal of Molecular Catalysis A: Chemical 320, 1-13. This paper was recognized as "**Editor's choice paper**". A version of this paper is included in Chapter 2.

   Catalyst preparation, catalyst characterization, catalyst testing, and the literature review were conducted by Shahin Goodarznia under supervision of Professor Kevin Smith. Preparation and writing of the paper was conducted by Shahin Goodarznia under supervision and final approval of Professor Kevin Smith.

2- S Goodarznia and K.J. Smith (2011) The effect of Cu loading on the formation of methyl formate and C_2-oxygenates from CH_3OH and CO over K- or Cs-promoted Cu-

MgO catalysts, Journal of Molecular Catalysis A: Chemical 353-354, 58-66. A version of this paper is included in Chapter 3.

Catalyst preparation, catalyst characterization, catalyst testing and the literature review were conducted by Shahin Goodarznia under supervision of Professor Kevin Smith. Preparation and writing of the paper was conducted by Shahin Goodarznia under supervision and final approval of Professor Kevin Smith.

Table of Contents

List of Tables

List of Figures

Glossary

$\text{Area}_{[\text{Cu } 2p_{3/2}(\text{stellite})]}$ = Area under Cu $2_{p_{3/2}}$ (satellite) peak gained from Cu 2p XPS spectra of Cs (K)-promoted Cu-MgO catalyst

$\text{Area}_{[\text{Cu } 2p_{3/2}(\text{parent})]}$ = Area under Cu $2_{p_{3/2}}$ (parent) peak gained from Cu 2p XPS spectra of Cs (K)-promoted Cu-MgO catalyst

a_{MgO} = Unit cell size of the MgO (nm)

BE = Binding energy (eV)

CO_2 TPD = CO_2 temperature-programmed desorption

C_2 oxygenates = oxygenates that contains two carbon atoms in their molecular structure

$C_{2+}OH$ = Alcohols that contain more than one carbon atom in their molecular structure

C_2 species = Ethanol and acetic acid

$C_{n+}OH$ = Alcohols that contain more than n carbon atoms in their molecular structure

DFT = Density function theory

dP = Difference in pressure (kPa)

d_p = Catalyst average pore diameter (nm)

dW = Difference in catalyst weight (g)

$d_{\text{Cu}}^{\text{XRD}}$ = Cu crystallite size inferred from X-ray powder diffraction (nm)

$d_{\text{Cu}}^{\text{N}_2\text{O}}$ = Cu crystallite size inferred from the N_2O adsorp-decomp. analysis (nm)

$d_{\text{CuO}}^{\text{XRD}}$ = CuO crystallite size (nm)

$d_{\text{MgO}}^{\text{XRD}}$ = MgO crystallite size (nm)

$d^{XRD}_{MgO-lattice}$	=	Distance between two adjacent lattice planes in MgO crystallite (nm)
E_a	=	CH$_3$OH apparent activation energy (kJ.mol^{-1})
EDX	=	Energy dispersive X-ray Spectroscopy
$(E_{CH_3OH})_{Cu-MgO}$	=	Methanol activation energy on Cu-MgO (kJ.mol^{-1})
$(E_{CH_3OH})_{Cu-ZnO}$	=	Methanol activation energy on Cu-ZnO (kJ.mol^{-1})
F	=	Volumetric flow rate of reactant gas/vapor entering plug flow reactor (cm^3(STP).min^{-1})
$\hat{f}_{i-in}$	=	Inlet fugacity of component i in mixture (kPa)
$\hat{f}_{i-out}$	=	Outlet fugacity of component i in mixture (kPa)
GC-MS	=	Gas Chromatograph – Mass Spectrometer
H$_2$ TPR	=	H$_2$ temperature programmed reduction
HC	=	Light hydrocarbons (methane, ethane and propane)
IR	=	Infrared
K_{CH_3OH}	=	Thermodynamic equilibrium constant for CH$_3$OH synthesis from CO/H$_2$
$K_{CH_3OH-calc}$	=	Calculated constant for CH$_3$OH synthesis from CO/H$_2$
$K_{HCOOCH_3(1)}$	=	Thermodynamic equilibrium constant for methyl formate synthesis from CO/CH$_3$OH
$K_{HCOOCH_3(2)}$	=	Thermodynamic equilibrium constant for methyl formate synthesis from CH$_3$OH
$K_{HCOOCH_3-calc\,(1)}$	=	Calculated constant for methyl formate synthesis from CO/CH$_3$OH
$K_{HCOOCH_3-calc\,(2)}$	=	Calculated constant for methyl formate synthesis from CH$_3$OH
K_{i_0}	=	pre-exponential adsorption constant for component i (kPa^{-1})

K_{WGS}	=	Thermodynamic equilibrium constant for water gas shift reaction
$K_{WGS-calc}$	=	Calculated constant for water gas shift reaction
k_0	=	CH_3OH pre-exponential constant ($mol.sec^{-1}\ kPa^{-2.5}.g^{-1}$)
LH	=	Langmuir-Hinshelwood
MF	=	Methyl formate
PR	=	Pressure regulator
P_{N2}	=	N_2 partial pressure (kPa)
P_{N2}^0	=	N_2 saturation pressure (kPa)
Q_i	=	adsorption energy for component i ($kJ.mol^{-1}$)
r_{CH_3OH}	=	CH_3OH reaction rate per mass of catalyst ($mol.sec^{-1}.g^{-1}$)
RDS	=	rate determining step
R_g	=	Universal gas constant ($8.28 \times 10^{-3}\ kPa.m^3.K^{-1}.mol^{-1}$)
SA_{BET}	=	Catalyst BET surface area ($m^2\ g^{-1}$)
$SA_{Cu^{2+}}$	=	Cu^{2+} surface area ($m^2\ g^{-1}$)
SA_{Cu^0}	=	Cu^0 surface area ($m^2\ g^{-1}$)
$SA_{Cu^{total}}$	=	$SA_{Cu^{2+}} + SA_{Cu^0}$ ($m^2\ g^{-1}$)
SEM	=	Scanning electron microscopy
STP	=	Standard condition (temperature of 298K and pressure of 101 kPa)
STY	=	space time yield ($g.kg_{catalyst}^{-1}.h^{-1}$)
S_{CO_2}	=	Selectivity of CO_2 (C-atom%)
S_{C_2}	=	Selectivity of C_2 species (C-atom%)
S_{MF}	=	Selectivity to methyl formate (C-atom%)

TCD	=	Thermal conductivity detector
TEM	=	Transmission electron microscopy
t_r	=	Response time (hr:min).
T_{STP}	=	temperature at standard condition (293K)
V_p	=	Catalyst pore volume ($cm^3 g^{-1}$)
W	=	Catalyst weight
XRD	=	X-ray powder diffraction
XPS	=	X-ray photoelectron spectroscopy
v_0	=	Volumetric flow rate at standard pressure and temperature ($cm^3 min^{-1}$)
σ_i	=	Standard deviation of parameter i
θ_V	=	Vacant site surface coverage
τ	=	Residence time (sec)
$\rho_{catalyst}$	=	catalyst density ($\approx 10^6 g.m^{-3}$)
$\widehat{\Phi}_i$	=	fugacity coefficient of component i in mixture
ΔH^o_{298K}	=	enthalpy of reaction at standard condition (temperature of 298K and pressure of 101 kPa)
ΔG^o_{298K}	=	standard Gibbs-energy change of reaction (temperature of 298K and pressure of 101 kPa)

Acknowledgements

I would like to express my sincerest gratitude to my doctoral supervisor, Professor Kevin J. Smith for his great insights, guidance, advices throughout my doctoral research. He showed me how to approach problems and critically analyze them. I certainly learned a lot from him and I hope I will be able to use his precious teachings and advices in my future career and my life.

I would like to thank my doctoral examination committee (Professor Madjid Mohseni, Professor Elod Gyenge and Professor Tom Troczynski), my university examiners (Professor David Wilkinson and Professor Steve Cockcroft) and my external examiner (Professor Jacques Monnier) for their valuable insights, advices, comments and corrections regarding my doctoral research.

I am thankful to the staff of the Chemical and Biological Engineering Department at the University of British Columbia for providing a helpful and friendly atmosphere. I would like to express my special thank you to Helsa Leong, Lori Tanaka, Amber Lee, Richard Ryoo, Joan Dean, Alex Thng and Doug Yuen for their support and help.

I would like to thank NSERC for their gracious financial support which enabled me to focus on my PhD research with peace of mind.

Dedication

To my beloved and supportive parents

and

to my loving grand parents

Chapter 1

Introduction

1.1   Introduction

The increasing social concerns related to fossil fuel use are due to the depletion of oil reservoirs, rising prices and a changing climate due to the greenhouse gas effect. Consequently, there is a growing interest in alternative fuels such as biofuels. The main advantages of biofuels compared to fossil fuels are attributed to the potential carbon neutral impact of biofuels on the environment and the low level of impurities such as S, N and metals that are present in biofuels [1]. Biomass is considered a promising resource for biofuel production as well as a precursor to valuable biochemicals [1]. Biomass can be converted to synthesis gas (a mixture of CO and H_2 with low concentrations of CO_2 which is also referred to as syngas) via gasification processes. The syngas can subsequently be converted to various valuable biochemicals and biofuels. Some examples and usages of biochemicals and biofuels include bio-methanol, which is a good ecological fuel for fuel cells, vehicles and gas turbines [2]. Bio-methanol has also been proposed as a good precursor for hydrogen transportation [3]. Bio-methanol is an important intermediate to bio-methyl formate [4,5], an industrial intermediate to formic acid, formamide, acetic acid, formaldehyde and dimethylformamide [2,4]. Bio-methyl formate is also a reagent in manufacturing perfumes and food flavouring

products [6], and is a precursor for syngas transportation [7]. Bio-ethanol is an important alternative fuel or additive to gasoline [8].

Syngas conversion and the related reactions over Cu-ZnO and alkali promoted Cu-ZnO catalysts have been studied extensively in the literature [9-28]. A wide range of carbonaceous products such as oxygenates (alcohols, ketones, esters, and ethers) and hydrocarbons are obtained from syngas conversion at typical operating conditions of 498 – 673 K, 5000 – 10000 kPa, feed CO/H_2 ratio of 0.3 – 2.3 (molar) and residence time of 0.2 sec -1.2 sec. Among these products, synthesis of oxygenates (such as methanol, ethanol and methyl formate) have received most attention in the literature [9-28]. Some of these studies have focused on the selective synthesis of C_1 oxygenates (such as methanol) from syngas over Cu-ZnO [9-16]. On the other hand, the addition of alkali promoters such as K or Cs to Cu-ZnO leads to a selective synthesis of C_{2+} oxygenates, such as iso-butanol, from the syngas [20,26-28]. Based on previous research, the alkali promoted Cu-ZnO catalysts showed low selectivity to C_2 oxygenates (such as ethanol, methyl formate, and acetic acid) from syngas. Several studies have focused on understanding the mechanism of C_2 oxygenates formation from syngas over Cu-metal oxide-based catalysts [20,29-34]. These studies suggest that the presence of basic sites plays an important role in the formation of the first C-C bond from C_1 species (CO and methanol) [20,29-34]. On the other hand, based on the linear chain growth mechanism proposed in previous studies, formation of the first C-C bond from C_1 species and the subsequent formation of C_2 oxygenates (such as ethanol) are the rate determining step for the formation of C_{3+} oxygenates [22,28].

Besides basic sites, the presence of copper sites was also identified as critical in the synthesis of oxygenates from syngas over alkali promoted Cu-metal oxide catalysts [20,29-35]. Copper sites are well known for their hydrogenating-dehydrogenating properties [35]. Based on previous mechanistic studies over mainly Cu-ZnO catalysts [20,29-35], it is apparent that the oxidation state of surface copper is an important variable in determining the catalyst activity for oxygenate synthesis.

Several studies have reported on the basicity of alkali promoted MgO [36-39], demonstrating that alkali promoted MgO possesses high basicity. For example, the basic site density of MgO has been reported as 2.2 – 7.2 μmol $CO_2.m^{-2}$ [36-39], whereas for ZnO-ZrO$_2$ a value of 0.9 μmol $CO_2.m^{-2}$ has been reported [40]. While a great deal of work has been focused on C_{2+} oxygenate synthesis from syngas over alkali promoted-Cu-ZnO catalysts, to the author's knowledge few studies have focused on the C_{2+} oxygenate synthesis from syngas over alkali promoted Cu-MgO catalysts [25,32]. Furthermore, none of these studies have focused on identifying correlations between the basic properties and the Cu properties of the catalysts and their activity for syngas conversion to C_{2+} oxygenates. To address the knowledge gap, catalyst characterization and testing of alkali-promoted Cu-MgO catalysts is required. Furthermore, identifying the differences between the catalyst properties/catalyst activity of alkali-promoted Cu-MgO and alkali-promoted Cu-ZnO, may provide a better understanding of the C_2 oxygenate synthesis routes from syngas over alkali promoted-Cu-metal oxide catalysts.

The synthesis of oxygenates from syngas over alkali-promoted Cu-metal oxide catalysts is typically conducted at high operating pressure (>5000 kPa) [9-28], since the syngas conversion reactions are thermodynamically favored at high pressures. However, catalytic testing at atmospheric pressure (101 kPa) is much simpler than when operating at high pressure. Since the first part of the present work is focused on C_2 oxygenate formation, methanol has been used as the reactant rather than syngas (CO/H_2). In this way the catalyst activity tests can be conducted at atmospheric pressure. Using methanol as reactant leads to the decomposition of methanol at low reaction pressure (101 kPa) and moderate reaction temperature (498 K – 523 K) that likely generates carbonaceous surface species such as formyl, formate and methoxy species that can react further to produce C_2 oxygenates. Since high operating pressure overcomes the thermodynamic yield limitation for methanol synthesis from syngas [27,33,35] and also C_{2+} oxygenates are more favorable thermodynamically at high pressure, the second part of the present work is focused on syngas conversion to oxygenates at high pressure (> 5000 kPa).

It is also important to note that some C_2 oxygenates could be intermediates for other C_2 oxygenates. For example methyl formate has been identified as an important intermediate species for ethanol synthesis from C_1 species over Cu-metal oxide catalysts [20,32] and therefore, monitoring the formation of C_2 oxygenates with respect to each other during catalytic testing of alkali-promoted Cu-metal oxide is essential for a better understanding of the formation mechanism of the C_2 oxygenates.

1.2   Objective of the thesis

The objectives of the present study are as follows:

1.   To identify the activity of Cu-MgO catalysts and Cs (K)-promoted Cu-MgO catalysts in the conversion of CO/CH_3OH to C_2 oxygenates such as ethanol, methyl formate and acetic acid at 101kPa and 498-523K. In particular, the objective was firstly, to determine the effect of catalyst basic properties and catalyst copper properties on the synthesis of C_2 oxygenates and secondly, to unravel the formation and decomposition mechanism of C_2 oxygenates on these catalysts based on the proposed mechanisms in the literature and the measured catalyst properties/activities in the present study.

2.   To identify the activity of a selected Cu-MgO catalyst for syngas (CO/H_2) conversion to oxygenates and other carbonaceous products (such as hydrocarbons) at typical industrial conditions (reaction pressure > 6000kPa and reaction temperature of 558-598K). The catalyst selected for this part of the study was the most active Cu-MgO catalyst in the synthesis of C_2 oxygenates from CO/CH_3OH at 101 kPa and 498-523K. The focus of the study was firstly, to develop a kinetic model for the dominant oxygenate product using the mechanistic information discussed in objective 1 and secondly, to compare the activity of the selected Cu-MgO-based catalyst in synthesis of oxygenates to the activity of a conventional-industrial Cu-ZnO catalyst reported in the literature. Subsequently the observed discrepancy in the activity of the catalysts is to be discussed based on the differences in the properties of the catalysts.

1.3   Approach of this thesis

An experimental approach was used to achieve the first objective of the present study. Preparation of MgO by thermal decomposition of the metal salts in the presence of palmitic acid was reported previously in the literature [41]. In the present study, this method of preparation was extended to the preparation of high surface area Cu-MgO and K or Cs promoted Cu-MgO. The Cu-MgO-based catalysts were tested in a plug flow reactor at 101 kPa to investigate the formation of C_2 oxygenates from CO and CH_3OH. The prepared catalysts were extensively characterized using different techniques such as N_2 physisorption-desorption isotherm, H_2 temperature program reduction (H_2 TPR), CO_2 temperature program desorption (CO_2 TPD), X-ray powder diffraction (XRD), X-ray photoelectron spectroscopy (XPS), N_2O pulse chemisorption, CHN analysis (to analyze carbon, hydrogen and nitrogen content). The results of the catalyst characterization and catalyst testing were used to establish correlations between the catalyst properties and the catalyst activity. Finally the formation and decomposition of C_2 oxygenates was examined in view of mechanistic details published in the literature.

The approach to achieve the second objective of the present study was also experimental. The Cu-MgO-based catalyst that showed the highest activity towards the formation of C_2 oxygenates from CH_3OH and CO at 101 kPa, was used for high pressure studies. The candidate catalyst was tested in a plug flow reactor at high operating pressure (>5000 kPa) to investigate the formation of oxygenates and other carbonaceous products (such as hydrocarbons) from syngas (CO/H_2). The kinetics of the CH_3OH synthesis reaction was

described using a Langmuir-Hinshelwood model. A systematic residence time study as well as a partial factorial design were used to specify the operating conditions of the kinetic study. The catalyst activity over the candidate catalyst was compared to the Cu-ZnO catalyst reported in previous studies. The differences between the activities of the two catalysts are discussed based on the properties of the catalysts.

1.4 Outline of the dissertation

The Ph.D. thesis is prepared in the following order:

Chapter 1: An introduction for oxygenate synthesis from C_1 species over alkali promoted Cu-metal oxide based catalysts is provided. Also the thesis objectives and thesis approach are explained.

Chapter 2: The detail of the catalyst preparation method and the results of characterization of MgO, 40wt% Cu-MgO and K or Cs promoted 40wt% Cu-MgO are reported. The catalyst activity towards formation and decomposition of C_2 oxygenates from/to C_1 species (CO and methanol) at 101 kPa are reported. The correlation between the formation of C_2 oxygenates and the basic properties of the prepared catalysts are reported and discussed.

Chapter 3: The results of characterization of the 5wt% Cu-MgO and K or Cs promoted 5wt% Cu-MgO catalysts are provided. The catalyst activity towards the formation and decomposition of C_2 oxygenates from/to C_1 species (CO and methanol) at 101 kPa are

reported. The catalyst activity for C_2 oxygenates over 5wt% Cu-MgO based catalysts and 40wt% Cu-MgO based catalysts are compared. The correlation between the formation of C_2 oxygenates and the copper properties of the prepared catalysts are also reported and discussed.

Chapter 4: Among the prepared alkali promoted Cu-MgO catalysts in the present study, the one that showed the highest activity towards C_2 oxygenates at 101 kPa were used in high pressure studies. The activity of the catalyst towards formation of oxygenates from syngas (CO/H_2) at high operating pressure (> 5000 kPa) were reported. A detailed kinetic model of the methanol synthesis and the parameter estimation results are also reported. The catalyst activity towards oxygenates at high pressure over the Cu-MgO-based catalyst is compared to the Cu-ZnO-based catalyst (reported in the literature) and the difference in the catalytic activity of the two mentioned catalysts is discussed based on the characteristics of the two catalysts.

Chapter 5: The conclusions of the previous chapters are summarized in this chapter and the recommendations for the future work are provided.

1.5 Syngas

Syngas (also known as synthesis gas) is a gas mixture that contains CO and H_2 with low concentration of CO_2. Syngas can be produced by biomass gasification, coal gasification and natural gas reforming. In the process of natural gas reforming, methane (from natural gas)

combines with water to generate syngas according to the following reaction: $CH_4 + H_2O \rightarrow$ $CO + 3H_2$. In the process of gasification, organic-based carbonaceous material (biomass) or fossil based carbonaceous material (coal) is reacted at high temperature (>700°C) without combustion in the controlled presence of air/oxygen and steam to produce syngas [42]. The produced syngas may contain sulfur-based impurities (such as H_2S) or nitrogen-based impurities (such NH_3) that must be removed before being used in other processes. Syngas can be converted to different fuels (such as gasoline and diesel) and valuable chemicals (such as oxygenates, paraffins and olefins) [42]. For example, the synthesis of fuels such as gasoline and diesel from syngas by Fischer– Tropsch (FT) synthesis using Fe-based and Co-based catalysts has been commercialized [43,44]. Another example is the well-established industrial synthesis of methanol (oxygenates) from syngas over (a) Cu-ZnO-based catalyst (i.e.: $ZnO-Al_2O_3$ and $Cu-ZnO-Cr_2O_3$) at reaction temperature of 523K and reaction pressure of 5000 kPa-10000 kPa or (b) ZnO-based catalyst (i.e: $ZnO-Cr_2O_3$) at reaction temperature of 673K and reaction pressure of 10000-20000 kPa [28,45-48].

1.6 Oxygenates

Since, synthesis of oxygenates from syngas over alkali promoted Cu-metal oxide catalysts is of interest in the present study, it is important to keep in mind the following definitions. Oxygenates are hydrocarbonacious compounds that contain oxygen atoms in their molecular structure. Some examples of oxygenates are alcohols, ketones, esters, and ethers. C_2 oxygenates are oxygenates that contain only two carbon atoms in their molecular structure.

Some examples of C_2 oxygenates are ethanol, methyl formate and acetic acid. C_{n+} oxygenates are oxygenates that contain $\geq$ n carbon atoms in their molecular structure.

1.7   Background on oxygenates synthesis from syngas over Cu-metal oxide

Syngas conversion over Cu-metal oxide catalysts at reaction pressure of 5000 kPa - 10000 kPa and reaction temperature of 523K – 598K, yields a wide range of oxygenated products such as alcohols, ketones, esters, and ethers [9-28]. Among many Cu-metal oxide catalysts, Cu-ZnO has received most attention due to its high activity for alcohols synthesis, especially methanol, and a low catalyst cost. Methanol synthesis over Cu-ZnO has been commercialized since 1920 [9,10,20,28,34,48-54]. During the 1980's, it was found that addition of alkali metals (such as K or Cs) to Cu-ZnO increased the catalyst selectivity to C_{3+} alcohols [9,17,18,20,22,27,51,55,56], forming principally C_3–C_4 alcohols. In most cases the dominant product was 2-methyl-1-propanol. C_2 oxygenates (mainly ethanol) were considered an important intermediate for the formation of heavier oxygenates. However, it is noteworthy that based on previous studies the alkali-promoted Cu-ZnO showed low selectivity towards C_2 oxygenates.

1.8   Mechanism of oxygenate synthesis from syngas over Cu-metal oxide

1.8.1   CH₃OH synthesis

The mechanism and kinetics of CH_3OH synthesis from syngas over Cu-metal oxide based catalysts has been extensively investigated in the past six decades. In the last 20 years there was much debate on the question of whether CO or CO_2 was the important source of carbon in methanol synthesis. In this regard there are several different proposed mechanisms for the methanol synthesis from syngas.

The first mechanism, shown in Figure 1, assumes that CO is the important source of carbon for methanol synthesis [20,31,47,57]. The mechanism assumes that the hydrogenation of a surface H_2CO^- to surface methoxy, is the rate determining step in the methanol synthesis [47,57]. Note that in order to simplify Figure 1 as well as subsequent figures, the reaction pathway and intermediates containing carbon atoms are shown, whereas the H, OH, H_2O and H_2 species are omitted.
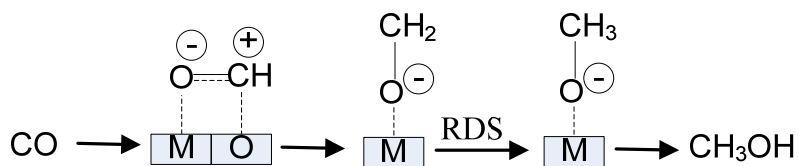
Figure 1. Methanol synthesis mechanism from CO over Cu-metal oxide [20,31,47,57]. Note: M stands for metal cation and RDS stands for rate determining step.

Some other mechanistic studies suggested that CO_2 is the important source of carbon for methanol synthesis [20,47,58]. Furthermore some of the previous kinetic studies showed the direct effect of CO_2 pressure on methanol synthesis from CO_2/H_2 [54]. For example kinetic studies on methanol synthesis from CO_2/H_2 over Cu-SiO_2, showed that an increase in the feed pressure from 2.5 bar to 6 bar, led to an increase in methanol turn over frequency (TOF) by a factor of three [54]. With respect to these kinetic and mechanistic studies, an alternative reaction mechanism for methanol synthesis was proposed in which CO_2 was assumed as the important source of carbon for methanol synthesis (Figure 2). It was suggested that in the methanol synthesis from CO_2/H_2, hydrogenation of a surface formate to surface methoxy is the rate determining step [47,57,58]. However, some mechanistic studies suggested that at dry CO_2/H_2 feed condition, the rate of direct hydrogenation of surface formate species to surface methoxy was not consistent with the rate of methanol synthesis [59]. Furthermore it was suggested that hydrogenation of surface formate to surface methoxy may be catalyzed in the presence of water-derived surface adsorbates.
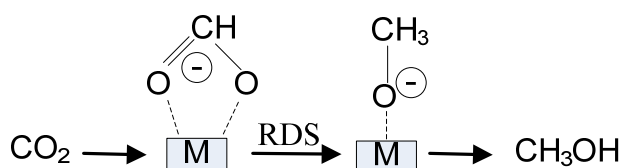
Figure 2. Mechanism 1 for methanol synthesis from CO_2 over Cu-metal oxide [20,47,58]. Note: M stands for metal cation and RDS stands for rate determining step.

On the other hand, recent density function theory (DFT) studies and infrared (IR) studies on methanol synthesis from CO_2 do not support the latter mechanism [53,54]. For example, based on a previous IR study, titration of formate on Cu-SiO_2 in H_2 rich atmosphere resulted

in less than 3 % methanol, while the rest of the formate was decomposed back to CO_2 and H_2 [54]. Also based on DFT studies, it was suggested that due to a high hydrogenation barrier of HCOO (Figure 2) and H_2COO (not shown in Figure 2), direct hydrogenation of surface formate to surface methoxy does not lead to the formation of methanol from CO_2,[53]. Furthermore an alternative hydrocarboxyl mechanism was proposed for methanol synthesis from wet CO_2/H_2, (Figure 3), in which the mechanistic steps were reported to be feasible based on DFT calculations. In this mechanism the decomposition of COHOH to COH and OH was reported as the rate limiting step.
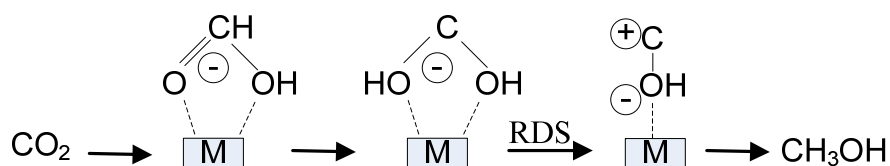
Figure 3. Mechanism 2 for methanol synthesis from CO_2 over Cu-metal oxide [53]. Note: M stands for Cu and RDS stands for rate determining step.

Another proposed mechanism assumes that CO and CO_2 are both important sources of carbon for methanol synthesis, with the hypothesis that they compete for the same active catalytic sites [48]. On the other hand, other mechanistic and activity studies have suggested that CO and CO_2 may be activated on different catalytic sites [45-47,60]. For example activity studies on methanol synthesis from CO/H_2 over alkali promoted-Cu-ZnO-Cr_2O_3 at high pressure suggested that when CO_2 was added to the feed, the catalyst became more active in methanol synthesis [47,60]. Furthermore it was proposed that CO is converted to CH_3OH over Cu/alkali interfaces of the catalyst, whereas CO_2 is converted to CH_3OH over Cu sites of the catalyst [47]. It is noteworthy that despite the debate on catalytic active sites

for CO and CO_2 conversion to CH_3OH, the reaction mechanisms regarding CO or CO_2 conversion to methanol are similar to the previously described mechanisms in Figure 1, Figure 2 and Figure 3.

1.8.2   Higher alcohol synthesis (HAS)

Based on previous studies of the HAS over Cu-metal oxide catalysts, three reaction pathways were proposed [22,28,47], which are shown in Figure 4. The mentioned reaction pathways are: 1- ℓ-reaction pathway which leads to linear alcohol formation, 2- β-reaction pathway which leads to branched alcohol formation and 3- α_0- reaction pathway which leads to methyl ester formation.
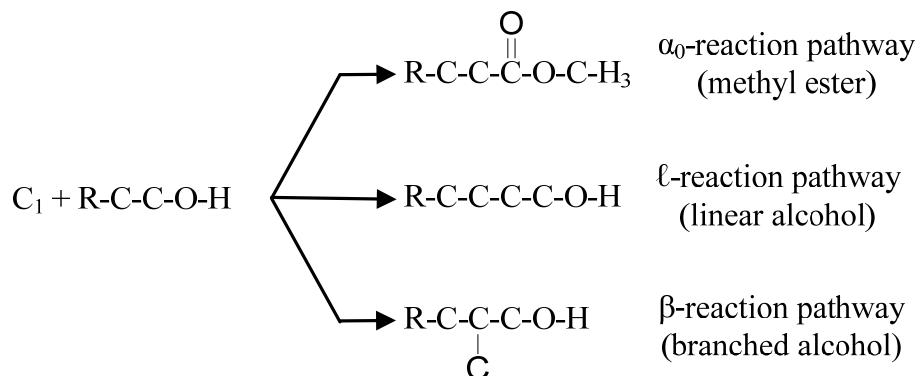
Figure 4. Reaction pathway for higher alcohol synthesis over Cu-metal oxide catalyst [22,28,47].

It was noted that the β-reaction pathway was kinetically much more favorable than ℓ-reaction pathway, which indicated that ethanol synthesis was a slow process [47]. It is noteworthy that some of the previous studies have suggested that the ℓ-reaction pathway proceeds via CO

insertion in to a surface alkoxide [28,61-63] yielding, for example ethanol. On the other hand, some studies proposed that the ℓ-reaction pathway proceeded as a nucleophilic substitution reaction (S_N2) between formaldehyde and an alcohol with the OH group of the alcohol as the leaving group [51]. The proposed mechanism for ℓ-reaction pathway was later supported by other studies in which a mixture of $^{13}CH_3OH$ and $^{12}CO/H_2$ were used to identify the coupling species [20,27,51]. The proposed mechanism for ℓ-reaction pathway could be considered as one the most likely mechanisms for ethanol synthesis from syngas over Cu-metal oxide catalysts.

1.8.3   Ethanol synthesis

Three different reaction pathways have been proposed for ethanol synthesis from syngas over Cu-metal oxide catalysts, described as follows [20]:

Direct synthesis from CO/H_2

$$2CO + 4H_2 \rightarrow C_2H_5OH + H_2O \ (\Delta H^o_{298K} = -256.1 \ \tfrac{kJ}{mol} \ \text{and} \ \Delta G^o_{298K} = -122.2 \ \tfrac{kJ}{mol}) \quad (R1)$$
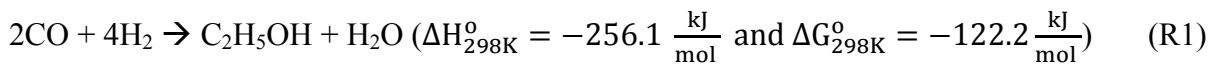
Homologation of methanol by CO/H_2

$$CH_3OH + CO + 2H_2 \rightarrow C_2H_5OH + H_2O \ (\Delta H^o_{298K} = -165.3 \ \tfrac{kJ}{mol} \ \text{and} \ \Delta G^o_{298K} = -97.0 \tfrac{kJ}{mol})$$

$$(R2)$$

Coupling reaction of two methanol molecules

$$2CH_3OH \rightarrow C_2H_5OH + H_2O \ (\Delta H^o_{298K} = -74.5 \ \frac{kJ}{mol} \ and \ \Delta G^o_{298K} = -71.8 \frac{kJ}{mol}) \tag{R3}$$
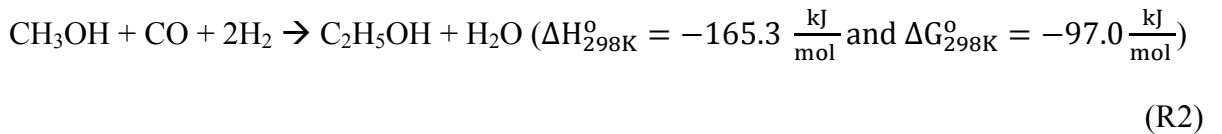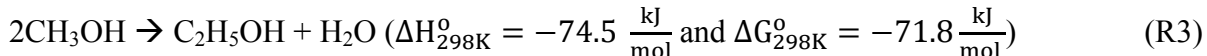
The source of C_2 oxygenates was investigated by using $^{13}CH_3OH$ and $^{12}CO/H_2$ as reactants and using ^{13}C NMR analysis to identify the appearance of $^{12}CH_2$, $^{13}CH_2$, $^{12}CH_3$ and $^{13}CH_3$ in the product [20]. Based on the NMR results, it was suggested that in the ethanol synthesis, methanol is the dominant reactant. Several mechanisms have been proposed for reaction R3. One of the previous mechanistic studies suggested that methanol is formed via a nucleophilic attack of an adsorbed formyl on formaldehyde over an alkali acetylide catalyst [51]. In this study it was assumed that both formyl and formaldehyde were preferentially formed from methanol, although it was noted that a small portion of these two intermediate species were provided by CO/H_2 reactants (Figure 5). Other studies supported this mechanism over a Cu-metal oxide-Al_2O_3 catalyst [33].
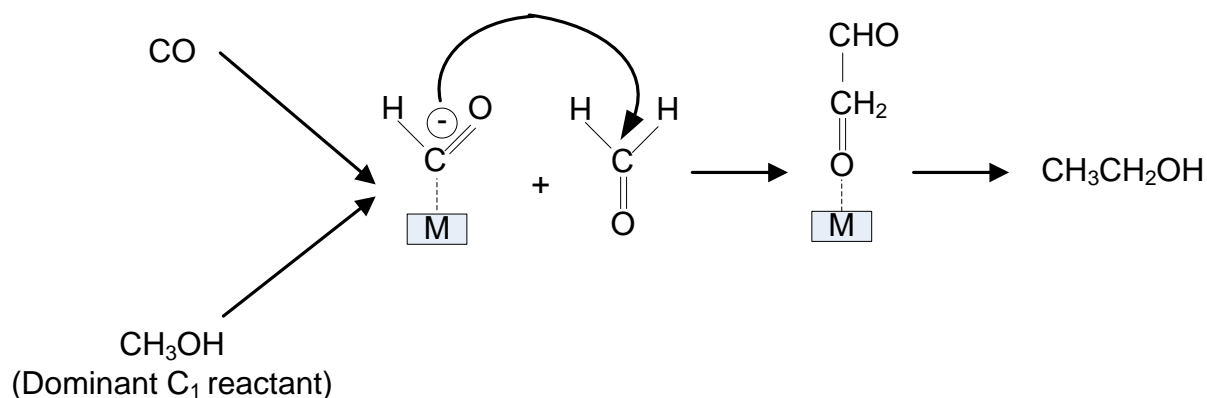
Figure 5. Mechanism 1 for ethanol synthesis from C1 reactant (methanol and CO) [20,33,51]. M stands for metal cation.

An alternative mechanism satisfying reaction R3, involves a nucleophilic attack of methanol by formyl species as presented in Figure 6 [20,64].
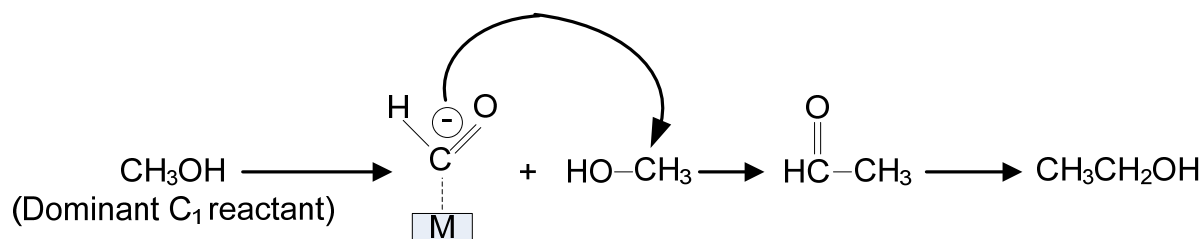
Figure 6. Mechanism 2 for ethanol synthesis from C_1 reactant (methanol) [20,64]. M stands for metal cation.

Another study suggested ethanol formation from $^{13}CO/H_2/^{12}CH_3OH$ occurred predominantly by direct reaction of ^{13}CO over alkali-promoted Cu-metal oxide [32]. In this study $^{12}CH_3OH$ did not show significant involvement in ethanol formation (Figure 7), which differs from previous mechanistic results (Figure 5 and Figure 6). This study proposed that formation of ethanol with $^{13}C-^{13}C$ bonding took place by the nucleophilic attack of the surface precursor $(CH_3O^{13}CO^-)$ on the $^{13}C^+$ in the formate or methyl formate as shown in Figure 7 (path I and II). Also it was proposed that the surface precursor $(CH_3O^{13}CO^-)$ could react with surface formaldehyde species derived from methanol to form ethanol with $^{12}C-^{13}C$ bonding (Figure 7-path III). However, it was stated that path I and II are predominant compared to path III in Figure 7. Based on path I and II in Figure 7, it is apparent that methyl formate and the derived formate species are considered as an important intermediate for ethanol synthesis from C_1 species which is in good agreement with previous mechanistic studies [20].
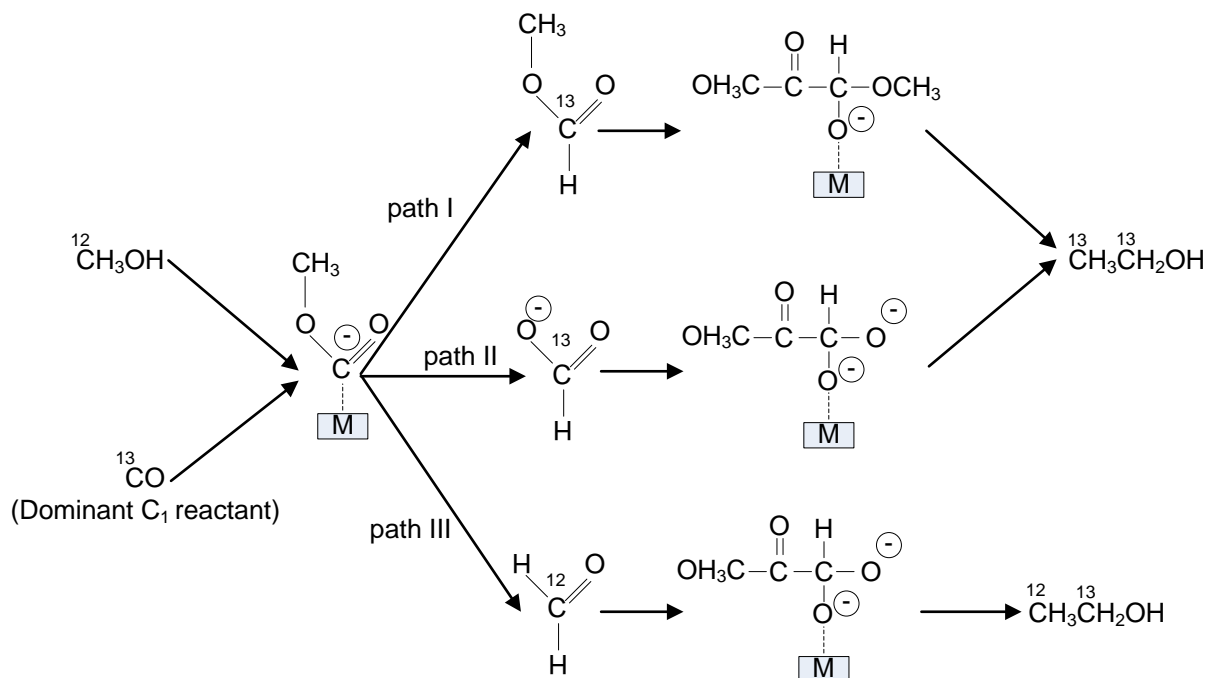
Figure 7. Mechanism 3 for ethanol synthesis from C_1 reactant (CO) [32]. M stands for metal cation or Cu.

Another study suggested an alternative ethanol synthesis mechanism from C_1 reactants (CO or methanol) over alkali-Cu catalyst. According to Klier [55], a CO insertion into an alkyl-metal bond followed by hydrogenation leads to ethanol formation (Figure 8).
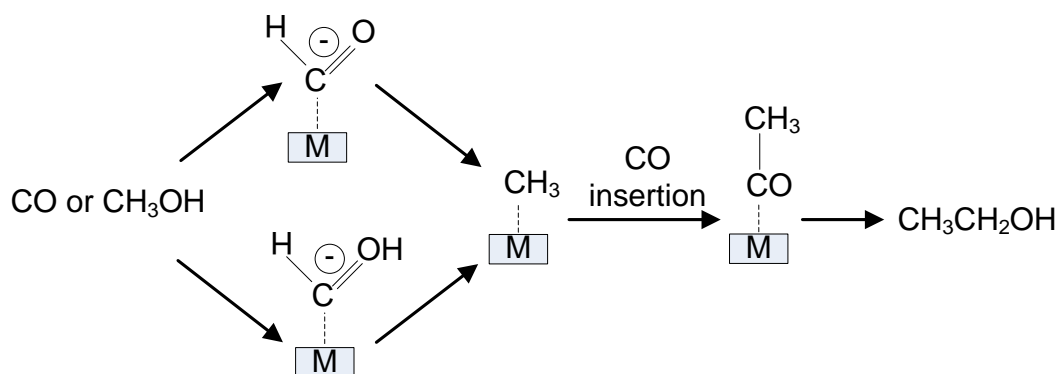
Figure 8. Mechanism 4 for Ethanol synthesis from C_1 reactant (CO) [55]. M stands for metal cation or Cu.

As explained earlier in this section, it was suggested that ethanol is formed by a coupling reaction of two methanol molecules given in reaction R3 [20]. Since this theory was supported by many other studies [33,51,64], in the present study methanol was chosen as a source of C_1 species for ethanol synthesis.

1.8.4 Methyl formate synthesis

C_1 species conversion to methyl formate over Cu-based catalysts and Cu-metal oxide based catalysts has also been well studied. Cu plays a significant role as an active catalyst for methyl formate formation [2,54,65]. Two reaction pathways have been proposed for methyl formate synthesis from C_1 species (CO and methanol) over Cu-metal oxide based catalysts [20]:

Direct carbonylation of methanol with CO

$$CH_3OH + CO \rightarrow CH_3OCOH \ (\Delta H^o_{298K} = -25.1 \ \frac{kJ}{mol} \ and \ \Delta G^o_{298K}) \quad\quad (R4)$$
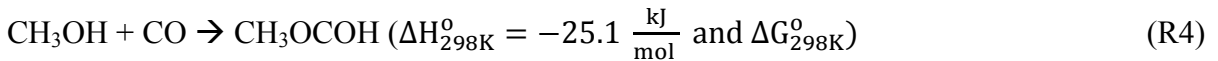
Dehydrogenation of methanol

$$2CH_3OH \rightarrow CH_3OCOH + 2H_2 \ (\Delta H^o_{298K} = 65.7 \ \frac{kJ}{mol} \ and \ \Delta G^o_{298K} = 27.4 \ \frac{kJ}{mol}) \quad\quad (R5)$$
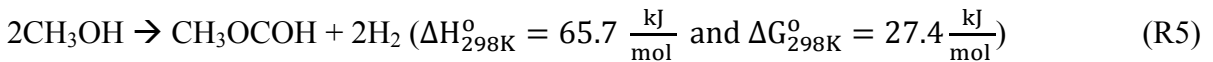
Several mechanistic studies focused on the synthesis of methyl formate from C_1 species over Cu-metal oxide catalysts [4,5,20]. Three mechanisms have been proposed:

Mechanism 1: Based on ^{13}C NMR analysis using [12]CO and [13]CH$_3$OH, the first proposed mechanism suggested that methyl formate formed by direct coupling of an intermediate methoxy anion and CO [20], shown in Figure 9. It was concluded that the methoxy species are derived from methanol, whereas the carbonyl groups are derived from CO.
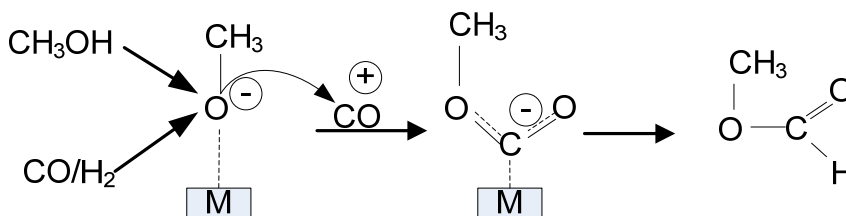
Figure 9 Mechanism 1 for methyl formate synthesis from C$_1$ reactants (CO+CH$_3$OH) [20]. M stands for Cu or metal cation.

Mechanism 2: Based on ^{13}C labeling studies as well as H/D studies for the synthesis of methyl formate from [13]CH$_3$OH (or CD$_3$OD/CH$_3$OD), it was proposed that methyl formate is formed via a nucleophilic attack of a surface methoxy species on a surface formyl species [4,5], shown in Figure 10. It was suggested that methoxy species and formyl species were derived from methanol.
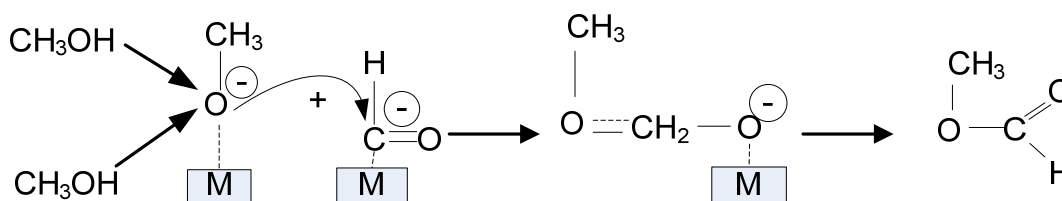
Figure 10 Mechanism 2 for methyl formate synthesis from C$_1$ reactants (CH$_3$OH) [4,5]. M stands for Cu or metal cation.

Mechanism 3: Based on ^{13}C labeling studies as well as H/D studies for the synthesis of methyl formate from [13]CH$_3$OH (or CD$_3$OD/CH$_3$OD), it was proposed that methyl formate is formed via a nucleophilic attack of a surface methoxy species on a surface formate species [4,5], shown in Figure 11. It was suggested that methoxy species and formate species were derived from methanol.
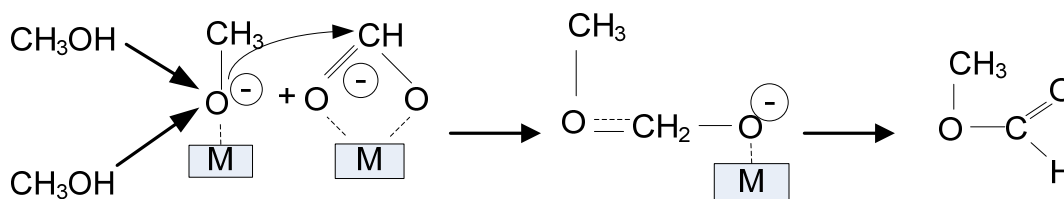
Figure 11 Mechanism 3 for methyl formate synthesis from C$_1$ reactants (CH$_3$OH) [4,5]. M stands for Cu or metal cation.

1.9   Synthesis of oxygenates over MgO-based catalysts

While a great deal of work has been reported on the oxygenate synthesis over transition metal oxide-based catalysts, to the author's knowledge few studies have focused on the oxygenate synthesis from syngas over Cu-alkali earth metal oxides, such as Cu-MgO [25,32]. The production of methanol and higher alcohols over Mg$_y$CeO$_x$ was reported previously [25]. In that study Mg$_5$CeO$_x$ catalyst was modified to K-Cu$_{0.5}$Mg$_5$CeO$_x$ and it was reported that the resulting catalyst was more selective towards the formation of isobutanol compared to Mg$_5$CeO$_x$. Another study reported the production of ethanol over K-Cu-Mg$_5$CeO$_x$ from [13]CO/H$_2$/[12]CH$_3$OH [32]. However, none of these studies focused on finding a correlation

21

between basic properties of the catalysts and their activity for oxygenate synthesis from syngas.

1.10 Basic properties of alkali promoted MgO

Previous work focused on studying the basicity of alkali promoted MgO catalysts [36,38,66]. For example, the number of basic sites in alkali promoted-MgO catalysts was measured using isothermal chemisorption of CO_2 at 298 K and CO_2 temperature program desorption (TPD) [36]. It was proposed that the addition of alkali metal ions to MgO increased the surface concentration of basic sites in the order of Na < K < Li ≈ Cs . On the other hand the strength of the basic sites was measured by deconvolution of the CO_2 TPD curve as well as by infrared spectroscopy (IR) [36]. The result showed that addition of alkali metal ions to MgO increased the strength of the basic sites in a slightly different order compared to the surface concentration of basic sites as shown accordingly: Li < Na < K < Cs. The enhancement effect of the alkali promoters on surface basicity of the MgO is due to a combination of two factors: the electron donating ability of the alkali oxide (A_2O) and the concentration of surface alkali ion (A^+) in the sample. The unique behavior of Li promoter in increasing the surface concentration of basic sites was attributed to the fact that Li was the only alkali metal that showed a solid solution effect with MgO crystallites [66]. It was proposed that due to a slightly smaller radius of Li^+(0.73A) in Li_2O compared to the radius of Mg^{2+}(0.86A) in MgO, the substitution of Li^+ with Mg^{2+} in MgO crystallites can occur easily which leads to a noticeable increase in concentration of basic sites in Li-MgO compared to other alkali promoted MgO catalysts [66].

Previous studies showed that MgO-based catalysts possessed higher basicity compared to traditional ZnO-based catalysts [36-40]. For example, the basic site density of MgO has been reported as $2.2 - 7.2$ μmol CO_2 m^{-2} [36-39], whereas for ZnO-ZrO$_2$ a value of 0.9 μmol CO_2 m^{-2} has been reported [40].

Chapter 2

The effect of catalyst basic properties on the formation of methyl formate and C$_2$-oxygenates from CH$_3$OH and CO over Cs (K)-promoted Cu-MgO catalysts at 101 kPa

2.1   Introduction

C$_2$ oxygenates, such as methyl formate, ethanol and acetic acid, are fuels as well as intermediates to valuable heavier chemicals, such as C$_{3+}$ oxygenates. Synthesis of oxygenates from syngas over Cs (K)-promoted Cu-metal oxide catalysts showed low selectivity towards C$_2$ oxygenates [20,26-28]. Previous mechanistic studies over the mentioned catalysts suggested that the presence of basic sites play an important role in the synthesis of C$_2$ oxygenates [20,29-34]. MgO possesses higher basic properties compared to ZnO [36-40]. While most of the activity studies have focused on Cs (K)-promoted-Cu-ZnO catalysts, only a few studies have focused on Cs (K)-promoted-Cu-MgO catalysts [25,32]. To the author's knowledge none of the activity studies on Cs (K)-promoted-Cu-MgO catalysts focused on determining a correlation between the catalyst basic properties and the catalyst activity to C$_{2+}$ oxygenates. In this chapter, the synthesis of high surface area Cs (K)-promoted Cu-MgO catalysts and their activity for synthesis of C$_2$ oxygenates from CH$_3$OH at 101 kPa is reported. Note that atmospheric pressure was used to simplify the experimental procedure. Also it was decided to use a mixture of CO/CH$_3$OH for the reactor feed stream. By using

CH$_3$OH as reactant and operating the reactor at low pressure (101 kPa) and moderate temperature (498 K – 523 K), the decomposition of the feed CH$_3$OH that will generate carbonaceous surface species that can react further to produce C$_2$ oxygenates was assured. The prepared catalysts in the present study were extensively characterized and the results of the characterization were used to establish a correlation between the basic properties of the prepared catalysts and their activity for C$_2$ oxygenate synthesis. Also, the basic properties of the Cs (K)-promoted-Cu-MgO were compared against a commercial Cs (K)-promoted-Cu-ZnO to understand the differences in their basic properties.

It is important to note that some C$_2$ oxygenates could be intermediates for other C$_2$ oxygenates. Methyl formate has been identified as an important intermediate for synthesis of C$_2$ species (ethanol and acetic acid) from CH$_3$OH/CO over Cu-metal oxide [20,32]. Therefore, in this chapter, for better understanding of the mechanism of the C$_2$ oxygenates synthesis, the formation of methyl formate and C$_2$ species with respect to each other over the Cs (K)-promoted Cu-MgO was studied

2.2   Experimental

2.2.1   Catalyst preparation

High surface area, MgO, Cu-MgO, alkali promoted Cu-MgO (0.5 wt % K-40wt% Cu-MgO, 4.4 wt % K-40wt% Cu-MgO, 0.5 wt % Cs-40wt% Cu-MgO and 13.5 wt % Cs-40wt% Cu-MgO) and bulk CuO were prepared by thermal decomposition of metal salts in the presence

of palmitic acid ($CH_3(CH_2)_{14}COOH$) [41]. Note that the 4.4 wt % K and the 13.5 wt % Cs promoted 40wt% Cu-MgO catalysts had the same alkali/Mg molar ratio of 0.08. $Mg(NO_3)_2.6H_2O$, $Cu(NO_3)_2.3H_2O$, Cs_2CO_3 and KNO_3 were used as the source of MgO, Cu, Cs_2O and K_2O/KOH, respectively. The molar ratio of palmitic acid to (Mg+Cu+alkali metal) was 2.5 [41]. Note that in all cases the catalysts were nominally 40 wt % Cu and 60 wt % MgO when in the reduced state. As an example, to prepare the 0.5 wt % Cs-40wt% Cu-MgO catalyst, 7.00 g of $Mg(NO_3)_2.6H_2O$ (Sigma-Aldrich, 99 %), 2.80 g of $Cu(NO_3)_2.3H_2O$ (AlfaAesar, 98-102 %), 0.01 g Cs_2CO_3 (Sigma-Aldrich, 99 %) and 25.00 g palmitic acid (Sigma-Aldrich, 98 %) were mechanically mixed in a crucible without adding water and placed in a furnace (Barnstead/Thermolyne 47900) in air at ambient pressure. Note that more detail on the mass loading of metal salts used in the catalyst preparation is shown in Appendix A. The mixture was heated from ambient temperature to 373 K at 40 $K.min^{-1}$ and was kept at this temperature for 90 min. Afterwards, the mixture was further heated to 443 K at 40 $K.min^{-1}$ and was kept at this temperature for 90 min. The solid catalyst precursor was obtained by subsequent calcination at 923 K. Calcination was achieved at a heat up rate of 0.8 $K.min^{-1}$ and the final temperature was held for 300 min before cooling to room temperature. Finally, the catalyst precursor was reduced by heating to 573 K at a rate of 10 $K.min^{-1}$ in 10 % H_2/He, with the final temperature held for 60 min in 10% H_2/He, yielding 1.85 g of the 0.5 wt % Cs-40wt% Cu-MgO catalyst.

Note that the final calcination temperature used for each catalyst precursor was determined by the highest decomposition temperature of the metal nitrates or carbonates present in the precursor. For MgO, Cu-MgO, K-Cu-MgO and Cs-Cu-MgO the calcination temperatures

were 673 K, 673 K, 873 K and 923 K, respectively. The effect of calcination temperature, calcination time and the amount of palmitic acid used in the preparation of the MgO was also examined. In addition, one sample of MgO was prepared without the use of palmitic acid and consequently, in this case, the thermal treatment prior to calcination that was conducted on the MgO-based catalysts (373 K for 60 min and 443 K for 60 min) was not necessary.

2.2.2 Catalyst characterization

Temperature programmed reduction (TPR) of the prepared catalyst precursors was performed in a 10 % H_2/Ar gas flow of 50 cm^3(STP).min^{-1} and heating at a ramp rate of 10 K.min^{-1} from 313 K to 623 K, with the final temperature held for 30 min. Prior to the TPR, samples (about 0.2 g) were pre-treated thermally in He at 50 cm^3(STP).min^{-1} and 393 K. Hydrogen consumption was monitored by a thermal conductivity detector (TCD) attached to a Micromeritics AutoChem II chemisorption analyzer. During the analysis the effluent gas was passed through a cold trap placed before the TCD in order to remove water from the exit stream of the reactor. Both CuO and Cu_2O (97 % purity, particle size < 5 micron, Sigma Aldrich) were also examined by TPR.

Catalyst BET surface areas (SA_{BET}) were measured before and after reduction whereas the catalyst pore volume (V_p) and pore diameter (d_p) were measured before reduction only. The mentioned properties of the un-reduced catalysts were determined from N_2 adsorption-desorption isotherms measured at 77K using a Micromeritics ASAP 2020 analyzer. Catalysts were degassed in 523 K for 24 h under vacuum (5 μm Hg) before being analyzed. Eight N_2

uptake measurements made in the range $0.06 < \frac{P_{N2}}{P_{N2}^0} < 0.20$ were used to calculate the catalyst

BET surface area. Note that P_{N2} and P_{N2}^0 are respectively the equilibrium pressure of N_2 and

saturation pressure of N_2 at 77K. The uptake of N_2 at $\frac{P_{N2}}{P_{N2}^0} = 0.975$ was used to specify the

catalyst pore volume. Pore diameter was calculated based on the pore size distribution

measured from the N_2 desorption in the range of $0.01 < \frac{P_{N2}}{P_{N2}^0} < 0.99$.

The BET surface area of the reduced catalysts was measured using the Micromeritics

AutoChem II chemisorption analyzer. The catalysts were first degassed in 50 cm^3(STP).min^{-1}

He by heating from ambient temperature to 523 K and holding at 523 K for 120 min. The

catalysts were then cooled to room temperature and the feed gas was switched from He to 10

% H_2 in Ar at a flow rate of 50 cm^3(STP).min^{-1}. The TPR analysis described above was then

conducted on the catalyst. Since MgO adsorbs CO_2 and H_2O, pre-treatment in He at high

temperature (773 K) was required [36,67,68] after reduction and prior to the surface area

measurement. Hence the gas flow was switched from 10 % H_2 in Ar to He at a flow rate of

50 cm^3(STP).min^{-1} and heated to 773 K at a rate of 10 K.min^{-1} for 60 min. The catalysts were

then cooled to room temperature and the feed gas switched from He to 30 vol % N_2 in He at a

flow rate of 50 cm^3(STP).min^{-1} . The single point BET surface area of the reduced catalyst

was calculated by measuring the N_2 uptake of the catalyst at 77 K using the liquid N_2 trap.

Basic properties of the reduced catalysts were determined by CO_2 temperature-programmed

desorption (TPD) using a Micromeritics AutoChem II chemisorption analyzer. The reduced

catalysts were pre-treated thermally by ramping to 773 K at 10 K.min^{-1} for 60 min in 50

cm^3(STP).min^{-1} of He. After cooling to 313 K, the sample was exposed to 50 cm^3(STP).min^{-1} of 10 vol % CO$_2$/He for 60 min. Physically adsorbed CO$_2$ was subsequently removed from the sample by flushing in He (50 cm^3(STP).min^{-1}) at 313 K for 60 min. The catalyst's basic properties were evaluated by observing the capacity of the samples to retain the CO$_2$ during the desorption that occurred in the He flow while increasing temperature from 313 K to 803 K at a rate of 10 K.min^{-1}. The obtained CO$_2$ TPD profile was integrated to determine the catalyst intrinsic basicity, defined as the total CO$_2$ uptake divided by the BET surface area, and taken as a measure of the catalyst basic site density. To quantify the strength of the basic sites, the CO$_2$ TPD profiles were de-convoluted to classify weak (353 - 373 K), medium (373 - 473 K) and strong (> 473 K) basic sites according to their temperature of desorption.

X-ray powder diffraction (XRD) patterns of the prepared catalysts were obtained with a Rigaku Multiflex diffractometer using Cu Kα radiation (λ=0.154 nm, 40 kV and 20 mA), a scan range of 2θ from 10° to 100° and a step size of 2 ^{o} per min. Crystallite size of the metal or metal oxide was estimated from the XRD data using the Scherrer equation. The Cu crystallite thickness (d_{Cu}^{XRD}) was estimated from the CuO crystallite size (d_{CuO}^{XRD}) determined from the XRD data of the non-reduced MgO-based catalysts, and the peak broadening at 2θ = 35.5^o. The Cu crystallite size was then estimated using equation E1. The MgO crystallite size (d_{MgO}^{XRD}) was measured based on the peak broadening at 2θ = 42.9^o.

$$d_{Cu}^{XRD} = \left(\frac{Cu^0 \text{ molar volume}}{CuO \text{ molar volume}}\right) \times d_{CuO}^{XRD} = \left(\frac{12.61\frac{cm^3}{mol}}{0.079\frac{cm^3}{mol}}\right) \times d_{CuO}^{XRD} = 0.56 \times d_{CuO}^{XRD} \tag{E1}$$

The Cu^0 dispersion of the reduced catalysts was measured by adsorption and decomposition of N$_2$O on the surface of Cu according to the stoichiometry: 2Cu^0+N$_2$O$\rightarrow$N$_2$+Cu$_2$O. The pulse titration technique was used. Following reduction, the catalysts were pre-treated thermally by heating to 773 K at a rate of 10 K.min^{-1} for 60 min in a flow of 50 cm^3(STP).min^{-1} of He. The catalysts were then cooled to room temperature before the N$_2$O pulse titration was initiated using 10% N$_2$O/N$_2$ as the pulse gas. A TCD attached to a Micromeritics AutoChem II chemisorption analyzer was used to detect the consumption of N$_2$O and Cu^0 dispersion was calculated from the total amount of N$_2$O consumed. A liquid Ar trap was used to condense N$_2$O from N$_2$ in the effluent, and hence only the N$_2$ was detected by the TCD.

The content of C, H and N in the prepared catalysts was identified using a combustion process to break down substances into simple compounds that were measured. The analysis was carried out with a Perkin-Elmer 2400(II) CHNS/O analyzer. Note that the CHN analysis was conducted on the passivated-Cs (K)-promoted-40wt% Cu-MgO catalysts. The reduced 40wt% Cu-MgO-based catalysts were passivated in a flow of 100 cm^3(STP).min^{-1} of 1% O$_2$/He for 120 min.

2.2.3   Catalyst testing

Catalyst testing was conducted in a stainless steel fixed bed tubular reactor shown in Figure 12 operated at atmospheric pressure with inert He and Ar mixed with CO, H$_2$ and CH$_3$OH as reactants. The catalyst (0.1 – 1.98 g) was loaded into the isothermal section of the reactor and

reduced in 10 % H_2/He at a flow rate of 100 cm^3(STP).min^{-1} and a ramp rate of 10 K.min^{-1} from ambient temperature to 573 K. After further heating in pure He to 773 K, the reactor was cooled to the desired reaction temperature. The desired reactant gases at a total flowrate of 73 cm^3(STP).min^{-1} passed through two saturators in series containing pure CH_3OH at 296K to generate the CH_3OH vapor (12 cm^3(STP).min^{-1}). Note that each of the methanol bubblers was placed inside a cooling bath filled with tap water and equipped with a thermometer. The temperature of the cooling baths was controlled by manual addition of tap water. The feed mixture then passed through a pre-heater at 383 K before entering the reactor. The gas flow lines between the pre-heater and the reactor as well as between the reactor and the mass spectrometer were held at the same temperature as the pre-heater (383K) using heating tapes. The reactor product composition was determined using a VG ProLab quadrupole mass spectrometer that continuously monitored the reactor exit gas line. In the present work, the focus was on the initial activity of the catalysts that were to be related to the properties of the fresh catalysts. Hence, after a 10 min reactor stabilization period, data were collected over the next 10 mins and the average of these analyses is reported herein. Calculation were used to confirm that at the chosen conditions, the catalyst activity data were free of both internal and external heat and mass transfer effects. For each experiment the performance of the catalyst was compared to an identical experiment conducted in the absence of the catalyst so that the effect of thermal reactions or activity from the wall of the reactor were accounted for. The data reported herein are net of the blank run conversions and product yields. In each experiment conversion was defined as the total C-atom conversion of CH_3OH or [CH_3OH + CO] in the case that CO was present in the feed. In most cases however, there was no net CO consumption since CH_3OH decomposed mostly

to CO. The product C-atom yield was calculated as the division of the total exit C-atom molar flow rate of the desired product by the total inlet C-atom molar flow rate of CO and CH_3OH. Product C-atom selectivity was determined as the C-atom yield of the desired product divided by the total C-atom conversion. More detail on calculation of net CO consumption, net CH_3OH conversion, product C-atom selectivity and product C-atom yield is given in Appendix F.
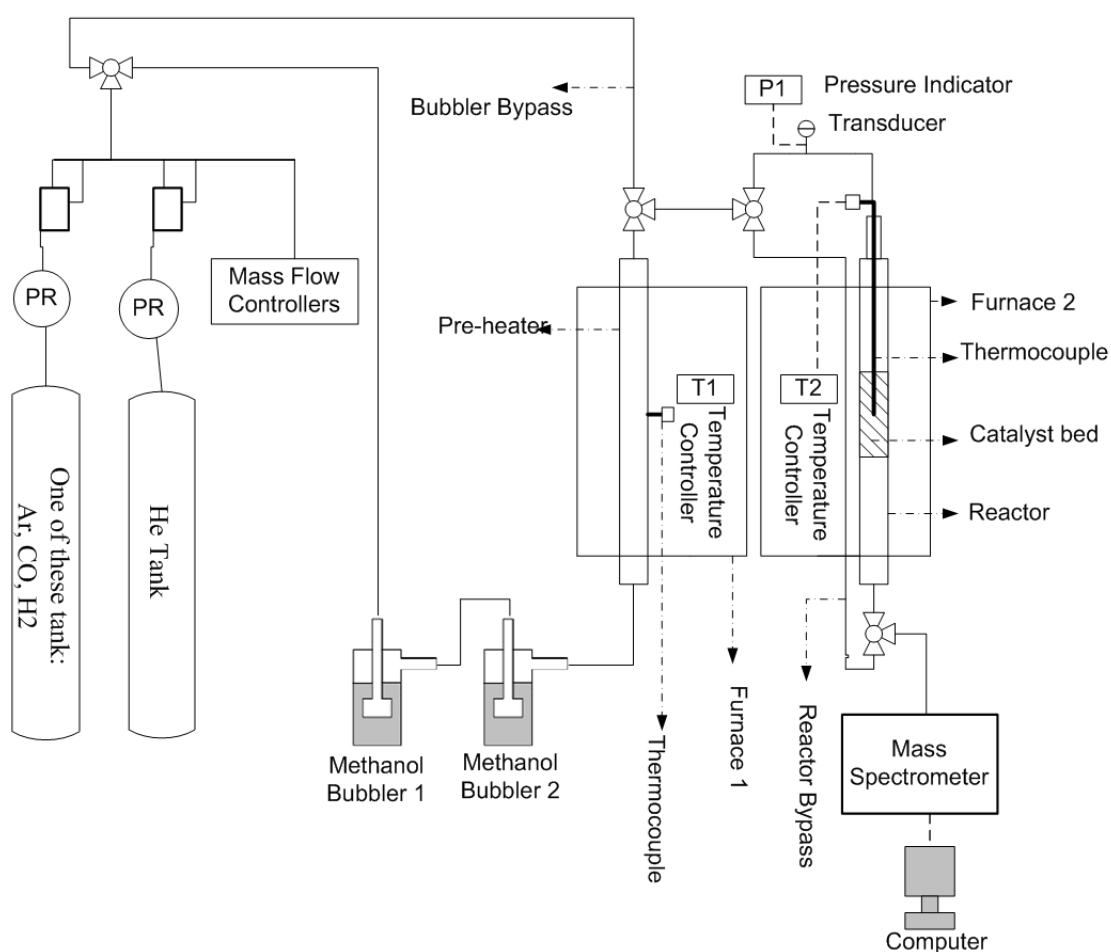
Figure 12 Schematic diagram of the reactor setup

2.3   Results

2.3.1   Catalyst characterization

The effect of preparation conditions on the properties of the MgO are reported in Table 1. Increased calcination temperature decreased the BET surface area (SA_{BET}) and the pore volume (V_p) of the MgO, most likely due to thermal sintering of the MgO crystallites. However, increased calcination time didn't affect SA_{BET} and V_p of the MgO noticeably. The SA_{BET} results of Table 1 also show that a decrease in the mole fraction of palmitic acid used in the catalyst preparation led to an increase in the SA_{BET} of the MgO. Following calcination, the MgO was grey in color, indicative of some carbonaceous residue from the palmitic acid not completely removed during calcination. With less palmitic acid, a lighter grey powder was produced, indicative of less carbonaceous impurity. The carbonaceous residue was likely responsible for the small decrease in surface area (through pore blockage) as the amount of palmitic acid increased. Note that the color of the MgO obtained from the thermal decomposition of $Mg(NO_3)_2.6H_2O$ in the absence of palmitic acid was white (Table 1, MgO-4). Cosimo et al. [38] prepared MgO by thermal decomposition of $Mg(OH)_2$ in a high flow of air and reported an MgO surface area of 119 m^2/g, whereas the SA_{BET} of MgO of the present study was 160 m^2/g (Table 1, MgO) and the thermal decomposition of $Mg(NO_3)_2.6H_2O$ in the absence of palmitic acid (Table 1, MgO-4) yielded MgO with a SA_{BET} of 7 $m^2.g^{-1}$. These results show the advantage of using palmitic acid to obtain higher surface area MgO. Palmitic acid plays an important role by limiting the sintering of the MgO, likely due to the fact that palmitic acid is a good chelating agent for Mg^{2+}. The method used herein to obtain

high surface area MgO is more convenient and simpler than conventional thermal decomposition methods, wherein high flows of purge gas are typically required to remove produced water and thereby limit sintering of the MgO [38].

To investigate the quantity of impurities in the alkali-promoted-40wt% Cu-MgO catalysts, CHN analysis was conducted on the passivated alkali-promoted-40wt% Cu-MgO catalysts and the results are shown in Table 2. The data show no presence of N in the alkali-promoted-40wt% Cu-MgO catalysts, indicating complete decomposition of the metal nitrates $(Mg(NO_3)_2$, $Cu(NO_3)_2$ and $KNO_3)$ present in the catalyst precursor to metal oxide/metal hydroxide. Also, the CHN analysis showed < 1wt% H as well as < 3wt% C in the alkali-promoted-40wt% Cu-MgO catalysts, which confirms almost complete combustion of the palmitic acid present in the catalyst precursor. Since the amount of H and C was < 3wt% for all of the prepared Cu-MgO-based catalysts and bearing in mind that these impurities were scattered through the bulk of these catalysts, it is likely that the concentration of these impurities present on the surface of these catalysts was much less than 3 wt%. Subsequently, we assume that the activity for C_2 species and methyl formate during catalytic testing is not significantly affected by these impurities.

Table 1 Effect of calcination temperature, calcination time and palmitic acid content on BET surface area, pore volume and pore size of MgO[d]

Catalyst	Calcination Temperature	Calcination Time	R^a	$SA_{BET}{}^b$	$V_p{}^b$	$d_p{}^b$
	(K)	(min)	-	$(m^2.g^{-1})$	$(cm^3.g^{-1})$	(nm)
MgO[c]	673	300	2.5	160	0.58	14.5
MgO-1	723	300	2.5	132	0.46	14.2
MgO-2	673	480	2.5	156	0.54	13.4
MgO-3	673	480	1.25	174	0.42	9.9
MgO-4	673	480	0.00	7	0.02	8.9

[a] R is molar ratio of palmitic acid to Mg+Cu+alkali metal

[b] SA_{BET} , V_P and d_P are respectively, BET surface area, pore volume and average pore size of MgO catalyst before reduction.

[c] These conditions have been used for preparation of all Cu-MgO-based catalysts of the present study.

[d] The detail of repeatability for SA_{BET}, V_p and d_p is shown in Appendix B.1. Note that $\sigma_{SA_{BET}} \leq \pm 5\ m^2.g^{-1}$, $\sigma_{V_p} \leq \pm 0.03\ cm^3.g^{-1}$ and $\sigma_{d_p} \leq \pm 2.6\ nm$.

Table 2 CHN analysis results for the 40wt% Cu-MgO and Cs or K promoted-40wt% Cu-MgO[a]

Catalyst	C, wt%	H, wt%	N, wt%
40wt% Cu-MgO (passivated)	2.31	0.78	0.00
0.5wt%K-40wt% Cu-MgO (passivated)	1.01	0.29	0.00
0.5wt%Cs-40wt% Cu-MgO (passivated)	1.23	0.41	0.00
4.4wt%K-40wt% Cu-MgO (passivated)	1.56	0.34	0.00
13.5wt%Cs-40wt% Cu-MgO (passivated)	0.92	0.22	0.00

[a] the repeatability of the CHN analysis is shown in Appendix B.2.

SA_{BET} and V_p and d_p for alkali-promoted 40wt% Cu-MgO catalysts are measured and reported in Table 3. The reported properties were compared to MgO properties (Table 1). It was found that addition of Cu to the MgO resulted in a loss of more than 50 % of the MgO SA_{BET} and V_p. The loss in SA_{BET} and V_p could be partially due the fact that the CuO blocks the pores of the MgO, as suggested by others [66]. The pore size distributions of the MgO-based catalysts after calcination are shown in Figure 13. The addition of the Cu to the MgO led to a significant increase in pore size, with the maxima of the pore size distribution occurring at much higher pore size compared to MgO (Figure 13a; b). This supports the assertion that the smaller pores of the MgO were blocked by the CuO (before reduction). Nonetheless, the preparation method used herein yielded 40wt% Cu-MgO with relatively high surface areas. For example, Nagaraja et al. [69] used co-precipitation to prepare Cu-MgO (nominally 40 wt % Cu and 60 wt % MgO) and reported an SA_{BET} of 28 $m^2.g^{-1}$ [69], whereas in the present study the SA_{BET} of the 40wt% Cu-MgO was 62 $m^2.g^{-1}$ and 74 $m^2.g^{-1}$ before and after reduction, respectively. For all of the prepared catalysts of Table 3, the

36

SA$_{BET}$ increased by about 20 % after reduction, a result of the water loss associated with the reduction of CuO to Cu^0. The catalyst average pore size (d$_p$) of the 40wt% Cu-MgO catalysts, also reported in Table 3, shows that all of the prepared catalysts were mesoporous.
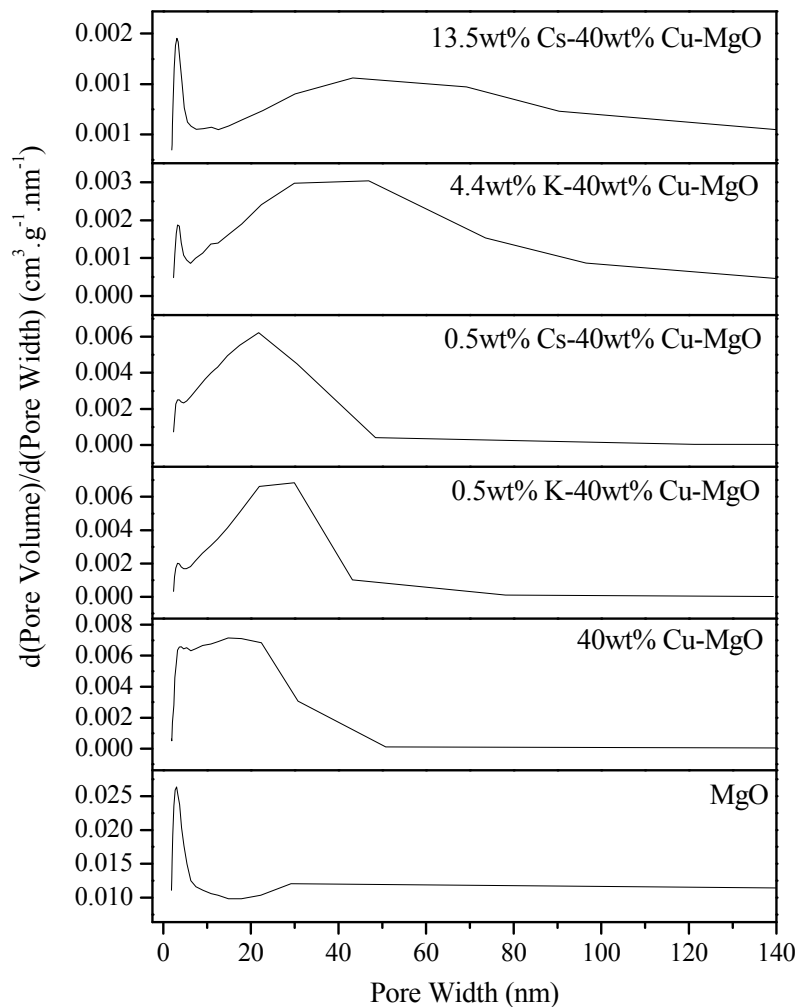
Figure 13 Pore volume distribution of MgO and unreduced 40wt% Cu-MgO-based catalysts

Table 3 BET surface area, pore volume and pore size of alkali promoted 40wt% Cu-MgO catalysts[a]

Catalyst	Catalyst composition (A/Cu/MgO)[b] (wt %)	SA_{BET}[c] $(m^2.g^{-1})$		V_p[c] $(cm^3.g^{-1})$	d_p[c] (nm)
		Before Reduction	After reduction		
40wt% Cu-MgO	0/40.3/59.7	62	74	0.23	15.0
0.5wt% K-40wt% Cu-MgO	0.5/40.1/59.3	35	42	0.20	23.1
0.5wt% Cs-40wt% Cu-MgO	0.5/40.1/59.4	38	44	0.20	20.8
4.4wt% K-40wt% Cu-MgO	4.4/38.2/56.5	26	30	0.17	26.4
13.5wt% Cs-40wt% Cu-MgO	13.5/34.6/51.1	15	18	0.06	16.1

[a] The detail of repeatability for SA_{BET}, V_p and d_p is shown in Appendix B.1. Note that $\sigma_{SA_{BET}} \leq \pm 5\ m^2.g^{-1}$, $\sigma_{V_p} \leq \pm 0.03\ cm^3.g^{-1}$ and $\sigma_{d_p} \leq \pm 2.6\ nm$.

[b] A is alkali metal.

[c] SA_{BET}, V_P and d_P are respectively, BET surface area, pore volume and average pore size of MgO catalyst before reduction.

Addition of Cs or K to the Cu-MgO also decreased the SA_{BET} and V_p. Noting that the K promoted 40wt% Cu-MgO and the Cs promoted 40wt% Cu-MgO precursors were calcined at higher temperatures than the MgO and the 40wt% Cu-MgO, it is likely that thermal sintering contributed to the decreased SA_{BET} and V_p of the alkali promoted 40wt% Cu-MgO. Table 3 also shows that increasing the K loading of the K-40wt% Cu-MgO catalyst from 0.5 wt % to 4.4 wt %, decreased the catalyst SA_{BET} and V_p. Similar effects were observed for the Cs promoted 40wt% Cu-MgO catalyst as the Cs loading increased from 0.5 wt % to 13.5 wt %. Pore blockage of MgO by Cs_2O or K_2O has been reported in the literature [66] and the trends observed with increased promoter concentration suggest that similar effects are important here as well. The pore size distribution data of Figure 13 (c, e) show that increasing the K loading of the K promoted 40wt% Cu-MgO catalyst from 0.5 wt % to 4.4 wt % , led to a significant increase in pore size with the maxima of the pore size distribution occurring at a higher pore size with increased K. The same trend was observed as the Cs loading of the Cs-40wt% Cu-MgO was increased from 0.5 wt % to 13.5 wt % (Figure 13-c,e). These observations support the assertion that the decreased SA_{BET} of the K or Cs promoted 40wt% Cu-MgO, compared to the 40wt% Cu-MgO, was partially due to MgO pore blockage by K_2O or Cs_2O. Also, note that the melting point and boiling point of palmitic acid are 336 K and 623 K, respectively [70] whereas for $Cu(NO_3)_2 \cdot 3H_2O$ the melting point and boiling point are 387 K and 443 K, respectively [70]. Clearly both the $Cu(NO_3)_2 \cdot 3H_2O$ and the palmitic acid are mixed in the liquid phase below 443 K, the temperature to which the catalyst precursors were heated during preparation. KNO_3 has a melting point and boiling point of 607 K and 673 K, respectively [70] whereas Cs_2CO_3 is reported to decompose to Cs_2O in the temperature range of 823K – 873K [71]. Hence, although the alkali promoters may be below

their melting points during the mixing of the components at elevated temperatures, the promoters are likely solubilized by the palmitic acid during synthesis of the promoted 40wt% Cu-MgO catalysts, and this ensured that the promoters were well dispersed throughout the catalysts.

Figure 14 shows the X-ray diffractograms of the MgO-based catalyst precursors, measured after calcination but prior to reduction. The data confirmed the presence of MgO (periclase, Fm3m(225)-cubic structure) and CuO (tenorite, C2/c(15) monoclinic structure) and the absence of Cu_2O in the precursor samples. In addition, no peaks associated with alkali metal oxides were observed, either because the alkali promoter was below the XRD detection limit (for the 0.5 wt % K and Cs samples) or they were present as amorphous, well dispersed alkali metal oxides (for the 4.4 wt % K and 13.5 wt % Cs samples). Using the data of Figure 14, the MgO crystallite thickness (d_{MgO}^{XRD}) and Cu crystallite thickness (d_{Cu}^{XRD}) were estimated using equation E1 and the results are shown in Table 4. Both d_{MgO}^{XRD} and d_{Cu}^{XRD} increased in the same order that the SA_{BET} of the MgO-based catalysts decreased, indicating that the loss in SA_{BET} was also partly due to thermal sintering of the MgO and the Cu.

The unit cell size of the MgO (a_{MgO}) was calculated from the XRD data for all of the MgO-based catalysts using the formula: $a_{MgO} = 2d_{MgO-lattice}^{XRD}$ since MgO has a cubic crystal structure. As shown in Table 4, the same unit cell size was obtained for all of the catalysts, indicating that there was no solid solution present in the un-reduced 40wt% Cu-MgO-based catalyst precursors. Hence it can be concluded that MgO and CuO crystallites were present as separate phases in the prepared catalysts.
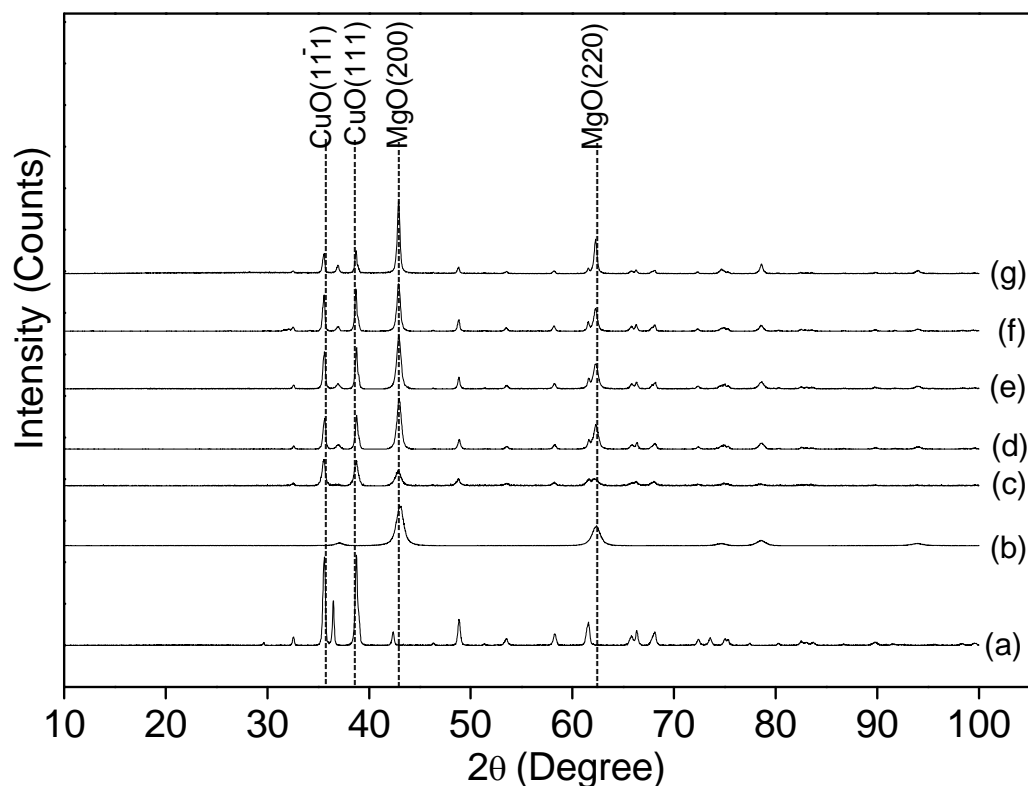
Figure 14 X-ray diffractograms of unreduced MgO-based catalysts: (a) CuO; (b) MgO; (c) 40wt% Cu-MgO ; (d) 0.5wt% K-40wt% Cu-MgO; (e) 0.5wt% Cs-40wt% Cu-MgO; (f) 4.4wt% K-40wt% Cu-MgO; (g) 13.5wt% Cs-40wt% Cu-MgO.

The Cu^0 dispersion of the 40wt% Cu-MgO-based catalysts, reported in Table 4, show that for all of the catalysts the Cu^0 dispersion was low (< 2 %). The Cu-MgO had the highest Cu^0 dispersion among all of the prepared catalysts and addition of K_2O or Cs_2O decreased Cu^0 dispersion. The Cu crystallite size ($d_{Cu}^{N_2O}$), as inferred from the N_2O adsorption-decomposition analysis was significantly higher than that determined from the XRD analysis (d_{Cu}^{XRD}), implying that most of the Cu crystallites (diameter < 30 nm), were occluded from the catalyst surface and not active to N_2O titration. The high Cu loading (> 34.6 wt %) in the prepared 40wt% Cu-MgO-based catalysts is the likely cause, resulting in significant agglomeration of

41

CuO crystallites. Cu thermal sintering at the higher calcination temperatures used for the alkali promoted 40wt% Cu-MgO catalysts, compared to the unpromoted 40wt% Cu-MgO catalyst, also contributed to the lower Cu^0 dispersion of the alkali promoted 40wt% Cu-MgO compared to the unpromoted 40wt% Cu-MgO.

Table 4 Copper dispersion, crystallite size and MgO unit cell size of catalysts as determined by N_2O pulse titration and XRD[a]

Catalyst	Cu^0 Dispersion	$SA_{Cu}^{N_2O\,b}$	$d_{Cu}^{N_2O}$	d_{Cu}^{XRD}	d_{MgO}^{XRD}	a_{MgO}
	(%)	(m^2.g^{-1})	(nm)	(nm)	(nm)	(nm)
MgO	-	-	-	-	13	0.42
40wt% Cu-MgO	1.54	2.64	65	15	17	0.42
0.5wt% K-40wt% Cu-MgO	0.19	0.50	519	21	20	0.42
0.5wt% Cs-40wt% Cu-MgO	0.28	0.58	362	24	20	0.42
4.4wt% K-40wt% Cu-MgO	0.24	0.60	420	26	24	0.42
13.5wt% Cs-40wt% Cu-MgO	0.52	0.76	194	27	32	0.42

[a] The detail of repeatability for Cu^0 Dispersion, $SA_{Cu}^{N_2O}$, d_{Cu}^{XRD}, $d_{Cu}^{N_2O}$, d_{MgO}^{XRD} and a_{MgO} is shown in Appendix B.3 and B.4. Note that $\sigma_{Cu^0\,Dispersion} \leq \pm 2.59$ %, $\sigma_{SA_{Cu}^{N_2O}} \leq \pm 0.36$ m^2.g^{-1} and $\sigma_{d_{Cu}^{N_2O}} \leq \pm 1$ nm.

[b] Copper metal surface area was calculated assuming 1.46×10^{19} copper atoms per m^2.

The TPR profiles of the calcined catalyst precursors of the present study are reported in Figure 15 and the reduction peak temperatures and calculated degrees of reduction are summarized in Table 5. For comparison, the TPR profiles of CuO and Cu_2O are also reported in Figure 15 and Table 5. Note that the degree of reduction was calculated using equation E2.

$$\text{Degree of Reduction} = \frac{\text{number of moles of } Cu^{2+} \text{ in the catalyst bulk which reduced to } Cu^0 \text{ during TPR analysis}}{\text{total number of moles of } Cu^{2+} \text{ in the catalyst bulk before TPR analysis}} \qquad \text{(E2)}$$

The CuO TPR profiles showed that bulk CuO had a reduction peak maximum at 516 K, in agreement with the literature [72]. The Cu_2O TPR profile showed a reduction peak maximum at 594 K. The degree of reduction for Cu_2O was 100 % whereas the degree of reduction for CuO was 88 %. The nominal particle size of all of the laboratory prepared catalysts as well as the bulk CuO of the present study was 267 μm, whereas the Cu_2O particle size was 5 μm. Hence it is likely that complete reduction of the CuO was hindered by H_2 diffusion to the core of the larger, partially reduced Cu-CuO particle. Assuming CuO as the only reducible species present in the calcined catalyst precursors, the TPR results of the 40wt% Cu-MgO-based catalysts revealed that, in all cases, the degree of reduction was more than 80 %. However, due to an interaction between the alkali metal oxide, the MgO and the CuO, two different reduction temperatures were observed. The TPR profiles were therefore de-convoluted (Figure 15) to quantify each of the CuO species. Except for the 13.5 wt % Cs-40wt% Cu-MgO, the first reduction peak occurred in the range of 506 K - 518 K and the second reduction peak occurred in the range of 535 K – 552 K. The first reduction peak was attributed to bulk CuO reduction and the second was assigned to CuO species that interacted with MgO and/or the alkali promoters and were consequently, more difficult to reduce. The weak CuO interaction with bulk MgO and its inhibiting effect on Cu reduction has been reported previously [72-74]. Addition of the alkali promoters to 40wt% Cu-MgO led to more CuO species that were more difficult to reduce, indicative of the K_2O and Cs_2O interaction with the CuO. The phenomenon of alkali metal oxide interaction with CuO and its inhibiting effect on CuO reduction, has also been noted in previous studies [75] and is apparent for all

43

the alkali promoted 40wt% Cu-MgO catalysts reported in Table 5. The TPR profile of the 0.5 wt % K-40wt% Cu-MgO showed reduction peaks at 506 K and 539 K with a significant increase in the CuO species reduced at high temperature compared to the case of 40wt% Cu-MgO. The TPR profile of the 0.5 wt % Cs-40wt% Cu-MgO showed reduction peaks at 518 K and 552 K and although these temperatures were slightly higher than for the 0.5 wt % K-40wt% Cu-MgO, the relative amounts of the two types of CuO species were very similar. Comparison of the TPR profile for 0.5 wt % K-40wt% Cu-MgO and 4.4 wt % K-40wt% Cu-MgO showed almost identical results, suggesting that increased K loading did not influence the interaction of K_2O with the CuO. However, the TPR profile of the 13.5 wt % Cs-40wt% Cu-MgO showed reduction peaks at 538K and 578K, significantly higher than for the other catalysts of Table 5. The first reduction peak was most likely due to the Cs_2O interaction with CuO described earlier. It is noticeable that except for the case of 13.5 wt% Cs-40wt% Cu-MgO, all of the 40wt% Cu-MgO based catalysts showed reduction peaks below the Cu_2O reduction peak temperature. This suggests that the high loading of Cs (13.5 wt%) led to the formation of a small amount of Cu_2O (< 10 wt%) in the Cs-40wt% Cu-MgO catalyst that was not detectable by XRD, but that led to the second reduction peak in the TPR profile that corresponded to the reduction peak for bulk Cu_2O. The non-Gaussian TPR profile of the 40wt% Cu-MgO based catalysts (Figure 15) is attributed to different Cu oxide species present in the catalyst that reduce at different temperatures (Table 5). However, the presence of a heterogeneous size distribution of copper particles in the 40wt% Cu-MgO catalyst may also contribute to the shape of the TPR curves, although in this case, higher N_2O uptakes from the smallest reduced Cu species would be expected to yield much higher overall N_2O uptakes than that reported in Table 4. Note that not having 100% degree of reduction (<90%)

for the 40wt% Cu-MgO-based catalysts of the present study could be attributed to the mentioned interactions between the alkali metal oxide, the MgO and the CuO.
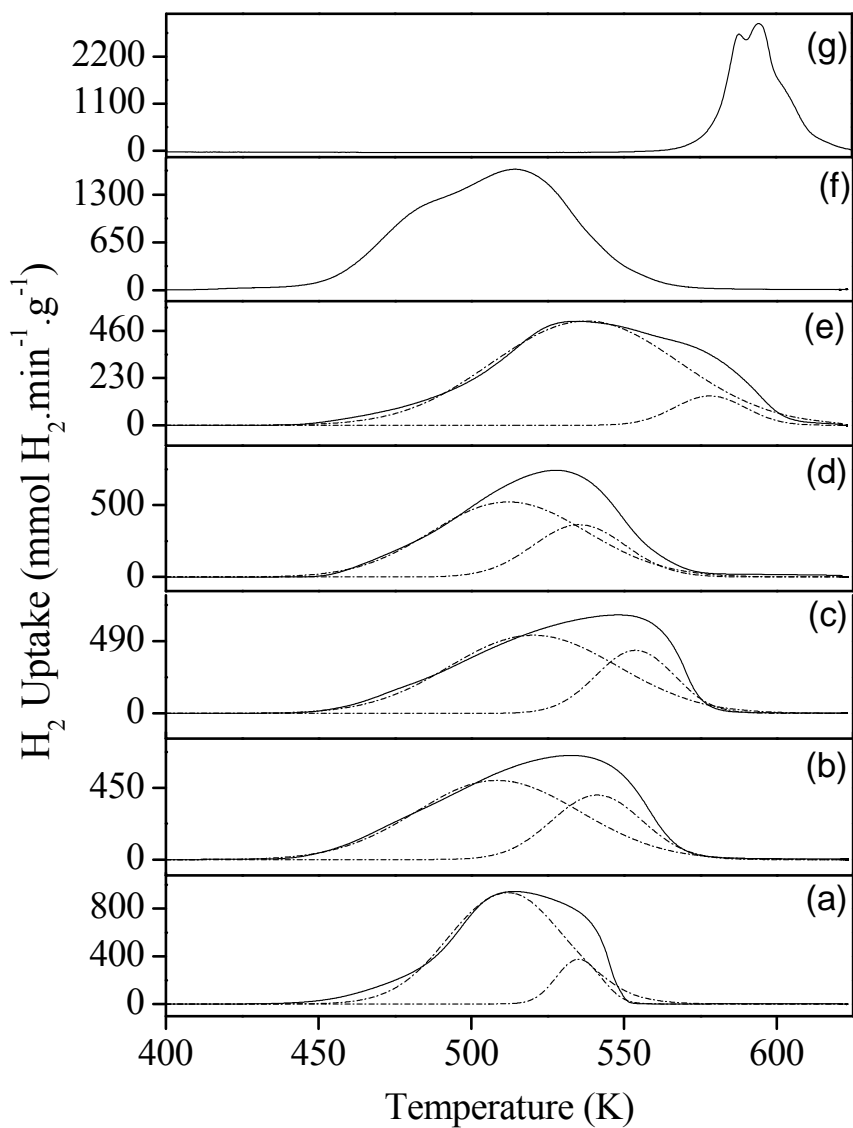
Figure 15 Temperature programmed reduction profile for: (a) 40wt% Cu-MgO; (b) 0.5wt% K-40wt% Cu-MgO; (c) 0.5wt% Cs-40wt% Cu-MgO; (d) 4.4wt% K-40wt% Cu-MgO; (e) 13.5wt% Cs-40wt% Cu-MgO; (f) CuO; (g) Cu$_2$O.

Table 5 Temperature programmed reduction results for 40wt% Cu-MgO-based catalysts[a]

Sample	Hydrogen Consumption (mmol.g^{-1} catalyst)	Distribution of Different Copper Oxide Species[b] (%)		Degree of Reduction (%)	Reduction Peak Temperature (K)	
		1	2		T_1	T_2
Cu$_2$O	6.84	100	-	100	594	-
CuO	11.06	100	-	88	516	-
40wt% Cu-MgO	5.08	87	13	88	512	535
0.5wt% K-40wt% Cu-MgO	4.77	69	31	83	506	539
0.5wt% Cs-40wt% Cu-MgO	4.89	73	27	85	518	552
4.4wt% K-40wt% Cu-MgO	4.56	71	29	83	512	535
13.5wt% Cs-40wt% Cu-MgO	4.20	90	10	84	538	578

[a] The detail of repeatability for Hydrogen Consumption, Degree of Reduction and Reduction Peak Temperature is shown in Appendix B.5. Note that $\sigma_{Hydrogen\ Consumption} \leq \pm 0.08$ mmol.g^{-1} catalyst, $\sigma_{Degree\ of\ Reduction} \leq \pm 5$ % and $\sigma_{Reduction\ Peak\ Temperature} \leq \pm 6$ K. [b] Copper oxide species corresponded to CuO in all cases except for Cu$_2$O catalyst.

The CO$_2$ TPD profiles for all of the catalysts, shown in Figure 16, were used to determine the catalyst intrinsic basicity and distribution of basic sites, as summarized in Table 6. The intrinsic basicity increased in the order: MgO < 40wt% Cu-MgO < 0.5wt% K-40wt% Cu-MgO < 0.5wt% Cs-40wt% Cu-MgO < 4.4wt% K-40wt% Cu-MgO < 13.5wt% Cs-40wt% Cu-MgO and follows the expected trend, based on the known basicities of K, Cs and MgO. MgO had an intrinsic basicity of 2.7 μmol CO$_2$.m^{-2} in agreement with the MgO basicity reported in the literature [36-39]. Addition of Cu to the MgO increased the intrinsic basicity but the distribution of basic sites was almost unchanged. Addition of alkali metal (0.5 wt % Cs or K) to the 40wt% Cu-MgO catalyst more than doubled the intrinsic basicity but the distribution of basic sites remained almost unchanged. The 4.39 wt % K-40wt% Cu-MgO catalyst had higher intrinsic basicity compared to the 0.50 wt % K-40wt% Cu-MgO catalyst, while the distribution of basic sites remained almost unchanged. Similar trends were observed for the Cs-40wt% Cu-MgO catalyst as the Cs loading increased from 0.5wt% to 13.5wt%, except that a small increase in the percentage of medium basic sites was observed. Therefore, it can be concluded that in all cases, addition of alkali promoter to the 40wt% Cu-MgO catalyst increased the intrinsic basicity while the distribution of basic sites remained almost unchanged.
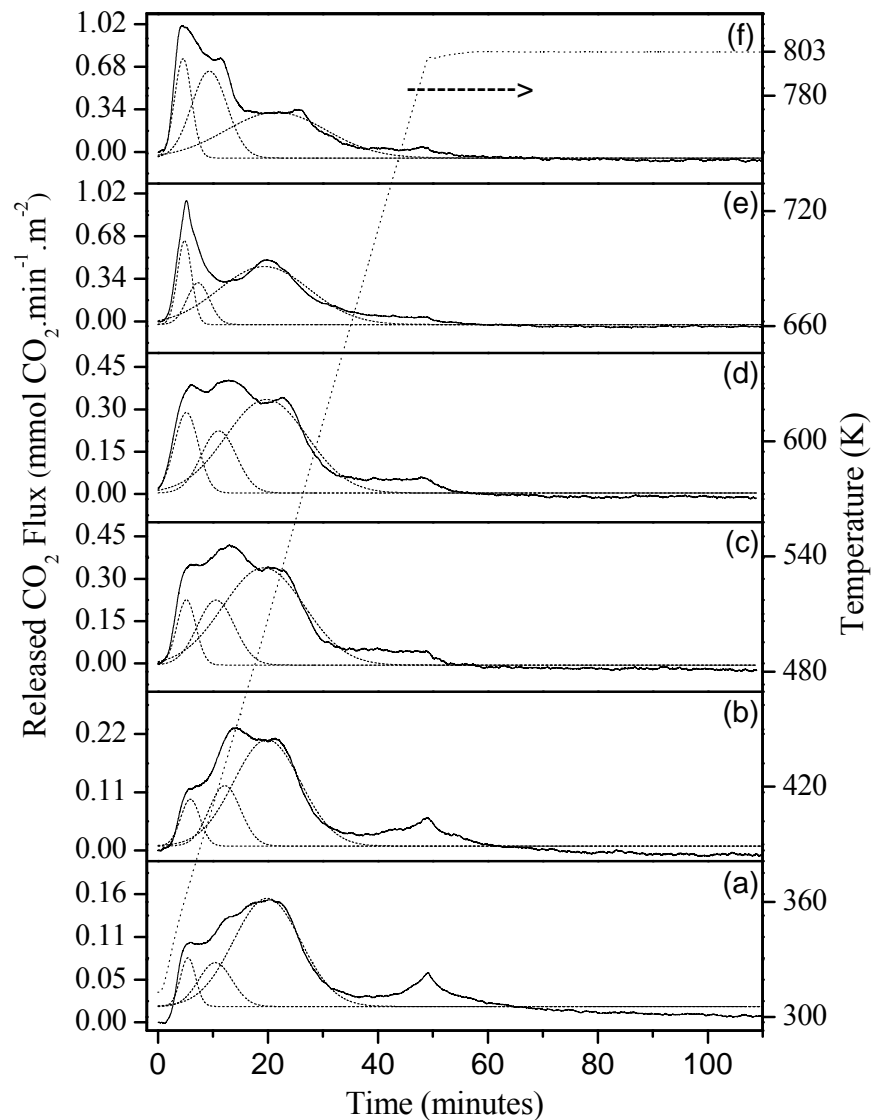
Figure 16 CO$_2$ temperature programmed desorption of (a) MgO;(b) 40wt% Cu-MgO ; (c) 0.5wt% K-40wt% Cu-MgO; (d) 0.5wCs-40wt% Cu-MgO; (e) 4.4wt% K-40wt% Cu-MgO; (f) 13.5wt% Cs-40wt% Cu-MgO.

The basicity of an oxide surface is generally related to the electron donating properties of the combined oxygen anions, so that the higher the partial negative charge on the combined oxygen anions, the more basic the oxide. Therefore, the oxygen partial negative charge reflects the electron donor properties of the oxygen in a single component oxide. Lopez et al.

[76] suggested that Cu bonds ionically to MgO and forms a stable Cu-O-Mg species. These authors claimed that Cu gains a large net positive charge while the Cu electron is transferred to MgO. This more likely leads to an increase in the oxygen partial negative charge in MgO and could explain the increase in the catalyst basic site density after Cu addition to MgO. The oxygen partial negative charge increased in the order $Cs_2O > K_2O > MgO$ according to calculations made by Diez et al. [36,66]. The basicity trend of the present study is in good agreement with these calculations.

Since the catalyst basicity is expected to play an important role in the formation of the first C-C bond in ethanol synthesis from syngas and methanol [20,29-33] a comparison of the basicity of the present catalysts to conventional Cu-ZnO-based catalysts is important. Cu-ZnO-ZrO$_2$ (Cu wt % = 41.20) has a reported intrinsic basicity of 0.4 µmol $CO_2.m^{-2}$ [40], whereas in the present study the 40wt% Cu-MgO intrinsic basicity was 4.3 µmolCO_2. m^{-2}. The intrinsic basicity of the Cu-MgO catalyst of the present study is approximately 10 times higher than that of Cu-ZnO-ZrO$_2$ [40]. Addition of K or Cs to the Cu-MgO increased the intrinsic basicity further, with a value of 9.3 µmol $CO_2.m^{-2}$ obtained for the 0.5 wt % K-40wt% Cu-MgO catalyst. The corresponding value for a 0.5 wt % K promoted Cu-ZnO-Al$_2$O$_3$ catalyst, measured at 196 K, was reported as 2.7 µmol $CO_2.m^{-2}$ [18].

Table 6 Basic properties of MgO-based catalyst measured by means of CO_2 TPD[a]

Catalyst	Specific Basicity (μmol $CO_2 \cdot g^{-1}$)	Intrinsic Basicity (μmol $CO_2 \cdot m^{-2}$)	Distribution of different basic sites on the catalyst (%)		
			Weak	Medium	Strong
MgO	432.0	2.7	8	15	77
40wt% Cu-MgO	315.5	4.3	9	19	72
0.5wt% K-40wt% Cu-MgO	392.4	9.3	11	21	69
0.5wt% Cs-40wt% Cu-MgO	415.9	9.5	16	19	65
4.4wt% K-40wt% Cu-MgO	403.0	13.4	16	13	71
13.5wt% Cs-40wt% Cu-MgO	305.7	17.0	18	33	49

[a] The detail of repeatability for Specific Basicity, Intrinsic Basicity and distribution of different basic sites on the surface of the above listed catalysts is shown in Appendix B.6. Note that $\sigma_{\text{Specific Basicity}} \leq \pm 17.0$ μmol $CO_2 \cdot g^{-1}$ and $\sigma_{\text{Intrinsic Basicity}} \leq \pm 0.2$ μmol $CO_2 \cdot m^{-2}$.

2.3.2 Product distribution over MgO-based catalyst

Previous work suggested that the formation of higher alcohols over Cu-ZnO-based catalysts is favoured at low H_2/CO ratios ($\leq$ 1) [18,28,61,62]. Furthermore, isotopic tracer studies and NMR studies of ethanol synthesis from syngas and methanol over Cu-ZnO-based catalysts, suggested that CO is the main source of carbon in ethanol formation [32], whereas others have suggested that methanol is the main source of carbon in ethanol formation [20]. Hence, in the present work, initial catalyst testing was done in a CH_3OH/CO feed in the absence of H_2. The catalysts were tested at 101 kPa, 498 K, with a feed composition of $He/CO/CH_3OH$ = 0.20/0.66/0.14 (molar) and contact time (W/F) of 12.3×10^{-3} g.min.$(cm^3(STP))^{-1}$. A summary of the product distribution and net conversion of reactants is given in Table 7. As expected, the total conversion of reactants over MgO was very low, whereas addition of Cu and alkali oxide to MgO increased the total conversion significantly. Note that in most cases the net CO consumption was negative, implying that the amount of CO incorporated into the formation of different carbonaceous products was less than the amount of CO generated by CH_3OH decomposition. In these cases, CO was treated as a product and its selectivity was included in the product selectivity calculations. The data of Table 7 show that the CO selectivity (S_{CO}) at 498 K decreased in the order: 40wt% Cu-MgO > 0.5 wt % K-40wt% Cu-MgO > 0.5 wt % Cs-40wt% Cu-MgO, whereas the reverse order was observed for methyl formate (S_{MF}), CO_2 (S_{CO_2}) and C_2 species (S_{C_2}) selectivities. The catalyst intrinsic basicity (Table 6) increased in the order 40wt% Cu-MgO < 0.5wt% K-40wt% Cu-MgO < 0.5 wt % Cs-40wt% Cu-MgO. Thus it can be concluded that an increase in the catalyst intrinsic basicity, led to an increase in S_{MF} and S_{C_2}. However, comparing the 0.5 wt % K-40wt% Cu-

MgO and the 4.4 wt% K-40wt% Cu-MgO as well as the 0.5 wt % Cs-40wt% Cu-MgO and the 13.5 wt% Cs-40wt% Cu-MgO catalysts, shows that increased K or Cs loading increased the S_{CO} and decreased in S_{MF} and S_{C_2}. Intrinsic basicity, however, increased with increased alkali metal loading (Table 6). Hence, among these catalysts, an increase in the catalyst intrinsic basicity led to a decrease in S_{MF} and S_{C_2}, whereas it led to an increase in S_{CO}. Together, these data suggest that an optimum intrinsic basicity exists that maximizes selectivity to methyl formate and C_2 species, as shown in Figure 17. Note that changes in catalyst intrinsic basicity were accompanied by changes in Cu^0 dispersion, SA_{BET}, V_P and their impact on S_{MF}, S_{C_2} and S_{CO} was reflected in the scatter of the data in Figure 17.

It is noteworthy to mention that the standard deviation for S_{MF} and S_{C_2}, used in Figure 17, are respectively $\leq \pm 2.9$ C-atom% and $\leq \pm 0.8$ C-atom% (calculation given in Appendix G.1). Furthermore, the standard deviation for catalyst intrinsic basicity, used in Figure 17, is $\leq \pm 0.2$ µmol $CO_2.m^{-2}$ (calculation given in Appendix B.6). The low standard deviation for these parameters implies high reliability of the results presented in Figure 17.

The product distribution over the 0.5 wt % K-40wt% Cu-MgO and the 0.5 wt % Cs-40wt% Cu-MgO catalysts at 498 K and 523 K (Table 7), show that increased temperature increased S_{CO} whereas S_{MF} and S_{C_2} decreased, implying that lower operating temperature favored C_2 species formation.

Table 7 Product distribution and catalyst activity over MgO-based catalysts using CO/He/CH$_3$OH feed[a]

Catalyst	Reaction Temperature (K)	Net CO consumption (C-atom %)	Net CH$_3$OH conversion (C-atom %)	Total Net Conversion[b] (C-atom %)	Product Selectivity (C-atom %)			
					CO	MF[c]	CO$_2$	C$_2$[d]
MgO	498	-1.2	6.4	5.3	100.0	0.0	0.0	0.0
40wt% Cu-MgO	498	-9.7	84.7	75.0	68.4	29.3	1.5	0.9
0.5wt% K-40wt% Cu-MgO	498	-7.9	70.0	62.0	63.9	30.0	2.7	3.3
	523	-10.8	81.8	71.0	78.2	16.9	2.9	2.1
0.5wt% Cs-40wt% Cu-MgO	498	-6.1	66.7	60.6	53.4	34.9	8.4	3.4
	523	-12.5	87.0	74.5	84.3	10.3	2.9	2.5
4.4wt% K-40wt% Cu-MgO	498	-10.0	70.1	60.2	82.9	14.8	1.1	1.2
13.5wt% Cs-40wt% Cu-MgO	498	-6.3	47.2	40.8	79.8	16.7	1.9	1.6

[a] Reaction Condition: 101 kPa, Feed He/CO/CH$_3$OH = 0.20/0.66/0.14 molar, Contact time (W/F) = 12.3×10^{-3} min.g.(cm^3(STP))$^{-1}$, Catalyst weight = 0.98 g, v_0 =84.4 cm^3(STP).min^{-1}. The detail of repeatability for Total Net Conversion, selectivity of CO (S_{CO}), selectivity of methyl formate (S_{MF}), selectivity of CO$_2$ (S_{CO_2}) and selectivity of C$_2$ species (S_{C_2}) is shown in Appendix G.1. Note that $\sigma_{\text{Total Net Conversion}} \leq \pm 5.6$ (C-atom%), $\sigma_{S_{CO}} \leq \pm 3.3$ (C-atom%), $\sigma_{S_{MF}} \leq \pm 2.9$ (C-atom%), $\sigma_{S_{CO_2}} \leq \pm 2.6$ (C-atom%) and $\sigma_{S_{C_2}} \leq \pm 1.0$ (C-atom%). [b] Total conversion = Net CO consumption + Net CH$_3$OH conversion. [c] MF stands for methyl formate. [d] C$_2$ (C$_2$ species) stands for ethanol and acetic acid.
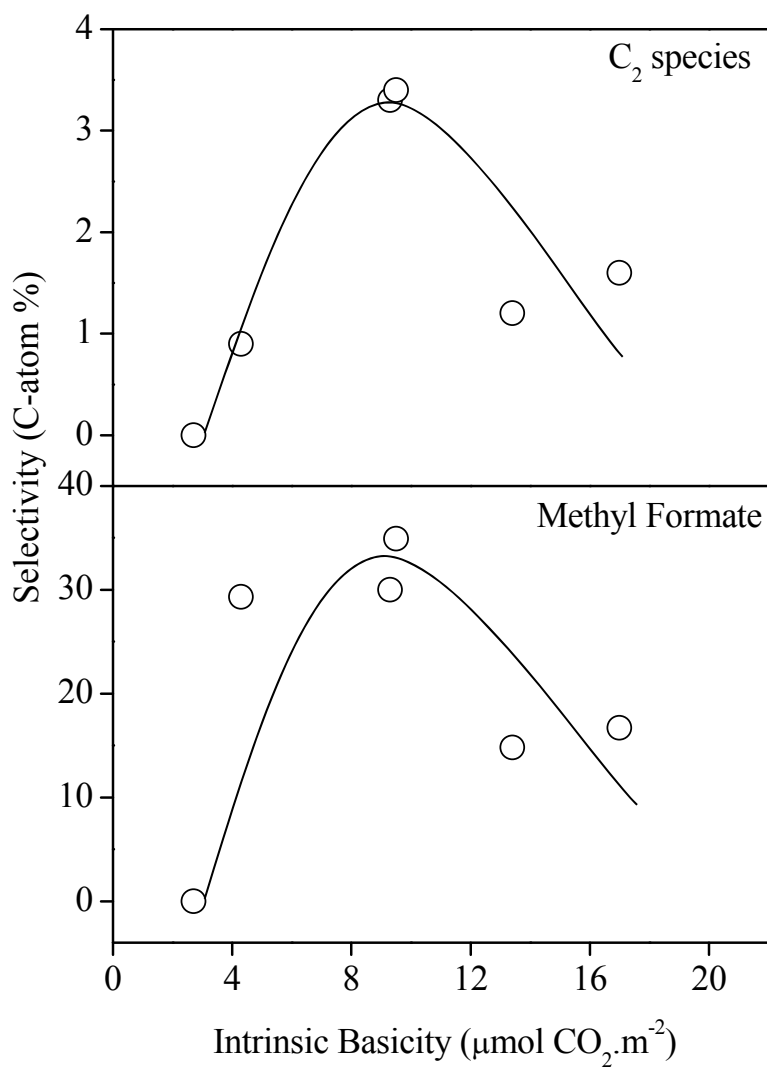
Figure 17 Selectivity from reaction of CH₃OH/CO over alkali promoted 40wt% Cu-MgO catalysts as a function of their intrinsic basicity. Reaction conditions: 101 kPa, 498 K, Feed composition He/CO/CH₃OH = 0.20/0.66/0.14 (molar) W/F=12.3×10⁻³ min.g.(cm³(STP))⁻¹, catalyst weight = 0.98 g. Note that based on Appendix G.1, standard deviation for selectivity of methyl formate ≤ ± 2.9 (C-atom%) and standard deviation for selectivity of C₂ species ≤ ± 0.8 (C-atom%). Furthermore, based on Appendix B.6, standard deviation for intrinsic basicity ≤ ± 0.2 μmol CO₂.m⁻².

Since the 0.5 wt % Cs-40wt% Cu-MgO catalyst showed the highest selectivity towards C_2 species among all the tested catalysts, further experiments were conducted as a function of contact time (W/F) using this catalyst and the results are presented in Figure 18. Also, to study the effect of Cs loading on the performance of the Cs promoted 40wt% Cu-MgO catalyst, the same series of contact time experiments was performed on the 13.5 wt % Cs-40wt% Cu-MgO, and the results are shown in Figure 19. For both the 0.5 wt % Cs-40wt% Cu-MgO and the 13.5 wt % Cs-40wt% Cu-MgO catalysts, it was observed that decreased contact time led to increased S_{MF} and decreased S_{CO}, whereas the S_{C_2} and S_{CO_2} remained almost unchanged. These observations imply that methyl formate was a primary product over both catalysts whereas CO was a secondary product, in agreement with previous studies [2,77].

The effect of different feed mixtures on the product distribution over the 13.5 wt % Cs-40wt% Cu-MgO catalyst was also examined using a feed of $Ar/He/CH_3OH$, $CO/He/CH_3OH$ and $H_2/He/CH_3OH$ and the results are shown in Table 8. The presence of either H_2 or CO in the feed stream compared to Ar, decreased the total conversion and the decrease in total conversion was more significant in the presence of H_2 than CO. Furthermore, the presence of H_2 in the feed decreased S_{MF} marginally, whereas the presence of CO in the feed, increased the S_{MF} compared to the presence of Ar in the feed. S_{C_2} decreased in the following order: $H_2/He/CH_3OH$ > $CO/He/CH_3OH$ > $Ar/He/CH_3OH$ revealing that the presence of H_2, as opposed to CO and Ar in the feed, improved S_{C_2}, but note that the CH_3OH conversion decreased significantly in the H_2 rich atmosphere.
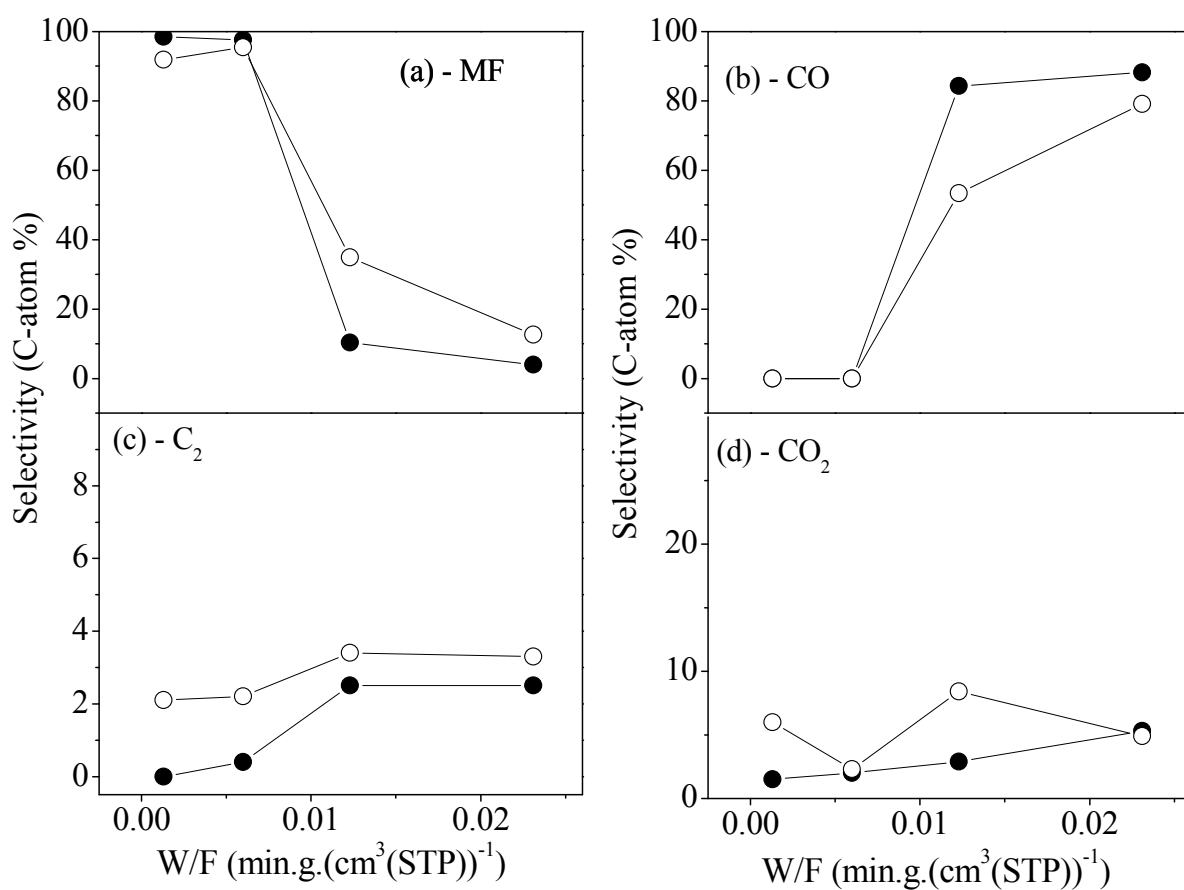
Figure 18 Selectivity from reaction of CH$_3$OH/CO over 0.5wt% Cs-40wt% Cu-MgO at (o) 498 K and (•) 523 K as a function of contact time (W/F) for: (a) methyl formate, (b) CO, (c) acetic acid and ethanol, (d) CO$_2$. Reaction conditions: 101 kPa, Feed composition He/CO/CH$_3$OH = 0.20/0.66/0.14 (molar), v_0 =84.4 cm^3(STP).min^{-1}.
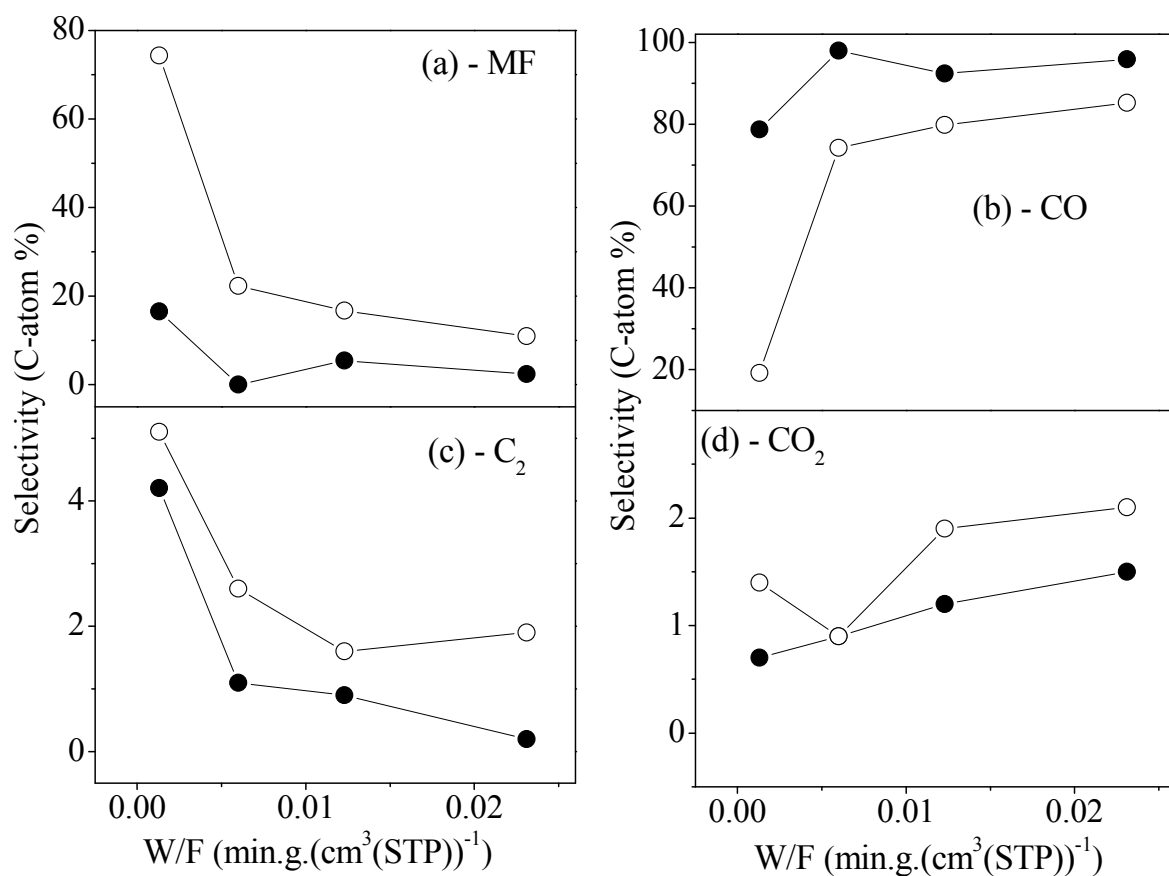
Figure 19 Selectivity from reaction of CH$_3$OH/CO over 13.5 wt % Cs-40wt% Cu-MgO at (o) 498 K and (●) 523 K as a function of contact time (W/F) for: (a) methyl formate, (b) CO, (c) acetic acid and ethanol, (d) CO$_2$. Reaction conditions: 101 kPa, Feed composition He/CO/CH$_3$OH = 0.20/0.66/0.14 (molar), v$_0$ =84.4 cm^3(STP).min^{-1}.

Table 8 Product distribution and catalyst activity over 13.5wt% Cs-40wt% Cu-MgO in different feed compositions[a]

T^b (K)	Feed Mixture	Net CO consumption (C-atom %)	Net CH_3OH conversion (C-atom %)	Total Conversion[c] (C-atom %)	Product Selectivity (C-atom %)			
					CO	MF^d	CO_2	C_2^e
498	$Ar/He/CH_3OH$	0.0	48.2	48.2	81.7	15.2	2.9	0.2
	$CO/He/CH_3OH$	-6.3	47.2	40.8	79.8	16.7	1.9	1.6
	$H_2/He/CH_3OH$	0.0	6.6	6.6	79.5	13.6	3.3	3.6
523	$Ar/He/CH_3OH$	0.0	62.1	62.1	97.6	1.6	0.8	0.0
	$CO/He/CH_3OH$	-7.3	47.0	39.7	92.4	5.4	1.2	0.9
	$H_2/He/CH_3OH$	0.0	22.8	22.8	96.1	1.6	1.1	1.2

[a] Reaction Condition: 101 kPa, Feed $X/He/CH_3OH$ = 0.66/0.20/0.14 molar (where X is Ar or CO or H_2), Contact time (W/F) = 12.3×10^{-3} min.g.$(cm^3(STP))^{-1}$, Catalyst weight = 0.98 g, υ_0=84.4 $cm^3(STP).min^{-1}$. The detail of repeatability for Total Net Conversion, selectivity of CO (S_{CO}), selectivity of methyl formate (S_{MF}), selectivity of CO_2 (S_{CO_2}) and selectivity of C_2 species (S_{C_2}) is shown in Appendix G.1. Note that $\sigma_{Total\ Net\ Conversion} \leq \pm 5.6$ (C-atom%), $\sigma_{S_{CO}} \leq \pm 3.3$ (C-atom%), $\sigma_{S_{MF}} \leq \pm 2.9$ (C-atom%), $\sigma_{S_{CO_2}} \leq \pm 2.6$ (C-atom%) and $\sigma_{S_{C_2}} \leq \pm 1.0$ (C-atom%). [b] T stands for reaction temperature. [c] Total conversion = Net CO consumption + Net CH_3OH conversion. [d] MF stands for methyl formate. [e] C_2 stands for ethanol and acetic acid.

2.4   Discussion

The present study has demonstrated the preparation of high surface area MgO by thermal decomposition of $Mg(NO_3)_2$ in the presence of palmitic acid, and this method has been extended to alkali-promoted 40wt% Cu-MgO catalysts. Using CO_2 TPD to quantify basicity, the alkali-promoted 40wt% Cu-MgO was shown to have a higher intrinsic basicity than conventional Cu-ZnO catalysts and alkali-promoted Cu-ZnO catalysts. The surface area of the MgO (160 m^2g^{-1}) was significantly higher than the 40wt% Cu-MgO (74 m^2g^{-1}), due mostly to pore blocking by the Cu. Further losses in surface area upon alkali promotion were shown to be due to both pore blocking and sintering effects. The latter was due to the higher calcination temperatures of the alkali promoted catalysts compared to the 40wt% Cu-MgO.

Several reaction mechanisms have been proposed for the conversion of syngas to CH_3OH and other oxygenated products as well as for the conversion of CH_3OH to methyl formate, C_2 species (mainly ethanol), CO and CO_2. A summary of the most consistent mechanisms proposed in the literature regarding the formation of these products over Cu/metal oxide catalysts is shown in Figure 20, Figure 21 and Figure 22. In order to simplify these figures, the reaction pathways and intermediates containing carbon atoms are shown, whereas H, OH, H_2O and H_2 species are omitted. Results from the present study are conveniently discussed in view of some of these mechanistic proposals.
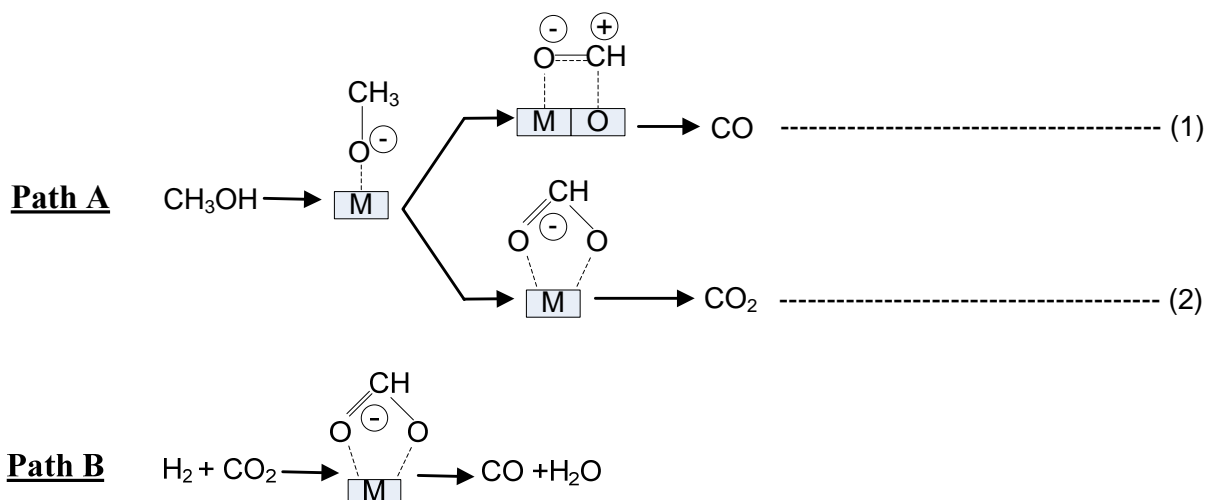
Figure 20 Pathway for: (A-1) CH_3OH decomposition to CO [20,31,47,57], (A-2) CH_3OH decomposition to CO_2 [20,47,58], (B) reverse water gas shift [54]. M stands for Cu or metal cation.

The present work showed that at 498 K on the high surface area MgO (Table 7) only a small amount of the feed CH_3OH was converted to CO but no methyl formate, dimethyl ether (DME), other C_2 oxygenates or CO_2 was produced. Addition of Cu to the MgO resulted in a significant increase in conversion (from 5.3 to 75.0 %, Table 7), with a high selectivity to methyl formate (29.3 %) and CO (68.4 %), and a low CO_2 (1.5 %) and C_2 (0.9 %) selectivity. Addition of the alkali promoters resulted in changes in the product selectivity, but in all cases, CO and methyl formate remained the major products. Clearly, although the basic MgO is able to convert CH_3OH to CO, most likely through the methoxy species shown in Path A-1 of Figure 20, Cu is needed to obtain products other than CO. However, there is a well established synergy between the Cu and the metal oxide present in the catalyst [78] that influences product selectivity. In the present work, the basic MgO and alkali promoters ensure that no dimethyl ether is formed [65,78], and the selectivities to methyl formate, CO_2 and C_2 oxygenates were all dependent on the catalyst formulation (Table 7). Furthermore,

60

both the reaction temperature and space velocity had a significant effect on the product selectivity. The data of Table 7 show that increased temperature resulted in higher methanol conversion and CO selectivity, with reduced selectivity to methyl formate and other C_2 oxygenates. Figure 18 and Figure 19 suggest that the initial product of reaction over the Cs-Cu-MgO catalyst was methyl formate, while CO was a secondary product. The selectivity to CO_2 was not a strong function of operating conditions.
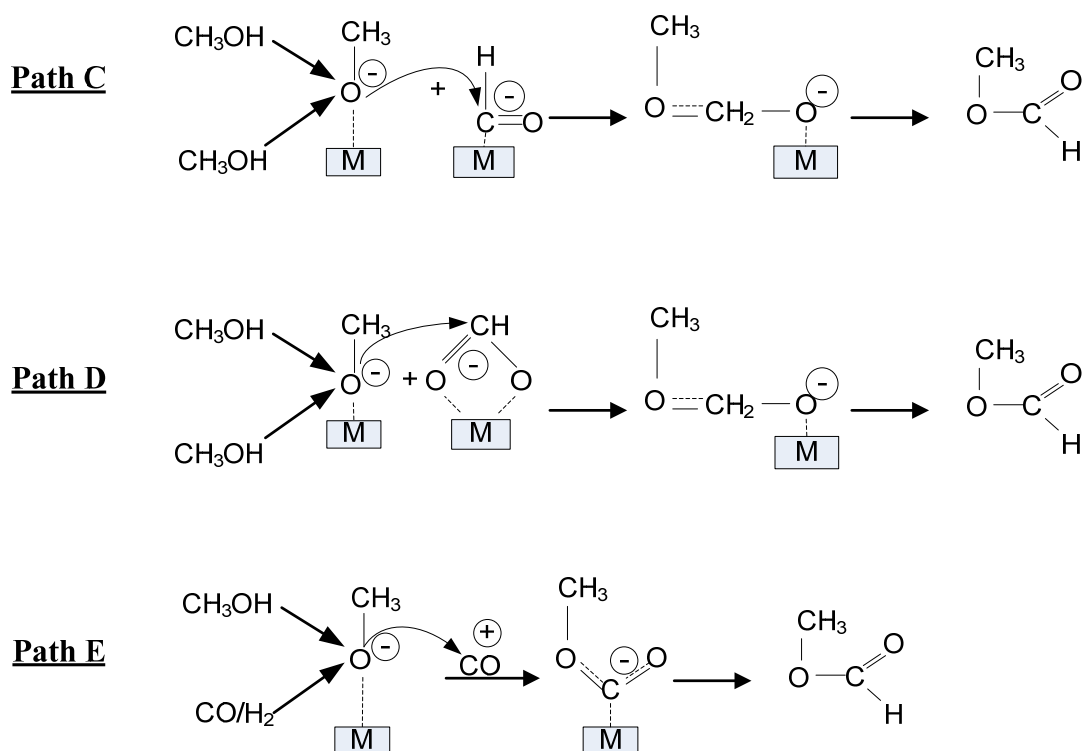
Figure 21 Pathway for: (C) CH₃OH dimerization to methyl formate via methoxy and formyl intermediates[4,5], (D) CH₃OH dimerization to methyl formate via methoxy and formate intermediates [4,5], (E) CH₃OH carbonylation to methyl formate [20]. M stands for Cu or metal cation.
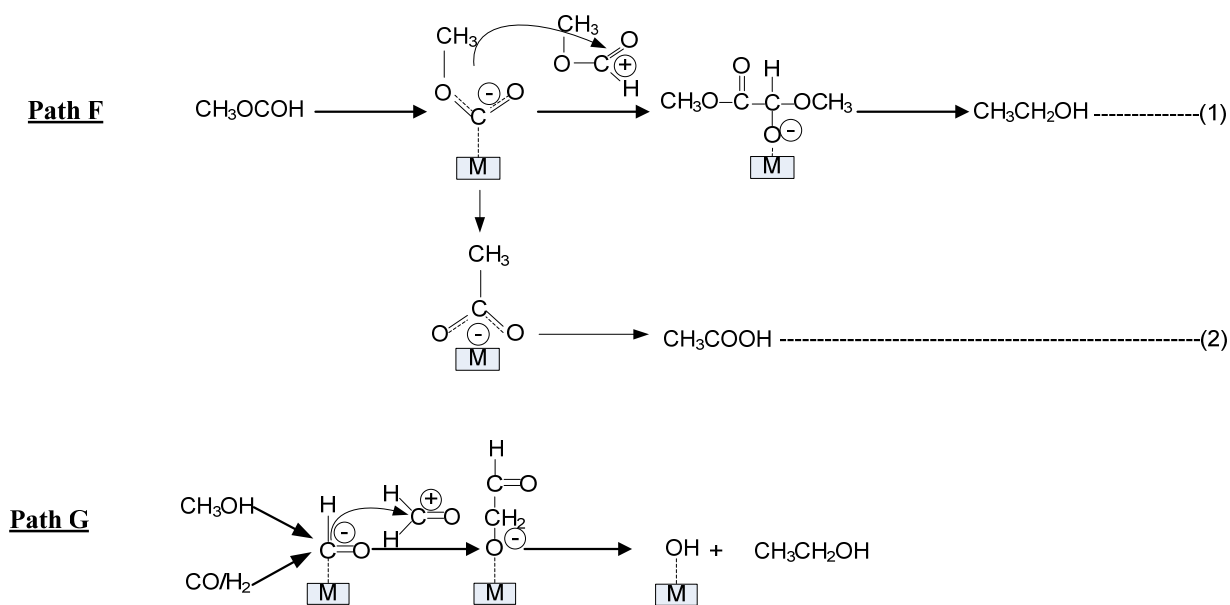
Figure 22 Pathway for: (F-1) Ethanol formation from methyl formate [32], (F-2) Acetic acid formation from methyl formate [20], (G) Ethanol formation from CH$_3$OH and CO [20]. M stands for Cu or metal cation.

Studies using ^{13}CO and ^{13}CO$_2$ and H$_2$ as reactant have shown that CH$_3$OH is produced mainly from CO$_2$ and H$_2$ rather than CO and H$_2$ on Cu catalysts [16]. Hence, the methanol synthesis on Cu-based catalysts can be described by the following two parallel reactions [31,54] which is shown in reaction R6 and R7.

$$CO_2 + H_2 \leftrightarrow CO + H_2O \ (\Delta H^o_{298K} = 41.2 \ \frac{kJ}{mol} \text{ and } \Delta G^o_{298K} = 28.6 \frac{kJ}{mol}) \tag{R6}$$

$$CO_2 + 3H_2 \leftrightarrow CH_3OH + H_2O \ (\Delta H^o_{298K} = -49.6 \ \frac{kJ}{mol} \text{ and } \Delta G^o_{298K} = 3.4 \frac{kJ}{mol}) \tag{R7}$$
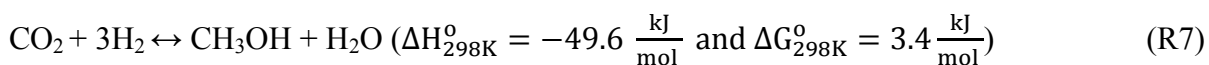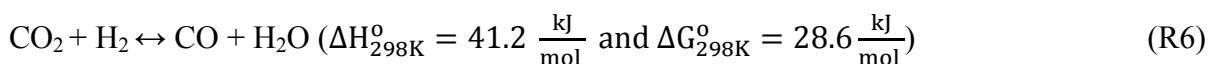
Most of the mechanistic studies on Cu catalysts agree that a formate species is formed from H$_2$ and CO$_2$ and further surface reaction leads to products CH$_3$OH and H$_2$O (the reverse of

Path A-2 of Figure 20) or CO and H_2O (Path B of Figure 20) [29,31,54]. Carbon isotopic tracer studies have shown that the rate of the reverse water gas shift (reaction R6) is higher than the rate of CH_3OH synthesis from CO_2/H_2 (reaction R7) [54]. In the present work, no H_2O was added in the feed and consequently the reverse of reaction R7 could not occur to any great extent. However, the data of Figure 18 and Figure 19 show that even at high space velocities some C_2 oxygenates were produced, and water is a co-product of these reactions. Consequently, the reverse of both reaction R6 and R7 occur but to a limited extent because of the low levels of water generated as a consequence of C_2 formation. In the presence of water it is likely that a portion of the CH_3OH present in the feed decomposed to CO_2 via path A-2 of Figure 20. Alternatively, the forward or reverse reaction shown as Path B of Figure 20 could occur, although this seems less likely in the present work given that the amount of CO_2 was not strongly dependent on the CO present in the feed (Table 8), nor on the C_2 selectivity (Figure 18 and Figure 19). It is noteworthy to mention that, as discussed in Section 1.8.1, a recent DFT study [53] proposed a new mechanism for reaction R7 (Figure 3) which does not support the conventional reaction mechanism shown in path A-2 of Figure 20. The work in the present chapter was conducted and published prior to this most recent report. In Chapter 5 (Section 5.2.1), a recommendation for future work is made to conduct a kinetic study to investigate reaction R7 and to develop a corresponding new LH model based on the recent DFT-based mechanism.

CH_3OH conversion to methyl formate over Cu-based catalysts has been well studied and it is known that Cu plays a significant role as active catalyst for methyl formate formation [2,54,65]. Figure 21 shows potential routes to methyl formate, but the mechanisms that have

received the most acceptance are the CH_3OH dimerization paths shown as Path C and D. Recent evidence based on H/D exchange experiments [4] and experiments using ^{13}C labelled methanol [5] suggested that methyl formate is generated via the nucleophilic attack of a surface methoxy species on a surface formyl species (Path C of Figure 21) or a formate species (Path D of Figure 21) [2,4,5,65,77]. Nunan et al. [20] provided thermodynamic and other arguments to suggest that methyl formate was generated by methanol carbonylation over their Cs-Cu-ZnO catalyst operated at high pressure (7.6 MPa). At the low pressure conditions of the present study, however, the methyl formate generated was about three orders of magnitude greater than the equilibrium yield from methanol carbonylation ($CH_3OH+CO \rightarrow HCOOCH_3$, $K_{HCOOCH_3(1)}(598K) = 2.11 \times 10^{-4}$ versus $K_{HCOOCH_3-calc(1)}(598K) = 3.45 \times 10^{-1}$), whereas it was less than the methanol dimerization equilibrium yield ($2CH_3OH \rightarrow HCOOCH_3+2H_2$, $K_{HCOOCH_3(2)}(598K) = 3.14 \times 10^{-2}$ versus $K_{HCOOCH_3-calc(2)}(598K) = 2.22 \times 10^{-2}$). The methanol dimerization reaction to methyl formate and hydrogen could occur directly from methoxy and formyl species derived from CH_3OH interacting with Cu as well as the basic sites of the present catalysts. Other studies on the effect of the state of Cu on methyl formate formation have suggested that CH_3OH decomposes to CO via a methyl formate intermediate over Cu^0, but no clear mechanism was proposed for this step [2,77]. In the present work it is likely that surface formyl, methoxy and formate all exist on the catalyst surface. Path C and Path D of Figure 21 yield methyl formate as a primary product. Subsequent decomposition of methyl formate to CH_3OH and CO, or to CO and H_2, would yield CO as a secondary product, in agreement with the experimental observations of Figure 18 and Figure 19. Hence it is likely that in the present study, part of the CH_3OH present in the feed stream was decomposed to CO via methyl formate over Cu^0.

Results of the present work showed that an increase in catalyst intrinsic basicity up to 9.5 μmol $CO_2.m^{-2}$ at low Cu^0 dispersion (< 1.54%), led to an increase in S_{MF} (Figure 17). The methyl formate selectivity decreased in the order: 0.5 wt % Cs-40wt% Cu-MgO > 0.5 wt % K-40wt% Cu-MgO $\approx$ 40wt% Cu-MgO. Also, addition of CO to CH_3OH in the feed led to a small increase in S_{MF}. The formation of methyl formate via nucleophilic attack by methoxide species on formyl species would be enhanced by increased basicity of the catalyst, as has been observed. An increase in catalyst intrinsic basicity also led to a small increase in S_{C_2}. Xu and Iglesia [32] have suggested that nucleophilic attack of the methyl formate by surface CH_3OCO^- species on a basic catalyst (metal cation) leads to the formation of an initial C-C bond that yields ethanol following several hydrogenation steps that are not shown in Path F-1 of Figure 22. Other mechanistic studies suggest that the nucleophilic attack of an adsorbed formyl species with formaldehyde on a basic site leads to the formation of the initial C-C bond which subsequently yields ethanol (Path G of Figure 22) [20]. Noting that formaldehyde was absent in both the feed and product streams of the present study, it is likely an increase in the catalyst intrinsic basicity led to a nucleophilic attack of the methyl formate by surface CH_3OCO^- species on a basic site, leading to ethanol formation and a small increase in C_2 formation (S_{C_2} < 5 C-atom %). Results of the present work showed that S_{C_2} decreased in the order: 0.5 wt % Cs-40wt% Cu-MgO $\approx$ 0.5 wt % K-40wt% Cu-MgO > 40wt% Cu-MgO suggesting that Path F-1 of Figure 22 took place over Cu/Mg^{2+} and addition of Cs_2O and K_2O to 40wt% Cu-MgO provided stronger basic sites (Cs^+ and K^+) for this reaction pathway.

To the author's knowledge, only one previous study has reported the formation of acetic acid from CH_3OH/CO over Cu-based catalysts [20]. The only mechanistic studies available for acetic acid synthesis suggest that nucleophilic attack of CO on methoxide over a basic site leads to CH_3OCO^- species. The rearrangement of CH_3OCO^- species to acetate species (CH_3COO^-) leads to C-C bond formation, and a final hydrogenation step yields acetic acid (Path F-2 of Figure 22) [20]. However, Nunan et al. [20] noted that the rearrangement step ($CH_3OCO^- \rightarrow CH_3COO^-$) had high activation energy (based on an analysis of gas phase reactions) and was not very likely to occur. In the present study, the increase in the catalyst intrinsic basicity up to 9.5 μmol $CO_2.m^{-2}$ led to a small increase in the S_{C_2} and it is likely that the high intrinsic basicity of the alkali-promoted 40wt% Cu-MgO catalysts facilitated the formation of small amounts of acetic acid (acetic acid selectivity < 3 C-atom %) on the catalyst surface as shown by Path F-2 of Figure 22.

The correlation between intrinsic basicity and S_{MF}, S_{C_2} and S_{CO} identified in the present study (Figure 17), suggests that at low Cu^0 dispersion (< 1.54%), an increase in the intrinsic basicity up to 9.5 μmol$CO_2.m^{-2}$, leads to an increase in S_{MF} and S_{C_2}, while a further increase in the intrinsic basicity leads to a decrease in S_{MF} and S_{C_2}. (In both cases the opposite trend was observed for S_{CO} compared to S_{MF} and S_{C_2}). As discussed earlier, methyl formate and C_2 species were most likely formed from methoxy, formyl and formate species adsorbed on the Cu/metal oxide and that nucleophilic attack lead to methyl formate and C_2 oxygenates. Subsequently, methyl formate was likely converted to CH_3OH and CO on Cu^0. Based on these observations and the correlation between intrinsic basicity and S_{MF}, S_{C_2} and S_{CO}, it can be speculated that a balance of metal and basic sites are required for maximum selectivity to

methyl formate and C_2 oxygenates. At very high intrinsic basicities (the high loading K or Cs promoted 40wt% Cu-MgO with intrinsic basicity > 9.5 $\mu molCO_2.m^{-2}$), although the formation of the methoxy species may be enhanced, the formyl and formate species would be reduced because of a reduced Cu surface area (Table 4). Note that Nunan et al. [20] also studied the effect of Cs loading on Cs-Cu-ZnO catalysts for methyl formate formation from syngas and concluded that there was an optimum Cs loading at which methyl formate yield reached a maximum value, in agreement with the present observations made regarding the effect of Cs loading on the Cs-Cu-MgO catalyst.

Hsiao and Lin [78] have studied the synthesis of methyl formate and higher alcohols over Cu-MgO-Al_2O_3 (Cu/MgO/Al_2O_3 = 4/5/91 wt %) at 523 K, 101 kPa and W/F = 106.1×10^{-3} min.g.$(cm^3(STP)^{-1})$. The study reported a total conversion of 82 % with CO, CO_2 and CH_3OCH_3 as the only products. The catalyst showed no activity towards methyl formate or C_2 species, whereas over Cu-MgO in the present study, high selectivity towards methyl formate (S_{MF} = 29.3 %, Table 7) and low selectivity towards C_2 species (S_{C_2} = 0.9 %, Table 7) was observed. The low Cu (4 wt %) and MgO (5 wt %) content of the Cu-MgO-Al_2O_3 catalyst used by Hsiao and Lin [78] and the presence of the acidic Al_2O_3 support, results in the formation of CH_3OCH_3, generated by the acid catalysed dehydration of methanol. The SA_{BET} and Cu^0 dispersion for Cu-MgO-Al_2O_3 were reported as 115 $m^2.g^{-1}$ and 60 %, respectively [78], whereas for the Cu-MgO of the present work, values of 74 $m^2.g^{-1}$ and 1.54 %, respectively were obtained (Table 3 and Table 4). These distinct differences, together with the higher temperature and W/F used by Hsiao and Lin [78] account for the differences in product distributions between the two studies.

2.5   Conclusion

High surface area MgO, 40wt% Cu-MgO and alkali (K_2O and Cs_2O) promoted 40wt% Cu-MgO were prepared by thermal decomposition of metal salts in the presence of palmitic acid. The basicity of the catalysts decreased in the order: 13.5wt% Cs-40wt% Cu-MgO > 4.4wt% K-40wt% Cu-MgO > 0.5wt% Cs-40wt% Cu-MgO > 0.5wt% K-40wt% Cu-MgO > 40wt% Cu-MgO > MgO. The intrinsic basicity of the 40wt% Cu-MgO was more than 10 times greater than a conventional Cu-ZnO catalyst while the intrinsic basicity of the alkali promoted 40wt% Cu-MgO catalysts was more than 3 times greater than a conventional alkali promoted Cu-ZnO catalyst. Over the alkali promoted 40wt% Cu-MgO catalysts at 101 kPa and 498 K with a $CO/He/CH_3OH$ (0.66/0.20/0.14) feed gas, methyl formate was the primary product while CO was a secondary product. C_2 species were also produced with low selectivity (S_{C_2} < 5%). Formation of methyl formate and C_2 species was attributed to basic sites and Cu^0 and there was an optimum basicity (9.5 μmol $CO_2.m^{-2}$) at which the S_{MF} and S_{C_2} reached a maximum.

Chapter 3

The effect of Cu loading on the formation of methyl formate and C_2-oxygenates from CH_3OH and CO over Cs (K)-promoted Cu-MgO catalysts at 101 kPa

3.1 Introduction

In Chapter 2 the role of basic sites over Cu-MgO-based catalysts in the synthesis of methyl formate and C_2 species from CO/CH_3OH at 101 kPa was studied. Besides basic sites, the presence of copper sites was also identified as critical in the synthesis of C_2 oxygenates from syngas over alkali promoted Cu-metal oxide catalysts [20,29-35]. However, in Chapter 2 the role of the copper sites over Cu-MgO-based catalysts in the synthesis of methyl formate and C_2 species was not addressed. Therefore, in the present chapter the effect of the copper sites was investigated. In Chapter 2, the Cu^0 dispersion of the Cs or K promoted-40wt% Cu-MgO catalysts was low (< 2%). In the present chapter, Cu^0 dispersion was improved by decreasing the Cu loading from 40wt% to 5wt% in the Cs or K promoted -Cu-MgO catalysts. Based on previous mechanistic studies over Cu-metal oxide-based catalysts [20,29-34,79], it is apparent that the state of surface copper (Cu^0 or Cu^{1+} or Cu^{2+}) is an important factor in determining the catalyst selectivity to C_2 oxygenates. Therefore, X-ray photoelectron spectroscopy (XPS) analysis was used to identify the state of the copper in the Cs or K promoted 5wt% Cu-MgO catalysts and the Cs or K promoted 40wt% Cu-MgO catalysts. The

copper characterization and activity of the Cs or K promoted 5wt% Cu-MgO catalysts are compared with the copper characterization and activity results for the alkali-promoted 40wt% Cu-MgO catalysts. Results of the comparison were used to establish a correlation between the copper properties of the prepared catalysts and their activity for C_2 oxygenate synthesis.

3.2   Experimental

3.2.1   Catalyst preparation

High surface area 5wt% Cu-MgO and alkali promoted 5wt% Cu-MgO (0.5 wt% K-5wt% Cu-MgO and 0.5 wt% Cs-5wt% Cu-MgO) were prepared by thermal decomposition of metal salts ($Mg(NO_3)_2.6H_2O$, $Cu(NO_3)_2.3H_2O$, Cs_2CO_3 and KNO_3) in the presence of palmitic acid ($CH_3(CH_2)_{14}COOH$). The details of the catalyst preparation procedure were reported in the previous chapter. Note that the final calcination temperature used for each catalyst precursor was determined by the highest decomposition temperature of the metal nitrates or carbonates present in the precursor and as a result, the calcination temperature for the 5wt% Cu-MgO, 0.5wt% K-5wt% Cu-MgO and 0.5wt% Cs-5wt% Cu-MgO were respectively 673 K, 873 K and 923 K. Following calcination, the catalyst precursors were reduced by heating to 573 K at a rate of 10 K/min in 10% H_2/He, with the final temperature held for 60 min.

3.2.2   Catalyst characterization

Temperature-programmed reduction (TPR) of the prepared catalyst precursors was performed using a Micromeritics AutoChem II chemisorption analyzer, with a 10 % H_2/Ar gas flow of 50 cm^3(STP).min^{-1} while heating from 313 K to 623 K at a ramp rate of 10 K.min^{-1}, with the final temperature held for 30 min. Prior to the TPR, samples (about 0.2 g) were pre-treated thermally in He at 50 cm^3(STP).min^{-1} and 393 K. The TPR profiles of the 5wt% Cu-MgO-based catalysts of the present study were compared to the TPR profiles of CuO and Cu_2O (97 % purity, particle size < 5 micron, Sigma Aldrich) reported in Figure 15.

Catalyst BET surface areas, pore volume, pore diameter and pore size distribution of the calcined 5wt% Cu-MgO catalyst precursors were measured using a Micromeritics ASAP 2020 analyzer (more detail given in Section 2.2.2). Catalyst BET surface area of the reduced 5wt% Cu-MgO-based catalysts were measured using Micromeritics AutoChem II chemisorption analyzer (more detail given in Section 2.2.2). Basic properties of the reduced catalysts were determined by CO_2 temperature-programmed desorption (TPD) using a Micromeritics AutoChem II chemisorption analyzer, details of which are provided in Section 2.2.2.

X-ray powder diffraction (XRD) patterns of the calcined catalyst precursors were obtained with a Rigaku Multiflex diffractometer using Cu Kα radiation (λ=0.154 nm, 40 kV and 20 mA), a scan range of 2θ from 10° to 100º and a step size of 2 º.min^{-1}. The MgO crystallite size (d_{MgO}^{XRD}) was determined from the XRD data using the Scherrer equation. The Cu

71

crystallite size (d_{Cu}^{XRD}) was estimated from the CuO crystallite size of the calcined samples, corrected for the differences in molar volume between CuO and Cu. Further detail of calculation for d_{MgO}^{XRD} and d_{Cu}^{XRD} were given in Section 2.2.2.

The Cu^0 dispersion and Cu surface area of the reduced 5wt% Cu-MgO-based catalysts were measured by adsorption and decomposition of N_2O on Cu sites using a Micromeritics AutoChem II chemisorption analyzer and the detail of the analysis is given in Section 2.2.2.

X-ray photoelectron spectroscopy (XPS) studies of the passivated, reduced catalysts, were conducted using a Leybold Max200 X-ray photoelectron spectrometer. Al Kα was used as the photon source generated at 15 kV and 20 mA. The pass energy was set at 192 eV for the survey scan and 48 eV for the narrow scan. The reduced Cu-MgO-based catalyst with Cu content of 34.6wt% - 40.1 wt% was passivated in a flow of 100 cm^3(STP).min^{-1} of 1% O_2/He for 120 min. All XPS spectra were corrected to the Mg 2p peak at 50.8 eV.

3.2.3 Catalyst testing

Catalyst testing was conducted in a plug flow micro-reactor, details of which have been reported previously in Section 2.2.3. Note that for all of the reaction experiments, 0.98 g of catalyst was used with a reactant mixture of CO/He/CH_3OH (0.66/0.20/0.14 molar). In each test, total net conversion was defined as the sum of the net CO consumption and the net CH_3OH conversion. In all cases net CO consumption was in the range of 3 C-atom% – 10 C-atom %, implying that the rate of CH_3OH decomposition to CO was lower than the rate of

CO conversion to different carbonaceous products. Therefore, the yield of CO and selectivity of CO in the product stream were assumed to be zero. The C-atom yield of each carbonaceous product was determined as C-atom molar flow rate of that product divided by C-atom total molar flow rate of all the carbonaceous products. The C-atom selectivity of each product was determined as the C-atom yield of that product divided by the total net conversion. Note that more detail on the calculation of the net CO consumption, net CH_3OH conversion, total net conversion, product C-atom yield and product C-atom selectivity is explained in Appendix F.

3.3   Results

3.3.1   Catalyst characterization

The nominal composition of the catalysts discussed in the present study are reported in Table 9. The catalyst BET surface area (SA_{BET}), pore volume (V_P) and average pore diameter (d_P) of the 5wt% Cu-MgO-based catalysts are compared to the 40wt% Cu-MgO-based catalysts in Table 10. Note that SA_{BET}, V_P and d_P for 40wt% Cu-MgO-based catalysts were taken from Table 3 in the previous chapter. For the 5wt% Cu-MgO-based catalysts, d_p was in the range 14 nm – 26 nm, indicative of a mesoporous catalyst. For the 5wt% Cu-MgO-based catalysts, the SA_{BET} remained unchanged after reduction compared to the SA_{BET} after calcination (Table 10). Since the catalyst Cu loading was low, only small amounts of water were generated during reduction of CuO to Cu^0. Consequently, there was a negligible change in porosity and SA_{BET} following reduction.

Table 9 Cu-MgO-based catalyst nominal name and composition

Catalyst Nominal Name	Catalyst Composition (wt %)			
	Cu	MgO	K	Cs
40wt% Cu-MgO[a]	40.3	59.3	0	0
0.5wt% K-40wt% Cu-MgO[a]	40.1	59.4	0.5	0
0.5wt% Cs-40wt% Cu-MgO[a]	40.1	59.4	0	0.5
5wt% Cu-MgO	5.0	95.0	0	0
0.5wt% K-5wt% Cu-MgO	5.0	94.5	0.5	0
0.5wt% Cs-5wt% Cu-MgO	5.0	94.5	0	0.5

[a] Catalysts reported previously in Chapter 2.

The pore size distributions of the calcined 5wt% Cu-MgO-based catalyst precursors are compared to those of the 40wt% Cu-MgO-based catalysts and MgO in Figure 23. Compared to MgO, the addition of 5 wt% Cu shifted the maxima of the pore size distribution to a higher pore diameter, whereas both the SA_{BET} and V_p decreased (Table 10). These observations are in good agreement with the trend reported previously for the 40wt% Cu-MgO-based catalysts (Figure 13). Comparison of the pore size distribution of the 5wt% Cu-MgO and 40wt% Cu-MgO (Figure 23), showed that an increase in Cu loading broadened the catalyst pore size distribution and led to a decrease in SA_{BET} and V_p of the Cu-MgO (Table 10). These observations imply that an increase in Cu loading most likely led to blockage of the small pores ($d_p < 10nm$) of MgO by CuO.

Table 10 BET surface area, pore volume and pore size of alkali promoted Cu-MgO catalysts

Catalyst	SA_{BET}^{a} $(m^2.g^{-1})$		V_p^{a} $(cm^3.g^{-1})$	d_p^{a} (nm)
	After calcinations	After reduction		
MgO^{b}	160	160	0.58	14.5
40wt% Cu-MgO^{b}	62	74	0.23	15.0
0.5wt% K-40wt% Cu-MgO^{b}	35	42	0.20	23.1
0.5wt% Cs-40wt% Cu-MgO^{b}	38	44	0.20	20.8
5wt% Cu-MgO	141	141	0.49	14.0
0.5wt% K-5wt% Cu-MgO	60	60	0.37	24.5
0.5wt% Cs-5wt% Cu-MgO	51	51	0.33	26.0

[a] SA_{BET}, V_p and d_p are respectively BET surface area, pore volume and average pore size of the calcined catalyst precursor. The detail of repeatability for SA_{BET}, V_p and d_p is shown in Appendix B.1. Note that $\sigma_{SA_{BET}} \leq \pm 5\ m^2.g^{-1}$, $\sigma_{V_p} \leq \pm 0.03\ cm^3.g^{-1}$ and $\sigma_{d_p} \leq \pm 2.6\ nm$.

[b] Characterization data taken from Table 3.

Addition of 0.5wt% Cs or 0.5wt% K to the 5 wt% Cu-MgO decreased the SA_{BET} and V_P (Table 10), as was similarly observed with the addition of 0.5wt% Cs or 0.5wt% K to 40 wt% Cu-MgO (Table 3). Previously, it was shown that a decrease in SA_{BET} and V_P after addition of Cs or K to the Cu-MgO was caused by (1) thermal sintering of the catalyst due to the higher calcination temperature of the alkali promoted Cu-MgO compared to the Cu-MgO and (2) pore blocking of MgO by K promoter or Cs promoter (Chapter 2). In the present study, the same effects of promoters and caclination temperature are apparent from the shift in the

maxima of the pore size distribution to higher pore diameter after addition of 0.5wt% Cs or 0.5wt% K to 5 wt% Cu-MgO (Figure 23).
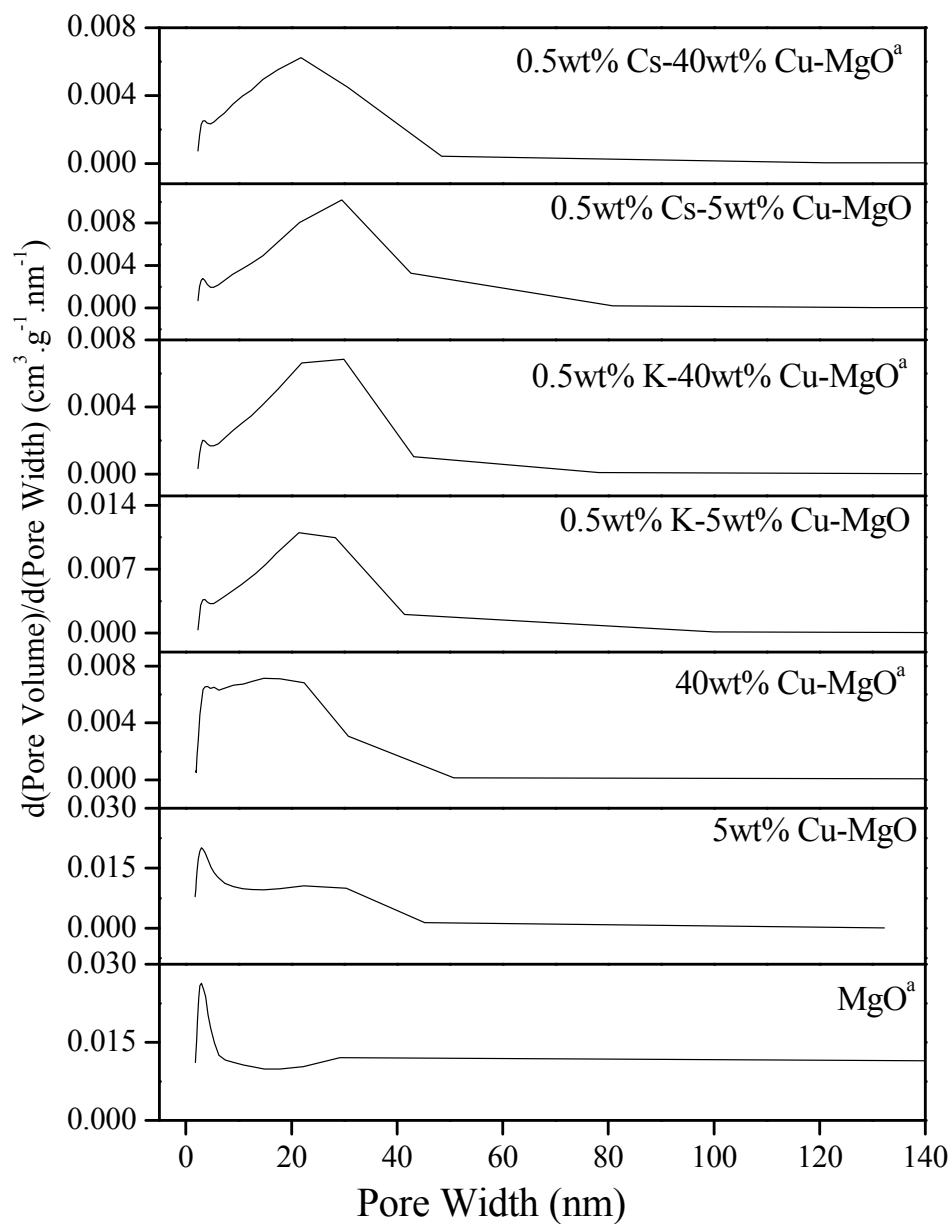
Figure 23 Pore volume distribution of MgO, unreduced 5wt% Cu-MgO-based catalysts and unreduced 40wt% Cu-MgO-based catalyst.[a] Data was taken from Figure 13.

Comparing the pore size distribution (Figure 23) of the 0.5 wt% K-5wt% Cu-MgO and the 0.5wt% K-40wt% Cu-MgO, reveals almost the same pore size distribution for both catalysts. The same trend was observed for the 0.5 wt% Cs-5wt% Cu-MgO and the 0.5wt% Cs-40wt% Cu-MgO (Figure 23). These observations show that an increase in Cu loading from 5wt% to 40wt% of the K- or Cs-promoted Cu-MgO doesn't affect the catalyst pore size distribution noticeably, implying that high temperature thermal sintering and the presence of the alkali promoters are the major factors determining the pore size distribution of the K- or Cs-promoted Cu-MgO.

The x-ray diffractogram of the calcined 5 wt% Cu-MgO catalyst precursors (Figure 24) showed the presence of MgO (periclase, Fm3m(225)-cubic structure) and CuO (tenorite, C2/c(15) monoclinic structure). No peaks associated with Cu_2O, K_2O or Cs_2O were detected. The observations are in good agreement with the XRD analysis of the 40wt% Cu-MgO-based catalysts (Figure 14). Note that the x-ray diffractograms of CuO and MgO which was reported previously in Figure 14 in Chapter 2, are also included in Figure 24 for comparison purposes. Using the data of Figure 24, the MgO crystallite thickness (d_{MgO}^{XRD}) and the Cu crystallite thickness (d_{Cu}^{XRD}) were estimated and the results are reported in Table 11. For the 5wt% Cu-MgO-based catalysts, d_{MgO}^{XRD} and d_{Cu}^{XRD} increased as the SA_{BET} and V_P decreased, supporting the assertion that the loss in SA_{BET} and V_P was partly due to thermal sintering of the Cu and MgO crystallites and in agreement with the results from the 40 wt% Cu-MgO catalysts (Chapter 2:). The data of Table 11 also show that a decrease in Cu loading from 40wt% to 5wt% led to almost no change in d_{MgO}^{XRD} and d_{Cu}^{XRD} for both the un-promoted and alkali-promoted catalysts.

Table 11 Copper dispersion, crystallite size and MgO unit cell size of 5wt% Cu-MgO-based catalysts[a]

Catalyst	Cu^0 Dispersion (%)	$SA_{Cu}^{N_2Ob}$ ($m^2.g^{-1}$)	$d_{Cu}^{N_2O}$ (nm)	d_{Cu}^{XRD} (nm)	d_{MgO}^{XRD} (nm)	a_{MgO} (nm)
MgO[c]	-	-	-	-	13	0.42
40wt% Cu-MgO[c]	1.54	2.64	65	15	17	0.42
0.5wt% K-40wt% Cu-MgO[c]	0.19	0.50	519	21	20	0.42
0.5wt% Cs-40wt% Cu-MgO[c]	0.28	0.58	362	24	20	0.42
5wt% Cu-MgO	13.52	1.24	8	17	15	0.42
0.5wt% K-5wt% Cu-MgO	2.98	0.26	34	21	19	0.42
0.5wt% Cs-5wt% Cu-MgO	13.24	1.10	8	26	20	0.42

[a] The detail of repeatability for Cu^0 Dispersion, $SA_{Cu}^{N_2O}$, d_{Cu}^{XRD}, $d_{Cu}^{N_2O}$, d_{MgO}^{XRD} and a_{MgO} is shown in Appendix B.3 and B.4. Note that $\sigma_{Cu^0\ Dispersion} \leq \pm 2.59\ \%$, $\sigma_{SA_{Cu}^{N_2O}} \leq \pm 0.36\ m^2.g^{-1}$ and $\sigma_{d_{Cu}^{N_2O}} \leq \pm 1$ nm.

[b] Copper metal surface area was calculated assuming 1.46×10^{19} copper atoms per m^2.

[c] Data taken from Table 4 of Chapter 2.

The XRD data were used to calculate the unit cell size of the MgO (a_{MgO}) as reported in Table 11. The results show that a_{MgO} remained unchanged with the addition of the CuO as well as the K promoter or Cs promoter to the 5wt% Cu-MgO, implying that there was no solid solution present in the catalyst. Similar observations were made for the 40 wt% Cu-MgO catalysts, suggesting that the preparation of the unreduced Cu-MgO-based catalysts using palmitic acid yields separate phases of MgO, CuO and alkali promoters (K or Cs), rather than solid solutions.
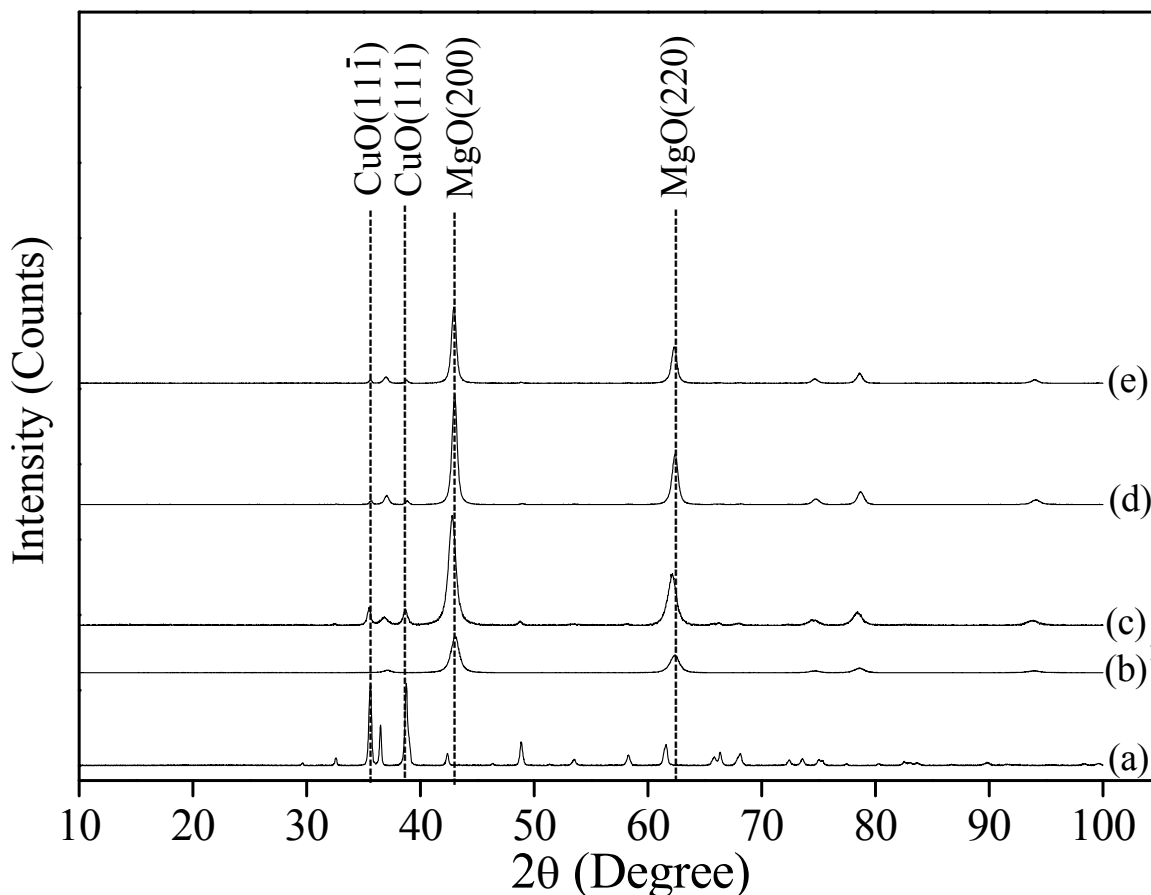
Figure 24 X-ray diffractograms of the unreduced MgO-based catalysts and bulk CuO: (a) CuO; (b) MgO; (c) 5wt% Cu-MgO ; (d) 0.5wt% K-5wt% Cu-MgO; (e) 0.5wt% Cs-5wt% Cu-MgO. [1] Data from Figure 14 of Chapter 2.

The Cu^0 dispersion of the 5wt% Cu-MgO-based catalysts was measured by N_2O adsorption-decomposition and the results, reported in Table 11, show that the Cu^0 dispersion varied from 2 % to 13 %. Addition of K to the 5 wt% Cu-MgO catalyst led to a decrease in Cu^0 dispersion, similar to the results obtained for the 40wt% Cu-MgO catalysts (Table 4). We assume that K_2O (or KOH) readily wets the Cu, which leads to a decrease in Cu^0 dispersion. Addition of Cs to the 5 wt% Cu-MgO catalyst did not affect the Cu^0 dispersion significantly, whereas addition of Cs to the 40wt% Cu-MgO decreased the Cu^0 dispersion (Table 11). These results

suggest a strong interaction between the Cs_2O and the MgO that prevents the Cs_2O from wetting the Cu. However, at high Cu loading some interaction between the Cs and the Cu must occur which leads to a decrease in Cu^0 dispersion. Comparing the Cu^0 dispersion of the 5wt% Cu-MgO-based catalysts (Table 11) with the 40wt% Cu-MgO-based catalysts (Table 11) shows that a decrease in Cu loading improved the Cu^0 dispersion. The Cu crystallite size of the 5wt% Cu-MgO catalysts measured by N_2O adsorption-decomposition ($d_{Cu}^{N_2O}$) as well as by XRD (d_{Cu}^{XRD}) are shown in Table 11. Both $d_{Cu}^{N_2O}$ and d_{Cu}^{XRD} are in good agreement for all of the 5wt% Cu-MgO-based catalysts, implying that the Cu crystallites (diameter < 30 nm) were not occluded from the surface and are well dispersed. On the other hand, the 40 wt% Cu-MgO-based catalysts had low Cu^0 dispersion and a significant difference between the $d_{Cu}^{N_2O}$ and d_{Cu}^{XRD} values, suggesting that the Cu was occluded from the surface of the 40wt% Cu-MgO-based catalysts (Table 4). Clearly, a decrease in Cu loading from 40wt% to 5wt%, led to an increase in Cu^0 dispersion.

The TPR profiles of the calcined catalyst precursors of the present study are shown in Figure 25 and the reduction peak temperatures and calculated degrees of reduction are summarized in Table 12. For comparison, the TPR profiles and results of CuO and Cu_2O are taken from Chapter 2 and reported in Figure 25 and Table 12. Note that the degree of reduction was calculated using equation E2, explained in Section 2.3.1. The TPR curve for bulk CuO was deconvoluted to show a reduction peak at 480 K and 520 K (Figure 25). The lower peak temperature is attributed to the reduction of CuO and the higher peak temperature is likely a consequence of the reduction of large CuO particles (diameter ~270 μm) via shrinking core kinetics. Reduction of the bulk (unsupported) CuO is initiated on the surface so that

subsequently, the sample consists of a layer of Cu^0 over a CuO core. Reduction of the core is therefore, limited by H_2 diffusion to the core of large, partially reduced Cu-CuO, and this is reflected in an apparent higher reduction temperature in the TPR profile. The Cu_2O showed a reduction peak at 594 K. The TPR profile of all the 5wt% Cu-MgO-based catalysts (Figure 25) show a reduction peak in the range of 479 K – 486 K (Table 10) that can be attributed to the reduction of bulk CuO, in agreement with the XRD results (Figure 24) that detected the presence of bulk CuO as the only reducible species in the calcined 5wt% Cu-MgO-based catalyst. These results show that the CuO of the 5wt% Cu-MgO-based catalysts was well dispersed, in good agreement with the high Cu^0 dispersion of the 5wt% Cu-MgO-based catalysts reported in Table 11, so that during reduction, H_2 diffusion into the core of the catalysts was not rate controlling. Since for all of the 5wt% Cu-MgO catalysts reduction peaks were significantly below the Cu_2O reduction peak temperature (Table 12), it can be concluded that no Cu_2O was present in the 5wt% Cu-MgO catalysts.

The TPR results of the 5 wt% Cu-MgO-based catalysts revealed that, in all cases, the degree of reduction of the CuO was only between 30 % - 40 %, likely due to the high Cu^0 dispersion of the 5wt% Cu-MgO-based catalysts (Table 11) and the associated strong interaction between CuO and MgO that prevented complete CuO reduction. On the other hand, previously we reported that all the 40wt% Cu-MgO-based catalysts had > 80% reduction but low Cu^0 dispersions (0.2% – 1.5%) (Table 4) which is indicative of weaker interaction between CuO and MgO that resulted in a higher degree of reduction. Addition of K- or Cs-promoter to the 5wt% Cu-MgO, caused a slight decrease in the CuO degree of reduction (Table 12).
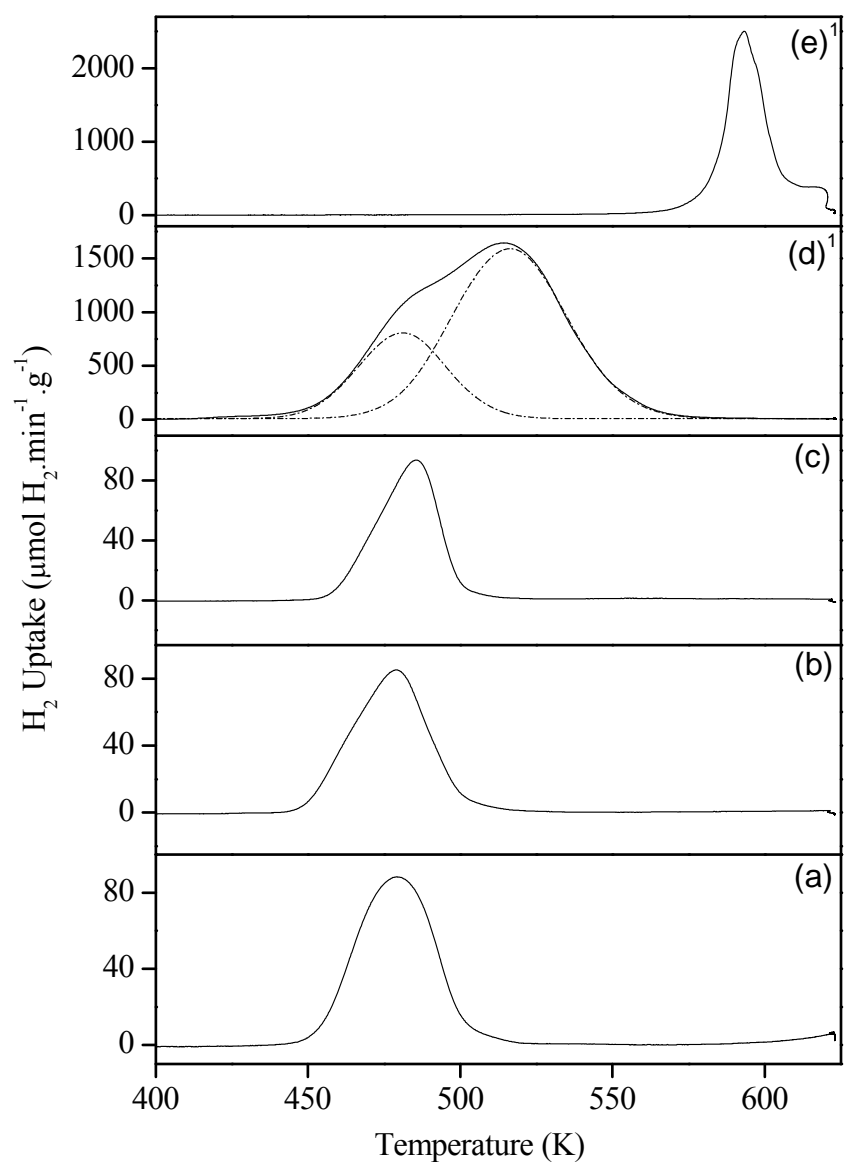
Figure 25 Temperature programmed reduction profile for: (a) 5wt% Cu-MgO; (b) 0.5wt% K- 5wt% Cu-MgO; (c) 0.5wt% Cs-5wt% Cu-MgO; (d) CuO; (e) Cu$_2$O.[1] Data were taken from Figure 15.

Table 12 Temperature programmed reduction results for 5wt% Cu-MgO-based catalysts[a]

Sample	Hydrogen Consumption (mmol.g^{-1} catalyst)	Degree of Reduction (%)	Reduction Peak Temperature (K)
Cu$_2$O-reference[b]	6.84	100	594
CuO-reference[b]	11.06	88	480 and 520
5wt% Cu-MgO	0.27	38	479
0.5wt% K-5wt% Cu-MgO	0.26	35	479
0.5wt% Cs-5wt% Cu-MgO	0.24	30	486

[a] The detail of repeatability for Hydrogen Consumption, Degree of Reduction and Reduction Peak Temperature is shown in Appendix B.5. Note that $\sigma_{Hydrogen\ Consumption} \leq \pm 0.08$ mmol.g^{-1} catalyst, $\sigma_{Degree\ of\ Reduction} \leq \pm 5$ % and $\sigma_{Reduction\ Peak\ Temperature} \leq \pm 6$ K.

[b] Data taken from Table 5.

The CO$_2$ TPD profiles for all of the 5wt% Cu-MgO-based catalysts are shown in Figure 26 and the corresponding results are summarized in Table 13. For the purpose of comparison, the catalyst intrinsic basicity and distribution of basic sites for the 40wt% Cu-MgO-based catalyst and MgO are also reported in Table 13. Addition of K or Cs to the 5wt% Cu-MgO, increased the intrinsic basicity while the distribution of basic sites was almost unchanged (Table 13). This observation is in good agreement with the observation made for the K or Cs promoted 40wt% Cu-MgO-based catalysts (Table 13).

Addition of 5wt% Cu to MgO increased the intrinsic basicity but the distribution of basic sites was almost unchanged compared to the MgO. Comparing the intrinsic basicity of the 5wt% Cu-MgO (3.9 µmol $CO_2.m^{-2}$) to that of the 40 wt% Cu-MgO (4.3 µmol $CO_2.m^{-2}$) (Table 13) shows that an increase in Cu loading from 5wt% to 40wt%, increased the intrinsic basicity but the distribution of basic sites remained unchanged. The same trend was observed for the 0.5wt% K-Cu-MgO (Table 13) and for the 0.5wt% Cs-Cu-MgO (Table 13), as the Cu loading was increased from 5wt% to 40wt%. Previous studies [76,79] suggested that in Cu-MgO, Cu gains a large net positive charge while the Cu electrons are transferred to MgO, which most likely leads to an increase in the oxygen partial negative charge in MgO. The results of the present study are in good agreement with this assertion. Of note is the fact that the specific basicity of the 0.5 wt % K and Cs promoted Cu-MgO were in a narrow range (385 – 415 µmol $CO_2.g^{-1}$) for both the 5 wt % Cu an the 40 wt % Cu catalysts.

Table 13 Basic properties of MgO-based catalyst measured by means of CO_2 TPD[a]

Catalyst	Specific Basicity (μmol $CO_2.g^{-1}$)	Intrinsic Basicity (μmol $CO_2.m^{-2}$)	Distribution of different basic sites on the catalyst (%)		
			Weak	Medium	Strong
MgO[b]	432.0	2.7	8	15	77
40wt% Cu-MgO[b]	315.5	4.3	9	19	72
0.5wt% K-40wt% Cu-MgO[b]	392.4	9.3	11	21	69
0.5wt% Cs-40wt% Cu-MgO[b]	415.9	9.5	16	19	65
5wt% Cu-MgO	547.1	3.9	9	17	75
0.5wt% K-5wt% Cu-MgO	394.8	6.6	5	11	84
0.5wt% Cs-5wt% Cu-MgO	384.5	7.5	10	23	67

[a] The detail of repeatability for Specific Basicity, Intrinsic Basicity and distribution of different basic sites on the surface of the above listed catalysts is shown in Appendix B.6. Note that $\sigma_{\text{Specific Basicity}} \leq \pm 17.0$ μmol $CO_2.g^{-1}$ and $\sigma_{\text{Intrinsic Basicity}} \leq \pm 0.2$ μmol $CO_2.m^{-2}$.

[b] Data from Table 6.
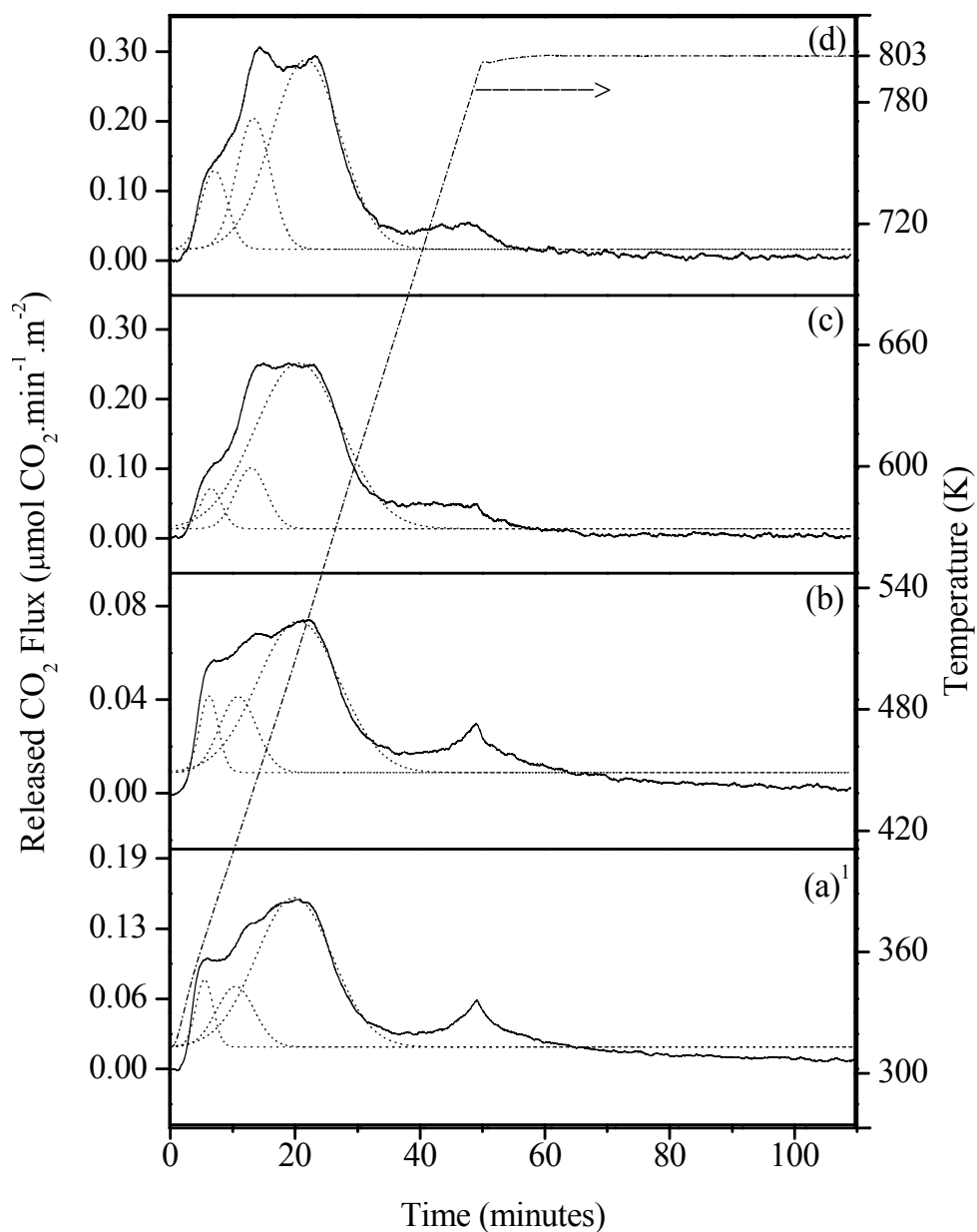
Figure 26 CO$_2$ temperature programmed desorption of (a) MgO;(b) 5wt% Cu-MgO ; (c) 0.5wt% K-5wt% Cu-MgO; (d) 0.5wt% Cs-5wt% Cu-MgO. [1] Data from Figure 16.

The surface composition of the K- or Cs-promoted 40wt% Cu-MgO catalysts, as measured by XPS, are summarized in Table 14. The Mg 2p spectra showed a binding energy of 50.86

eV (Table 14) which corresponds to Mg^{2+} in MgO [80]. The C 1s spectra showed a peak at BE 285.88 eV to 286.74 eV (Table 14) which indicates carbon contamination of the Cu-MgO-based catalyst due to MgO bonding with $HCOOCH_3$ [81] that occurs because of the presence of palmitic acid in the catalyst precursor. Note that XPS analysis conducted on the 0.5wt% K-5wt% Cu-MgO and the 0.5wt% Cs-5wt% Cu-MgO (not reported herein) showed similar Mg 2p and C 1s peaks compared to the K- or Cs-promoted-40wt% Cu-MgO catalysts, but no peak corresponding to Cu was detected, likely due to the surface Cu concentration being lower than the detection limit of the XPS unit. For the 0.5 wt% K-40wt% Cu-MgO and the 0.5 wt% Cs-40wt% Cu-MgO, no XPS peaks associated with Cs or K were observed, because the alkali promoter surface concentration was below the XPS detection limit. Consequently, catalysts with higher concentrations of alkali metal were prepared for XPS analysis. Previous studies have shown that the K 2p BE of 297.3 eV is attributable to the presence of K_2O whereas a K 2p BE of 292.8 eV – 293.1 eV is attributable to the presence of KOH [82]. XPS analysis conducted on a 4.4 wt% K-40 wt% Cu-MgO catalyst showed a K 2p BE of 294.65 eV, which indicated the presence of mostly KOH. However, since the K 2p BE of the present study is slightly higher than the KOH K 2p BE, the presence of small amounts of K_2O is also possible. This reveals that KNO_3 was successfully decomposed to KOH and K_2O during catalyst calcination of the 4.4 wt% K-40 wt% Cu-MgO catalyst. Results of the XPS analysis of a 13.5 wt% Cs-40 wt% Cu-MgO showed a Cs 3d BE of 725.89 eV, which reveals the presence of Cs^+ in the form of Cs_2O on the surface of the catalyst [83]. This reveals that Cs_2CO_3 was successfully decomposed to Cs_2O during catalyst calcination of the 13.5 wt% Cs-40 wt% Cu-MgO catalyst. Note that oxidation state of the promoters determined by XPS analysis of the 4.4 wt% K-40 wt% Cu-MgO and 13.5 wt% Cs-

40 wt% Cu-MgO, is assumed to also be valid for the 0.5wt% alkali promoted-40 wt% Cu-MgO catalyst, in agreement with other studies [82,83].

Cu 2p XPS spectra of the passivated K- or Cs-promoted-40wt% Cu-MgO catalysts are shown in Figure 27 and the corresponding Cu $2_{p_{1/2}}$(satellite), Cu $2_{p_{1/2}}$ (parent), Cu $2_{p_{3/2}}$ (satellite) and Cu $2_{p_{3/2}}$ (parent) BEs are reported in Table 15. Based on the XPS results, all the passivated alkali promoted-40wt%Cu-MgO catalysts showed the presence of CuO on the catalyst surface. The ratio of the area under the Cu $2_{p_{3/2}}$ (satellite) peak to the area under the Cu $2_{p_{3/2}}$ (parent) peak ($\frac{\text{Area}_{[\text{Cu }2p_{3/2}(\text{stellite})]}}{\text{Area}_{[\text{Cu }2p_{3/2}(\text{parent})]}}$), indicative of the degree of Cu oxidation [69], were calculated for all the passivated Cs (K)-promoted 40wt%Cu-MgO catalysts and are reported in Table 15. Note that the area under the Cu $2_{p_{3/2}}$ (satellite) peak ($\text{Area}_{[\text{Cu }2p_{3/2}(\text{stellite})]}$) and the area under the Cu $2_{p_{3/2}}$ (parent) peak ($\text{Area}_{[\text{Cu }2p_{3/2}(\text{parent})]}$) were calculated by numerical integration of the corresponding peaks presented in Figure 27. The $\frac{\text{Area}_{[\text{Cu }2p_{3/2}(\text{stellite})]}}{\text{Area}_{[\text{Cu }2p_{3/2}(\text{parent})]}}$ ratio of all the passivated alkali promoted-40wt% Cu-MgO catalysts was noticeably lower than the $\frac{\text{Area}_{[\text{Cu }2p_{3/2}(\text{stellite})]}}{\text{Area}_{[\text{Cu }2p_{3/2}(\text{parent})]}}$ ratio in CuO (Table 15), which confirms the presence of Cu^0 in all the passivated K- or Cs-promoted-40wt% Cu-MgO catalysts. The presence of CuO on the catalyst surface may be partly due to the fact that the K- or Cs-promoted-40wt% Cu-MgO was passivated before XPS analysis. Hence the amount of Cu^0 on the catalyst surface estimated by XPS, represents the minimum amount of Cu^0 on the surface of the freshly reduced K- or Cs-promoted-40wt% Cu-MgO present under reaction operating conditions.

Table 14 Catalyst surface composition, binding energies for Mg 2p, C 1s, Cs 3d and K 2p along with the Cu/Mg atomic ratio

Catalyst	Composition (atomic %)						$\dfrac{Cu^{total}}{Mg}$ [a] (atom ratio)	Binding energy (eV)			
	C	O	Mg	Cu	K	Cs		Mg 2p	C 1s	Cs 3d	K 2p
0.5wt% K-40wt% Cu-MgO[b]	26.5	40.2	31.5	1.9	-	-	0.06	50.86	285.88	-	-
0.5wt% Cs-40wt% Cu-MgO[b]	23.6	39.3	35.5	1.6	-	-	0.04	50.84	285.92	-	-

[a] $\sigma_{\frac{Cu^{total}}{Mg}} \leq \pm 0.01$. [b] The catalysts were passviated in 1% O_2/He for 120 min.

Table 15 Binding energy value for Cu 2p$_{1/2}$, Cu2p$_{3/2}$ and ratio of area under Cu2p$_{3/2}$ (satellite) peak to area under Cu2p$_{3/2}$ (parent) peak

Catalyst	Binding Energy (eV)				$\dfrac{Area_{[Cu\,2p_{3/2}(stellite)]}}{Area_{[Cu\,2p_{3/2}(parent)]}}$
	Cu 2p$_{1/2}$ (satellite)	Cu 2p$_{1/2}$ (parent)	Cu 2p$_{3/2}$ (satellite)	Cu 2p$_{3/2}$ (parent)	
CuO[a]	962.1	953.6	942.2	933.5	0.7164
Cu^{0} [b]	-	952.5	-	932.7	-
0.5wt% K-40wt% Cu-MgO[c]	963.5	953.6	943.2	933.8	0.2082
0.5wt% Cs-40wt% Cu-MgO[c]	962.9	953.6	943.3	933.7	0.1504

[a] Data from previous study [69]. [b] Data from previous study [84]. [c] The catalysts were passviated in 1% O_2/He for 120 min.
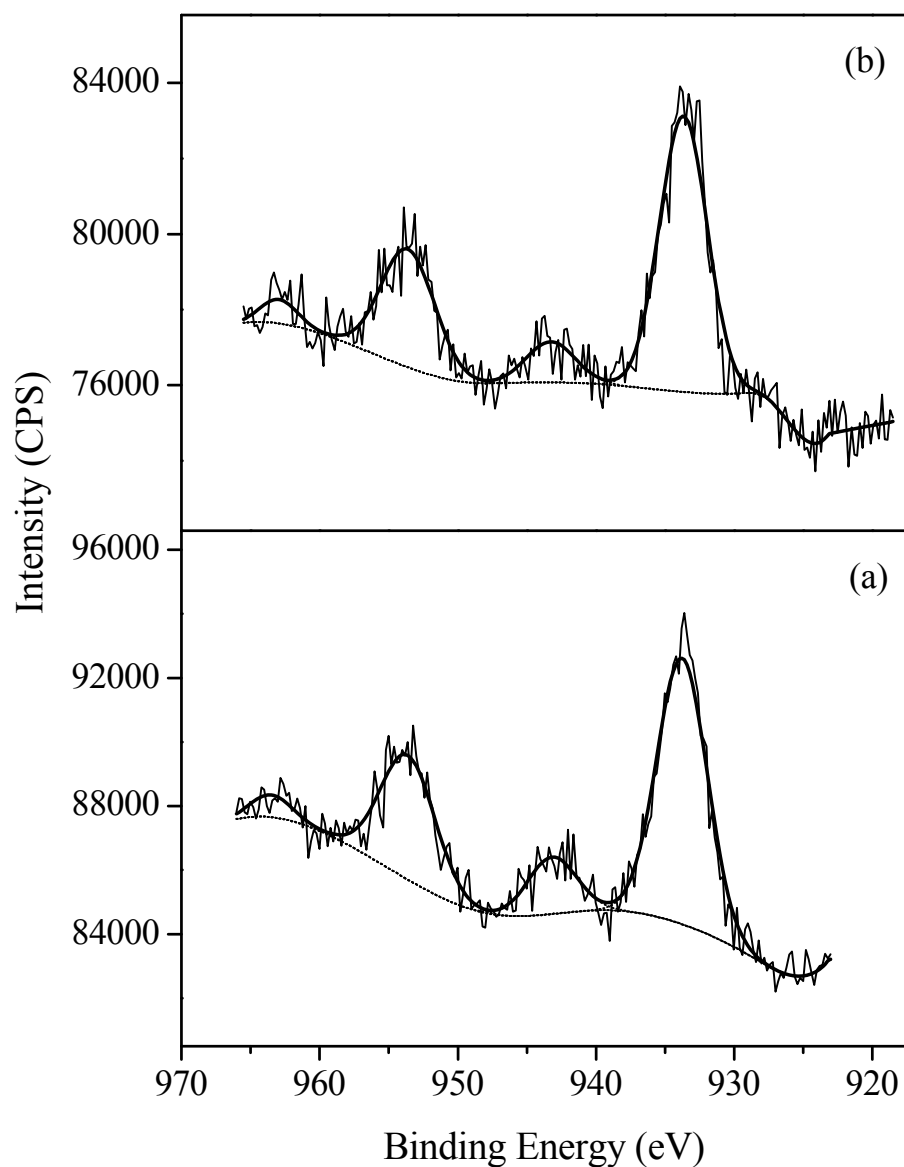
Figure 27 Cu 2p XPS spectra for (a) 0.5wt% K-40wt% Cu-MgO, (b) 0.5wt% Cs-40wt% Cu-MgO

In the binary CuO-MgO system, it is very important to thermally treat the system well below the eutectic melting point to avoid a drastic loss in the BET surface area of CuO-MgO. The eutectic melting point of 40wt% CuO-MgO is 1400 K [85]. As discussed in Section 2.2.1, calcination of 40wt% CuO-MgO catalysts and Cs (K)-promoted-40wt% CuO-MgO catalysts

was conducted in the temperature range of 673 K – 923 K. This range of calcination temperatures is well below the eutectic melting point of 40wt% CuO-MgO, which ensures no drastic loss of BET surface area in the catalysts due to melting of the eutectic CuO-MgO crystallites.

Based on XPS results in this section, K_2O and Cs_2O were identified respectively on the surface of the 4.4 wt% K-40wt% Cu-MgO catalyst and 13.5wt% Cs-40wt% Cu-MgO catalyst. To the author's knowledge, no study has focused on determining the phase diagram for the binary K_2O-MgO system and the binary Cs_2O-MgO system. However, some studies have focused on determining the phase diagram for the K_2O-MgO-SiO_2 system [86,87] and Cs_2O-SiO_2 system [88]. The eutectic melting point for the 4.4 wt% K_2O-MgO-SiO_2 is 1447 K [86] and the eutectic melting point for the 13.5wt% Cs_2O-SiO_2 is 1123 K [88]. On the other hand the melting point of pure MgO is 3073 K whereas the melting point of pure SiO_2 is 1743 K. Therefore, it is likely that the eutectic melting point of the 4.4 wt% K_2O-MgO is > 1447 K and eutectic melting point of the 13.5 wt% Cs_2O-MgO is > 1123 K. The eutectic melting points of the 4.4 wt% K_2O-MgO and the 13.5 wt% Cs_2O-MgO are well above the calcination temperature of the 4.4wt% K-40wt% Cu-MgO catalyst (873K) and the 13.5 wt% Cs_2O-MgO catalyst (923K), which ensures no drastic loss of BET surface area in these catalysts due to melting of the eutectic K_2O-MgO crystallites or Cs_2O-MgO crystallites. Note that more accurate eutectic melting point for the 4.4wt% K-40wt% Cu-MgO catalyst and the 13.5 wt% Cs- 40wt% Cu-MgO catalyst, should be identified based on eutectic point of the tertiary 4.4wt% K_2O-40wt% CuO-MgO system and the tertiary 13.5 wt% Cs_2O-40wt% CuO-

MgO system. However to the author's knowledge, no study has focused on determining the phase diagram for these systems.

3.3.2   Product distribution over MgO-based catalyst

Catalyst activity was determined for the 5wt% Cu-MgO and the Cs- or K-5wt% Cu-MgO at 101 kPa and 498K, with a feed composition of He/CO/CH$_3$OH=0.20/0.66/0.14 (molar) and a contact time (W/F) of 12.3×10^{-3} g.min.(cm^3(STP))$^{-1}$. A summary of the product distribution and the total net conversion of the reactants is given in Table 16. Over the 5wt% Cu-MgO, the total net conversion was low (10.0 C-atom %) and methyl formate was the dominant product, whereas selectivity of CO$_2$ (S$_{CO_2}$) and C$_2$ species (S$_{C_2}$) was low (< 6 C-atom%). Also, no CO was produced in the reaction. The total net conversion was increased as Cs or K was added to the 5wt% Cu-MgO catalyst and the order of increase in the total net conversion was: 5wt% Cu-MgO < 0.5wt% K-5wt% Cu-MgO < 0.5wt% Cs-5wt% Cu-MgO. Results of Table 16 showed that the selectivity to methyl formate (S$_{MF}$) at 498K increased in the order: 5wt% Cu-MgO < 0.5wt% K-5wt% Cu-MgO < 0.5wt% Cs-5wt% Cu-MgO, whereas the reverse order was observed for S$_{CO_2}$ and S$_{C_2}$. The trend observed for total net conversion, S$_{MF}$ and S$_{CO_2}$ are in good agreement with previous results reported for the 40 wt% Cu-MgO catalysts (Table 7), whereas the trend observed for S$_{C_2}$ is opposite to what was observed previously (Table 7).

Over all of the 5wt% Cu-MgO-based catalysts, an increase in operating temperature from 498K to 523K led to a small increase in S$_{MF}$ and a small decrease in S$_{CO_2}$ and S$_{C_2}$ (Table 16),

implying that an increase in operating temperature does not favour the C_2 species formation, as observed previously over 40wt% Cu-MgO-based catalyst (Table 7)

The total net conversion of the reactants decreased significantly for the Cu-MgO and alkali promoted Cu-MgO catalysts as the Cu loading decreased from 40 wt% to 5 wt%. The product distribution was also changed noticeably as a result of the change in the Cu loading and net conversions. Over the 40wt% Cu-MgO-based catalysts at 498K and 12.3×10^{-3} min.g$(cm^3(STP))^{-1}$, the selectivity to CO was highest among all the carbonaceous products whereas over the 5wt% Cu-MgO-based catalysts at the same operating conditions, S_{CO} dropped to zero and selectivity to methyl formate was the highest among all the carbonaceous products.

Table 16 Product distribution and catalyst activity over MgO-based catalysts[a]

Catalyst	W/F (min.g.(cm^3(STP))$^{-1}$)	T[b] (K)	Net CO consumption (C-atom %)	Net CH$_3$OH conversion (C-atom %)	Total net Conversion[c] (C-atom %)	Product Selectivity (C-atom %)			
						CO	MF[d]	CO$_2$	C$_2$[e]
40wt% Cu-MgO[f]	12.3×10^{-3}	498	-9.7	84.7	75.0	68.4	29.3	1.5	0.9
0.5wt% K-40wt% Cu-MgO[f]	12.3×10^{-3}	498	-7.9	70.0	62.0	63.9	30.0	2.7	3.3
0.5wt% Cs-40wt% Cu-MgO[f]	1.3×10^{-3}	498	1.8	27.9	29.7	0.0	91.9	6.0	2.1
	12.3×10^{-3}	498	-6.1	66.7	60.6	53.4	34.9	8.4	3.4
5wt% Cu-MgO	12.3×10^{-3}	498	3.3	6.6	10.0	0.0	92.5	5.2	2.3
	12.3×10^{-3}	523	4.2	12.5	16.7	0.0	95.4	2.4	2.2
0.5wt% K-5wt% Cu-MgO	12.3×10^{-3}	498	3.3	13.0	16.4	0.0	96.4	2.7	0.9
	12.3×10^{-3}	523	5.3	20.0	25.3	0.0	98.5	1.5	0.0
0.5wt% Cs-5wt% Cu-MgO	12.3×10^{-3}	498	7.8	26.4	34.2	0.0	98.0	1.5	0.5
	12.3×10^{-3}	523	9.3	34.6	43.9	0.0	98.8	1.0	0.2

[a] Reaction Conditions:101 kPa, Feed He/CO/CH$_3$OH = 0.20/0.66/0.14 molar, v_0 =84.4 cm^3(STP).min^{-1}. For W/F =12.3×10^{-3} (min.g(cm^3(STP))$^{-1}$ the catalyst weight is 0.98 g and for W/F =1.3×10^{-3} (min.g(cm^3(STP))$^{-1}$ the catalyst weight is 0.1 g. The detail of repeatability for Total Net Conversion, selectivity of CO (S$_{CO}$), selectivity of methyl formate (S$_{MF}$), selectivity of CO$_2$ (S$_{CO_2}$) and selectivity of C$_2$ species (S$_{C_2}$) is shown in Appendix G.1. Note that $\sigma_{Total Net Conversion} \leq$ ± 5.6 (C-atom%), $\sigma_{S_{CO}} \leq$ ± 3.3 (C-atom%), $\sigma_{S_{MF}} \leq$ ± 2.9 (C-atom%), $\sigma_{S_{CO_2}} \leq$ ± 2.6 (C-atom%) and $\sigma_{S_{C_2}} \leq$ ± 1.0 (C-atom%). [b] T stands for reaction temperature. [c] Total conversion = Net CO consumption + Net CH$_3$OH conversion. [d] MF stands for methyl formate. [e] C$_2$ stands for C$_2$ species (ethanol and acetic acid). [f] Experimental data were taken from Table 7

3.4 Discussion

Over Cs- or K-promoted 5wt% Cu-MgO-based catalysts, methyl formate was a dominant product (Table 16). In Chapter 2 it was demonstrated that on alkali promoted Cu-MgO, the product selectivity to methyl formate and C_2 was strongly influenced by the catalyst intrinsic basicity. Furthermore, it was noted that the presence of Cu on the surface of the Cs- or K-promoted Cu-MgO catalysts is important for the formation of methyl formate from CH_3OH/CO (Figure 21). XPS studies suggested that the surface copper is present as Cu^{2+} and Cu^0 over Cs- or K- promoted Cu-MgO catalysts (Table 15). To investigate the effect of the Cu loading on methyl formate yield, the Cu^0 surface area (SA_{Cu^0}) and Cu^{2+} surface area ($SA_{Cu^{2+}}$) were determined for the Cs- or K-promoted 5wt% Cu-MgO catalysts and the Cs- or K- promoted 40wt% Cu-MgO catalysts. These catalysts had similar intrinsic basicities (Table 13) so that differences in methyl formate yield must be due to differences in SA_{Cu^0} and $SA_{Cu^{2+}}$ and not due to differences in basicity. SA_{Cu^0} was measured by N_2O chemisoption/decomposition. $SA_{Cu^{2+}}$ for Cs- or K-40wt% Cu-MgO was estimated as $SA_{Cu^{2+}} = SA_{Cu^{total}} - SA_{Cu^0}$, where $SA_{Cu^{total}}$ is the total copper surface area. To obtain an estimate of $SA_{Cu^{total}}$ (Table 17) the Cu^{total}/Mg was obtained from the XPS analysis and we assumed that $SA_{Cu^{total}} \cong SA_{BET} \times (Cu^{total}/Mg)$. For the Cs- or K-5wt% Cu-MgO, $SA_{Cu^{2+}}$ could not be estimated in this way because as already discussed, the XPS analysis on K or Cs-promoted-5wt% Cu-MgO catalysts showed no peak corresponding to Cu. However, based on previously reported XPS studies on a 5.2wt% Cu-MgO by Nagaraja et al. [69], who showed that Cu^{2+} was not detected on the catalyst surface, $SA_{Cu^{2+}}$ was also assumed zero for the 5wt% Cu-MgO catalysts in the present work. The methyl formate yield is plotted versus

95

SA_{Cu^0} (measured by N_2O adsorption) for the K- and Cs-promoted Cu-MgO catalysts in Figure 28. The results show that an increase in SA_{Cu^0} led to an increase in methyl formate yield. On the other hand no correlation between $SA_{Cu^{2+}}$ and methyl formate yield was found. Over the 0.5wt% K-5wt% Cu-MgO and the 0.5wt%Cs-5wt% Cu-MgO catalyst, methyl formate was formed in the absence of Cu^{2+}. Based on these observations, it can be concluded that the formation of methyl formate was enhanced by Cu^0 (as opposed to Cu^{2+}).

Table 17 Cu^{2+} surface area and Cu^{total} surface area of Cu-MgO catalysts

Catalyst	$\dfrac{Cu^{total}}{Mg}$ [a] (molar)	$SA_{Cu^{2+}}$ (m² g⁻¹)	$SA_{Cu^{total}}$ (m² g⁻¹)
0.5wt% K-40wt% Cu-MgO	0.06	2.03[b]	2.53[b]
0.5wt% Cs-40wt% Cu-MgO	0.04	1.39[b]	1.97[b]
0.5wt% K-5wt% Cu-MgO	-	0.00[c]	0.26[c]
0.5wt% Cs-5wt% Cu-MgO	-	0.00[c]	1.10[c]

[a] $\dfrac{Cu^{total}}{Mg}$ was measured based on XPS results

[b] For Cu-MgO catalyst with Cu wt% = 40wt%:

$SA_{Cu^{total}} = SA_{BET} \times (\frac{Cu^{total}}{Mg})$

$SA_{Cu^{+2}} = SA_{Cu^{total}} - SA_{Cu^0}$

Calculation of standard deviation for $SA_{Cu^{2+}}$ and $SA_{Cu^{total}}$ is shown in Appendix B.5. Note that for 0.5wt% Cs-40wt% Cu-MgO catalyst, $\sigma_{SA_{Cu^{2+}}} \leq \pm 0.06$ m².g⁻¹ and $\sigma_{SA_{Cu^{total}}} \leq \pm 0.49$ m².g⁻¹

[c] For Cu-MgO catalyst with Cu wt% = 5wt%:

$SA_{Cu^{+2}} = 0$ based on [69]

$SA_{Cu^{total}} = SA_{Cu^{+2}} + SA_{Cu^0} = SA_{Cu^0}$
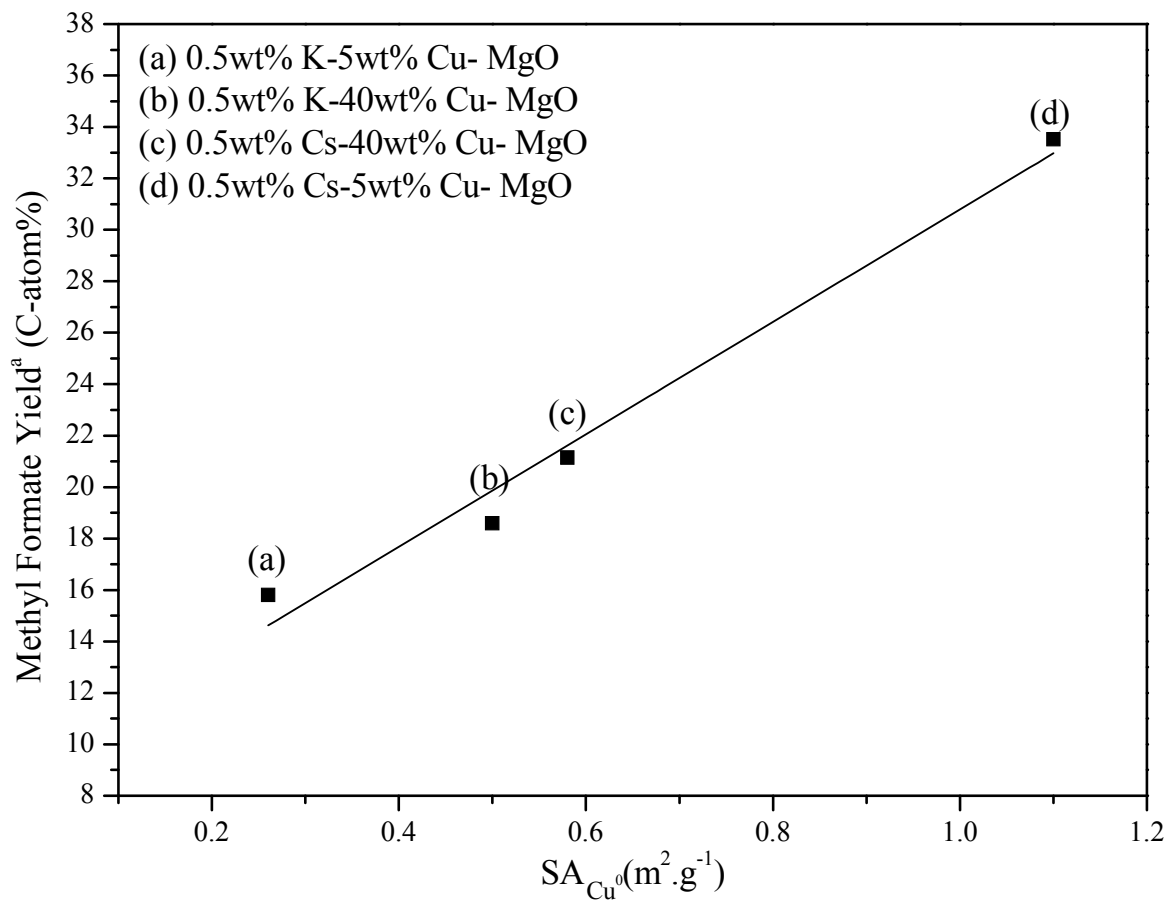
Figure 28 Correlation between surface area of Cu^0 and methyl formate yield.[a] Methyl formate yield is defined as the product of total net conversion and methyl formate selectivity

Previously it was suggested that CH$_3$OH dimerization was a dominant pathway for the formation of methyl formate over Cu-MgO-based catalysts (Section 2.4) and that methyl formate was formed by nucleophilic attack of a surface methoxy species on a surface formyl or formate species over the Cu-MgO-based catalysts [4,5,79]. IR studies suggest that the formation of formate species likely occurs on Cu sites over Cu-SiO$_2$ catalyst [54] and DFT studies suggest that formate species and formyl species can be formed on Cu sites of a Cu-ZnO catalyst [89]. On the other hand, based on in situ IR studies, formation of methoxy

species was reported to take place on Cs^+ sites on Cs-Cu-ZnO catalysts [20]. Based on these reports, we propose that over the Cu-MgO-based catalysts, methyl formate was formed by nucleophilic attack of a surface methoxy on a surface formyl or formate species. The methoxy species is adsorbed on metal cation sites (Mg^{2+}, K^+, Cs^+), and the formyl or formate is adsorbed on copper sites of the Cu-MgO catalysts [4,5,79]. Based on these mechanistic proposals and the observed effect of S_{Cu^0} on methyl formate yield, it can be concluded that surface formyl or formate species were most likely adsorbed on Cu^0 sites (as opposed to Cu^{2+} sites). The corresponding mechanism for CH_3OH dimerization to methyl formate is shown in Figure 29. (Note that for simplicity, the hydrogenation-dehydrogenation steps are not shown in Figure 29). It is important to note that based on DFT studies, it has been suggested that formyl species are not very stable on the Cu sites of Cu-ZnO catalysts and most likely dissociate to CO [89]. Consequently, path B of Figure 29 may be considered the dominant pathway for the formation of methyl formate by CH_3OH dimerization on the alkali promoted Cu-MgO catalysts of the present work.

The data of Table 16 show that the CH_3OH conversion and product selectivity changed noticeably as the Cu loading decreased from 40wt% to 5wt% in the Cs- or K-promoted Cu-MgO (Table 16). The changes in selectivity could be due to the fact that the conversion decreased noticeably as a result of a decrease in the Cu loading. In order to investigate the effect of Cu loading on the formation mechanism of the different carbonaceous products (mainly methyl formate and C_2 species) over Cs- or K-promoted Cu-MgO, the product selectivity over the Cs- or K-promoted 5wt% Cu-MgO and the Cs- or K-promoted 40wt% Cu-MgO should be compared at the same conversion. Such data are summarized in Table 16.

Comparing the product distribution over the 0.5wt% Cs-40wt% Cu-MgO at W/F= 1.3×10^{-3} min.g.(cm^3(STP))$^{-1}$ and a total net conversion of 29.7 %, with the 0.5wt% Cs-5wt% Cu-MgO at W/F= 12.3×10^{-3} min.g.(cm^3(STP))$^{-1}$ and a total net conversion of 34.2 %, shows relatively the same product distribution over both catalysts. A decrease in Cu loading from 40wt% to 5wt% in the 0.5wt%Cs-Cu-MgO catalyst, did not affect the product distribution noticeably at the same conversion. Furthermore, it can be concluded that the corresponding mechanisms for the formation of methyl formate and C$_2$ species from CH$_3$OH and CO over the 5wt% Cu-MgO-based catalyst and the 40wt% Cu-MgO-based catalysts are the same.
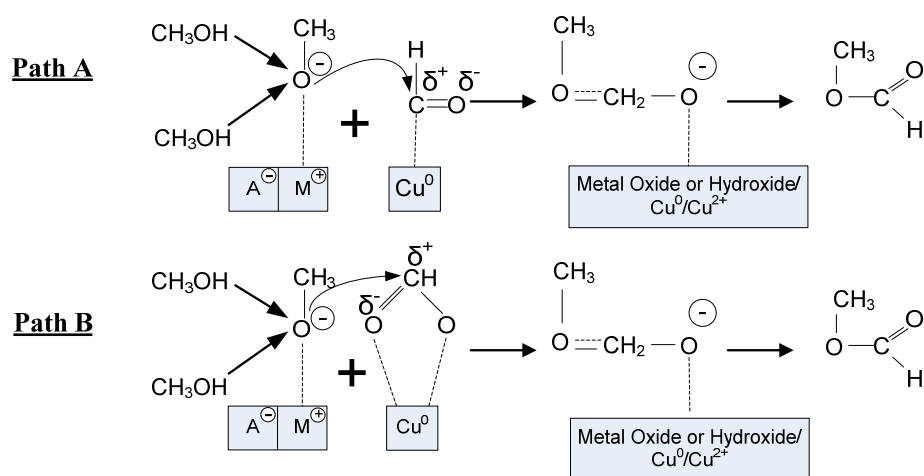
Figure 29 Pathway for: (A) CH$_3$OH dimerization to methyl formate via methoxy and formyl intermediates, (B) CH$_3$OH dimerization to methyl formate via methoxy and formate intermediates. M$^+$ stands for Mg^{2+}, K^{1+} or Cs^{1+} and A$^-$ stands for O^{2-} or OH^{-1}

CHN analysis results given in Table 2 of Chapter 2 showed < 3wt% C contamination in the bulk of the passivated alkali-promoted-40wt% Cu-MgO catalysts. On the other hand, XPS results given in Table 14 of the present Chapter showed C contamination between 23 atomic % - 27 atomic % at the surface of the passivated alkali-promoted-40wt% Cu-MgO catalysts.

Previous studies suggested that MgO-based catalysts adsorb CO_2 on their surface while exposed to air [36,67,68]. During XPS analysis the catalysts were briefly exposed to air when transferred from the passivation unit to the XPS unit. The discrepancy between C contamination at the surface and the bulk of the catalysts is attributed to adsorption of CO_2 on the surface of the catalysts while being transferred to the XPS unit.

3.5   Conclusion

Cu-MgO, 0.5wt%K-Cu-MgO and 0.5wt%Cs-Cu-MgO with 5wt% Cu loading were prepared by thermal decomposition of the metal salts in the presence of palmitic acid. The results of catalytic tests over the catalysts at 101 kPa, 498 K and W/F = 12.3×10^{-3} min.g.$(cm^3(STP))^{-1}$ with a CO/He/CH_3OH (0.66/0.20/0.14) feed gas, showed that in all cases, methyl formate was the dominant product. It was found that the corresponding mechanisms for the formation of methyl formate and C_2 species from CH_3OH and CO over the 5 wt% Cu-MgO-based catalyst and the 40wt% Cu-MgO-based catalysts were the same. For the 5wt% Cu-MgO-based catalysts and the 40wt% Cu-MgO-based catalysts, the correlation between the S_{Cu^0} and methyl formate yield at approximately constant specific basicity (384.5 µmol CO_2.g^{-1} – 415.9 µmol CO_2.g^{-1}) showed that an increase in S_{Cu^0} led to an increase to methyl formate yield, whereas no correlation between $S_{Cu^{2+}}$ and methyl formate yield were observed, suggesting that formation of methyl formate was enhanced by the presence of Cu^0 sites as opposed to Cu^{2+} sites.

Chapter 4

Oxygenate synthesis from CO/H$_2$ over 0.5wt% Cs-40wt% Cu-MgO at high pressure

4.1 Introduction

As discussed in Chapter 2 and 3, the 0.5wt% Cs-40wt% Cu-MgO catalyst showed the highest selectivity and highest yield for the synthesis of C$_2$ oxygenates from CH$_3$OH/CO at 101 kPa compared to the other Cu-MgO catalysts and Cs (K)-promoted Cu-MgO catalysts tested. Since the synthesis of oxygenates from syngas is thermodynamically favored at high pressure, the 0.5wt% Cs-40wt% Cu-MgO catalyst was selected for high pressure studies. Oxygenate synthesis from CO/H$_2$ over this catalyst was conducted at reaction pressures of 6200kPa – 9000 kPa. The effects of residence time, reaction pressure, reaction temperature and feed molar CO/H$_2$ ratio on the selectivity of different oxygenates was studied. Since CH$_3$OH was the dominant oxygenate, the kinetics of CH$_3$OH synthesis were also investigated. Finally, the difference between the activity of the 0.5wt% Cs-40wt% Cu-MgO and a conventional-industrial Cs-Cu-ZnO catalyst was examined. The observed differences are discussed based on the properties of the catalysts.

4.2   Experimental

4.2.1   Catalyst preparation

The 0.5wt% Cs- 40wt% Cu- MgO catalyst was prepared by thermal decomposition of the metal salts $Mg(NO_3)_2.6H_2O$, $Cu(NO_3)_2.3H_2O$ and Cs_2CO_3 in the presence of palmitic acid $(CH_3(CH_2)_{14}COOH)$. The details of the catalyst preparation procedure have been reported previously in Section 2.2.1. The mass loading of metal salts used in the catalyst preparation are shown in Appendix A.

4.2.2   Catalyst testing

4.2.2.1   Reactor setup

The reactor setup used for high pressure studies is shown in Figure 30. The reactor consisted of a Cu-lined, stainless steel tube (0.5 cm inner-diameter and 10 cm bed-height). A Lindberg/Blue-M furnace (model number: TF55035A-1) was used to heat up the reactor and the reactor temperature was controlled by a Lindberg/Blue-M PID temperature controller (model number: UP150). The inlet lines to the reactor were divided into low pressure lines (101kPa) and high pressure lines (>6000 kPa), which were respectively equipped with low pressure mass flow controllers and high pressure mass flow controllers. The low pressure lines were separated from the high pressure lines using two 3-way-valves, installed before and after the reactor. In order to operate the reactor at high pressure, a back pressure

regulator was installed at the reactor exit line. To increase the reactor pressure, the pressure of the inlet line to the reactor was increased gradually using the high pressure mass flow controller, while the back pressure regulator was closed accordingly. The liquid products and gas products were separated in a condenser submerged in an ice-water bath, which was installed on the reactor exit line. To avoid product condensation after the reactor and before the condenser, the line was heated to 383 K using a heating box and a heating tape. The liquid products and gas products were analyzed using a Perkin-Elmer Gas Chromatograph 550 – Mass Spectrometer 560 (GC-MS). A relief valve was installed on the gas line before entering the GC-MS to ensure low pressure at the GC-MS entrance.
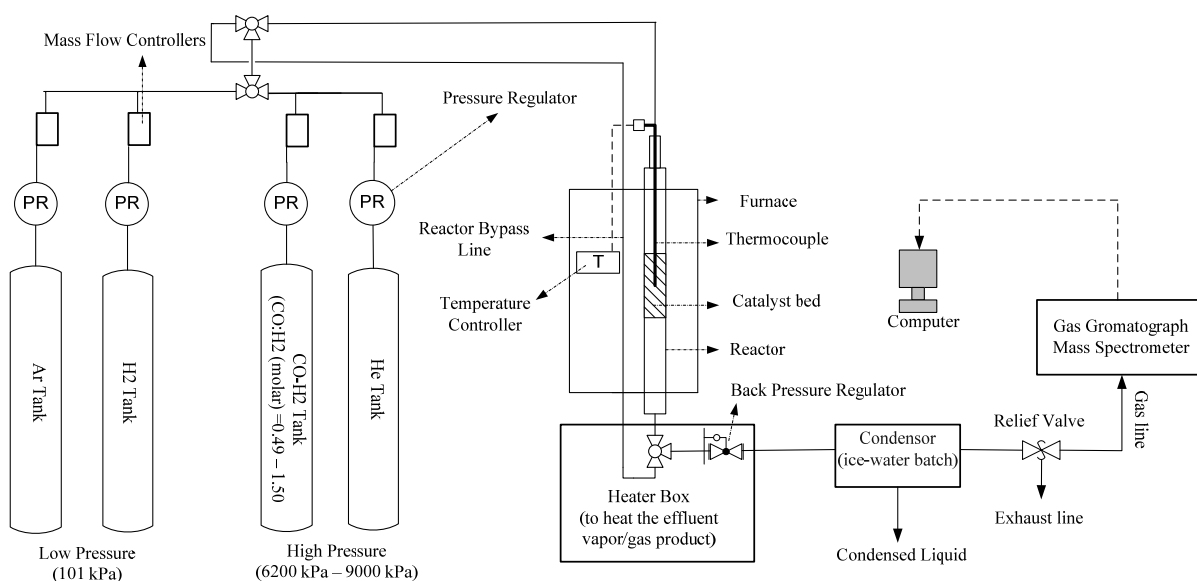
Figure 30 Schematic diagram of the reactor for syngas conversion at high pressure (6200 kPa – 9000 kPa)

4.2.2.2   Reactor operation

Tests of the 0.5wt% Cs-40wt% Cu-MgO catalyst were conducted in the plug flow reactor, operated at 6200 kPa to 9000 kPa with a CO/H_2 mixture as reactants. The calcined catalyst

(2.0 g) was loaded into the isothermal section of the reactor and reduced at 101 kPa in 10 % H_2/Ar at a flow rate of 100 cm^3(STP).min^{-1}. The reduction temperature was increased at ramp rate of 10 K.min^{-1} from ambient to 573 K and was held for 120 minutes. After further heating in pure He to 773 K at a ramp rate of 10 K.min^{-1} and holding for 60 minutes, the reactor was cooled to ambient temperature. Then the He gas flow was switched to a CO/H_2 gas flow and the reactor pressure was increased from 101 kPa to the desired reaction pressure using the back pressure regulator. Once a stable reaction pressure was achieved, the reactor temperature was increased from ambient temperature to the desired reaction temperature at a ramp rate of 5 K.min^{-1}. After passing the reactant mixture through the reactor, the obtained product gas/vapor effluent was condensed in the condenser to separate the vapor product from the gas product. The exit gas product composition was determined using the GC-MS that monitored the reactor exit gas line every 30 minutes. Note that the volumetric flow rate of the gas product was measured manually at desired times using a bubble flow meter. The liquid was recovered from the condenser and weighed at the end of each catalyst test and the product liquid composition was determined using the GC-MS.

4.2.2.3   Operating conditions for residence time studies and kinetic studies

The range of reaction operating conditions were specified based on the typical reaction conditions in which synthesis of oxygenates form CO/H_2 over alkali promoted Cu-ZnO occurs [27,90-92]. The list of all the experiments along with their operating conditions used for the residence time studies and kinetic studies are shown in Table 18. In order to systematically study the effect of residence time in the synthesis of oxygenates, the feed flow

rate was changed from 28 $cm^3(STP).min^{-1}$ - 380 $cm^3(STP).min^{-1}$, while other reaction parameters were held constant at the following conditions: reaction pressure ≈ 9000 kPa, reaction temperature: 573K, Feed CO/H_2 (molar)=1.00 and catalyst weight = 2 g (experiment 6-8 and 11-12 in Table 18). The residence time experimental results were partially used for development of a kinetic model. The operating conditions of the remaining experiments required to complete the kinetic study were specified using a partial factorial design.

It is important to note that the synthesis of oxygenates from CO/H_2 over alkali promoted Cu-ZnO catalysts at high pressure (5000 kPa – 10000kPa) typically occurs at reaction temperature of 523 K – 598K [27,90-92]. A similar range of reaction temperatures was used to investigate the synthesis of oxygenates from CO/H_2 over 0.5wt% Cs- 40wt% Cu-MgO catalyst at high pressure (Table 18). However, as explained in Chapter 2, the synthesis of C_2 oxygenates from CH_3OH/CO over 0.5wt% Cs- 40wt% Cu-MgO catalyst at 101 kPa was mainly conducted at a reaction temperature of 498K (Table 7), which is below the range of reaction temperatures used for high pressure catalyst testing in the present Chapter. The activity results over 0.5wt% Cs- 40wt% Cu-MgO catalyst at 101 kPa (Table 7), showed that an increase in reaction temperature from 498 K to 523 K, led to a noticeable increase in the selectivity of CO and a noticeable decrease in the selectivity of C_2 oxygenates. Therefore to avoid CH_3OH decomposition to CO and accommodate the formation of C_2 oxygenates from CH_3OH at 101 kPa, the reaction temperature was kept ≤ 523K. On the other hand, at high reaction pressure, formation of CH_3OH from CO/H_2 is thermodynamically more favored compared to atmospheric reaction pressure, and the produced CH_3OH does not decompose to CO. Therefore catalytic testing at high pressure can be conducted at reaction temperature ≥

523K. These observations and explanations justify the mentioned discrepancy between the range of operating temperature used for the catalyst testing at 101 kPa (Chapter 2 and 3) and the range of operating temperature used for the catalyst testing at high pressure (present Chapter).

Table 18 Experiment number and corresponding reaction conditions at high pressure

Experiment Number	T^a (K)	P^b (kPa)	τ^c (sec)	Feed CO:H$_2$ (molar)	Feed Flowrate $(cm^3(STP).min^{-1})$
1		8966	0.6	1.50	201
2		6207	1.3	1.00	93
3	558	8966	3.0	1.50	41
4		8966	4.1	0.49	29
5		8966	4.2	1.00	28
6		8966	0.3	1.00	380
7		8966	0.6	1.00	199
8		8966	1.3	1.00	93
9	573	8966	1.3	0.49	93
10		6207	1.3	0.49	93
11		8966	3.0	1.00	40
12		8966	4.2	1.00	28
13		8966	0.6	1.00	199
14		6207	0.6	0.49	200
15	598	8966	1.3	1.50	92
16		8966	4.1	0.49	29
17		6207	4.2	1.50	28

[a] T stands for reaction temperature.
[b] P stands for reaction pressure.
[c] τ= residence time = $\frac{\text{catalyst weight(g)/catalyst density (g.cm}^{-3})}{\text{feed flow rate (cm}^3(STP).min^{-1})}$, catalyst density $\approx$ 1 g.cm^{-3}.

4.3 Results and discussion

4.3.1 Catalyst activity and product distribution

In the present work the data at $3 \times$ response time ($3 \times t_r$), was used for CO conversion and product selectivity calculations. The response time (t_r), is the time the system (reactor, condenser and pipe lines) needed to react to a given change in reaction operating conditions. The calculation of the response time is shown in Appendix H. Note that the details of the calculation for CO conversion, product selectivity and space time yield (STY) are shown in Appendix D.

The CO conversion and product selectivity over the 0.5wt% Cs- 40wt% Cu-MgO at the desired reaction conditions are shown in Table 19. CO_2 was identified as one of the carbonaceous products at all reaction conditions which most likely was the result of the water gas shift reaction that occurs on the Cu-metal oxide catalysts. The occurrence of the water gas shift reaction over Cu-ZnO and Cu-MgO has been reported in the literature [20,27,34,79,93,94] and was discussed in Section 2.4. The CO_2-free product selectivity in Table 19 shows three groups of oxygenated products: CH_3OH, $C_{2+}OH$ (ethanol, i-propanol, 1-propanol, 2-butanol, 2-methyl-1-propanol, 1-butanol and 3-pentanol) and ketones-esters (acetic acid methyl ester, acetone and methyl formate). In all experiments, CH_3OH was the dominant oxygenate. Also, low selectivity (< 24 C-atom%) to light hydrocarbons (methane, ethane and propane) was observed.

Table 19 Syngas conversion activity and product distribution to different carbonaceous products over 0.5wt% Cs-40wt% Cu-MgO at high pressure

Experiment Number	T^a (K)	P^b (kPa)	τ^c (sec)	Feed CO/H$_2$ (molar ratio)	CO Conversion^d (C-atom %)	CO$_2$ Selectivity^d (C-atom %)	Product Selectivity (CO$_2$ free, C-atom%)^d Oxygenates CH$_3$OH	$C_{2+}OH^e$	ketones-esters^f	HC^g
1	558	8966	0.6	1.50	1.88	13.12	84.42	10.13	3.05	2.40
2		6207	1.3	1.00	1.48	14.21	99.41	0.00	0.59	0.00
3		8966	3.0	1.50	6.24	16.78	76.55	0.00	5.00	1.67
4		8966	4.1	0.49	23.53	10.75	91.40	2.45	1.64	4.51
5		8966	4.2	1.00	16.70	11.64	90.50	2.24	3.39	3.86
6	573	8966	0.3	1.00	0.72	24.97	93.38	0.00	3.68	2.93
7		8966	0.6	1.00	2.09	16.99	90.24	4.78	2.54	2.44
8		8966	1.3	1.00	8.97	17.78	82.08	10.15	3.65	4.12
9		8966	1.3	0.49	8.27	7.15	92.73	3.33	0.95	2.98
10		6207	1.3	0.49	7.64	18.80	82.33	8.73	2.77	6.17
11		8966	3.0	1.00	19.49	21.90	78.03	8.41	4.58	8.98
12		8966	4.2	1.00	29.02	37.22	64.84	8.71	8.79	17.66
13	598	8966	0.6	1.00	2.01	15.69	87.68	6.07	2.36	3.90
14		6207	0.6	0.49	1.58	32.71	76.04	0.00	6.07	17.89
15		8966	1.3	1.50	5.48	32.29	66.25	13.43	6.27	14.04
16		8966	4.1	0.49	32.82	33.32	68.89	6.08	3.25	21.78
17		6207	4.3	1.50	11.06	44.05	75.37	0.00	1.50	23.13

^{a} T stands for reaction temperature. ^{b} P stands for reaction pressure^c τ= residence time = $\frac{\text{catalyst weight(g)/catalyst density (g.cm}^{-3})}{\text{feed flow rate (cm}^3\text{(STP).min}^{-1})}$, catalyst density $\approx$ 1 g.cm^{-3}. ^{d} Experiment repeatability is shown in Appendix G.2. Note that $\sigma_{CO\ Conversion} \leq \pm 1.59$ C-atom%, $\sigma_{S_{CO_2}} \leq \pm 2.19$ C-atom %, $\sigma_{S_{CH_3OH}} \leq \pm 3.69$ C-atom %, $\sigma_{S_{C_{2+}OH}} \leq \pm 2.13$ C-atom %, $\sigma_{S_{HC}} \leq \pm 1.50$ C-atom % and $\sigma_{S_{ketones-esters}} \leq \pm 0.48$ C-atom %. ^{e} C_{2+}OH: Alcohols heavier than CH$_3$OH (ethanol, i-propanol, 1-propanol, 2-butanol, 2-methyl-1-propanol, 1-butanol and 3-pentanol). ^{f} ketones-esters: acetic acid methyl ester, acetone and methyl formate. ^{g} HC: total hydrocarbon (methane, ethane and propane).
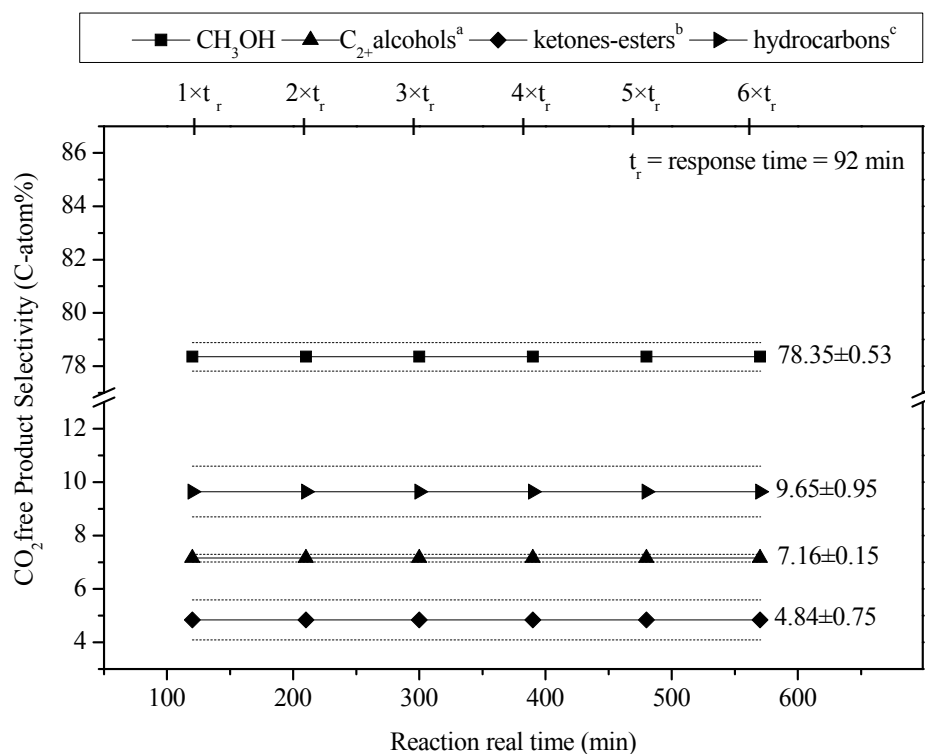
Figure 31 Stability of the 0.5wt% Cs- 40wt% Cu-MgO catalyst during CO/H$_2$ conversion to different carbonaceous products. Reaction conditions: P = 8966 kPa, T= 573K, CO/H$_2$=1.00 (molar), τ = 3.0 sec, 2 g catalyst. [a] C$_{2+}$ alcohols stands for ethanol, i-propanol, 1-propanol, 2-butanol, 2-methyl-1-propanol, 1-butanol and 3-pentanol. [b] ketones-esters stands for acetic acid methyl ester, acetone and methyl formate. [c] hydrocarbons stands for methane, ethane and propane.

To monitor the catalyst stability in the synthesis of the different products, each of the experiments of Table 18 was conducted for a long period of time (> 3×t$_r$). For example, the selectivity of the 0.5wt% Cs-40wt% Cu-MgO catalyst towards oxygenates and hydrocarbons for experiment 11 (Table 18) is shown in Figure 31. In this Figure, the average selectivity of the products and their stability standard-deviations were calculated using six experimental data points. The repeatability standard-deviation for experiment 11 was also calculated and is reported in Table 62. For all of the product selectivities, the stability standard-deviation was

$\le$ to the repeatability standard-deviation, which implies that no catalyst deactivation was observed. Note that the catalyst was stable in all other experiments reported in Table 18 and therefore, their stability results are not shown.

4.3.2   Langmuir-Hinshelwood kinetic model for CH_3OH synthesis from CO/H_2

4.3.2.1   Langmuir-Hinshelwood model development

As mentioned in Section 4.2.2, the catalyst activity results shown in Table 19 were used for kinetic analysis. The product distribution results given in Table 19 showed that for all reaction conditions, the CO_2 free selectivity to CH_3OH was higher than 66 C-atom%. The mechanism of CH_3OH synthesis from CO/H_2 over Cu-metal oxide catalysts was reviewed in Section 2.4. The mechanistic studies suggested that both reactants (CO and H_2) in the CH_3OH synthesis over Cu-metal oxide catalysts were chemisorbed on the catalyst surface [29,31,47,54,57,79,95]. Therefore, based on the proposed mechanism a Langmuir-Hinshelwood (LH) kinetic model was developed. The details of the LH kinetic model development are shown in Appendix I. Note that the rate determining step was chosen based on previous mechanistic studies [47,57]. For the CH_3OH reaction rate equation, different dominant chemisorbed species were assumed and as a result three different CH_3OH reaction rate equations (Model LH_1, LH_2 and LH_3 in Table 20) were obtained. The reason for assuming different dominant chemisorbed species for the mentioned models and their comparison to each other will be discussed in Section 4.3.2.4.

To determine whether or not the reversible term of the CH_3OH reaction rate equation, given in Table 20, was necessary, the thermodynamic equilibrium of the CH_3OH synthesis was examined. Therefore, the thermodynamic equilibrium constant (K_{CH_3OH}) and calculated equilibrium constant ($K_{CH_3OH-calc}$) corresponding to the reaction of synthesis gas to CH_3OH were calculated for all the high pressure experiments of Table 18 and the results are summarized in Table 21. Note that K_{CH_3OH} was calculated by Aspen plus V7.1 (23.0.4507) software using an equilibrium reactor with SR-POLAR property method. $K_{CH_3OH-calc}$ was calculated using the following equations:

$$K_{CH_3OH-calc} = \frac{(\frac{\hat{f}_{CH_3OH}}{P_o})}{(\frac{\hat{f}_{CO}}{P_o}) \times (\frac{\hat{f}_{H_2}}{P_o})^2}.$$

(E3)

In which P_o stands for standard pressure (101 kPa) and f_i stands for fugacity of component i in the product stream. The results showed that for most of the experiments, $\frac{K_{CH_3OH-calc}}{K_{CH_3OH}}$ was larger than 0.1, which implies that it is necessary to include the reversible term in the CH_3OH reaction rate equation (Table 20) under the reaction conditions given in Table 18.

Table 20 LH reaction rate for CH₃OH synthesis from CO/H₂

Model Number	θ_V [a] (unitless)	r_{CH_3OH} [b] (mol.sec⁻¹.g⁻¹)
LH₁	1	$k\,\hat{f}_{H_2}{}^{1.5}\hat{f}_{CO} \times \left(1 - \dfrac{\hat{f}_{CH_3OH}}{K_{CH_3OH}\hat{f}_{CO}\hat{f}_{H_2}{}^2}\right)$
LH₂	$\dfrac{1}{1 + K_{CO}\hat{f}_{CO}}$	$\dfrac{k\,\hat{f}_{H_2}{}^{1.5}\hat{f}_{CO}}{(1 + K_{CO}\hat{f}_{CO})^2} \times \left(1 - \dfrac{\hat{f}_{CH_3OH}}{K_{CH_3OH}\hat{f}_{CO}\hat{f}_{H_2}{}^2}\right)$
LH₃	$\dfrac{1}{1 + K_{H_2}K_{CO}\hat{f}_{H_2}\hat{f}_{CO}}$	$\dfrac{k\,\hat{f}_{H_2}{}^{1.5}\hat{f}_{CO}}{(1 + K_{H_2}K_{CO}\hat{f}_{H_2}\hat{f}_{CO})^2} \times \left(1 - \dfrac{\hat{f}_{CH_3OH}}{K_{CH_3OH}\hat{f}_{CO}\hat{f}_{H_2}{}^2}\right)$

[a] θ_V stands for vacant site surface coverage.

[b] r_{CH_3OH} stands for CH₃OH reaction rate per weigh of catalyst which was derived based on LH kinetic model given in Appendix I. K_{CH_3OH} is the thermodynamic equilibrium constant for CH₃OH synthesis from CO/H₂. K_{CO} is the CO adsorption equilibrium constant on 0.5wt% CS-40wt% Cu-MgO catalyst. K_{H_2} is the H₂ adsorption equilibrium constant on 0.5wt% CS-40wt% Cu-MgO catalyst.

Table 21 Thermodynamic equilibrium constant and calculated constant for CH₃OH synthesis from CO/H₂ reaction over 0.5wt% Cs-40wt% Cu-MgO

Experiment Number	Temperature (K)	reaction ($CO + 2H_2 \rightarrow CH_3OH$)		
		$K_{CH_3OH-calc}$ [a]	K_{CH_3OH} [b]	$\dfrac{K_{CH_3OH-calc}}{K_{CH_3OH}}$
1	558	8.51E-06	5.18E-04	0.016
2		1.34E-05		0.026
3		3.61E-05		0.070
4		1.35E-04		0.260
5		1.42E-04		0.274
6	573	2.45E-06	2.96E-04	0.008
7		7.96E-06		0.027
8		2.97E-05		0.100
9		4.31E-05		0.146
10		3.94E-05		0.133
11		1.21E-04		0.408
12		1.26E-04		0.425
13	598	7.62E-06	1.23E-04	0.062
14		5.85E-06		0.048
15		1.75E-05		0.142
16		1.06E-04		0.863
17		7.80E-05		0.634

[a] $K_{CH_3OH-calc} = \dfrac{(\frac{\hat{f}_{CH_3OH}}{P_o})}{(\frac{\hat{f}_{CO}}{P_o}) \times (\frac{\hat{f}_{H_2}}{P_o})^2}$. Po is standard pressure and is 101 kPa. $\hat{f}_i$ is the fugacity of component i in the product stream. [b] K_{CH_3OH} is equilibrium constant for CH_3OH synthesis from CO/H₂ calculated by Aspen plus V7.1 (23.0.4507) software using an equilibrium reactor with SR-POLAR property method.

4.3.2.2   Parameter estimation methodology and statistical analysis

The parameter estimation was achieved using a Nelder-Mead simplex (direct search) method by minimizing the objective function (S) shown in equation E4. The Matlab 7.1 software was

used for the parameter estimation and the corresponding Matlab m-files are shown in Appendix M.

$$S = \sum_{i=1}^{N}\left(\left(\hat{f}_{CH_3OH-out}\right)_{experimental} - \left(\hat{f}_{CH_3OH-out}\right)_{calculated}\right)^2 \tag{E4}$$

Note that $\left(\hat{f}_{CH_3OH-out}\right)_{experimental}$ was obtained from experimental catalytic testing (Appendix K), whereas $\left(\hat{f}_{CH_3OH-out}\right)_{calculated}$ was calculated by numerical integration of the r_{CH_3OH} (given in Table 20) according to equation E5. The inlet fugacity of the reactants $\left(\hat{f}_{CO-in}\right.$ and $\left.\hat{f}_{H_2-in}\right)$ which were used for numerical integration of the r_{CH_3OH} are shown in Appendix K. Note that in equation E5, $\rho_{catalyst}$ stands for catalyst density ($\approx 10^6$ g.m^{-3}), T_{STP} stands for temperature at standard condition (293K), R_g stands for universal gas constant ($=8.28\times10^{-3}$ kPa.m^3.K^{-1}.mol^{-1}) and τ stands for reaction residence time with sec as the unit. Furthermore, in equation E5, the units for r_{CH_3OH} and $\left(\hat{f}_{CH_3OH-out}\right)_{calculated}$ are respectively mol.sec^{-1}.g^{-1} and kPa.

$$\left(\hat{f}_{CH_3OH-out}\right)_{calculated} = R_g \times T_{STP} \times \rho_{catalyst} \times \int_0^\tau (r_{CH_3OH})\, d\tau \tag{E5}$$

Note that the CH$_3$OH reaction rate equations (Table 20) were compared to each other based on three factors:

1-the value of the objective function (S)
2-the significance of the standard deviation for each of the estimated parameters

3-the value of $(P - value)_{CH_3OH}$, which is calculated based on the one-way analysis of variance (ANOVA). Note that a $(P - value)_{CH_3OH}$ is in the range of 0 to 1, in which a $(P - value)_{CH_3OH}$ of 1, implies the best fit possible. The closer the $(P - value)_{CH_3OH}$ to 1, the closer the mean value of the calculated response variable to the mean value of the experimental response variables.

More detail on the ANOVA analysis and standard deviation calculation can be found in Appendix M. To improve the standard deviation of the calculated parameters, the experimental data at three different reaction real times were used. The detail of the reaction real time is shown in Appendix K. To estimate the kinetic parameters the following constraints were applied to ensure that the estimated parameters had physio-chemical meaning.

Constraint 1-CH₃OH apparent activation energy $(E_a) > 0$

$\quad\quad$ in reaction rate constant equation $(k = k_0 e^{\frac{-E_a}{RT}})$.

Constraint 2-CH₃OH apparent pre-exponential constant $(k_0) > 0$

$\quad\quad$ in reaction rate constant equation $(k = k_0 e^{\frac{-E_a}{RT}})$.

Constraint 3-pre-exponential adsorption constant for component i $(K_{i_0}) > 0$

$\quad\quad$ in adsorption equilibrium constant equation for component i $(K_i = K_{i_0} e^{\frac{-Q_i}{RT}})$.

$\quad\quad$ Note component i refers to CO or H₂.

Constraint 3-adsorption energy for component i $(Q_i) < 0$

in adsorption equilibrium constant equation for component i ($K_i = K_{i_0} e^{\frac{-Q_i}{RT}}$).

Note component i refers to CO or H_2.

4.3.2.3   Elimination of the experimental data with high outlet fugacity of CO_2

The parameter estimation was first conducted on Model LH_1 (Table 20) and the summary of the parameter estimation results at each reaction temperature are shown in Table 22. The results showed that removal of the experimental data that possess high $\hat{f}_{CO_2-out}$, (trial number 2 in Table 22), reduced the value of the objective function noticeably in all reaction temperatures and improved the $(P - value)_{CH_3OH}$ for reaction temperatures of 558K and 598K. In order to better understand the effect of $\hat{f}_{CO_2-out}$ on the value of the objective function, the objective function was calculated for each of the experimental data separately, which will be referred to as pseudo objective function. For trial number 1 in Table 22, the pseudo objective function was plotted versus $\hat{f}_{CO_2-out}$ for each reaction temperature separately and the summary of the results is shown in Figure 32-Figure 34. The data showed that an increase in the $\hat{f}_{CO_2-out}$, led to an increase in the value of the pseudo objective function. Some of the previous studies on the synthesis of CH_3OH from CO or CO_2 over Cu-metal oxide, suggested both CO and CO_2 as the source of carbon for CH_3OH synthesis [45-48,60]. Accordingly an increase in the value of the pseudo objective function with an increase in f_{CO_2-out} was attributed to the fact that the rate for CH_3OH synthesis from CO_2 was not included in the CH_3OH reaction rate shown in Table 20. Noting that for all the conducted experiments in Table 18, no CO_2 was present in the feed, it is important to

understand why CO_2 was present in the product. CO_2 is produced as a result of the following consecutive reactions:

$C_{2+}OH$ formation reaction from CO/H_2

$$n\ CO + 2n\ H_2 \rightarrow C_nH_{2n+2}O + (n\text{-}1)\ H_2O\ (\Delta H^o_{298K} < 0 \text{ and } \Delta G^o_{298K} = -28.6\frac{kJ}{mol})\quad n\geq2\quad (R8)$$
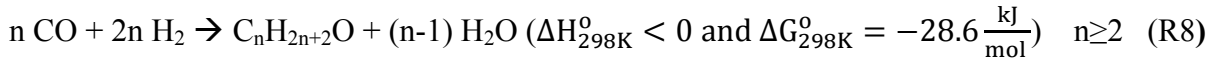
CO_2 formation via water gas shift reaction:

$$CO + H_2O \rightarrow CO_2 + H_2\ (\Delta H^o_{298K} = -41.2\ \frac{kJ}{mol} \text{ and } \Delta G^o_{298K} = -28.6\frac{kJ}{mol})\qquad\qquad (R9)$$
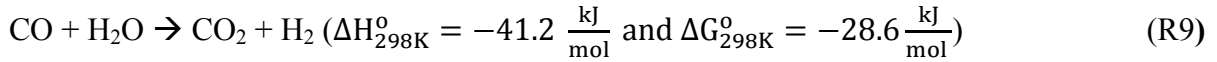
It is apparent that at a CO conversion higher than 10 C-atom% (Table 19), the formation of $C_{2+}OH$ and CO_2 increased via reaction R8 and R9. Therefore, at high CO conversion, due to high yield of CO_2, the reaction rate equation for CH_3OH synthesis from CO_2 should be added to CH_3OH reaction rate equation in Table 20. Along with this addition, the reaction rate equation corresponding to reaction R8 and R9, should also be added to the kinetic model. However, the parameter estimation for additional kinetic models to account for these reactions require more experimental data including experiments containing CO_2 in the feed. At low CO conversion (<10 C-atom%), the formation of CO_2 is negligible due to few side reactions. Therefore, to focus on CH_3OH synthesis from CO, only the experimental data that showed low CO conversion (exp. 1-3, 6-9 and 13-15 in Table 18) were used for the parameter estimation of the CH_3OH synthesis from CO.

Table 22 Parameter estimation for model LH$_1$ at each reaction temperature separately

Model Number	Reaction Temperature (K)	Trial Number	k_0 (mol.sec^{-1} kPa$^{-2.5}$.g^{-1})	S[c]	$(P-value)_{CH_3OH}$	Comment
	558	1[a]	$(5.35\pm0.00)\times10^{-14}$	5745	0.92	
		2[b]	$(2.67\pm0.00)\times10^{-14}$	28	0.99	$\hat{f}_{CO_2-out}$> 60 kPa were removed
LH$_1$	573	1[a]	$(5.93\pm0.00)\times10^{-14}$	3965	0.39	
		2[b]	$(2.97\pm0.00)\times10^{-14}$	1651	0.08	$\hat{f}_{CO_2-out}$> 60 kPa were removed
	598	1[a]	$(6.75\pm0.00)\times10^{-14}$	2284	0.85	
		2[b]	$(3.45\pm0.00)\times10^{-14}$	5	0.93	$\hat{f}_{CO_2-out}$> 105 kPa were removed

[a] Trial 1 was conducted using all the experimental data (Table 18) at the desired reaction temperature

[b] Trial 2 was conducted using the experimental data containing low $\hat{f}_{CO_2-out}$ (Table 18) at the desired reaction temperature.

[c] S stands for objective function.
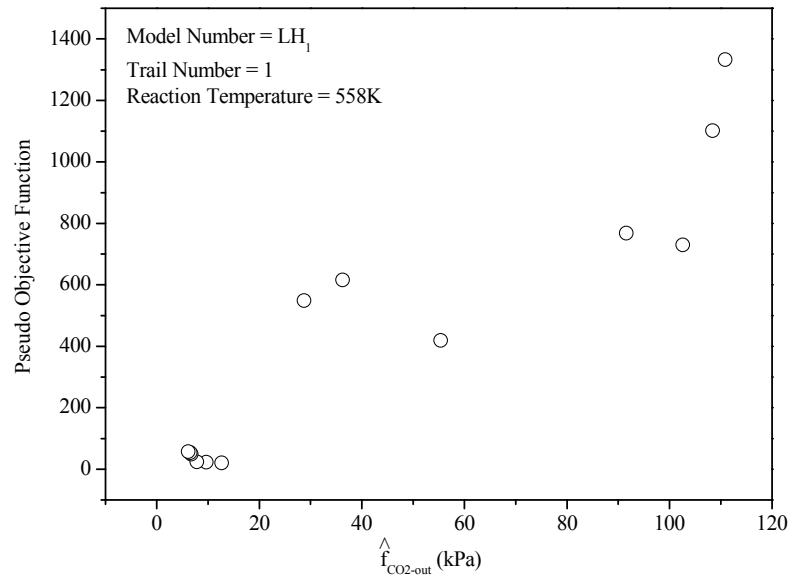
Figure 32 Pseudo objective function versus outlet fugacity of CO$_2$ for LH$_1$ model at reaction temperature 558K
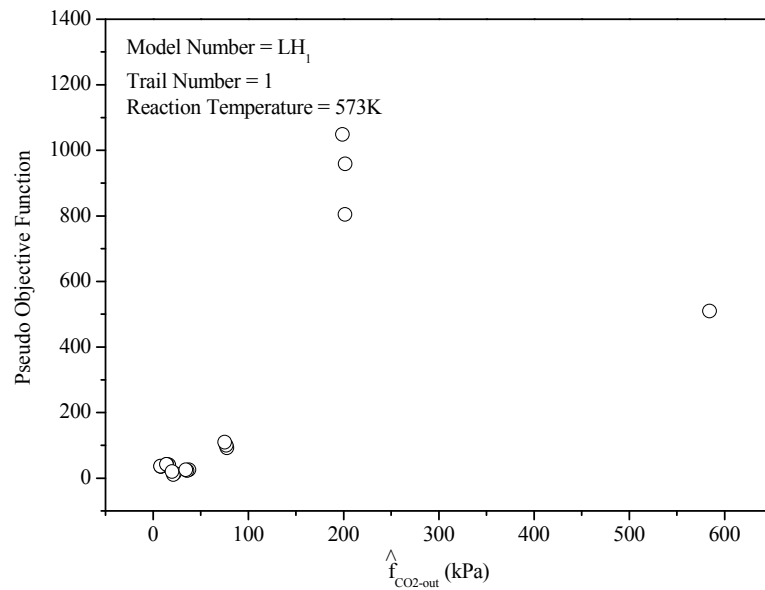
Figure 33 Pseudo objective function versus outlet fugacity of CO$_2$ for LH$_1$ model at reaction temperature 573K
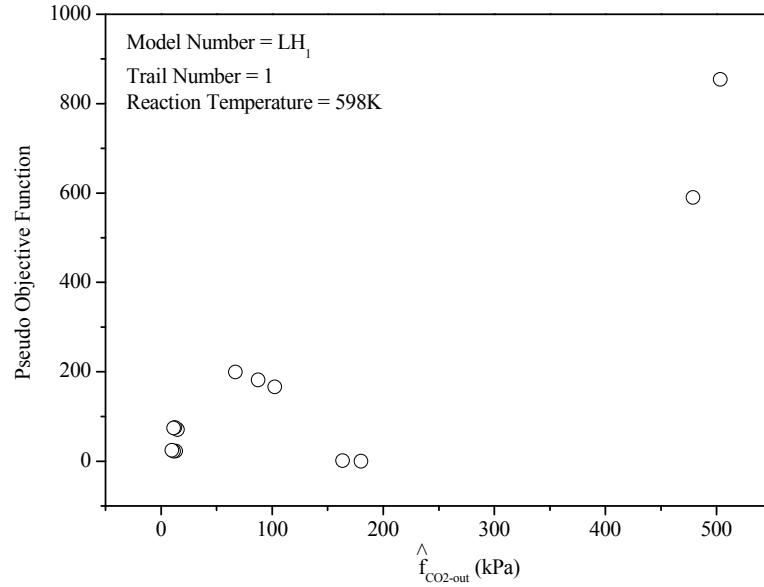
Figure 34 Pseudo objective function versus outlet fugacity of CO$_2$ for LH$_1$ model at reaction temperature 598K

4.3.2.4   Parameter estimation and comparison of kinetic models

In the present study the first LH model that was developed was LH$_1$. In this model for simplicity it was assumed that $\theta_V = 1$. In order to calculate the pre-exponential factor (k_0) and apparent activation energy (E_a) for CH$_3$OH synthesis from CO/H$_2$, the parameter estimation of LH$_1$ model was conducted using the experimental data at all reaction temperatures. The LH$_1$ in terms of the pre-exponential factor and apparent activation energy is shown in equation E6.

$$r_{CH_3OH} = k_0 e^{\frac{-E_a}{RT}} \hat{f}_{H_2}^{1.5} \hat{f}_{CO} \times (1 - \frac{\hat{f}_{CH_3OH}}{K_{CH_3OH} \hat{f}_{CO} \hat{f}_{H_2}^{2}}) \tag{E6}$$

120

The summary of the parameter estimation results are shown in Table 23. Also the experimental fugacity versus calculated fugacity for CH_3OH and CO for LH_1 is shown in Figure 35. The results showed that $(P-value)_{CH_3OH}$ was almost 1. However, the objective function (S) was very high and the standard deviation for k_0 was close to 100%, which implied that the CH_3OH reaction rate equation would require further improvement.
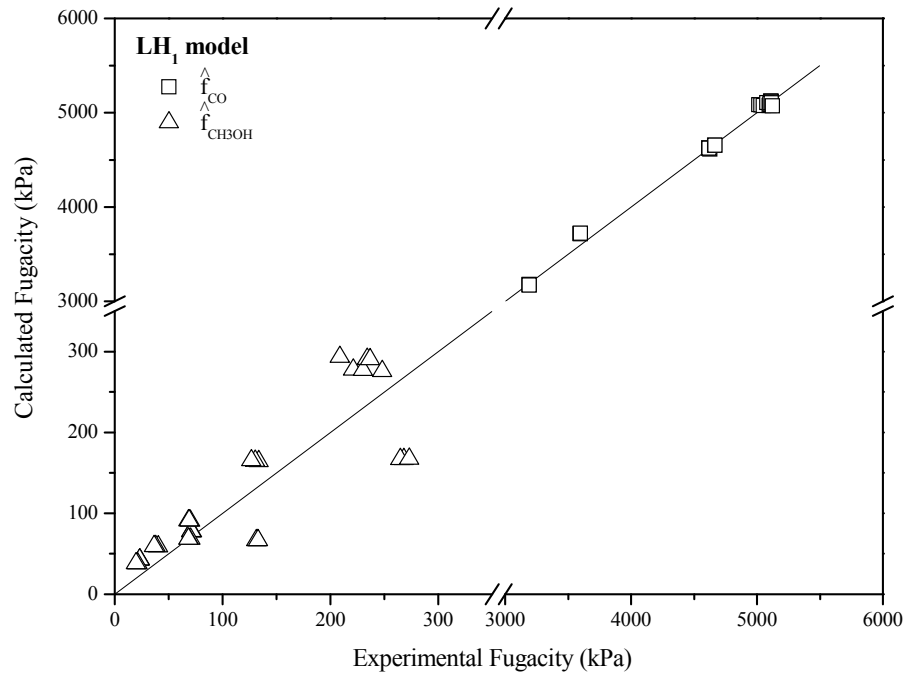
Figure 35 Experimental fugacity versus estimated fugacity for CH₃OH and CO using LH₁ model

Table 23 Parameter estimation results for LH₁ model

Model	Estimated parameters and standard deviations		S^b	$(P-value)_{CH_3OH}$
Number	k_0 (mol.sec^{-1} kPa$^{-2.5}$.g^{-1})	E_a (kJ mol^{-1})		
$LH_1{}^a$	$(2.43\pm2.14)\times10^{-12}$	19.70 ± 0.00	1244	0.99

^{a} All the experimental data reported in Appendix K was used in the parameter estimation except for experiment number 4, 5, 10, 11, 12, 16 and 17. The mentioned experiments were not used in the parameter estimation due to high value of $\hat{f}_{CO_2-out}$ as was discussed in Section 4.3.2. ^{b} S stands for objective function.

To improve the LH_1 model, it is important to understand the significance of $\hat{f}_{CO}$ and $\hat{f}_{H_2}$ on the CH_3OH reaction rate equation. Therefore, a power law CH_3OH reaction rate equation with respect to $\hat{f}_{CO}$ and $\hat{f}_{H_2}$ was developed as shown in equation E7. This model will be referred to as PL_1. The parameter estimation results for PL_1 are shown in Table 24. Also the experimental fugacity versus calculated fugacity for CH_3OH and CO for PL_1 is shown in Figure 36.

$$r_{CH_3OH} = k_0 e^{\frac{-E_a}{RT}} \hat{f}_{H_2}{}^{n_{H_2}} \hat{f}_{CO}{}^{n_{CO}} \times \left(1 - \frac{\hat{f}_{CH_3OH}}{K_{CH_3OH}\hat{f}_{CO}\hat{f}_{H_2}{}^2}\right) \tag{E7}$$
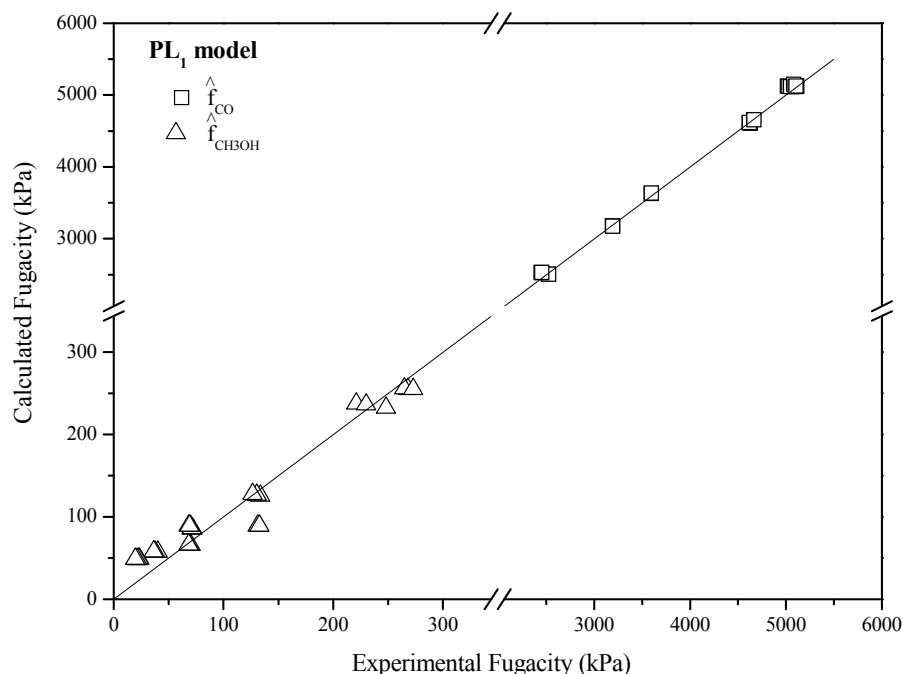
Figure 36 Experimental fugacity versus estimated fugacity for CH_3OH and CO using PL_1 model

Table 24 Parameter estimation results for PL_1 model

Model	Estimated parameters and standard deviations				S^b	$(P - value)_{CH_3OH}$
Number	k_0 (mol.sec^{-1} kPa$^{-2.5}$.g^{-1})	E_a (kJ mol^{-1})	n_{H_2}	n_{CO}		
PL_1^a	$(2.99\pm0.57)\times10^{-15}$	5.23 ± 0.00	2.97 ± 0.00	0.12 ± 0.00	299	0.82

^{a} All the experimental data reported in Appendix Kwas used in the parameter estimation except for experiment

number 4, 5, 10, 11, 12, 16 and 17. The mentioned experiments were not used in the parameter estimation due

to high value of $\hat{f}_{CO_2-out}$ as was discussed in Section 4.3.2. ^{b} S stands for objective function.

The PL_1 showed much lower value for the objective function compared to LH_1, while the

$(P - value)_{CH_3OH}$ for PL_1 decreased slightly compared to LH_1. The parameter estimation

results for PL_1 suggested that the CH_3OH reaction rate equation was much more dependent

on $\hat{f}_{H_2}$ compared to $\hat{f}_{CO}$. Hence model LH_2 was developed by assuming that CO was the dominant chemisorbed species on the catalyst surface. The LH_2 model is shown in equation E8.

$$r_{CH_3OH} = \frac{k_0 e^{\frac{-E_a}{RT}} \hat{f}_{H_2}^{1.5} \hat{f}_{CO}}{\left(1 + k_{CO_0} e^{\frac{-Q_{CO}}{RT}} \hat{f}_{CO}\right)^2} \times \left(1 - \frac{\hat{f}_{CH_3OH}}{K_{CH_3OH} \hat{f}_{CO} \hat{f}_{H_2}^2}\right) \tag{E8}$$

The parameter estimation was conducted for LH_2 and the summary of the results shown in Table 25. Also the experimental fugacity versus calculated fugacity for CH_3OH and CO for LH_2 is shown in Figure 37. The objective function for LH_2 was lower than LH_1, however, the $(P - value)_{CH_3OH}$ for LH_2 decreased slightly compared to LH_1. Also, it was observed that the standard deviation for k_0 estimated by LH_2 improved noticably compared to k_0 estimated by LH_1. These observations implies that LH_2 describes the CH_3OH synthesis from CO/H_2 with much higher accuracy than LH_1.

Table 25 Parameter estimation results for LH_2 model

No.[a]	Estimated parameters and standard deviations				S^c	$(P - value)_{CH_3OH}$
	k_0 (mol.sec^{-1} kPa$^{-2.5}$.g^{-1})	E_a (kJ mol^{-1})	K_{CO_0} (kPa^{-1})	Q_{CO} (kJ mol^{-1})		
$LH_2{}^b$	$(2.49\pm0.00)\times10^{-12}$	10.00 ± 0.00	$(2.45\pm0.53)\times10^{-4}$	-2.25 ± 0.00	640	0.69

[a] No. stands for model number. [b] All the experimental data reported in Appendix K was used in the parameter estimation except for experiment number 4, 5, 10, 11, 12, 16 and 17. The mentioned experiments were not used in the parameter estimation due to high value of $\hat{f}_{CO_2-out}$ as was discussed in Section 4.3.2. [c] S stands for objective function.
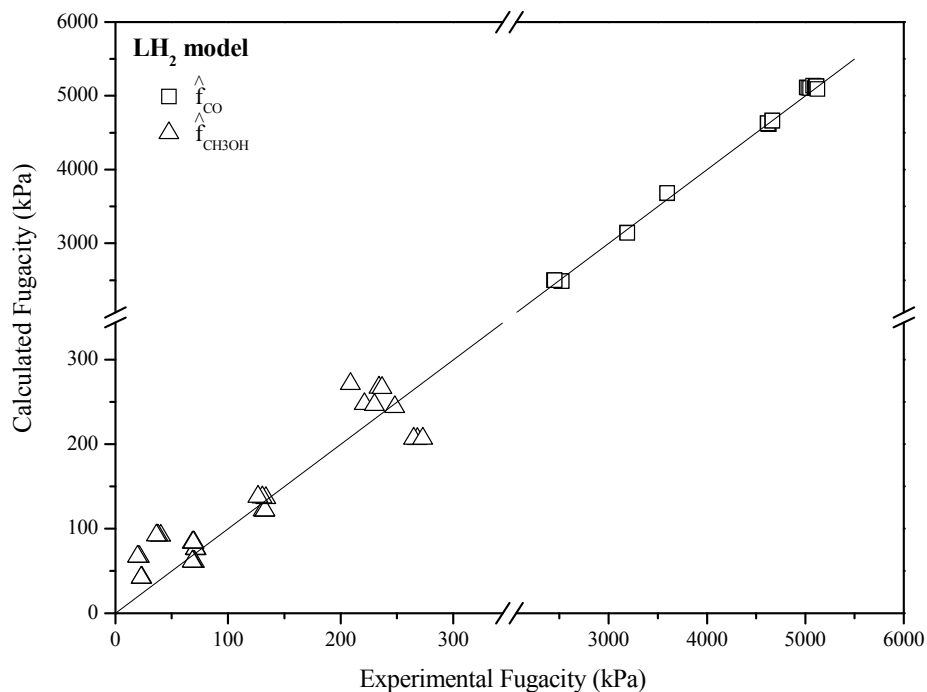
Figure 37 Experimental fugacity versus estimated fugacity for CH₃OH and CO using LH₂ model

Beside the approach that was used for identifying θ_V in the LH_2, another approach was used which resulted in model LH_3. In this approach, the dominant chemisorbed species on the catalyst surface was determined based on $\hat{f}_{CO-out}$, $\hat{f}_{H_2-out}$ and $\hat{f}_{CH_3OH-out}$ at real time $=3 \times t_r$ (Appendix K) and the derived formula for $1 - \theta_V$ (Appendix I), which leads to identifying the dominant chemisorbed species as CO and H_2. The detail of identifying θ_V for LH_3 is explained in Appendix L. The LH_3 model in terms of the pre-exponential factor and the activation energy is given in equation E7 and the parameter estimation results are shown in Table 26. Also the experimental fugacity versus calculated fugacity for CH_3OH and CO for LH_2 is shown in Figure 38. To reduce the number of unknown parameters in equation E9, the

125

value for K_{CO_0} and $K_{H_{2_0}}$ were lumped together as $(K_{H_{2_0}} \times K_{CO_0})$ and the value for Q_{H_2} and Q_{CO} were lumped together as $(Q_{H_2} + Q_{CO})$.

$$r_{CH_3OH} = \frac{k_0 e^{\frac{-E_a}{RT}} \hat{f}_{H_2}^{1.5} \hat{f}_{CO}}{\left(1 + (k_{H_{2_0}} k_{CO_0}) e^{\frac{-(Q_{H_2} + Q_{CO})}{RT}} \hat{f}_{H_2} \hat{f}_{CO}\right)^2} \times (1 - \frac{\hat{f}_{CH_3OH}}{K_{CH_3OH} \hat{f}_{CO} \hat{f}_{H_2}^2}) \qquad (E9)$$

Comparing the parameter estimation results for the LH_2 (Table 25) and LH_3 (Table 26), showed that the $(P - value)_{CH_3OH}$ for LH_3 improved slightly compared to the $(P - value)_{CH_3OH}$ for LH_2. However, the LH_2 had a noticeably lower objective function compared to LH_3. Also, the standard deviations obtained for the all the estimated parameters using LH_2 was found insignificant whereas the standard deviation for k_0 and $(K_{CO_0} \times K_{H_{2_0}})$ in LH_3 was noticebly higher. These observations showed that LH_2 can describe CH_3OH synthesis from CO/H_2 with much higher accuracy compared to LH_3. Overall it can be concluded that the LH_2 best described the CH_3OH synthesis from CO/H_2 compared to the other tested LH models (LH_1 and LH_3).

Parameter estimation results for LH_2 (Table 25) were used to calculate the CH_3OH reaction rate per unit mass of catalyst (r_{CH_3OH}) as well as CH_3OH reaction rate per unit area of catalyst (r'_{CH_3OH}) at the exit of the plug flow reactor for all the high pressure experiments used in parameter estimation of LH_2 (experiment 1-3, 6-9 and 13-15 in Table 18) and the summary of the results are shown in Table 27. The results of Table 27 showed that for all

cases, r_{CH_3OH} is in the range of $30 - 70$ µmol.sec^{-1}.g^{-1} and r'_{CH_3OH} is in the range of $0.70 -$ 1.60 µmol.sec^{-1}.m^{-2}.

Table 26 Parameter estimation results for LH$_3$ model

No.[a]	Estimated parameters and standard deviations				S	$(P - value)_{CH_3OH}$
	k_0	E_a	$K_{CO_0} \times K_{H_{2_0}}$	$Q_{CO}+Q_{H_2}$		
	(mol.sec^{-1} kPa$^{-2.5}$.g^{-1})	(kJ mol^{-1})	(kPa^{-2})	(kJ mol^{-1})		
LH$_3$[b]	$(2.40\pm1.14)\times10^{-13}$	20.00 ± 0.00	$(1.39\pm0.97)\times10^{-9}$	-2.86 ± 0.00	1196	0.93

[a] No. stands for model number. [b] All the experimental data reported in Appendix Kwas used in the parameter estimation except for experiment number 4, 5, 10, 11, 12, 16 and 17. The mentioned experiments were not used in the parameter estimation due to high value of $\hat{f}_{CO_2-out}$ as it was discussed in Section 4.3.2.
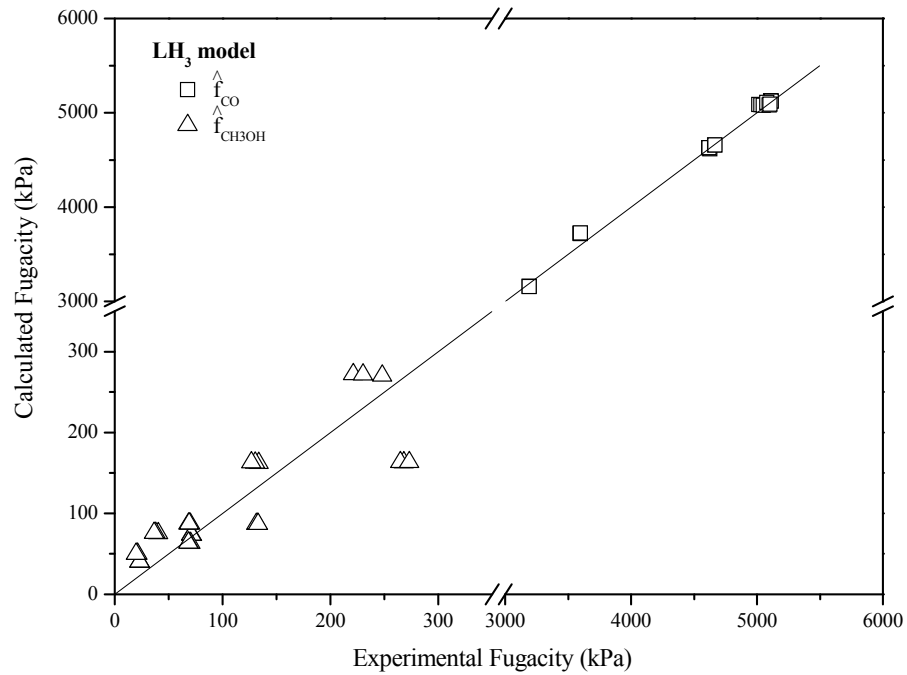
Figure 38 Experimental fugacity versus estimated fugacity for CH$_3$OH and CO using LH$_3$ model

Table 27 Calculated methanol reaction rate based on LH$_2$ model

Experiment Number[a]	Real time[b] (hr:min) & ($\times t_r$)	r_{CH_3OH}[c] (μmol.sec^{-1}.g^{-1})	r'_{CH_3OH}[d] (μmol.sec^{-1}.m^{-2})
1	1:00 ($\approx 3 \times t_r$)	41.64	0.95
2	2:00 ($\approx 3 \times t_r$)	30.90	0.70
3	5:00 ($\approx 3 \times t_r$)	36.55	0.83
6	0:30 ($\approx 3 \times t_r$)	54.95	1.25
7	1:00 ($\approx 3 \times t_r$)	53.32	1.21
8	2:00 ($\approx 3 \times t_r$)	68.15	1.55
9	2:00 ($\approx 3 \times t_r$)	41.79	0.95
13	1:00 ($\approx 3 \times t_r$)	59.90	1.36
14	1:00 ($\approx 3 \times t_r$)	50.50	1.15
15	2:00 ($\approx 3 \times t_r$)	48.34	1.10

[a] Experimental condition is given in Table 18.

[b] t_r stands for response time in the reactor which is the time the system (reactor, condenser and pipe lines) needed to react to a given change in reaction operating conditions.

[c] r_{CH_3OH} stands for CH$_3$OH reaction rate per unit mass of catalyst.

[d] r'_{CH_3OH} stands for CH$_3$OH reaction rate per unit area of catalyst and was calculated using the following equation: $r'_{CH_3OH} = \frac{r_{CH_3OH}}{SA_{BET}}$ in which SA$_{BET}$= 44 m^2.g^{-1}.

4.3.2.5   CH$_3$OH activation energy based on LH$_2$ model

The CH$_3$OH activation energy ($(E_{CH_3OH})_{Cu-MgO}$) over the 0.5wt% Cs-40wt% Cu-MgO catalyst was calculated based on the LH$_2$ parameter estimation. In order to calculate E_{CH_3OH}, the reaction rate constant in LH$_2$ was re-written as shown in equation E10. Note that all the parameters used in equation E10 were previously defined in Section 4.3.2.2, except for

$k_{CH_3OH_0}$ and E_{CH_3OH}, which respectively stand for CH_3OH pre-exponential factor and CH_3OH activation energy.

$$k = k_0 e^{\frac{-E_a}{RT}} = k_{CH_3OH_0} K_{CO_0} K_{H_{2_0}} e^{\frac{-(E_{CH_3OH} + Q_{CO} + 1.5Q_{H_2})}{RT}} \qquad \text{(E10)}$$

Therefore, E_{CH_3OH} can be calculated as follows:

$$E_{CH_3OH} = E_a - Q_{CO} - 1.5Q_{H_2} \qquad \text{(E11)}$$

The value of E_a and Q_{CO} are known from the LH2 parameter estimation results (Table 25). However, the results do not provide the value for Q_{H_2} and therefore, this value was taken from the literature. Previous density function theory (DFT) calculations for the CH_3OH synthesis over a Cu cluster, reported Q_{H_2} as -32.80 kJ.mol^{-1}[89]. To use this value in the present study, it was assumed that H_2 mostly adsorbs on Cu sites. Previous mechanistic-kinetic studies supported this assumption over Cu-metal oxide catalysts [48,96,97]. For example, DFT studies reported dissociative adsorption of H_2 on Cu sites of a Cu-based catalyst [53,89,96]. Also, mechanistic studies on CH_3OH synthesis from CO/H_2, reported dissociative adsorption of H_2 on Cu sites of the Cu-metal oxide catalyst [97]. Furthermore some kinetic studies assume H_2 adsorbs only on Cu sites for development of LH models for CH_3OH synthesis from CO/H_2 over Cu-metal oxide catalysts [48]. Therefore, Q_{H_2} over the 0.5wt% Cs-40wt% Cu-MgO was assumed to be the same as that calculated by DFT over a Cu cluster [89]. Subsequently, based on equation E11, E_{CH_3OH} was calculated as follows:

$(E_{CH_3OH})_{Cu-MgO}$ = 10.00 - (-2.25) - 1.5(-32.80) = 61.45 kJ.mol^{-1}

In previous kinetic studies of CH_3OH synthesis from CO/H_2, the CH_3OH activation energy over Cu-ZnO $(E_{CH_3OH})_{Cu-ZnO}$ was reported as 34.4 kJ mol^{-1}[10]. By comparing the value of $(E_{CH_3OH})_{Cu-MgO}$ to $(E_{CH_3OH})_{Cu-ZnO}$, it was found that $(E_{CH_3OH})_{Cu-MgO}$ is approximately 2 times larger than $(E_{CH_3OH})_{Cu-ZnO}$. Note that the molar ratio of Cu/metal oxide for both of the mentioned catalysts was 30/70.

4.3.3   Discussion of catalyst activity and product distribution

As discussed in Section 4.2.2, a systematic residence time study was conducted on the 0.5wt% Cs-40wt% Cu-MgO catalysts (experiment 6-8 and 11-12 of Table 19). The CO_2-free selectivity of these products versus residence time is plotted in Figure 39. The results show that an increase in the residence time from 0.3 sec to 4.2 sec, led to an increase in the selectivity to C_{2+} alcohols, light hydrocarbons and ketones-esters, whereas it led to a decrease in the selectivity to CH_3OH. This implies that CH_3OH is the primary product, whereas other oxygenates and light hydrocarbons are secondary products. This observation is in good agreement with the reaction pathways proposed in the literature for synthesis of higher alcohols and esters from CO/H_2, in which CH_3OH is assumed to be an intermediate for these oxygenates over Cu-metal oxide catalyst [22,28,47].
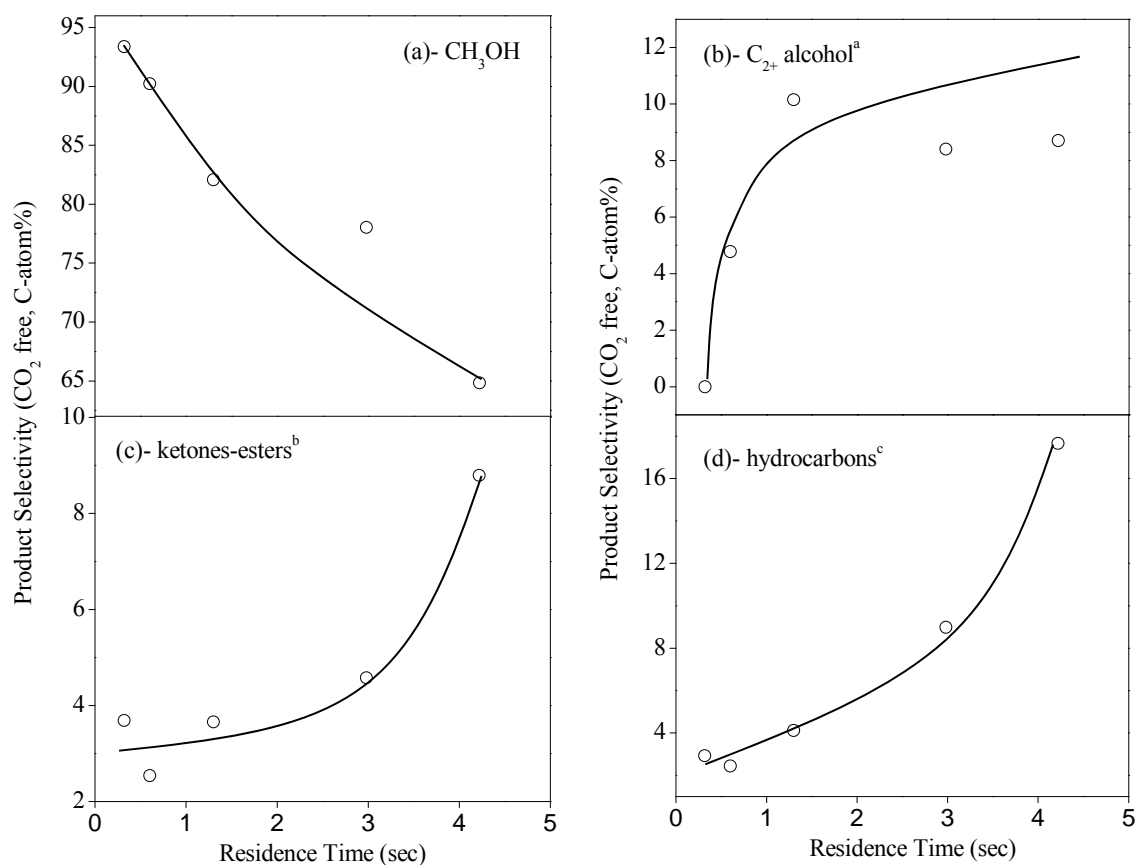
Figure 39 Effect of residence time on selectivity of (a) CH₃OH, (b) C₂₊ alcohols, (c) ketones-esters and (d) hydrocarbons at the reaction condition of: reaction pressure = 8966 kPa, reaction temperature = 573K, CO/H₂=1.00 (molar), 2 g catalyst. ᵃ C₂₊OH: Alcohols heavier than CH₃OH (ethanol, i-propanol, 1-propanol, 2-butanol, 2-methyl-1-propanol, 1-butanol and 3-pentanol). ᵇ ketones-esters: acetic acid methyl ester, acetone and methyl formate. ᶜ hydrocarbon: methane, ethane and propane.

In order to study the effect of reaction pressure on the STY of the CO_2-free carbonaceous products, the reaction pressure was increased from 6200 kPa to 9000 kPa while other reaction conditions remained constant (experiment 9 and 10 in Table 18). The corresponding summary of the results is shown in Figure 40. These results showed that an increase in the reaction pressure from 6200 kPa to 9000 kPa , led to an increase in the STY of CH_3OH while

it led to a decrease in the STY of the C_{2+} alcohols, ketones-esters and light hydrocarbons. As discussed in Section 4.3.1, CH_3OH was the dominant product over 0.5wt% Cs- 40wt% Cu-MgO, produced from CO/H_2 by the following reaction:

$$CO+2H_2 \leftrightarrow CH_3OH \ (\Delta H^o_{298K} = -90.8 \ \frac{kJ}{mol} \text{ and } \Delta G^o_{298K} = -25.2 \frac{kJ}{mol}) \qquad (R10)$$

Based on thermodynamic equilibrium calculation discussed in Section 4.3.2.1, it was found that reaction R10 is far from equilibrium $(0.10 \leq \frac{K_{CH_3OH-calc}}{K_{CH_3OH}} < 0.15)$, which implies that this reversible reaction is kinetically controlled. Baring this in mind, an increase in reaction pressure, leads to an increase in f_{CO} and f_{H_2}, which shifts the reaction forward, leading to a higher CH_3OH reaction rate (r_{CH_3OH} in Table 20) and therefore, higher STY of CH_3OH in the product stream.
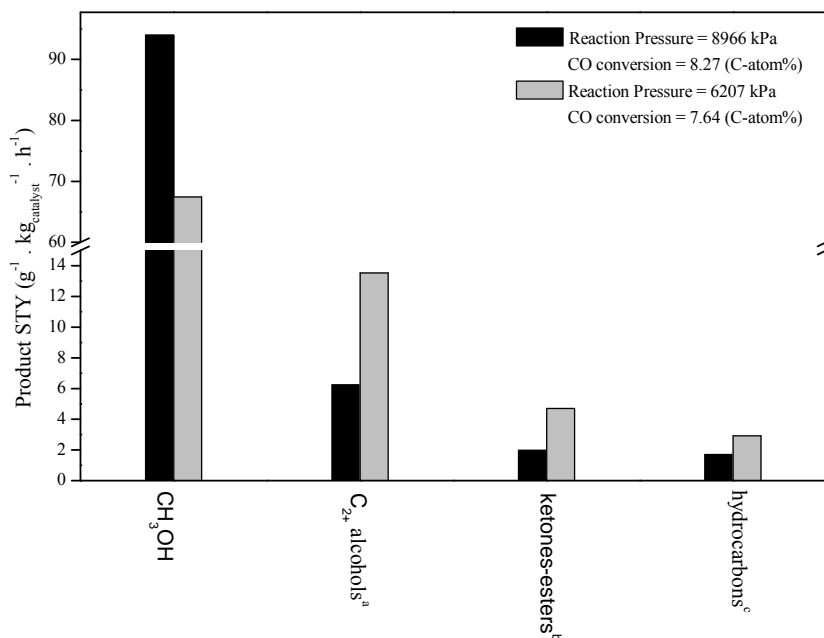
Figure 40 Effect of reaction pressure on STY of CH₃OH , C₁₊ alcohols, ketones-esters and hydrocarbons at reaction condition of: reaction temperature = 573 K, CO/H₂=0.49 (molar), residence time = 1.30 sec, 2 g catalyst. ᵃ C₁₊ alcohols: Alcohols heavier than CH₃OH (ethanol, i-propanol, 1-propanol, 2-butanol, 2-methyl-1-propanol, 1-butanol and 3-pentanol). ᵇ ketones-esters: acetic acid methyl ester, acetone and methyl formate. ᶜ hydrocarbons: methane, ethane and propane.

In order to study the effect of reaction temperature on the STY of the CO_2-free carbonaceous products, the reaction temperature was changed from 558 K to 573 K, while other reaction conditions remained constant (experiment 5 and 12 in Table 18). The corresponding summary of the results is shown in Figure 41. The results showed that an increase in the reaction temperature from 558 K to 573 K, led to a decrease in the STY of CH_3OH while it led to an increase in the STY of the C_{2+} alcohols, ketones-esters and light hydrocarbons. It was discussed earlier that the CH_3OH synthesis reaction from CO/H_2 (reaction R10) is kinetically controlled. Also this reaction is known to be exothermic. Baring that in mind, an increase in reaction temperature, leads to lower K_{CH_3OH} (Table 21), which shifts the reaction

133

backward due to the reversible term in r_{CH_3OH} (Table 20). The lower r_{CH_3OH}, subsequently causes lower STY of CH_3OH in the product stream.
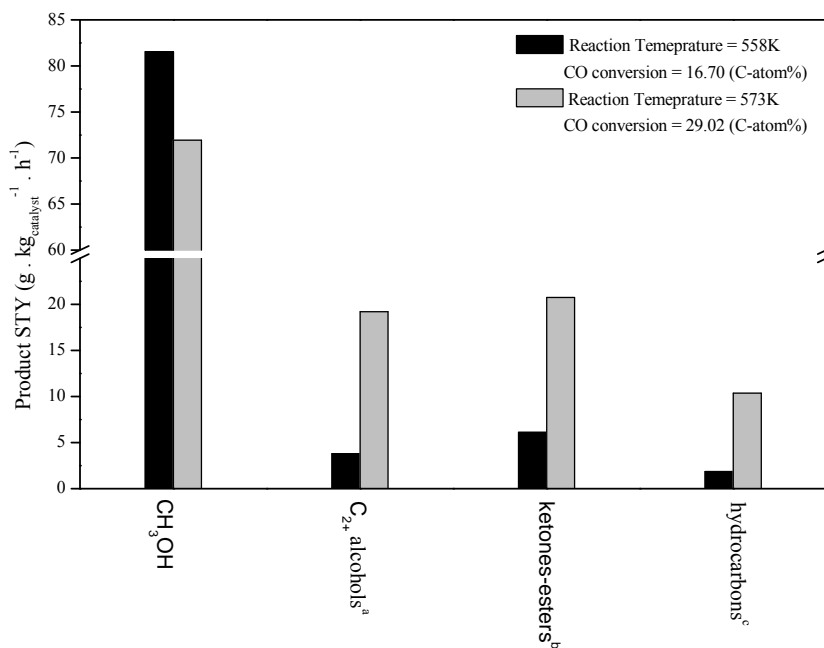
Figure 41 Effect of reaction temperature on STY of CH₃OH , C₂₊ alcohols, ketones-esters and hydrocarbons at reaction condition of: reaction pressure = 8966 kPa, CO/H₂=1.00 (molar), residence time = 4.22 sec, 2 g catalyst. ᵃ C₂₊ alcohols: alcohols heavier than CH₃OH (ethanol, i-propanol, 1-propanol, 2-butanol, 2-methyl-1-propanol, 1-butanol and 3-pentanol). ᵇ ketones-esters: acetic acid methyl ester, acetone and methyl formate. ᶜ hydrocarbons: methane, ethane and propane.

In order to study the effect of feed molar ratio of CO/H_2 on the selectivity of the CO_2-free carbonaceous products, feed molar ratio of CO/H_2 was changed from 0.49 to 1.00 while other reaction conditions remained constant (experiment 8 and 9 in Table 18). The corresponding summary of the results is shown in Figure 42. Note that as reported in Figure 42, the CO conversion for the two mentioned experiments was the same, which made the selectivity comparison between the two experiments valid. Results showed that an increase in feed

134

molar ratio of CO/H_2, led to a decrease in the CO_2-free-selectivity of CH_3OH and ketones-esters while it led to an increase in the CO_2-free-selectivity of the C_{2+} alcohols. On the other hand the selectivity of light hydrocarbons remained almost unchanged. Some of the previous mechanistic studies suggested that the reaction chain growth responsible for C_{2+} alcohols synthesis from CO/H_2 over Cu-metal oxide catalyst can be carried out via CO insertion in to a surface alkoxide [28,61-63]. Therefore, it is expected that an increase in CO/H_2 molar ratio leads to higher CO_2-free-selectivity of the C_{2+} alcohols.
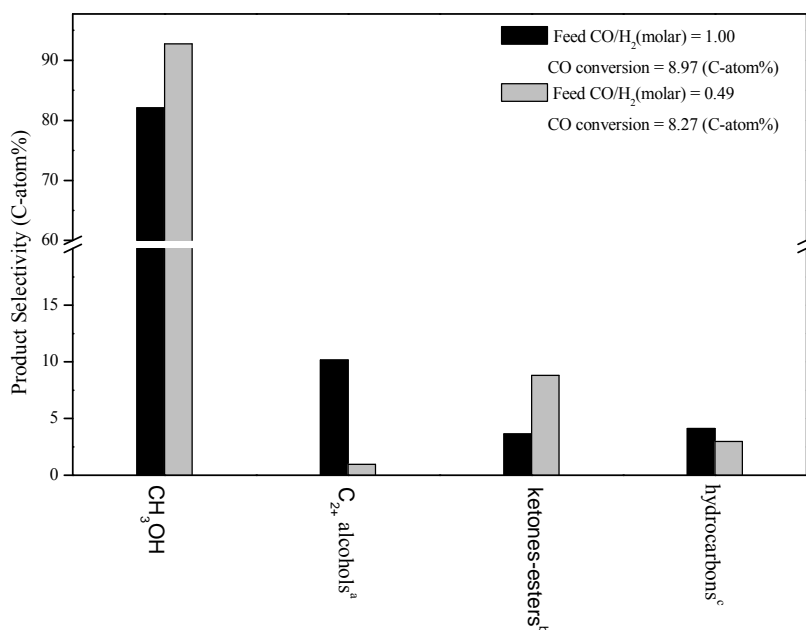
Figure 42 Effect of feed molar ratio on CO_2 free selectivity of CH_3OH , C_{2+} alcohols, Ketones & Esters and Hydrocarbons at reaction condition of: reaction pressure = 8966 kPa, reaction temperature = 573 K, residence time = 1.3 sec, 2 g catalyst. [a] C_{1+} alcohols: Alcohols heavier than CH_3OH (Ethanol, i-Propanol, 1-propanol, 2-butanol, 2-methyl-1-propanol, 1-butanol and 3-pentanol). [b] ketones-esters: acetic acid methyl ester, acetone and methyl formate. [c] hydrocarbon (methane, ethane and propane).

Previous studies showed that modified Fischer-Tropsch catalysts, such as alkali promoted-CuO-CoO-ZnO-Al$_2$O$_3$, primarily generate linear alcohols from CO/H$_2$ at reaction temperature of 533 -613 K and reaction pressure > 6000 kPa [98]. It was reported that synthesis of the linear alcohols over these catalysts follows the Anderson-Schulz-Flory (ASF) distribution. In the present study, to investigate whether the synthesis of linear alcohols from CO/H$_2$ over 0.5wt% Cs-40wt% Cu-MgO at reaction temperature of 558-598K and reaction pressure > 6000 kPa follows the ASF distribution, the weight fraction of all the produced alcohols over the catalyst for experiment 15 (Table 18) was reported in Table 28 as an example. The weight fraction of linear alcohols was also calculated based on the ASF model given in Equation E12 [98,99] and is also reported in Table 28. In Equation E12, W$_n$ is the weight fraction of a linear alcohol containing n carbon atoms and α is the chain growth probability. The value of α was calculated so that the weight fraction of methanol calculated by the ASF model was equal to the weight fraction of methanol in experiment 15 (Table 28) which resulted in α value of 0.1605.

$$W_n = n(1-\alpha)^2\alpha^{n-1} \tag{E12}$$

The results in Table 28 show that the weight fraction of the C$_{2+}$ linear alcohols from experiment 15 do not match the weight fraction of the C$_{2+}$ linear alcohols calculated by the ASF model, which implies that formation of linear alcohols from CO/H$_2$ over 0.5wt% Cs-40wt% Cu-MgO catalyst do not follow the ASF distribution. On the hand, the results in Table 28 showed that beside linear alcohols, secondary alcohols and branched alcohols were also produced in experiment 15. Since the ASF model can only describe linear alcohol

136

formation from CO/H_2 over metal oxide-based catalysts via the chain growth mechanism [98,99], the formation of secondary alcohols and branched alcohols over the 0.5wt% Cs-40wt% Cu-MgO catalyst leads to a deviation in the linear alcohol distribution over the catalyst compared to the ASF distribution.

Table 28 Weight fraction of produced alcohols over 0.5wt% Cs- 40wt% Cu-MgO

Experiment Number	Weigh Fraction[b]							
	Linear Alcohols				Secondary Alcohols and Branched Alcohols			
	MeOH	EtOH	PrOH	BuOH	i-PrOH	2-m-PrOH	2-BuOH	3-PeOH
15[a]	0.705	0.060	0.000	0.003	0.080	0.084	0.014	0.055
ASF distribution[c]	0.705	0.226	0.054	0.012	----------------not applicable -----------------			

[a] Data taken from experiment 15 of Table 18. [b] MeOH stands for methanol. EtOH stands for ethanol. PrOH stands for propanol. BuOH stands for butanol. i-PrOH stands for i-propanol. 2-m-PrOH stands for 2-methyl-propanol. 2-BuOH stands for 2-butanol. 3-PeOH stands for 3-pentanol. [c] ASF distribution stands for Anderson-Schulz-Flory distribution.

4.3.4   Comparison of Cs-Cu-MgO activity versus Cs-Cu-ZnO activity

In this section, the catalyst activity for synthesis of oxygenates from CO/H_2 over Cs-Cu-ZnO and Cs-Cu-MgO are compared. Also, the observed differences between the activity of the two catalysts towards different carbonaceous products is discussed, based on the characteristics of the catalysts.

4.3.4.1   Observed differences in the activity of Cs-Cu-MgO and Cs-Cu-ZnO

Since the loading of Cs and Cu in Cs-Cu-metal oxide (ZnO or MgO) play a role in determining the catalyst activity toward oxygenates from C_1 species (CO and CH_3OH) [20,26,27,79,100], a comparison between Cs-Cu-MgO catalyst and Cs-Cu-ZnO catalyst must be done at the same Cs/Cu loading. One point comparisons were conducted between the STY of the alcohols and carbonaceous byproducts from CO/H_2 over 0.5wt% Cs-40wt% Cu-MgO (Cs/Cu/MgO (molar) = 0.2/30.0/69.8) in the present study (experiment number 15 in Table 18) and a Cs-Cu-ZnO (Cs/Cu/ZnO (molar) = 0.3/29.9/69.8) catalyst reported previously by Nunan et al. [27]. The summary of the results is shown in Table 29 and Table 30.

.

Table 29 Comparison between selectivity of alcohols and carbonaceous byproducts over Cs-Cu-MgO and Cs-Cu-ZnO from CO/H$_2$

Catalyst	Cs/Cu/(Metal Oxide) (molar ratio)	T[a] (K)	P[a] (kPa)	τ[a] (sec)	Feed CO/H$_2$ (molar ratio)	Total STY[b] (g.Kg$_{catalyst}^{-1}$.h^{-1})	CO$_2$ Selectivity (C-atom %)	Product Selectivity (CO$_2$ free, C-atom%)			
								CH$_3$OH	C$_{2+}$OH[c]	Carbonaceous byproducts	
										HC[c]	Other oxygenates[c]
Cs-Cu-ZnO[d]	(0.3/29.9/69.8)	583	7600	0.9	2.22	793.0	34.87	28.65	49.75	5.04	16.56
0.5wt% Cs- 40wt% Cu-MgO[e]	(0.2/30.0/69.8)	598	8966	1.3	1.50	168.7	32.29	66.25	13.43	14.04	6.27

[a] T is reaction temperature and P is reaction pressure and τ = residence time = $\frac{\text{catalyst weight(g)/catalyst density (g.cm}^{-3})}{\text{feed flow rate (cm}^3(\text{STP).min}^{-1})}$, catalyst density ≈ 1 g.cm^{-3}. [b] total STY = space time yield to all carbonaceous products. [c] C$_{2+}$ OH = All alcohols that contain 2 or more C atoms in their molecular structure. HC = light hydrocarbons (methane + ethane + propane). Other oxygenates = ketones + esters + aldehydes. [d] Data from reference [27]. [e] Data taken from experiment 15 of Table 18.

Table 30 Comparison between selectivity of different alcohols over Cs-Cu-MgO and Cs-Cu-ZnO from CO/H$_2$

Catalyst	Cs/Cu/(Metal Oxide) (molar ratio)	T[a] (K)	P[a] (kPa)	τ[a] (sec)	Feed CO:H$_2$ (molar)	Alcohol STY (g.Kg$_{catalyst}^{-1}$.h^{-1})	Alcohol Selectivity (C-atom%)[b]							
							MeOH	C$_{2+}$ OH						
								EtOH	PrOH	BuOH	i-PrOH	2-m-PrOH	2-BuOH	3-PeOH
Cs-Cu-ZnO[c]	(0.3/29.9/69.8)	583	7600	0.9	2.22	317.6	36.55	5.50	14.19	3.30	0	19.56	0.72	20.17
0.5wt% Cs- 40wt% Cu-MgO[d]	(0.2/30.0/69.8)	598	8966	1.3	1.50	85.0	82.72	4.87	0.00	0.16	4.99	4.24	0.70	2.33

[a] T is reaction temperature. P is reaction pressure. τ = residence time = $\frac{\text{catalyst weight(g)/catalyst density (g.cm}^{-3})}{\text{feed flow rate (cm}^3(\text{STP).min}^{-1})}$, catalyst density ≈ 1 g.cm^{-3}. [b] MeOH stands for methanol. EtOH stands for ethanol. PrOH stands for propanol. BuOH stands for butanol. i-PrOH stands for i-propanol. 2-m-PrOH stands for 2-methyl-propanol. 2-BuOH stands for 2-butanol. 3-PeOH stands for 3-pentanol. [c] Data from reference [27]. [d] Data taken from experiment 15 of Table 18.

The total STY values in Table 29 show that Cs-Cu-ZnO is noticeably more active than 0.5wt%Cs-40wt%Cu-MgO in the synthesis of alcohols, CO_2 and carbonaceous byproducts from CO/H_2. The selectivity to CO_2 was similar over both catalysts. However, the CO_2 STY (CO_2 STY = total STY $\times$ CO_2 selectivity) is much higher over Cs-Cu-ZnO compared to 0.5wt% Cs-40wt% Cu-MgO. As discussed in Section 4.3.1 the presence of the water gas shift reaction is most likely responsible for the formation of CO_2 from CO. To identify how far the water gas shift reaction was from the thermodynamic equilibrium, the thermodynamic equilibrium constant (K_{WGS}) and calculated equilibrium constant ($K_{WGS-calc}$) corresponding to water gas shift reaction were calculated for all the high pressure experiments in the present study (Experiment 1 − 17 of Table 18) and the results are shown in Table 31. The results showed that in all experiments the $\frac{K_{WGS-calc}}{K_{WGS}}$ is smaller than 0.14, which implies that the water gas shift over 0.5wt% Cs- 40wt% Cu-MgO is far from thermodynamic equilibrium. On the other hand previous studies suggested that at reaction temperature $\geq$ 558 K, the water gas shift reaction over Cs-Cu-ZnO-based catalyst has most likely reached thermodynamic equilibrium [47,101]. Based on these thermodynamic observations, higher CO_2 STY over Cs-Cu-ZnO compared to 0.5wt% Cs-40wt% Cu-MgO is expected.

The overall CO_2-free selectivity of the carbonaceous byproduct in Table 29 (hydrocarbons and non-alcohol oxygenates), was the same over Cs-Cu-ZnO and the 0.5wt% Cs-40wt% Cu-MgO. However, CO_2-free selectivity of hydrocarbons was higher over the 0.5wt% Cs-40wt% Cu-MgO compared to Cs-Cu-ZnO.

Table 31 thermodynamic equilibrium constant and calculated equilibrium constant for water gas shift reaction over 0.5wt% Cs-40wt% Cu-MgO

Experiment Number	Temperature (K)	water gas shift reaction ($CO + H_2O \rightarrow CO_2 + H_2$)		
		$K_{WGS-calc}$ [a]	K_{WGS} [b]	$\dfrac{K_{WGS-calc}}{K_{WGS}}$
1	558	0.172	51.09	0.003
2		0.200		0.004
3		0.207		0.004
4		0.189		0.004
5		0.124		0.002
6	573	0.54	40.96	0.013
7		0.28		0.007
8		0.13		0.003
9		0.53		0.013
10		0.31		0.008
11		0.33		0.008
12		2.36		0.058
13	598	0.25	29.10	0.009
14		1.72		0.059
15		1.36		0.047
16		2.05		0.070
17		3.95		0.136

[a] $K_{WGS-calc} = \dfrac{(\frac{\hat{f}_{CO_2}}{P_o}) \times (\frac{\hat{f}_{H_2}}{P_o})}{(\frac{\hat{f}_{CO}}{P_o}) \times (\frac{\hat{f}_{H_2O}}{P_o})}$. Po is standard pressure and is 101 kPa. $\hat{f}_i$ is the fugacity of component i in the product stream.

[b] K_{WGS} is equilibrium constant for water gas shift reaction calculated by Aspen plus V7.1 (23.0.4507) software using an equilibrium reactor with SR-POLAR property method.

Looking at the selectivity of CH_3OH and $C_{2+}OH$ in Table 29, it can be seen that Cs-Cu-ZnO was more selective in the synthesis of C_{2+} alcohols whereas the 0.5wt% Cs-40wt% Cu-MgO was more selective in the synthesis of CH_3OH. The two mentioned catalysts showed very different product distributions towards C_{2+} alcohols (Table 30). Cs-Cu-ZnO is more selective

towards 2-methyl-propanol, whereas 0.5wt% Cs-40wt% Cu-MgO is equally selective towards ethanol, i-propanol and 2-methyl–propanol. STY_{CH_3OH} over the 0.5wt% Cs-40wt% Cu-MgO and Cs-Cu-ZnO were calculated by multiplication of total STY and selectivity of CH_3OH (Table 30). The STY_{CH_3OH} over the 0.5wt% Cs-40wt% Cu-MgO catalyst was calculated as 70.3 g.kg$_{catalyst}^{-1}$.h^{-1} whereas STY_{CH_3OH} over Cs-Cu-ZnO was calculated as 116.1 g.kg$_{catalyst}^{-1}$.h^{-1}. It was reported in Section 4.3.2.5, that $(E_{CH_3OH})_{Cu-MgO}$ is 2 times larger than $(E_{CH_3OH})_{Cu-ZnO}$, which is in good agreement with the noticeably lower STY_{CH_3OH} over 0.5wt% Cs-40wt% Cu-MgO compared to STY_{CH_3OH} over Cs-Cu-MgO (Table 30).

4.3.4.2   Discussing the observed activity differences based on the catalyst characteristics

In this section the lower activity of the 0.5wt% Cs-40wt% Cu-MgO compared to the Cs-Cu-ZnO towards the synthesis of alcohols from CO/H$_2$ is discussed based on the differences in the characteristics of the two catalysts.

4.3.4.2.1   Metal oxide conductivity

The noticeable difference in product distribution towards alcohols over Cs-Cu-ZnO and 0.5wt% Cs-40wt% Cu-MgO (Table 29 and Table 30) could be partly attributed to the conductive properties of the ZnO and MgO. Previous studies have reported a MgO band gap of 6.1 eV [102] and a ZnO band gap of 3.2 eV [103], which shows that MgO is an insulator [104] whereas ZnO is a semi-conductor. In MgO, the valence electrons are moved down in

energy, away from the Fermi level and therefore, they tend to be inactive for chemical surface bonding [104]. Due to the lower band gap of ZnO compared to MgO, the energy of the valence electrons is closer to the Femi level and the electrons can be excited into the conductive band easily at higher temperatures compared to MgO [104]. However, it is noteworthy that for both MgO and ZnO, the surface defects (such as oxygen vacancies) and impurities (such as addition of alkali promoters or Cu), can furnish unpaired electrons which lead to more active metal oxide surface [104].

4.3.4.2.2   The chemical state of copper in Cu-metal oxide catalysts

Another reason for the observed differences in the catalyst activity and product distribution towards alcohols over the Cs-Cu-ZnO and the 0.5wt% Cs-40wt% Cu-MgO (Table 29 and Table 30) catalysts can be attributed to the difference in the state of copper and the resulting active sites in Cs-Cu-ZnO compared to 0.5wt% Cs-40wt% Cu-MgO. Note that the Cu-ZnO (non-alkali-promoted version of the Cs-Cu-ZnO reported in Table 29 and Table 30) was prepared by co-precipitation, details of which have been given in previous work [49]. The catalyst was characterized using TEM, SEM and EDX. Based on the characterization results, two forms of Cu were identified at the surface of Cu-ZnO (Cu/ZnO=30/70 (molar)) [49]. The first form was attributed to Cu^{1+} crystallites which were dissolved in ZnO crystallites and therefore, interacted strongly with ZnO, whereas the other form is Cu^0 metal crystallites, that were dispersed (Cu^0 dispersion > 10%) as separate crystallites on ZnO crystallites and interacted weakly and donated electrons to the Cu/ZnO interface [49].

On the other hand as discussed in section 2.3.1, the XRD results of the 40wt% Cu-MgO and 0.5wt% Cs- 40wt% Cu-MgO showed no change in the MgO unit cell size (a_{MgO}), which implies that Cu crystallites are formed as separate crystallites on MgO crystallites and were likely interacting with MgO at the Cu/MgO interface. The XPS results in Section 3.4 showed the presence of two copper states (Cu^0 and Cu^{2+}) on the catalyst surface. It was found previously that the dispersion of Cu^0 was 0.28% (Section 2.3.1) and the dispersion of Cu^{2+} was calculated as 0.67%. The low dispersion of copper on MgO crystallites led to low concentration of Cu/MgO interfaces. The low dispersion of copper (<1%) in 0.5wt% Cs-40wt% Cu-MgO compared to a high dispersion of copper (>10%) in Cu-ZnO partially explains the low activity of the 0.5wt% Cs-40wt% Cu-MgO compared to Cs-Cu-ZnO towards different carbonaceous products. As already mentioned no solid solution of copper in MgO was observed over 0.5wt% Cs-40wt% Cu-MgO, while a solid solution of copper in ZnO was observed over Cs-Cu-ZnO. Also previous studies stated that the copper solution in ZnO in Cu-ZnO-based catalyst, leads to a strong interaction between copper and ZnO [49]. The lack of a presence of a solid solution of Cu and MgO in the 0.5wt% Cs-40wt% Cu-MgO catalyst could be another reason for the lower activity of the 0.5wt% Cs-40wt% Cu-MgO compared to Cs-Cu-ZnO.

4.3.4.2.3   Hydrogenation on the metal oxide

The activity of the Cu-metal oxide catalyst for the formation of oxygenates from syngas is highly dependent on the hydrogenation properties of the catalyst. Generally, H_2 interacts weekly with most metal oxides (such as MgO and ZnO), which likely leads to lack of activity

of metal oxide sites (metal cation and oxygen anion) for H_2 adsorption [104]. However, strong interaction between Cu cation dissolved in some metal oxides (such as ZnO), can make the metal oxide surface active for heterolytic dissociative adsorption of H_2 [97,104]. As discussed, in Cu-ZnO, two forms of Cu were observed: 1-Cu^0 dispersed on ZnO, 2-Cu^{1+} in solid solution with ZnO. In Cu^0-ZnO, the weak interaction between Cu^0 and ZnO, leaves Cu^0 sites as the only active sites for the dissociative adsorption of H_2. Whereas for Cu^{1+}-ZnO, the strong interaction between Cu^{1+} and ZnO due to solid solution effect, makes (Zn^{2+} and O^{2-}) pairs, the dominant active sites for heterolytic bond-dissociation of H_2. Subsequently, Cu^0 sites and ZnO sites (Zn^{2+} and O^{2-}) are both active in adsorption of H_2 in Cu-ZnO. On the other hand, on Cu-MgO, two forms of Cu were observed: 1-Cu^0 dispersed on MgO, 2-Cu^{2+} dispersed on MgO. Since Cu^0 and Cu^{2+} interact weakly with MgO, it can be assumed that over the Cu-MgO, only surface Cu^0 sites and surface Cu^{2+} sites are active in H_2 dissociative adsorption. Furthermore, most likely, MgO sites (Mg^{2+} and O^{2-}) are not active in heterolytic adsorption of H_2 in Cu-MgO. It was discussed in the previous section that the dispersion of Cu^0 and Cu^{2+} on Cu-MgO (<1%) was noticeably lower than the dispersion of Cu^0 on Cu-ZnO (>10%). Therefore, due to a noticeably lower dispersion of Cu^0 and Cu^{2+} on Cu-MgO compared to the dispersion of Cu^0 on Cu-ZnO and the lack of a presence of active hydrogenating metal oxide sites in Cu-MgO compared to Cu-ZnO, the lower hydrogenation activity on Cu-MgO is expected. These observation can partially justify the lower activity of Cu-MgO towards oxygenates compared to Cu-ZnO.

4.3.4.2.4   Basicity of Cu-metal oxide catalyst

It was found that the intrinsic basicity of the 0.5wt% K- 40wt% Cu-MgO catalyst was approximately 4 times higher than that of the 0.5wt% K- 40wt% Cu-ZnO catalyst (Section 2.3.1). By analogy, the same trend is expected for the 0.5wt% Cs-40wt% Cu-MgO catalyst and 0.5wt% Cs-40wt% Cu-ZnO catalyst. On the other hand, formation of C_2 oxygenates (ethanol and methyl formate) from CO/H_2 over Cu-metal oxide catalysts are dependent not only on the catalyst intrinsic basicity, but also on the concentration of Cu^0 sites. However, as discussed in Section 4.3.4.2.2, surface dispersion of Cu^0 sites on the 0.5wt% Cs-40wt% Cu-MgO catalyst was 10 times lower than surface dispersion of Cu^0 sites on the unprompted 40wt% Cu-ZnO catalyst. By analogy, the same trend is expected for the 0.5wt% Cs-40wt% Cu-MgO catalyst and 0.5wt% Cs-40wt% Cu-ZnO catalyst. Therefore, despite higher intrinsic basicity of 0.5wt% Cs-40wt% Cu-MgO catalyst compared to 0.5wt% Cs-40wt% Cu-ZnO catalyst, due to a shortage of Cu^0 sites on the first catalyst compared to the latter catalyst, lower activity of the first catalyst towards C_{2+} alcohols is expected.

4.4   Conclusions

The 0.5wt% Cs- 40wt% Cu-MgO catalyst was tested at reaction pressures of 6200kPa – 9000 kPa, reaction temperatures of 558K, 573K and 598K, feed CO/H_2 (molar ratio) of 0.49 -1.50 and residence time of 0.3 sec – 4.3 sec. Based on the CO_2-free activity results, three groups of oxygenate products were identified: 1-CH_3OH, 2-$C_{2+}OH$ (C_2 – C_5 linear and branched alcohols) and 3-ketones-esters (acetic acid methyl ester, acetone and methyl formate).

CH$_3$OH was the dominant oxygenate (> 66 C-atom%). Also in all cases low selectivity to hydrocarbons (< 24 C-atom%) was observed. CH$_3$OH was the primary product whereas other oxygenates and hydrocarbons were secondary products. CH$_3$OH formation from CO/H$_2$ was found to be kinetically controlled at the studied operating conditions.

The kinetic behavior of CH$_3$OH synthesis from CO/H$_2$ over the 0.5wt% Cs-40wt% Cu-MgO catalyst was successfully modeled using a Langmuir-Hinshelwood kinetic equation derived from previous mechanistic studies [47,57]. The CH$_3$OH activation energy over Cu-MgO ($(E_{CH_3OH})_{Cu-MgO}$) was estimated as 61.45 kJ mol^{-1}. It was found that at the same catalyst composition (Cu/metal oxide = 30/70 molar), $(E_{CH_3OH})_{Cu-MgO}$ is approximately 2 times larger than the CH$_3$OH activation energy over Cu-ZnO ($(E_{CH_3OH})_{Cu-ZnO}$).

The results of the 0.5wt% Cs-40wt% Cu-MgO (Cs/Cu/MgO=0.2/30.0/69.8(molar)) activity measurement for synthesis of oxygenates from CO/H$_2$ was compared with results of Cs-Cu-ZnO (Cs/Cu/ZnO=0.3/29.9/69.8(molar)) reported in a previous study [27]. The 0.5wt% Cs-40wt% Cu-MgO was more selective towards CH$_3$OH synthesis, whereas Cs-Cu-ZnO was more selective towards C$_{2+}$OH. Despite the different distribution in the oxygenate selectivity over the two catalysts, Cs-Cu-ZnO was noticeably more active in the synthesis of oxygenates than 0.5wt% Cs-40wt% Cu-MgO. Several reasons were proposed for the observed discrepancy: the fact that MgO is an insulator whereas ZnO is a semi conductor; the low dispersion of copper (<1%) in the 40wt% Cu-MgO compared to a high dispersion of copper in (>10%) in Cu-ZnO; the lack of solid solution formation between Cu and MgO in the 40wt% Cu-MgO as opposed to presence of solid solution effect between Cu and ZnO in Cu-

ZnO and activity of the ZnO sites in H_2 dissociative adsorption as opposed to lack of activity of MgO sites in H_2 dissociative adsorption.

Chapter 5

Conclusions and recommendations

5.1　Conclusions

Preparation of MgO by thermal decomposition of the metal salts in the presence of palmitic acid has been reported in the literature [41]. In the present study this method of preparation was successfully extended to the preparation of high surface area Cu-MgO and Cs (K)-promoted Cu-MgO. The prepared catalysts had low C and H impurity (< 3 wt%), indicating almost complete combustion of palmitic acid during catalyst calcination. The catalysts had higher surface area compared to Cu-MgO prepared by co-precipitation [69]. Also, the preparation method used in the present study is simpler than the co-precipitation method in which high air flow rates are required for thermal decomposition of $Mg(OH)_2$ [69]. The intrinsic basicity of the Cu-MgO–based catalysts was noticeably greater than that of a conventional Cu-ZnO-based catalyst. The Cu^0 surface area was found to be low (<3 $m^2.g^{-1}$) over all the prepared Cu-MgO-based catalysts, however, a decrease in copper loading from 40wt% to 5wt%, increased the Cu^0 dispersion from 2% to 13%.

The activity of Cs (K)-promoted Cu-MgO catalysts for the synthesis of C_2 oxygenates from CO and CH_3OH at 101 kPa and 498 - 523 K was studied. The following carbonaceous products were identified: C_2 oxygenates (methyl formate, ethanol and acetic acid), CO and CO_2. Note that ethanol and acetic acid were referred to as C_2 species. Methyl formate was the

dominant C_2 oxygenate, while selectivity to the other C_2 oxygenates (C_2 species) was low (< 5 C-atom%). Methyl formate was the primary product while CO was a secondary product. The reaction mechanisms for the decomposition of CH_3OH to CO or CO_2, water gas shift reaction and conversion of CH_3OH to C_2 oxygenates were discussed using previous mechanistic studies. Formation of C_2 oxygenates was attributed to the basic sites and copper site. It was found that at low Cu^0 surface area (< 2 $m^2.g^{-1}$) and low Cu^0 dispersion (< 2%), there was an optimum basicity (9.5 μmol $CO_2.m^{-2}$) at which the selectivity to C_2 species and methyl formate reached a maximum. On the other hand, at constant specific basicity (384.5 μmol $CO_2.g^{-1}$ – 415.9 μmol $CO_2.g^{-1}$), an increase in SA_{Cu^0} led to an increase in methyl formate yield, whereas no correlation between $SA_{Cu^{2+}}$ and methyl formate yield were observed, suggesting that formation of methyl formate was enhanced by the presence of Cu^0 sites as opposed to Cu^{2+} sites.

The 0.5wt% Cs- 40wt% Cu-MgO catalyst had the highest selectivity to C_2 oxygenates among all the tested catalysts at 101 kPa, and was selected for high pressure studies. The catalyst was tested at pressures of 6200 – 9000 kPa, reaction temperatures of 558K - 598K, feed CO/H_2 (molar ratio) of 0.49 -1.50 and residence time of 0.3 sec – 4.3 sec. Three groups of oxygenate products were identified: CH_3OH, $C_{2+}OH$ (C_2 – C_5 linear and branched alcohols) and ketones-esters (acetic acid methyl ester, acetone and methyl formate). CH_3OH was the dominant oxygenate (> 66 C-atom%). Also, in all cases low selectivity to hydrocarbons (< 24 C-atom%) was observed. CH_3OH was the primary product whereas other oxygenates and hydrocarbons were secondary products. CH_3OH formation from CO/H_2 was found to be kinetically controlled at the studied operating conditions. The reaction kinetics of CH_3OH

was modeled using a Langmuir-Hinshelwood model derived from the previously discussed CH_3OH reaction mechanism. The activation energy for CH_3OH formation over the present catalyst was approximately 2 times larger than the activation energy for CH_3OH formation over the traditional Cu-ZnO [10], which showed that Cu-ZnO-based catalyst was more active than Cu-MgO-based catalyst for the synthesis of CH_3OH from CO/H_2.

The present catalyst was more selective towards the synthesis of CH_3OH, whereas traditional Cs-Cu-ZnO [27] was more selective towards $C_{2+}OH$. Overall, the present catalyst was noticeably less active towards the synthesis of oxygenates compared to traditional Cs-Cu-ZnO which was ascribed to the fact that MgO is an insulator whereas ZnO is a semi conductor; the low dispersion of copper ($< 1\%$) in the 0.5wt% Cs-40wt% Cu-MgO catalyst compared to high dispersion of copper ($> 10\%$) in Cu-ZnO-based catalyst; the lack of the presence of a solid solution between Cu and MgO in the 0.5wt% Cs-40wt% Cu-MgO catalyst as opposed to the presence of a solid solution between Cu and ZnO in Cu-ZnO-based catalyst and the activity of the ZnO sites for dissociative H_2 adsorption as opposed to the lack of activity of MgO sites for dissociative H_2 adsorption.

5.2   Recommendations

5.2.1   Effect of addition of CO_2 and H_2O in CH_3OH activity and kinetics

Some of the previous mechanistic studies over Cu-based catalysts suggested CO_2 as a main source of C_1 species in syngas conversion to CH_3OH [20,47,53,58]. Furthermore, recent IR

studies suggested that water-derived surface species on Cu-based catalysts are crucial in CH_3OH synthesis from CO_2 [53,59]. Since in the high pressure studies over the 0.5wt% Cs-40wt% Cu-MgO catalyst, CO_2 and H_2O were not included in the syngas feed stream (CO/H_2), and there is no work in the literature addressing this issue over Cu-MgO-based catalysts, addition of CO_2 and H_2O to the syngas feed stream (CO/H_2) should be investigated. The CO_2 and H_2O could potentially be important in controlling the catalyst activity towards CH_3OH. Furthermore, to investigate whether CO or CO_2 is the main source of carbon in the synthesis of CH_3OH from syngas over 0.5wt% Cs-40wt% Cu-MgO catalyst, it is recommended to conduct carbon labeling studies by having a syngas feed mixture of $^{12}CO/^{13}CO_2/H_2/H_2O$ and monitoring the extent of involvement of ^{12}CO and $^{13}CO_2$ in the formation of CH_3OH and other produced oxygenates. Based on the result of the carbon labeling study, if CO_2 was identified as a main source of C_1 species in syngas conversion to CH_3OH over the 0.5wt% Cs-40wt% Cu-MgO catalyst, then it is recommended to conduct kinetic studies for synthesis of CH_3OH from CO_2 over this catalyst. As discussed in Section 1.8.1, recent DFT studies proposed a new mechanism for CH_3OH synthesis from CO_2/H_2 in the presence of H_2O (Figure 3) over Cu-based catalysts. It is recommended to use that mechanism to develop a LH model for CH_3OH synthesis from wet CO_2/H_2 over the catalyst and compare it to a LH model developed from older CH_3OH mechanism (Figure 2). This could potentially be crucial in identifying which mechanism can better describe the reaction of CH_3OH synthesis from wet CO_2/H_2.

5.2.2   Promotion of Cu-MgO catalyst with Li instead of Cs or K

As discussed in Section 4.3.4.2.1, non-defective (perfect) MgO crystallites are good insulators and typically are not involved in chemical bonding with adsorbates [104]. However, interaction between crystallite impurities such as alkali promoters can refurnish the unpaired electrons and lead to a more active MgO surface [104]. High interaction between alkali promoter and MgO can be achieved by solid solution of alkali metal cation in MgO crystallites. The XRD results on K or Cs promoted-Cu-MgO catalysts (Chapter 2 and 3), showed no solid solution effect between Cs^{1+} or K^{1+} and MgO crystallites. On the other hand previous studies showed the presence of a solid solution between Li^{1+} and MgO [66]. It was proposed that due to a slightly smaller radius of Li^{1+}(0.73A) in Li_2O compared to the radius of Mg^{2+}(0.86A) in MgO, the substitution of Mg^{2+} with Li^{1+} in MgO crystallites can easily occur. Therefore, preparation and characterization of Li promoted-Cu-MgO catalyst is recommended. The catalyst should also be tested for oxygenate synthesis from CO/H_2 at high pressure (> 6000 kPa). Subsequently the activity/characterization results over Li promoted-Cu-MgO should be compared to Cs and K promoted Cu-MgO.

5.2.3   Alkali loading in Cu-MgO-based catalysts

As discussed in Section 2.3.1, it was found that an increase in K loading from 0.5wt% to 4.4 wt% in K-promoted 40wt% Cu-MgO catalyst, led to an increase in intrinsic basicity of the catalyst. Furthermore, the same trend was observed for Cs-promoted 40wt% Cu-MgO as the Cs loading was increased from 0.5wt% to 13.5 wt%. However, it is noteworthy that these

results were obtained based on the two point comparison between low loading of alkali metal and high loading of alkali metal in Cs (K)-promoted Cu-MgO catalysts and it is not clear if these catalysts would show the same behavior with different loading of alkali promoter. In a previous study, Li promoted MgO catalyst with five different loadings of Li between 0.13wt% to 2.6 wt%, were prepared and the intrinsic basicity of the catalysts were measured [66]. The result showed an optimum Li loading (0.5wt%) at which the intrinsic basicity of the catalyst was maximized. By analogy, the occurrence of this phenomenon is probable over Cs (K)-promoted Cu-MgO catalysts. Therefore, it is recommended to prepare Cs (K)-promoted Cu-MgO catalysts with a minimum of five different loadings of Cs or K promoter. The intrinsic basicity of the prepared catalysts should be measured and the correlation between the loading of alkali promoter in these catalysts and the intrinsic basicity of these catalysts should be identified.

5.2.4   Effect of addition of ZnO to Cu-MgO based catalyst

As discussed in Section 4.3.4.2.1, ZnO is a semi-conductor whereas MgO is an insulator. On the other hand, the results of the present study showed that Cu-MgO catalyst possessed higher intrinsic basicity compared to Cu-ZnO catalyst. Therefore, addition of ZnO to Cu-MgO could potentially increase the conductivity of the catalyst while high intrinsic basicity of the catalyst could be retained compared to the Cu-ZnO catalyst. Therefore, it is recommended that different amounts of ZnO be added to the Cu-MgO and alkali promoted Cu-MgO. The Cu-MgO and alkali promoted Cu-MgO can be prepared by thermal decomposition of the metal salts in the presence of palmitic acid, as was explained in Chapter

2 and Chapter 3. ZnO can subsequently be added to the catalysts by vapor deposition procedure explained in previous literature [105]. The basic properties of the Cu-MgO-ZnO and alkali promoted- Cu-MgO-ZnO catalysts should be determined. Furthermore, the catalysts should be tested for oxygenate synthesis from syngas at high pressure. Also, the results of the catalyst testing and characterization over Cu-MgO-ZnO-based catalysts should be compared with the Cu-MgO-based and Cu-ZnO-based catalysts available in the literature.

5.2.5   Cu loading in Cu-MgO-based catalysts

It was found that a decrease in Cu loading from 40wt% to 5wt% in the Cu-MgO-based catalysts, increased the Cu^0 dispersion, but decreased the degree of reduction of CuO to Cu^0. However, there is no information on the effect of Cu loading between 5wt% and 40wt% on Cu^0 dispersion and Cu degree of reduction. Therefore, it is recommended to prepare Cu-MgO-based catalysts with Cu loading between 5wt% and 40wt%. The Cu^0 dispersion and degree of reduction of CuO to Cu^0 should be measured. It is probable that there will be an optimum Cu loading in which Cu^0 dispersion and degree of reduction of CuO to Cu^0 is maximized.

5.2.6   Washing the Cs (K)-promoted Cu-MgO catalysts with organic solvent

CHN analysis results given in Table 2 of Chapter 2 showed < 3wt% C contamination in the bulk of the passivated Cs (K)-promoted Cu-MgO catalysts, which confirms almost complete combustion of the palmitic acid present in the catalyst precursor during the calcination

process. However, for Cs (K)-promoted Cu-MgO catalysts with low loading of alkali promoters (0.5wt%), it is likely that alkali oxides and alkali hydroxides present on the surface of the catalysts were occluded from the surface by the < 3wt% C contamination residue left after combustion of the palmitic acid. In the present study, to avoid this phenomenon, the catalysts were pretreated thermally in He flow at 573 K before being tested. It is recommended to take additional measurs to remove the carbon by washing the catalysts with an appropriate organic solvent. For example, methylene chloride is a good organic solvent for polar carbon impurity and carbon tetrachloride is a good organic solvent for non-polar carbon impurity. Based on the XPS result given in Table 14 of Chapter 3, $HCOOCH_3$ was identified as carbon impurity present on the surface of the passivated Cs (K)-promoted Cu-MgO catalysts. Therfore it is recommended to wash the catalysts with methylene chloride and subsequently characterize them by CHN analysis to investigate the quantity of C impurity.

Bibliography

[1] V. Karkania, E. Fanara, A. Zabaniotou, Renew. Sust. Energ. Rev. 16 (2012) 1426-1436.

[2] T. Tsoncheva, T. Venkov, M. Dimitrov, C. Minchev, K. Hadjiivanov, J. Mol. Catal. A: Chem. 209 (2004) 125-134.

[3] M. Saito, Catal. Surv. Jpn. 2 (1998) 175-184.

[4] L. Domokos, T. Katona, A. Molnar, Catal. Lett. 40 (1996) 215-221.

[5] M.J. Chung, D.J. Moon, K.Y. Park, S.K. Ihm, J. Catal. 136 (1992) 609-621.

[6] S. Lee, J. Chem. Phys. 129 (2008) 194304-1-194304-8.

[7] J.S. Francisco, J. Am. Chem. Soc. 125 (2003) 10475-10480.

[8] G.A. Deluga, J.R. Salge, L.D. Schmidt, X.E. Verykios, Science (Washington, DC, US). 303 (2004) 993-997.

[9] K. Klier, Adv. Catal. 31 (1982) 243-313.

[10] K. Klier, V. Chatikavanij, R.G. Herman, G.W. Simmons, J. Catal. 74 (1982) 343-360.

[11] J.C.J. Bart, R.P.A. Sneeden, Catal. Today. 2 (1987) 1-124.

[12] G.W. Bridger, M.S. Spencer, Catalyst Hand Book, 2nd ed, Wolfe Publ. Co., London (1989)

[13] R.G. Herman, New Trends in CO Activation, Elsevier, Amsterdam (1991).

[14] J.R. LeBlanc, R.V. Schneider III, R.B. Strait, Methanol Production and Use, Marcel Dekker, New York (1994).

[15] P.B. Rasmussen, P.M. Holmblad, T. Askgaard, C.V. Ovesen, P. Stoltze, J.K. Noerskov, I. Chorkendorff, Catal. Lett. 26 (1994) 373-381.

[16] G.C. Chinchen, P.J. Denny, J.R. Jennings, M.S. Spencer, K.C. Waugh, Appl. Catal. 36 (1988) 1-65.

[17] K.J. Smith, R.B. Anderson, J. Catal. 85 (1984) 428-436.

[18] K.J. Smith, R.B. Anderson, Can. J. Chem. Eng. 61 (1983) 40-46.

[19] E. Tronconi, N. Ferlazzo, P. Forzatti, I. Pasquon, Ind Eng Chem Res. 26 (1987) 2122-2131.

[20] J.G. Nunan, C.E. Bogdan, K. Klier, K.J. Smith, C.W. Young, R.G. Herman, J. Catal. 113 (1988) 410-433.

[21] D.J. Elliot, F.J. Pennella, J. Catal. 114 (1988) S99-S109.

[22] K.J. Smith, C.W. Young, R.G. Herman, K. Klier, Ind Eng Chem Res. 30 (1991) 61-71.

[23] R.G. Herman, Catal. Today. 55 (2000) 233-245.

[24] H. Trevino, G.D. Lei, W.M.H. Sachtler, J. Catal. 154 (1995) 245-252.

[25] C.R. Apesteguia, B. De Rites, S. Miseo, S. Soled, Catal. Lett. 44 (1997) 1-5.

[26] J.G. Nunan, C.E. Bogdan, R.G. Herman, K. Klier, Catal. Lett. 2 (1989) 49-55.

[27] J.G. Nunan, C.E. Bogdan, K. Klier, K.J. Smith, C.W. Young, R.G. Herman, J. Catal. 116 (1989) 195-221.

[28] G.A. Vedage, P.B. Himelfarb, G.W. Simmons, K. Klier, ACS Symp. Ser. 279 (1985) 295-312.

[29] T.S. Askgaard, J.K. Norskov, C.V. Ovesen, P. Stoltze, J. Catal. 156 (1995) 229-242.

[30] D.B. Clarke, A.T. Bell, J. Catal. 154 (1995) 314-328.

[31] S. Fujita, M. Usui, H. Ito, N. Takezawa, J. Catal. 157 (1995) 403-413.

[32] M. Xu, E. Iglesia, Catal. Lett. 51 (1998) 47-52.

[33] M. Xu, E. Iglesia, J. Catal. 188 (1999) 125-131.

[34] J. Nunan, K. Klier, C. Young, P.B. Himelfarb, R.G. Herman, J. Chem. Soc. , Chem. Commun. (1986) 193-195.

[35] W. Cheng, H.H. Kung, Methanol Production and Use, Marcel Dekker, New York (1994).

[36] V.K. Diez, C.R. Apesteguia, J.I. Di Cosimo, Catal. Today. 63 (2000) 53-62.

[37] M. Bolognini, F. Cavani, D. Scagliarini, C. Flego, C. Perego, M. Saba, 75 (2002) 103-111.

[38] J.I. Di Cosimo, V.K. Diez, C.R. Apesteguia, Appl. Catal. A. 137 (1996) 149-166.

[39] M. Di Serio, M. Ledda, M. Cozzolino, G. Minutillo, R. Tesser, E. Santacesaria, Ind Eng Chem Res. 45 (2006) 3009-3014.

[40] F. Arena, G. Italiano, K. Barbera, S. Bordiga, G. Bonura, L. Spadaro, F. Frusteri, Appl. Catal. , A. 350 (2008) 16-23.

[41] S. Takenaka, S. Sato, R. Takahashi, T. Sodesawa, Phys. Chem. Chem. Phys. 5 (2003) 4968-4973.

[42] S.F. Zaman, PhD Dissertation: An Investigation of MoP Catalysts for Alcohol Synthesis, UBC. (2010) 7-10.

[43] A.Y. Khodakov, W. Chu, P. Fongarland, Chem. Rev. 107 (2007) 1692-1744.

[44] Q. Zhang, J. Kang, Y. Wang, ChemCatChem. 2 (2010) 1030-1058.

[45] G. Liu, D. Willcox, M. Garland, H.H. Kung, J. Catal. 96 (1985) 251-260.

[46] S.D. Jackson, J. Catal. 115 (1989) 247-249.

[47] E.M. Calverley, K.J. Smith, Ind Eng Chem Res. 31 (1992) 792-803.

[48] G.H. Graaf, E.J. Stamhuis, A.A.C.M. Beenackers, Chem. Eng. Sci. 43 (1988) 3185-3195.

[49] S. Mehta, G.W. Simmons, K. Klier, R.G. Herman, J. Catal. 57 (1979) 339-360.

[50] R.G. Herman, K. Klier, G.W. Simmons, B.P. Finn, J.B. Bulko, T.P. Kobylinski, J. Catal. 56 (1979) 407-429.

[51] J. Fox, F. Pesa, B. Curatolo, J. Catal. 90 (1984) 127-138.

[52] T. Tagawa, G. Pleizier, Y. Amenomiya, Appl. Catal. 18 (1985) 285-293.

[53] Y. Zhao, Y. Yang, C. Mims, C.H.F. Peden, J. Li, D. Mei, J. Catal. 281 (2011) 199-211.

[54] Y. Yang, C.A. Mims, R.S. Disselkamp, D. Mei, J. Kwak, J. Szanyi, C.H.F. Peden, C.T. Campbell, Catal. Lett. 125 (2008) 201-208.

[55] K. Klier, in: W.R. Moser(Ed.), Catalysis in Organic Synthesis, Dekker. New York (1982) 195-218.

[56] K.J. Smith, PhD Dissertation: The Synthesis of Alcohols from Carbon Monoxide and Hydrogen, McMaster University (1982).

[57] G.C. Chinchen, M.S. Spencer, K.C. Waugh, D.A. Whan, J. Chem. Soc. , Faraday Trans. 1. 83 (1987) 2193-2212.

[58] Y. Yang, C.A. Mims, R.S. Disselkamp, C.H.F. Peden, C.T. Campbell, Top. Catal. 52 (2009) 1440-1447.

[59] Y. Yang, C.A. Mims, R.S. Disselkamp, J. Kwak, C.H.F. Peden, C.T. Campbell, J. Phys. Chem. C. 114 (2010) 17205-17211.

[60] E.M. Calverley, K.J. Smith, J. Catal. 130 (1991) 616-626.

[61] G. Natta, U. Colombo, I. Pasquon, in: Emmett P.H. (Ed.), Chapter 3 in Catalysis, Volume 5, Reinhold Inc. New York (1957).

[62] K. Klier, R.G. Herman, C.W. Young, Prepr. Pap. - Am. Chem. Soc., Div. Fuel Chem. 29 (1984) 273-280.

[63] T.J. Mazanec, J. Catal. 98 (1986) 115-125.

[64] A. Kiennemann, J.P. Hindermann, R. Breault, H. Idriss, Abstr. Pap. Am. Chem. Soc. 191 (1986) 109-112.

[65] S. Sato, M. Iijima, T. Nakayama, T. Sodesawa, F. Nozaki, J. Catal. 169 (1997) 447-454.

[66] V.K. Diez, C.R. Apesteguia, J.I. Di Cosimo, J. Catal. 240 (2006) 235-244.

[67] H. Hattori, Appl. Catal. , A. 222 (2001) 247-259.

[68] C. Chizallet, G. Costentin, M. Che, F. Delbecq, P. Sautet, J. Am. Chem. Soc. 129 (2007) 6442-6452.

[69] B.M. Nagaraja, A.H. Padmasri, B.D. Raju, K.S.R. Rao, J. Mol. Catal. A: Chem. 265 (2007) 90-97.

[70] W.M. Haynes, in: Anonymous CRC Handbook of Chemistry and Physics, 91st ed. National Institute of Standards and Technology. Boulder, Colorado, USA (2010-11) 4-57-4-83.

[71] H. Liao, L. Chen, Z. Xu, G. Li, Y. Yang, Appl. Phys. Lett. 92 (2008) 173303-1-173303-3.

[72] F. Chang, W. Kuo, K. Lee, Appl. Catal. , A. 246 (2003) 253-264.

[73] B.M. Nagaraja, V.S. Kumar, V. Shashikala, A.H. Padmasri, S.S. Reddy, B.D. Raju, K.S.R. Rao, J. Mol. Catal. A: Chem. 223 (2004) 339-345.

[74] M. Varga, A. Molnar, G. Mulas, M. Mohai, I. Bertoti, G. Cocco, J. Catal. 206 (2002) 71-81.

[75] A.S. Ahmed, Egypt. J. Chem. 50 (2007) 223-234.

[76] N. Lopez, F. Illas, J. Phys. Chem. 100 (1996) 16275-16281.

[77] A.Y. Rozovskii, Kinet. Catal. 44 (2003) 360-378.

[78] T.C. Hsiao, S.D. Lin, Catal. Lett. 119 (2007) 72-78.

[79] S. Goodarznia, K.J. Smith, J. Mol. Catal. A: Chem. 320 (2010) 1-13.

[80] Y. Inoue, I. Yasumori, Bull. Chem. Soc. Jpn. 54 (1981) 1505-1510.

[81] H. Onishi, C. Egawa, T. Aruga, Y. Iwasawa, Surf Sci. 191 (1987) 479-491.

[82] S.F. Zaman, K.J. Smith, Appl. Catal. , A. 378 (2010) 59-68.

[83] S. Yang, C.W. Bates Jr., Appl. Phys. Lett. 36 (1980) 675-677.

[84] R.J. Bird, P. Swift, J. Electron Spectrosc. Relat. Phenom. 21 (1980) 227-232.

[85] M. Paranthaman, K. David, T. Lindemer, Mater. Res. Bull. 32 (1997) 165-173.

[86] E. Roedder, Am. J. Sci. 249 (1951) 81-130.

[87] E. Roedder, Am. J. Sci. 249 (1951) 224-240.

[88] S. Kim, T. Sanders, J Am Ceram Soc. 74 (1991) 1833-1840.

[89] Y. Yang, J. Evans, J.A. Rodriguez, M.G. White, P. Liu, Phys. Chem. Chem. Phys. 12 (2010) 9909-9917.

[90] A. Beretta, Q. Sun, R.G. Herman, K. Klier, Ind Eng Chem Res. 35 (1996) 1534-1542.

[91] J.G. Nunan, R.G. Herman, K. Klier, J. Catal. 116 (1989) 222-229.

[92] V. Mahdavi, M.H. Peyrovi, 7 (2006) 542-549.

[93] R.J. Madon, D. Braden, S. Kandoi, P. Nagel, M. Mavrikakis, J.A. Dumesic, J. Catal. 281 (2011) 1-11.

[94] V. Subramani, S.K. Gangwal, Energy Fuels. 22 (2008) 814-839.

[95] J. Sehested, S. Dahl, J. Jacobsen, J.R. Rostrup-Nielsen, J Phys Chem B. 109 (2005) 2432-2438.

[96] M.Z. Zhaksibaev, S.E. Malykhin, Y.V. Larichev, A.M. Pak, Kinet. Catal. 49 (2008) 527-530.

[97] J.M. Thomas, W.J. Thomas, Principle and Practice of Heterogeneous Catalysis, VCH, Germany (1997).

[98] P.L. Spath, D.C. Dayton, Preliminary Screening Technical and Economic Assessment of Synthesis Gas to Fuels and Chemicals with Emphasis on the Potential for Biomass-Derived Syngas, National Renewable Energy Laboratory-Midwest Research Institute-Battelle, Golden, Colorado (2003).

[99] R.B. Anderson, The Fischer-Tropsch Synthesis, Academic Press Inc., Orlando, Florida (1984).

[100] S. Goodarznia, K.J. Smith, J. Mol. Catal. A: Chem. 353-354 (2012) 58-66.

[101] G.C. Chinchen, P.J. Denny, D.G. Parker, M.S. Spencer, D.A. Whan, Appl. Catal. 30 (1987) 333-338.

[102] O.E. Taurian, M. Springborg, N.E. Christensen, Solid State Commun. 55 (1985) 351-355.

[103] K. Sivaramakrishnan, N.D. Theodore, J.F. Moulder, T.L. Alford, J. Appl. Phys. 106 (2009) 063510-1-063510-8.

[104] I. Chorkendorff, J.W. Niemantsverdriet, in: Anonymous Concepts of Modern Catalysis and Kinetics, Wiley-VCH Verlag GmbH & Co. KGaA, Weinheim (2003) 243-244.

[105] H. Zhuang, J. Li, Superlattices Microstruct. 51 (2012) 80-85.

[106] A. Peneloux, E. Rauzy, R. Freze, Fluid Phase Equilib. 8 (1982) 7-23.

[107] J. Schwartzentruber, H. Renon, Ind Eng Chem Res. 28 (1989) 1049-1055.

[108] G. Soave, Chem. Eng. Sci. 27 (1972) 1197-1203.

[109] P. Englezos, N. Kalogerakis, Applied Parameter Estimation for Chemical Engineers, Marcel-Dekker. New York (2001) 175-176.

Appendices

Appendix A   Catalyst preparation: calculation of required chemicals

The calculation of required chemicals for the preparation of 0.5wt% Cs-40wt% Cu- MgO is shown in this section.

1- required amount of 0.5wt% Cs-40wt% Cu- MgO (non-reduced)

   = 2 g

2- amount of $Mg(NO_3)_2.6H_2O$

   = 7 g (0.027 mol) (calculated by assuming 59.5wt% MgO in the bulk catalyst)

3- molar ratio of Cs to Mg

   = 0.003 (calculated by assuming 0.5wt% Cs and 59.5 wt% MgO in the bulk catalyst)

4- mass of Cs_2CO_3

   $$=0.027 \text{ mol Mg(NO3)2.6H2O} \times \frac{0.003 \text{ mol Cs}}{\text{mol Mg}} \times \frac{1 \text{ mol Cs2CO3}}{2 \text{ mol Cs}} \times \frac{326 \text{ g Cs2CO3}}{\text{mol Cs2CO3}} = 0.013 \text{ g}$$

5- molar ratio of Cu to Mg

   = 0.429 (calculated by assuming 40.0 wt% Cu and 59.5 wt% MgO in the bulk catalyst)

6- mass of $Cu(NO_3)_2.3H_2O$

   $$=0.027 \text{ mol Mg(NO3)2.6H2O} \times \frac{0.429 \text{ mol Cu}}{\text{mol Mg}} \times \frac{1 \text{ mol Cu2(NO3).3H2O}}{1 \text{ mol Cu}} \times \frac{242 \text{ g Cu2(NO3).3H2O}}{\text{mol Cu2(NO3).3H2O}}$$

   =2.803 g

7- total metal

   = 0.027 mol Mg + 0.012 mol Cu + 0.00007 mol Cs = 0.03907 mol

8- molar ratio of palmitic acid to total metal

=2.5 (obtained from previous study

9- mass of palmitic acid

$$=0.03907 \text{ mol total metal} \times \frac{2.5 \text{ mol palmitic acid}}{1 \text{ mol total metal}} \times \frac{256 \text{ g palmitic acid}}{1 \text{ mol palmitic acid}} = 25 \text{ g}$$

Appendix B   Repeatability for catalyst characterization

B.1   BET surface area, pore volume and pore size analysis

The repeatability for the measured BET surface area (SA_{BET}), pore volume (V_p) and pore size (d_p) for MgO and Cs (K)-prompted-Cu-MgO using N_2 adsorption-desorption isotherms are shown in Table 32-Table 35.

Table 32 Repeatability for SA_{BET}, V_p and d_p gained for MgO-3

Catalyst	Calcination Temperature	Calcination Time	R^a	SA_{BET}^b	V_p^b	d_p^b
	(K)	(min)	-	$(m^2.g^{-1})$	$(cm^3.g^{-1})$	(nm)
MgO-3	673	480	1.25	170	0.42	10.1
				182	0.48	10.5
				174	0.40	9.4
				174	0.40	9.4
				172	0.40	9.5
Average				174	0.42	9.9
Standard deviation				5	0.03	0.5

[a] R is molar ratio of palmitic acid to Mg+Cu+alkali metal. [b] SA_{BET}, V_P and d_p are respectively, BET surface area, pore volume and average pore size of the catalysts.

Table 33 Repeatability for SA$_{BET}$, V$_p$ and d$_p$ gained for MgO-2

Catalyst	Calcination Temperature (K)	Calcination Time (min)	R[a] -	SA$_{BET}$[b] (m^2.g^{-1})	V$_p$[b] (cm^3.g^{-1})	d$_p$[b] (nm)
MgO-2	673	480	2.5	151	0.52	13.9
				158	0.54	13.2
				158	0.54	13.2
Average				156	0.54	13.4
Standard deviation				4	0.01	0.4

[a] R is molar ratio of palmitic acid to Mg+Cu+alkali metal. [b] SA$_{BET}$, V$_P$ and d$_p$ are respectively, BET surface area, pore volume and average pore size of the catalysts.

Table 34 Repeatability for SA$_{BET}$, V$_p$ and d$_p$ gained for 13.5wt% Cs-40wt% Cu-MgO

Catalyst	SA$_{BET}$[a] (m^2.g^{-1}) Before Reduction	V$_p$[a] (cm^3.g^{-1})	d$_p$[a] (nm)
13.5wt% Cs-40wt% Cu-MgO	15	0.06	16.1
	17	0.09	20.8
	17	0.08	19.2
Average	17	0.08	18.7
Standard deviation	1	0.02	2.4

[a] SA$_{BET}$, V$_P$ and d$_p$ are respectively, BET surface area, pore volume and average pore size of the catalysts before reduction.

Table 35 Repeatability for SA_{BET}, V_p and d_p gained for 4.4wt% K-40wt% Cu-MgO

Catalyst	SA_{BET}^{a} $(m^2.g^{-1})$	V_p^{a} $(cm^3.g^{-1})$	d_p^{a} (nm)
	Before Reduction		
4.4wt% K-40wt% Cu-MgO	26	0.17	26.4
	25	0.20	31.5
	27	0.18	25.7
	25	0.17	27.6
Average	26	0.18	27.8
Standard deviation	1	0.01	2.6

[a] SA_{BET}, V_P and d_p are respectively, BET surface area, pore volume and average pore size of the catalysts before reduction.

B.2   CHN analysis

The repeatability for the CHN analysis for the 40wt% Cu-MgO-based catalysts were shown in Table 36, Table 37, Table 38, Table 39 and Table 40.

Table 36 Repeatability of CHN analysis of 40wt% Cu-MgO

Catalyst	C, wt%	H, wt%	N, wt%
40wt% Cu-MgO (passivated)	2.30	0.78	0.00
	2.31	0.78	0.00
Average	2.31	0.78	0.00

Table 37 Repeatability of CHN analysis of 0.5wt%K-40wt% Cu-MgO

Catalyst	C, wt%	H, wt%	N, wt%
0.5wt%K-40wt% Cu-MgO (passivated)	1.10	0.31	0.00
	0.91	0.26	0.00
Average	1.01	0.29	0.00

Table 38 Repeatability of CHN analysis of 0.5wt%Cs-40wt% Cu-MgO

Catalyst	C, wt%	H, wt%	N, wt%
0.5wt%Cs-40wt% Cu-MgO (passivated)	1.30	0.40	0.00
	1.15	0.41	0.00
Average	1.23	0.41	0.00

Table 39 Repeatability of CHN analysis of 4.4wt%K-40wt% Cu-MgO

Catalyst	C, wt%	H, wt%	N, wt%
4.4wt%K-40wt% Cu-MgO (passivated)	1.45	0.32	0.00
	1.66	0.36	0.00
Average	1.56	0.34	0.00

Table 40 Repeatability of CHN analysis of 13.5wt%Cs-40wt% Cu-MgO

Catalyst	C, wt%	H, wt%	N, wt%
13.5wt%Cs-40wt% Cu-MgO (passivated)	0.77	0.17	0.00
	1.07	0.26	0.00
Average	0.92	0.22	0.00

B.3   XRD analysis

The repeatability for d_{Cu}^{XRD}, d_{MgO}^{XRD} and a_{MgO} based on the XRD analysis are shown in Table 41 and Table 42.

Table 41 Repeatability of XRD analysis of MgO

Catalyst	d_{Cu}^{XRD} (nm)	d_{MgO}^{XRD} (nm)	a_{MgO} (nm)
MgO	-	13	0.42
	-	14	0.42
Average	-	14	0.42

Table 42 Repeatability of XRD analysis of 0.5wt% K-40wt% Cu-MgO

Catalyst	d_{Cu}^{XRD} (nm)	d_{MgO}^{XRD} (nm)	a_{MgO} (nm)
0.5wt% K-40wt% Cu-MgO	21	20	0.42
	20	24	0.42
Average	20	22	0.42

B.4   N₂O pulse titration analysis

The repeatability for Cu^0 Dispersion, $SA_{Cu}^{N_2O}$ and $d_{Cu}^{N_2O}$ based on the N_2O pulse titration analysis are shown in Table 43 and Table 44.

Table 43 Repeatability of N₂O pulse titration analysis of 5wt% Cu-MgO

Catalyst	Cu^0 Dispersion (%)	$SA_{Cu}^{N_2O}$[a] $(m^2.g^{-1})$	$d_{Cu}^{N_2O}$[b] (nm)
5wt% Cu-MgO	13.52	1.24	8
	13.19	1.59	7
	17.83	1.95	6
Average	14.85	1.59	7
Standard deviation	2.59	0.36	1

[a] $SA_{Cu}^{N_2O}$ stands for Cu crystallite size inferred from the N_2O adsorption-decomposition analysis.

[b] $d_{Cu}^{N_2O}$ stands for Cu crystallite size inferred from the N_2O adsorption-decomposition analysis.

Table 44 Repeatability of N$_2$O pulse titration analysis of 0.5wt% Cs-5wt% Cu-MgO

Catalyst	Cu^0 Dispersion (%)	SA$_{Cu}^{N_2O a}$ (m^2.g^{-1})	d$_{Cu}^{N_2O b}$ (nm)
0.5wt% Cs-5wt% Cu-MgO	13.24	1.10	8
	15.59	1.63	6
	15.36	1.76	7
Average	14.73	1.50	7
Standard deviation	1.30	0.35	1

[a] SA$_{Cu}^{N_2O}$ stands for Cu crystallite size inferred from the N$_2$O adsorption-decomposition analysis.

[b] d$_{Cu}^{N_2O}$ stands for Cu crystallite size inferred from the N$_2$O adsorption-decomposition analysis.

B.5   H$_2$ temperature programmed reduction analysis

The repeatability for hydrogen consumption, degree of reduction and reduction peak temperature gained from H$_2$ temperature programmed reduction analysis are shown in Table 45 - Table 48.

Table 45 Repeatability of H$_2$ temperature programmed reduction analysis of 5wt% Cu-MgO

Sample	Hydrogen Consumption (mmol.g^{-1} catalyst)	Degree of Reduction (%)	Reduction Peak Temperature (K)
5wt% Cu-MgO	0.27	38	479
	0.26	34	477
	0.27	34	481
	0.29	37	484
	0.26	34	484
	0.26	33	480
Average	0.27	35	481
Standard deviation	0.01	2	3

Table 46 Repeatability of H$_2$ temperature programmed reduction analysis of 0.5wt% K-5wt% Cu-MgO

Sample	Hydrogen Consumption (mmol.g^{-1} catalyst)	Degree of Reduction (%)	Reduction Peak Temperature (K)
0.5wt%K-5wt% Cu-MgO	0.26	35	479
	0.21	26	483
	0.19	25	483
	0.17	22	485
	0.22	28	474
Average	0.21	27	481
Standard deviation	0.04	5	4

Table 47 Repeatability of H$_2$ temperature programmed reduction analysis of 0.5wt% Cs-5wt% Cu-MgO

Sample	Hydrogen Consumption (mmol.g^{-1} catalyst)	Degree of Reduction (%)	Reduction Peak Temperature (K)
0.5wt%Cs-5wt% Cu-MgO	0.24	30	486
	0.20	26	484
	0.28	33	478
	0.20	26	473
Average	0.23	29	480
Standard deviation	0.04	3	6

Table 48 Repeatability of H_2 temperature programmed reduction analysis of 40wt% Cu-MgO

Sample	Hydrogen Consumption (mmol.g^{-1} catalyst)	Degree of Reduction (%)	Reduction Peak Temperature[1] (K)
40wt% Cu-MgO	5.08	88	514
	5.03	87	518
	5.19	90	518
Average	5.10	88	517
Standard deviation	0.08	2	2

[1] The reduction peak temperature is based on the non-deconvoluted H_2 temperature program reduction profile.

B.6 CO$_2$ temperature programmed desorption analysis

The repeatability for specific bascity, intrinsic bascity and distribution of basic sites gained from CO$_2$ temperature programmed desorption analysis are shown in Table 49 and Table 50.

Table 49 Repeatability of CO$_2$ temperature program desorption analysis for MgO

Catalyst	Specific Basicity (μmol CO$_2$.g^{-1})	Intrinsic Basicity (μmol CO$_2$.m^{-2})	Distribution of different basic sites on the catalyst (%)		
			Weak	Medium	Strong
MgO	432	2.7	8	15	77
	407	2.5	8	29	63
Average	417	2.6	8	22	70
Standard deviation	17	0.1	0	10	10

Table 50 Repeatability of CO$_2$ temperature program desorption analysis for 40wt%Cu-MgO

Catalyst	Specific Basicity (μmol CO$_2$.g^{-1})	Intrinsic Basicity (μmol CO$_2$.m^{-2})	Distribution of different basic sites on the catalyst (%)		
			Weak	Medium	Strong
40wt% Cu-MgO	316	4.3	9	19	72
	301	4.1	14	28	58
Average	308	4.2	12	24	65
Standard deviation	10	0.2	4	6	10

B.7 Cu^{total} surface area and Cu^{2+} surface area

In this section the standard deviations of $SA_{Cu^{total}}$ and $SA_{Cu^{2+}}$ for 0.5wt% Cs-40wt% Cu-MgO catalyst were calculated.

$SA_{Cu^{total}}$ and $SA_{Cu^{+2}}$ were calculated using the following formula:

$$SA_{Cu^{total}} = SA_{BET} \times \left(\frac{Cu^{total}}{Mg}\right)$$

$$SA_{Cu^{+2}} = SA_{Cu^{total}} - SA_{Cu^0}$$

The standard deviation calculation for $SA_{Cu^{total}}$ was shown below:

$$SA_{BET} \pm \sigma_{SA_{BET}} = 44 \pm 1 \ m^2.g^{-1}$$

$$\frac{Cu^{total}}{Mg} \pm \sigma_{\frac{Cu^{total}}{Mg}} = 0.04 \pm 0.01 \ (molar)$$

$$\left(\begin{array}{c} SA_{Cu^{total}} = 1.97 \ m^2.g^{-1} \\ \sigma_{S_{Cu^{total}}} = \sqrt{\left(\frac{\sigma_{SA_{BET}}}{SA_{BET}}\right)^2 + \left(\frac{\sigma_{\frac{Cu^{total}}{Mg}}}{\frac{Cu^{total}}{Mg}}\right)^2} \times SA_{Cu^{total}} = 0.49 \ m^2.g^{-1} \end{array} \right) \Rightarrow 1.97 \pm 0.49 \ m^2.g^{-1}$$

The standard deviation calculation for $SA_{Cu^{+2}}$ was shown below:

$$SA_{Cu^0} \pm \sigma_{SA_{Cu^0}} = 0.58 \pm 0.35 \ m^2.g^{-1}$$

$$\left(\begin{array}{c} SA_{Cu^{+2}} = 1.39 \ m^2.g^{-1} \\ \sigma_{SA_{Cu^{+2}}} = \sqrt{\sigma_{SA_{Cu^{total}}}{}^2 + \sigma_{SA_{Cu^0}}{}^2} = 0.60 \ m^2.g^{-1} \end{array} \right) \Rightarrow 1.39 \pm 0.60 \ m^2.g^{-1}$$

Appendix C   Mass Spectrometer calibration for high pressure

The Clarus 560 mass spectrometer (MS) was used for identifying the carbonaceous substances in the product stream at high pressure experiments (Table 18). The calibration factor calculation (α) is shown in equation E13 and E14.

$$\alpha_{gas}(i) = \frac{\text{mole fraction (i)}}{\text{Area(i)}} \tag{E13}$$

$$\alpha_{liquid}(i) = \frac{\text{mass fraction (i)}}{\text{Area(i)}} \tag{E14}$$

$\alpha_{gas}(i)$ is the gas calibration factor for the carbonaceous substance i in gas stream. $\alpha_{liquid}(i)$ is the liquid calibration factor for the carbonaceous substance i in liquid stream. "Area(i) " is the MS Area which was obtained from the peak integration at "retention time (i)" over the spectrum for substance i. "mole fraction (i)" is the mole fraction of substance i in the gas calibration mixture. "mass fraction (i)" is the mass fraction of substance i in the liquid calibration mixture.

Table 51 Calibration for carbonaceous substances in the gas stream using Clarus 560 MS

Substance	Retention time (min)	Mass at which the spectrum was collected	α_{gas} (Gas Calibration factor)
carbon monoxide	3.49	28	6.93E-09
carbon dioxide	4.01	44	1.00E-09
Methane	3.69	16	1.21E-08
Ethane	4.84	30	1.22E-09
Propane	7.17	29	5.08E-10
Methanol	7.63	31	4.31E-09
Ethanol	10.02	31	5.51E-09
methyl formate	9.54	60	2.76E-09
acetic acid methyl ether	12.41	43	2.79E-09
Acetone	11.70	43	2.79E-09

Table 52 Calibration for carbonaceous substances in the liquid stream using Clarus 560 MS

Substance	Retention time (min)	Mass at which the spectrum was collected	α_{liquid} (Liquid Calibration factor)
Methanol	2.50	TIC[a]	2.86E-09
Ethanol	3.01	TIC	1.38E-09
methyl formate	3.10	TIC	3.61E-09
iso-propanol	3.42	TIC	1.23E-09
1-propanol	4.29	TIC	1.21E-09
2-butanol	4.87	TIC	8.39E-10
2-methyl-1-propanol	5.41	TIC	8.39E-10
1-butanol	6.07	TIC	8.39E-10
3-pentanol	6.60	TIC	8.48E-10

[a] TIC = total ion chromatogram

Appendix D Calculation of CO conversion, product selectivity, product yield and product STY at high pressure

In this section the calculation of CO conversion, product selectivity, product yield and product STY for catalytic testing over 0.5wt% Cs-40wt% Cu-MgO at high pressure (operating conditions given in Table 18) is explained.

Mole Fraction $(i)_{gas}$= A$(i)_{gas}$ ×α$(i)_{gas}$[1]

Mass Fraction $(i)_{liquid}$=A$(i)_{liquid}$×α$(i)_{liquid}$[2]

Volume Flow$(i)_{gas}$ (cm^3 min^{-1})= Mole Fraction$(i)_{gas}$×Volume Flow$_{total-gas}$×n(i)[3]

Volume Flow$(i)_{vapor}$(cm^3 min^{-1})=$\dfrac{\text{Mass Fraction}(i)_{liquid} \times \text{Mass Flow}_{total-liq}}{\text{MW}(i)}$ ×22400 cm^3.mol^{-1} ×n(i)[4]

Volume Flow$(i)_{total}$(cm^3 min^{-1})=Volume Flow$(i)_{gas}$+Volume Flow$(i)_{vapor}$[5]

---

[1] Mole Fraction $(i)_{gas}$= mole fraction of carbonaceous substance i in the product gas stream

A$(i)_{gas}$ = area detected by the Clarus 560 MS for the carbonaceous substance i during gas analysis

α$(i)_{gas}$= calibration factor for carbonaceous substance i gained by gas calibration of the Clarus 500 GC –Clarus 560 MS

[2] Mass Fraction $(i)_{liquid}$= mass fraction of carbonaceous substance i in the product liquid stream

A$(i)_{liquid}$ = area detected by the Clarus 560 MS for the carbonaceous substance i during liquid analysis

α$(i)_{liquid}$ = calibration factor for carbonaceous substance i gained by liquid calibration of the Clarus 500 GC –Clarus 560 MS

[3] Volume Flow$(i)_{gas}$= volumetric flow rate for carbonaceous substance i in the product gas stream

Volume Flow$_{total-gas}$= total volumetric flow rate in the product gas stream measured by a bubble flow meter and a stop watch

n(i)=number of carbon atoms in the carbonaceous substance i

[4] Volume Flow$(i)_{vapor}$= volumetric flow rate for carbonaceous substance i in the vapor product stream.

Mass Flow$_{total-liq}$= total mass flow rate in the product liquid stream; was calculated by dividing the mass of the liquid collected in the condenser at the end of the experiment by the real time at which the liquid in the condenser was collected.

MW(i)= molecular weight for carbonaceous substance i

$$\text{Volume Flow}_{\text{total}}(\text{cm}^3 \text{ min}^{-1}) = \sum \text{Volume Flow}(i)_{\text{total}} \quad ^6$$

$$\text{Volume Flow}(i)_{\text{total-normalized}}(\text{cm}^3 \text{ min}^{-1}) = \frac{\text{Volume Flow}(i)_{\text{total}}}{\text{Volume Flow}_{\text{total}}} \times \text{Volume Flow}_{\text{total-calib}} \quad ^7$$

$$X_{CO} \text{ (C-atom\%)} = \frac{\text{Volume Flow}_{\text{total-calib}} - \text{Volume Flow (CO)}_{\text{total-normalized}}}{\text{Volume Flow}_{\text{total-calib}}} \times 100 \quad ^8$$

$$Y(i) \text{ (C-atom\%)} = \frac{\text{Volume Flow}(i)_{\text{total-normalized}}}{\text{Volume Flow}_{\text{total-calib}}} \times 100 \quad ^9$$

$$S(i) \text{ (C-atom\%)} = \frac{Y(i)}{X_{CO}} \times 100 \quad ^{10}$$

$$S(i)_{\text{CO2-free}} \text{ (C-atom\%)} = \frac{S(i)}{100 - S(CO_2)} \times 100 \quad ^{11}$$

$$STY(i) \text{ (g.kg}_{\text{catalyst}}^{-1}.\text{h}^{-1}) = \frac{\text{Volume Flow}(i)_{\text{total-normalized}}}{\text{catalyst weight} \times 22400 \text{ cm}^3\text{mol}^{-1}} \times (1000 \text{ mmol mol}^{-1}) \times MW(i) \quad ^{12}$$

---

[5] Volume Flow(i)$_{\text{total}}$=total volumetric flow rate (gas + vapor) of carbonaceous substance i

[6] Volume Flow$_{\text{total}}$=total volumetric flow rate (gas + vapor) of all the carbonaceous substances present in the product stream

[7] Volume Flow(i)$_{\text{total-normalized}}$= normalized total volumetric flow rate (gas + vapor) of carbonaceous substance i

Volume Flow$_{\text{total-calib}}$= total volumetric flow rate (gas + vapor) of all the carbonaceous substances present in the product stream based on the mass flow controller calibration

[8] X_{CO}= CO conversion (C-atom %)

[9] Y(i)= yield of carbonaceous substance i in the product stream

[10] S(i)= selectivity of the carbonaceous substance i in the product stream

[11] S(i)$_{\text{CO2-free}}$= CO$_2$-free selectivity of the carbonaceous substance i in the product stream

[12] STY(i)= space time yield for the carbonaceous substance i in the product stream

Appendix E   Mass Spectrometer calibration at 101 kPa

The VG ProLab quadrupole mass spectrometer (MS) was used for identifying the carbonaceous substances in the product stream at 101kPa experiments (Chapter 2 and 3). The calibration factor calculation (α) is shown in equation E15.

$$\beta(i) = \frac{\frac{y(i)}{y(He)}}{\frac{Intensity(i)}{Intensity(He)}} \tag{E15}$$

$\beta(i)$ is the calibration factor for the carbonaceous substance i. "Intensity(i)" is the MS intensity for substance i which was obtained from the MS spectrum at the mass number corresponding to substance i. "Intensity(He)" is the MS intensity for helium which was obtained from the MS spectrum at the mass number 4. And "y(i)" is the mole fraction of substance i in the calibration mixture. "y(He)" is the mole fraction of helium in the calibration mixture.

Table 53 Calibration for carbonaceous substances in the gas/vapor stream using VG ProLab quadrupole MS[a]

Substance	Mass at which the substance intensity was collected	β (Calibration factor)
carbon monoxide	28	0.3092
methanol	32	0.2050
acetic acid	60	0.4321
carbon dioxide	44	1.3391
ethanol	46	0.1776
methyl formate	60	1.5702
methane	15	1.3391

[a] Note that during calibration, the flow rate of helium were kept constant at 17 cm^3(STP).min^{-1}.

Appendix F   Calculation of net CO consumption, net methanol conversion, product selectivity and product yield at 101 kPa

In this section the calculation of net CO consumption, net CH_3OH conversion, total net conversion, product selectivity and product yield for catalytic testing over Cs or K promoted Cu-MgO and Cu-MgO at 101 kPa (Chapter 2 and Chapter 3) is explained.

$y(i) / y(He) = \beta(i) \times Intensity(i) / Intensity(He)$ [13]

$V(i) \, (cm^3 \, min^{-1}) = y(i) / y(He) \times V(He)$ [14]

$F(i) \, (mol \, min^{-1}) = P \times V(i) \times n(i) / (R \times T_{line}) = F(i) \times n(i) / (82.06 \, cm^3 \, atm \, K^{-1} \, mol^{-1}) \times T_{line})$ [15]

$F_{total} (cm^3 \, min^{-1}) = \sum F(i)_{total}$ [16]

$F(CO)_{in} = y(CO)_{in} \times F_{total}$

$F(CH_3OH)_{in} = y(CH_3OH)_{in} \times F_{total}$

---

[13] $y(i)$= mole fraction of carbonaceous substance i in the product stream

Intensity (i) = MS intensity for substance i which was obtained from the MS spectrum at the mass number corresponding to substance i

$\beta(i)$= calibration factor for carbonaceous substance i gained by carbonaceous product calibration of VG ProLab quadrupole MS

[14] $V(i)$ = volumetric flow rate for carbonaceous substance i in the product stream

[15] $F(i)$ = molar flow rate for carbonaceous substance i in the product stream

P = reaction pressure = 101 kPa (1 atm)

$n(i)$=number of carbon atoms in the carbonaceous substance i

R = gas universal constant = 82.06 cm^3 atm K^{-1} mol^{-1}

T_{line} = temperature of the stream line leaving the reactor which is controlled by a heating tape

[16] F_{total} = total molar flow rate of all the carbonaceous substances present in the product stream

X_{CO} (C-atom%)=(F(CO)$_{in}$ -F(CO) / F(CO)$_{in}$ ×100[17]

X_{CH3OH} (C-atom%)=(F(CH$_3$OH)$_{in}$ -F(CH$_3$OH)) / F(CH$_3$OH)$_{in}$ ×100[18]

X_{total} = X_{CO} + X_{CH3OH}[19]

Y(i) (C-atom%)= (F(i)/F$_{total}$)$_{reaction}$ - (F(i)/F$_{total}$)$_{blank run}$ ×100[20]

S(i) (C-atom%)=Y(i)/X$_{total}$× 100[21]

S_{total} = $\sum$ S(i)

S(i)$_{normalized}$ = S(i) / S$_{total}$ × 100[22]

---

[17] X_{CO}= net CO consumption (C-atom %).

Note that if X_{CO} < 0, then it was considered as a carbonaceous product and the corresponding yield of CO

and selectivity of CO were calculated accordingly.

[18] X_{CH3OH}= net CH$_3$OH conversion (C-atom %)

[19] X_{total} = total net conversion

[20] Y(i)= yield of carbonaceous substance i in the product stream

[21] S(i)= selectivity of the carbonaceous substance i in the product stream

[22] S(i)$_{normalized}$ = normalized selectivity of the carbonaceous substance i in the product stream

Note that S(i)$_{normalized}$ was reported as the product selectivity of the carbonaceous products in Chapter 2

and Chapter 3.

Appendix G   Repeatability for catalytic testing

G.1   Experiment repeatability at low pressure (101kPa)

Table 54 Repeatability for product distribution and catalyst activity in CH$_3$OH/CO conversion over 40wt% Cu-MgO at reaction temperature of 498K

Catalyst	Reaction temperature (K)	Net CO consumption (C-atom%)	Net CH$_3$OH conversion (C-atom%)	Total net Conversion (C-atom%)	Product Selectivity (C-atom%)			
					CO	MF	CO$_2$	C$_2$[c]
		-10.1	85.4	75.3	70.5	27.1	1.2	1.3
40wt%Cu-MgO	498	-9.8	84.6	74.9	68.3	29.3	1.5	0.9
		-9.2	84.0	74.8	66.3	31.4	1.9	0.4
Average		-9.7	84.7	75.0	68.4	29.3	1.5	0.9
Standard deviation		0.4	0.7	0.3	2.1	2.2	0.3	0.4

Reaction condition: 101kPa, feed He/CO/CH$_3$OH=0.20/0.66/0.14 molar, contact time(W/F)=12.3×10^{-3} ming(cm^3(STP))$^{-1}$, catalyst weight =0.98g, v_0=84.4 cm^3(STP)min^{-1}.[a] Total conversion=Net CO consumption+Net CH$_3$OH conversion[b] MF stands for methyl formate.[c] C$_2$ stands for ethanol and acetic acid

Table 55 Repeatability for product distribution and catalyst activity in CH₃OH/CO conversion over 0.5wt%K-40wt%Cu-MgO at reaction temperature of 498 K

Catalyst	Reaction temperature (K)	Net CO consumption (C-atom%)	Net CH₃OH conversion (C-atom%)	Total net Conversion (C-atom%)	Product Selectivity (C-atom%)			
					CO	MF[b]	CO₂	C₂[c]
0.5wt%K-40wt%Cu-MgO	498	-7.6	68.2	60.7	64.9	30.2	2.3	2.7
		-8.1	71.5	63.3	60.3	32.8	2.6	4.3
		-8.1	70.2	62.1	66.7	27.0	3.3	3.0
Average		-7.9	70.0	62.0	64.0	30.0	2.7	3.3
Standard deviation		0.3	1.6	1.3	3.3	2.9	0.5	0.8

Reaction condition: 101kPa, feed He/CO/CH₃OH=0.20/0.66/0.14 molar, contact time(W/F)=12.3×10⁻³ ming(cm³(STP))⁻¹, catalyst weight =0.98g,v₀=84.4 cm³(STP)min⁻¹. [a] Total conversion=Net CO consumption+Net CH₃OH conversion. [b] MF stands for methyl formate. [c] C₂ stands for ethanol and acetic acid.

Table 56 Repeatability for product distribution and catalyst activity in CH$_3$OH/CO conversion over 0.5wt%K-40wt%Cu-MgO at reaction temperature of 523 K

Catalyst	Reaction temperature (K)	Net CO consumption (C-atom%)	Net CH$_3$OH conversion (C-atom%)	Total net Conversion (C-atom%)	Product Selectivity (C-atom%)			
					CO	MF[b]	CO$_2$	C$_2$[c]
		-10.0	83.3	73.3	80.3	14.1	3.6	2.0
0.5wt%K-40wt%Cu-MgO	523	-9.8	78.6	68.8	77.0	17.0	2.9	3.1
		-12.7	83.4	70.8	77.3	19.4	2.0	1.2
Average		-10.8	81.8	71.0	78.2	16.9	2.9	2.1
Standard deviation		1.6	2.8	2.3	1.8	2.6	0.8	1.0

Reaction condition: 101kPa, feed He/CO/CH$_3$OH=0.20/0.66/0.14 molar, contact time(W/F)=12.3×10^{-3} ming(cm^3(STP))$^{-1}$, catalyst weight =0.98g,v$_0$=84.4 cm^3(STP)min^{-1}. [a] Total conversion=Net CO consumption+Net CH$_3$OH conversion. [b] MF stands for methyl formate. [c] C$_2$ stands for ethanol and acetic acid

Table 57 Repeatability for product distribution and catalyst activity in CH$_3$OH/CO conversion over 0.5wt%Cs-5wt%Cu-MgO at reaction temperature of 498 K

Catalyst	Reaction temperature (K)	Net CO consumption (C-atom%)	Net CH3OH conversion (C-atom%)	Total Net Conversion[a] (C-atom%)	Product Selectivity (C-atom%)			
					CO	MF[b]	CO$_2$	C$_2$[c]
		8.7	25.6	34.4	0.0	99.1	0.5	0.4
0.5wt%Cs-5wt%Cu-MgO	498	7.7	27.4	35.2	0.0	98.0	1.0	1.0
		7.0	26.0	33.0	0.0	96.8	3.0	0.2
Average		7.8	26.4	34.2	0.0	98.0	1.5	0.5
Standard deviation		0.9	1.0	1.1	0.0	1.1	1.3	0.4

Reaction condition: 101kPa, feed He/CO/CH$_3$OH=0.20/0.66/0.14 molar, contact time(W/F)=12.3×10^{-3} ming(cm^3(STP))$^{-1}$, catalyst weight =0.98g,v_0=84.4 cm^3(STP)min^{-1}. [a] Total conversion=Net CO consumption+Net CH$_3$OH conversion. [b] MF stands for methyl formate. [c] C$_2$ stands for ethanol and acetic acid

Table 58 Repeatability for product distribution and catalyst activity in CH₃OH/CO conversion over 0.5wt%Cs-5wt%Cu-MgO at reaction temperature of 523 K

Catalyst	Reaction temperature (K)	Net CO consumption (C-atom%)	Net CH3OH conversion (C-atom%)	Total Net Conversion[a] (C-atom%)	Product Selectivity (C-atom%)			
					CO	MF[b]	CO_2	C_2[c]
0.5wt%Cs-5wt%Cu-MgO	523	9.0	38.7	47.7	0.0	98.0	1.9	0.1
		10.3	36.3	46.6	0.0	99.4	0.3	0.3
		8.7	28.8	37.5	0.0	98.9	0.9	0.2
Average		9.3	34.6	43.9	0.0	98.8	1.0	0.2
Standard deviation		0.9	5.2	5.6	0.0	0.7	0.8	0.1

Reaction condition: 101kPa, feed He/CO/CH₃OH=0.20/0.66/0.14 molar, contact time(W/F)=12.3×10⁻³ ming(cm³(STP))⁻¹, catalyst weight =0.98g,v_0=84.4 cm³(STP)min⁻¹. [a] Total conversion=Net CO consumption+Net CH₃OH conversion. [b] MF stands for methyl formate. [c] C_2 stands for ethanol and acetic acid.

Table 59 Repeatability for product distribution and catalyst activity in CH$_3$OH/CO conversion over 13.5wt%Cs-5wt%Cu-MgO at reaction temperature of 498 K

Feed Mixture	Catalyst	T^d (K)	Net CO consumption (C-atom%)	Net CH$_3$OH conversion (C-atom%)	Total Net Conversion^a (C-atom%)	Product Selectivity (C-atom%)			
						CO	MF^b	CO$_2$	C$_2^c$
CH$_3$OH/H$_2$/He	13.5wt%Cs-40wt%Cu-MgO	498	0.0	5.3	5.3	81.1	14.3	1.4	3.2
			0.0	8.0	8.0	77.9	13.0	5.1	4.0
Average			0.0	6.6	6.6	79.5	13.6	3.3	3.6
Standard deviation			0.0	1.9	1.9	2.3	0.9	2.6	0.6

Reaction condition: 101kPa, feed He/CO/CH$_3$OH=0.20/0.66/0.14 molar, contact time(W/F)=12.3×10^{-3} ming(cm^3(STP))$^{-1}$, catalyst weight =0.98g,v_0=84.4 cm^3(STP)min^{-1}. ^{a} Total conversion=Net CO consumption + Net CH$_3$OH conversion. ^{b} MF stands for methyl formate. ^{c} C$_2$ stands for ethanol and acetic acid. ^{d} T stands for reaction temperature.

Table 60 Repeatability for product distribution and catalyst activity in CH$_3$OH/CO conversion over 13.5wt%Cs-5wt%Cu-MgO at reaction temperature of 498 K

Feed Mixture	Catalyst	T^d (K)	Net CO consumption (C-atom%)	Net CH$_3$OH conversion (C-atom%)	Total Net Conversion^a (C-atom%)	Product Selectivity (C-atom%)			
						CO	MF^b	CO2	C$_2^c$
CH$_3$OH/Ar/He	13.5wt%Cs-40wt%Cu-MgO	498	0.0	50.0	50.0	83.5	14.5	1.9	0.1
			0.0	46.3	46.3	80.0	15.9	3.9	0.2
Average			0.0	48.2	48.2	81.7	15.2	2.9	0.2
Standard deviation			0.0	2.6	2.6	2.4	1.0	1.4	0.1

Reaction condition: 101kPa, feed He/CO/CH$_3$OH=0.20/0.66/0.14 molar, contact time(W/F)=12.3×10^{-3} ming(cm^3(STP))$^{-1}$, catalyst weight =0.98g,v_0=84.4 cm^3(STP)min^{-1}. ^{a} Total conversion=Net CO consumption+Net CH$_3$OH conversion. ^{b} MF stands for methyl formate. ^{c} C$_2$ stands for ethanol and acetic acid. ^{d} T stands for reaction temperature.

Table 61 Repeatability for product distribution and catalyst activity in CH₃OH/CO conversion over 13.5wt%Cs-5wt%Cu-MgO at reaction temperature of 498 K

Feed Mixture	Catalyst	T^d (K)	Net CO consumption (C-atom%)	Net CH₃OH conversion (C-atom%)	Total Net Conversion[a] (C-atom%)	Product Selectivity (C-atom%)			
						CO	MF[b]	CO2	C_2[c]
CH₃OH/CO/He	13.5wt%Cs-40wt%Cu-MgO	498	-4.7	48.4	43.7	81.5	16.4	1.0	1.1
			-8.0	46.0	38.0	78.2	17.0	2.8	2.0
Average			-6.3	47.2	40.8	79.8	16.7	1.9	1.6
Standard deviation			2.3	1.7	4.0	2.3	0.4	1.2	0.6

Reaction condition: 101kPa, feed He/CO/CH₃OH=0.20/0.66/0.14 molar, contact time(W/F)=12.3×10⁻³ ming(cm³(STP))⁻¹, catalyst weight =0.98g,v_0=84.4 cm³(STP)min⁻¹.[a] Total conversion=Net CO consumption + Net CH₃OH conversion. [b] MF stands for methyl formate.. [c] C_2 stands for ethanol and acetic acid. [d] T stands for reaction temperature

G.2   Experiment repeatability at high pressure (9000 kPa)

Table 62 Repeatability for product distribution and catalyst activity in syngas conversion over 0.5 wt%Cs-5wt%Cu-MgO at reaction temperature of 573K

T^a (K)	P^b (kPa)	Residence time (sec)	Feed $CO:H_2$ (molar)	CO Conversion (C-atom %)	CO_2 Selectivity (C-atom %)	Product Selectivity (CO_2 free, C-atom%)			
						CH_3OH	$C_{2+}OH^c$	HC^d	ketones-esters^e
				18.98	20.28	78.90	7.24	9.24	4.62
573	8966	3.0	1.00	18.21	21.04	81.21	7.12	7.36	4.31
				21.27	24.39	73.99	10.86	10.34	4.81
	Average			19.49	21.90	78.03	8.41	8.98	4.58
	Standard Deviation			1.59	2.19	3.69	2.13	1.50	0.25

^{a} T stands for temperature

^{b} P stands for pressure

^{c} $C_{2+}OH$: ethanol, i-propanol, 1-propanol, 2-butanol, 2-methyl-1-propanol, 1-butanol and 3-pentanol

^{d} HC: methane, ethane and propane

^{e} ketones-esters: acetic acid methyl ester, acetone and methyl formate

Table 63 Repeatability for product distribution and catalyst activity in syngas conversion over 0.5 wt%Cs-5wt%Cu-MgO at reaction temperature of 598K

T^a	P^b	Residence time	Feed $CO:H_2$	CO Conversion	CO_2 Selectivity	Product Selectivity (CO_2 free, C-atom%)			
(K)	(kPa)	(sec)	(molar)	(C-atom %)	(C-atom %)	CH_3OH	$C_{2+}OH^c$	HC^d	ketones-esters^e
598	8966	1.3	1.50	5.85	33.35	65.27	13.64	14.48	6.61
				5.11	31.23	67.23	13.22	13.61	5.93
Average				5.48	32.29	66.25	13.43	14.04	6.27
Standard Deviation				0.52	1.50	1.39	0.29	0.61	0.48

^{a} T stands for temperature

^{b} P stands for pressure

^{c} $C_{2+}OH$: ethanol, i-propanol, 1-propanol, 2-butanol, 2-methyl-1-propanol, 1-butanol and 3-pentanol

^{d} HC: methane, ethane and propane

^{e} ketones-esters: acetic acid methyl ester, acetone and methyl formate

Appendix H   Response time (t_r) calculation in the high pressure reactors

The response time in the high pressure reactor is the time required for the gas stream of reactants to travel from the mass flow meters to the Perkin-Elmer Gas Chromatograph 550 – Mass Spectrometer 560 (Figure 30). A sample calculation for response time (experiment number 1 in Table 18) is shown below:

Reaction condition :

reaction pressure = 8966 kPa, reaction temperature: 573K, Residence time = 1.3 sec, Feed $CO:H_2$ (molar) = 1.50 and feed flow rate = 40 cm^3(STP).min^{-1}.

Calculation:

F_{feed} (feed flow rate) = 40 cm^3(STP).min^{-1}

System volume at 101 kPa (V_1) $\approx$ 170 cm^3

System volume at 8966 kPa (V_2) $\approx$ 40 cm^3

$$t_r \text{ (response time)} = \frac{V_1}{F_{feed}} + \frac{V_2}{\frac{F_{feed}}{8966\ kPa} \times 101\ kPa} = \frac{170\ cm^3}{40\ cm^3(STP).min^{-1}} + \frac{40\ cm^3}{\frac{40\ cm^3(STP).min^{-1}}{8966\ kPa} \times 101\ kPa}$$

t_r (response time) = 92 min (1:32 hr:min).

Appendix I   Development of Langmuir-Hinshelwood (LH) equations for CO/H$_2$ conversion to CH$_3$OH

Table 64 Development of Langmuir-Hinshelwood (LH) equations for CO/H$_2$ conversion to CH$_3$OH

No.[a]	Reaction step	LH equation	RDS[b]
		Reaction: CO + 2H$_2$ → CH$_3$OH	
1	H$_2$ + 2s → 2Hs	$\hat{f}_{H_2} \times \theta_V^2 = k_1 \times \theta_H^2$ $\rightarrow \theta_H = k_H \times \hat{f}_{H_2}^{0.5} \times \theta_V$ (1)	
2	CO + s → COs	$\hat{f}_{CO} \times \theta_V = k_2 \times \theta_{CO}$ $\rightarrow \theta_{CO} = k_{CO} \times \hat{f}_{CO} \times \theta_V$ (2)	
3	COs + Hs → HCOs + s	$\theta_{CO} \times \theta_H = k_3 \times \theta_{HCO} \times \theta_V$ $\xrightarrow{(1)\ and\ (2)} \theta_{HCO} = k_{HCO} \times \hat{f}_{H_2}^{0.5} \times \hat{f}_{CO} \times \theta_V$ (3)	
4	HCOs + Hs → H$_2$COs + s	$\theta_{HCO} \times \theta_H = k_4 \times \theta_{H_2CO} \times \theta_V$ $\xrightarrow{(1)\ and\ (3)} \theta_{H_2CO} = k_{H_2CO} \times \hat{f}_{H_2} \times \hat{f}_{CO} \times \theta_V$ (4)	
5	H$_2$COs + Hs → H$_3$COs + s	$r_{CH_3OH} = k_5 \times \theta_{H_2CO} \times \theta_H$ $\xrightarrow{(1)\ and\ (3)} r_{CH_3OH} = k_5 \times k_{H_1} \times k_{H_2CO} \times \hat{f}_{H_2}^{1.5} \times \hat{f}_{CO} \times \theta_V^2$ $r_{CH_3OH} = k \times \hat{f}_{H_2}^{1.5} \times \hat{f}_{CO} \times \theta_V^2$ (5)	$\sqrt{}$[c]
6	H$_3$COs + Hs → CH$_3$OHs + s	$\theta_{H_3CO} \times \theta_H = k_6 \times \theta_{CH_3OH} \times \theta_V$ $\xrightarrow{(1)\ and\ (6)} \theta_{H_3CO} = k_{H_3CO} \times \hat{f}_{CH_3OH} \times \hat{f}_{H_2}^{-0.5} \times \theta_V$	
7	CH$_3$OHs → CH$_3$OH + s	$\theta_{CH_3OH} = k_7 \times \hat{f}_{CH_3OH} \times \theta_V = k_{CH_3OH} \times \hat{f}_{CH_3OH} \times \theta_V$ (6)	
		θ_V calculation:	

$\theta_V + \theta_H + \theta_{CO} + \theta_{HCO} + \theta_{H_2CO} + \theta_{H_3CO} + \theta_{CH_3OH} = 1$

$$\theta_V = \frac{1}{1 + k_H \times \hat{f}_{H_2}^{0.5} + k_{CO} \times \hat{f}_{CO} + k_{HCO} \times \hat{f}_{H_2}^{0.5} \times \hat{f}_{CO} + k_{H_2CO} \times \hat{f}_{H_2} \times \hat{f}_{CO} + k_{H_3CO} \times \hat{f}_{CH_3OH} \times \hat{f}_{H_2}^{-0.5} + k_{CH_3OH} \times \hat{f}_{CH_3OH}}$$

[a] No. stands for step number. [b] RDS stands for rate determining step. [c] Reaction mechanism for synthesis of CH$_3$OH from CO/H$_2$ over the 0.5wt% Cs-40wt% Cu-MgO catalyst was developed based on previous proposed mechanism over Cu-metal oxide catalysts [47,57]. Furthermore the rate determinant step was chosen based on these studies.

Appendix J   Fugacity coefficient calculation

In order to calculate the fugacity coefficient ($\widehat{\Phi}$) for CO, CO_2, CH_3OH and H_2 in the product stream for all the experiments given in Table 18, Aspen plus V7.1 (23.0.4507) software with SR-POLAR property method was used. To calculate the fugacity coefficients; reaction pressure, reaction temperature and mole fraction of the products (CO, CH_3OH, CO_2, H_2 and H_2O) corresponding to each experiment were imported to the Aspen plus V7.1 (23.0.4507) software. The calculated fugacity coefficients are shown in Table 65. Note that SR-POLAR property method is based on an equation of state model by Schwarzentruber and Renon, which is an extension of the Redlich-Kwong-Soave equation of state [106-108].

Table 65 Calculated fugacity coefficient for CO, CO₂, CH₃OH and H₂ using Aspen Plus V7.1 (23.0.4507)

Experiment Number	Temperature	Pressure	τ^{a}	Feed CO:H₂	$\widehat{\Phi}$ (Fugacity Coefficient) (unit less)				
	(K)	(kPa)	(sec)	(molar)	CO	CH₃OH	CO₂	H₂	H₂O
1	558	8966	0.6	1.50	1.05	1.03	1.03	1.04	0.99
2		6207	1.3	1.00	1.03	1.02	1.02	1.02	0.99
3		8966	3.0	1.50	1.05	1.01	1.02	1.04	0.97
4		8966	4.1	0.49	1.05	0.95	1.01	1.05	0.92
5		8966	4.2	1.00	1.05	0.96	1.01	1.05	0.93
6	573	8966	0.3	1.00	1.04	1.02	1.03	1.03	0.98
7		8966	0.6	1.00	1.04	1.01	1.02	1.03	0.98
8		8966	1.3	1.00	1.04	1.00	1.02	1.03	0.97
9		8966	1.3	0.49	1.03	1.00	1.01	1.02	0.98
10		6207	1.3	0.49	1.04	0.98	1.01	1.03	0.96
11		8966	3.0	1.00	1.04	0.95	1.00	1.04	0.93
12		8966	4.2	1.00	1.04	0.95	1.00	1.04	0.93
13	598	8966	0.6	1.00	1.05	1.04	1.03	1.03	1.00
14		6207	0.6	0.49	1.03	1.03	1.03	1.02	1.00
15		8966	1.3	1.50	1.05	1.03	1.03	1.03	0.99
16		8966	4.1	0.49	1.05	0.99	1.02	1.04	0.96
17		6207	4.3	1.50	1.03	1.02	1.02	1.02	0.99

$^{a}\,\tau = \text{residence time} = \dfrac{\text{catalyst weight(g)/catalyst density (g.cm}^{-3})}{\text{feed flow rate (cm}^{3}\text{(STP).min}^{-1})}$, catalyst density ≈ 1 g.cm^{-3}.

.

Appendix K   Calculation of the fugacity for CO, CO$_2$, CH$_3$OH and H$_2$ at high pressure

The fugacity of CO and H$_2$ in the feed stream as well as the fugacity of CO, H$_2$, CH$_3$OH, CO$_2$ and H$_2$O in the product stream were calculated using the experimental results gained from the analysis of experiments 1- 17 mentioned in Table 18 and the calculated fugacity coefficient ($\widehat{\Phi}$) in Appendix J. The summary of the calculated fugacities are shown in the following tables.

Table 66 Calculated fugacity for CO. CO$_2$, CH$_3$OH and H$_2$ at 558K

Experiment Number	$t_r{}^a$ (hr:min)	Real time (hr:min) & ($\times t_r$)	Pressure (kPa)	τ^b (sec)	Feed CO:H$_2$ (molar)	Outlet Fugacity^c (kPa)					Inlet Fugacity^d (kPa)	
						$\hat{f}_{CO-out}$	$\hat{f}_{CH_3OH-out}$	$\hat{f}_{CO_2-out}$	$\hat{f}_{H_2-out}$	$\hat{f}_{H_2O-out}$	$\hat{f}_{CO-in}$	$\hat{f}_{H_2-in}$
1	0:18	1:00 (≈3×t$_r$)	8966	0.6	1.50	5127	71	13	4076	59	5210	4135
		3:00 (≈9×t$_r$)				5130	69	10	4078	59	5209	4137
		5:00 (≈16×t$_r$)				5132	69	8	4077	61	5208	4138
2	0:40	2:00 (≈3×t$_r$)	6207	1.3	1.00	3202	40	7	3105	33	3249	3138
		3:30 (≈5×t$_r$)				3202	38	7	3110	31	3247	3141
		5:00 (≈7×t$_r$)				3203	37	6	3113	30	3245	3142
3	1:31	5:00 (≈3×t$_r$)	8966	3.0	1.50	5098	249	56	3732	197	5402	3928
		6:30 (≈4×t$_r$)				5115	222	36	3774	183	5373	3957
		8:00 (≈5×t$_r$)				5124	231	29	3751	198	5384	3949
4	2:07	6:30 (≈3×t$_r$)	8966	4.1	0.49	3449	779	109	4150	694	4337	4844
		8:30 (≈4×t$_r$)					801	3441	4114	710	4354	4825
5	2:10	6:30 (≈3×t$_r$)	8966	4.2	1.00	4608	672	103	3251	586	5383	3837
		9:00 (≈4×t$_r$)				4620	677	92	3243	594	5389	3837

^{a} t_r = response time. ^{b} τ = residence time = $\dfrac{\text{catalyst weight(g)/catalyst density (g.cm}^{-3})}{\text{feed flow rate (cm}^3\text{(STP).min}^{-1})}$, catalyst density ≈ 1 g.cm^{-3}. ^{c} $\hat{f}_{i-out} = \widehat{\Phi}_i \times P_{i-out}$. Subscript i stands for component i in the prduct stream. ^{d} $\hat{f}_{CO-in} = \hat{f}_{CO-out} + \hat{f}_{CH_3OH-out} + \hat{f}_{CO_2-out}$ and $\hat{f}_{H_2-in} = \hat{f}_{H_2-out} + \hat{f}_{H_2O-out}$.

Table 67 Calculated fugacity for CO. CO_2, CH_3OH and H_2 at 573K

Experiment Number	$t_r{}^a$ (hr:min)	Real time (hr:min) & (×t_r)	Pressure (kPa)	$\tau{}^b$ (sec)	Feed CO:H_2 (molar)	Outlet Fugacity^c (kPa)					Inlet Fugacity^d (kPa)	
						$\hat{f}_{CO-out}$	$\hat{f}_{CH_3OH-out}$	$\hat{f}_{CO_2-out}$	$\hat{f}_{H_2-out}$	$\hat{f}_{H_2O-out}$	$\hat{f}_{CO-in}$	$\hat{f}_{H_2-in}$
6	0:10	0:30 (≈3×t_r)	8966	0.3	1.00	4644	23	8	4574	15	4675	4590
		1:00 (≈6×t_r)				4644	23	8	4574	15	4676	4589
		1:30 (≈9×t_r)				4644	23	8	4575	15	4675	4590
7	0:19	1:00 (≈3×t_r)	8966	0.6	1.00	4633	72	17	4481	56	4722	4537
		3:00 (≈9×t_r)				4635	71	15	4481	57	4721	4538
		5:00 (≈16×t_r)				4636	71	14	4480	58	4721	4538
8	0:40	2:00 (≈3×t_r)	8966	1.3	1.00	3609	269	23	5077	249	3901	5325
		3:30 (≈5×t_r)				3611	266	21	5084	246	3898	5329
		6:00 (≈8×t_r)				3611	274	20	5067	255	3905	5322
9	0:40	2:00 (≈3×t_r)	8966	1.3	0.49	2458	133	38	3592	104	2629	3696
		3:30 (≈5×t_r)				2460	132	36	3593	104	2628	3698
		6:00 (≈8×t_r)				2461	133	34	3588	108	2629	3696
10	0:40	2:00 (≈3×t_r)	6207	1.3	0.49	4560	288	78	4058	225	4926	4283
		3:00 (≈4×t_r)				4561	291	77	4053	228	4929	4280
		3:30 (≈5×t_r)				4563	294	76	4046	231	4932	4277
11	1:32	5:00 (≈3×t_r)	8966	3.0	1.00	4426	595	202	3385	469	5224	3854
		6:30 (≈4×t_r)				4426	579	202	3418	455	5208	3873
		8:00 (≈5×t_r)				4429	604	199	3362	480	5233	3843
12	2:10	7:00 (≈3×t_r)	8966	4.2	1.00	4017	612	586	3529	218	5215	3747

^{a} t_r = response time. ^{b} τ = residence time = $\dfrac{\text{catalyst weight(g)/catalyst density (g.cm}^{-3})}{\text{feed flow rate (cm}^3\text{(STP).min}^{-1})}$, catalyst density ≈ 1 g.cm^{-3}. ^{c} $\hat{f}_{i-out} = \widehat{\Phi}_i \times P_{i-out}$. Subscript i stands for

component i in the prduct stream. ^{d} $\hat{f}_{CO-in} = \hat{f}_{CO-out} + \hat{f}_{CH_3OH-out} + \hat{f}_{CO_2-out}$ and $\hat{f}_{H_2-in} = \hat{f}_{H_2-out} + \hat{f}_{H_2O-out}$.

Table 68 Calculated fugacity for CO. CO$_2$, CH$_3$OH and H$_2$ at 598K

Experiment Number	t_r[a] (hr:min)	Real time (hr:min) & ($\times t_r$)	Pressure (kPa)	τ[b] (sec)	Feed CO:H$_2$ (molar)	Outlet Fugacity[c] (kPa)					Inlet Fugacity[d] (kPa)	
						$\hat{f}_{CO-out}$	$\hat{f}_{CH_3OH-out}$	$\hat{f}_{CO_2-out}$	$\hat{f}_{H_2-out}$	$\hat{f}_{H_2O-out}$	$\hat{f}_{CO-in}$	$\hat{f}_{H_2-in}$
13	2:10	1:00 ($\approx$3$\times t_r$)	8966	0.6	1.00	4680	70	15	4499	57	4765	4555
		3:00 ($\approx$5$\times t_r$)				4683	69	12	4501	57	4764	4558
		5:00 ($\approx$7$\times t_r$)				4684	69	11	4499	58	4764	4557
14	0:19	1:00 ($\approx$3$\times t_r$)	6207	0.6	0.49	2529	21	13	3793	11	2563	3804
		3:00 ($\approx$9$\times t_r$)				2531	21	11	3791	13	2564	3804
		6:00 ($\approx$19$\times t_r$)				2534	20	10	3794	12	2563	3806
15	0:40	2:00 ($\approx$3$\times t_r$)	8966	1.3	1.50	5034	134	103	3958	59	5271	4018
		3:30 ($\approx$5$\times t_r$)				5048	131	88	3961	66	5267	4027
		6:00 ($\approx$8$\times t_r$)				5069	127	67	3960	77	5263	4037
16	2:07	6:30 ($\approx$3$\times t_r$)	8966	4.1	0.49	3039	645	481	4531	350	4164	4881
		8:30 ($\approx$4$\times t_r$)				3003	676	505	4482	365	4184	4847
17	2:12	7:00 ($\approx$3$\times t_r$)	6207	4.3	1.50	3333	172	181	2608	36	3686	2644
		9:00 ($\approx$4$\times t_r$)				3350	179	164	2585	55	3694	2640

[a] t_r = response time. [b] τ = residence time = $\frac{\text{catalyst weight(g)/catalyst density (g.cm}^{-3})}{\text{feed flow rate (cm}^3\text{(STP).min}^{-1})}$, catalyst density $\approx$ 1 g.cm^{-3}. [c] $\hat{f}_{i-out} = \hat{\Phi}_i \times P_{i-out}$. Subscript i stands for component i in the prduct stream. [d] $\hat{f}_{CO-in} = \hat{f}_{CO-out} + \hat{f}_{CH_3OH-out} + \hat{f}_{CO_2-out}$ and $\hat{f}_{H_2-in} = \hat{f}_{H_2-out} + \hat{f}_{H_2O-out}$.

Appendix L   Estimating the quantity of adsorbed species on 0.5wt% Cs-40wt% Cu-MgO for the Langmuir-Hinshelwood model developed in Appendix H.

In this section the quantity of adsorbed species on the surface of the 0.5wt%-40wt% Cu-MgO was estimated based on the $\hat{f}_{CO-out}$, $\hat{f}_{H_2-out}$ and $\hat{f}_{CH_3OH-out}$ at real time $=3\times t_r$ (Appendix K) and the derived surface converge $(1-\theta_V)$ in the Langmuir Hinshelwood model (given in Appendix I) and the results are summarized in Table 69. The most abundant adsorbed species based on the results in Table 69, are $\hat{f}_{CO-out}\times\hat{f}_{H_2-out}$.

Table 69 Estimation of adsorbed species on 0.5wt% Cs-40wt% Cu-MgO based on the LH model developed in Appendix H

T^a	P^b	Residence time	Feed CO:H_2	$\hat{f}_{H_2-out}^{0.5}$	$\hat{f}_{CO-out}$	$\hat{f}_{CO-out} \times \hat{f}_{H_2-out}^{0.5}$	$\hat{f}_{CO-out} \times \hat{f}_{H_2-out}$	$\hat{f}_{CH_3OH-out} \times \hat{f}_{H_2-out}^{-0.5}$	$\hat{f}_{CH_3OH-out}$
(K)	(kPa)	(sec)	(molar)	(kPa$^{0.5}$)	(kPa)	(kPa$^{1.5}$)	(kPa^2)	(kPa$^{0.5}$)	(kPa)
558	8966	0.6	1.50	64	5127	327312	20896371	1	71
	6207	1.3	1.00	56	3202	178444	9943963	1	40
	8966	3.0	1.50	61	5098	311402	19022991	4	249
	8966	4.1	0.49	64	3449	222183	14312910	12	779
	8966	4.2	1.00	57	4608	262745	14981011	12	672
573	8966	0.3	1.00	68	4644	314088	21243190	0	23
	8966	0.6	1.00	67	4633	310135	20760342	1	72
	8966	1.3	1.00	71	3609	257124	18320142	4	269
	8966	1.3	0.49	60	2458	147299	8827706	2	133
	6207	1.3	0.49	64	4560	290528	18508370	5	288
	8966	3.0	1.00	64	4560	290528	18508370	5	288
	8966	4.2	1.00	58	4426	257518	14982132	10	595
598	8966	0.6	1.00	67	4680	313905	21054494	1	70
	6207	0.6	0.49	62	2529	155774	9593217	0	21
	8966	1.3	1.50	63	5034	316716	19926592	2	134
	8966	4.1	0.49	67	3039	204546	13768783	10	645
	6207	4.3	1.50	51	3333	170230	8693551	3	172

[a] T stands for reaction temperature.

[b] P stands for reaction pressure

Appendix M   Matlab codes related to kinetic modeling

The Matlab software version 7.1.0.246(R14) was used for the parameter estimation in 4.3.2. A Nelder-Mead simplex (direct search) method was used for minimizing the objective function. The M-file corresponding to the simplex method is called "fminsearchbnd". The three M-files along with fminsearchbnd M-file were used for the parameter estimation in section 4.3.2 and the detail of the mentioned M-files are shown in section M.3, M.4 and M.5. The detail of the standard deviation calculation and P-value calculation were given in M.1and M.2.

M.1   Standard deviation calculation

The standard deviation calculation for the estimated parameters (K*) was done using the method described by Englezos et al.[109]. The calculation of the standard deviation (σ_{K_i}) is shown in equation E16.

$$\sigma_{K_i} = \sigma_\varepsilon \times \sqrt{\{|A^*|^{-1}\}_{ii}} \qquad (E16)$$

A* is calculated at K* and is gained by the product of the Jacobian matrix and the inverse of Jacobian matrix. $\sigma_\varepsilon{}^2$ is the variance and is calculated by the formula given in equation E17.

$$\sigma_\varepsilon{}^2 = \frac{\text{Objective function}(K^*)}{\text{degree of freedon}} = \frac{\text{Objective function}(K^*)}{\text{Number of depandant variable} \times \text{number of data point} - \text{number of pramaters}} \qquad (E17)$$

M.2   P-value calculation

One-way analysis of variance (ANOVA) was conducted on the calculated and experimental response variables. To perform the calculation the anoval toolbox in Matalb software was used. This toolbox returns the P-value which is an index for how far the mean value of the calculated response variable is from the mean value of the experimental response variables. The closer the P-value to 1, the closer the mean value of the calculated response variable to the mean value of the experimental response variables. The anoval toolbox was used in the Matalb M-file shown in M.3.

M.3   Main body M-file

clear all

clc

global PH2i PH2Oi PCO2i Pt PCOi PMi dt PCO0 PM0 PH20 PH2O0 iteration DATA_initial

XCOx T PCO_end PM_end PCO2_end PH2_end PH2O_end Temp Rxn_Temp

% h value for calculating standard deviation --

h=1e-10;

%Data at all Temperatures ---

DATA_end=

0.320	673.37	3.36	1.21	663.29	2.19	0.72	0.00	0.00	0.00	0.00	0.1	573
0.321	673.39	3.4	1.19	663.25	2.22	0.72	0	0	0	0	0.07	573
0.322	673.42	3.34	1.17	663.3	2.21	0.71	0	0	0	0	0.09	573
0.6	671.79	10.45	2.4	649.73	8.15	2.09	0	0	0	0.2	0.26	573
0.601	672.07	10.33	2.14	649.71	8.29	2.03	0	0	0	0.2	0.26	573
0.602	672.17	10.36	2.03	649.65	8.37	2.02	0	0	0	0.2	0.2	573
0.603	678.61	10.18	2.15	652.32	8.22	2	0	0	0	0.25	0.41	598
0.604	678.97	9.96	1.81	652.67	8.23	1.9	0	0.00	0	0.25	0.29	598
0.605	679.13	10.05	1.65	652.33	8.47	1.89	0	0	0	0.26	0.29	598
0.606	366.77	3	1.91	549.93	1.67	1.58	0	0.00	0	0	0.64	598
0.607	367.04	3.09	1.66	549.76	1.87	1.49	0	0	0	0	0.52	598
0.608	367.37	2.88	1.41	550.06	1.81	1.33	0	0	0	0	0.41	598
0.609	743.40	10.23	1.84	591.00	8.51	1.88	0.00	0.00	0.00	0.42	0.28	558

```
0.61  743.82 10.01  1.41  591.29 8.61  1.77  0  0  0  0.42  0.16  558

0.611 744.09 9.96   1.14  591.14 8.81  1.72  0  0  0  0.42  0.16  558

 1.29 523.27 39.02  3.3   736.11 36.08 8.27  0  0  0  0.52  1.19  573

1.291 523.61 38.56  3.1   737.11 35.64 8.13  0  0  0  0.52  1.02  573

1.292 523.53 39.75  2.91  734.72 36.97 8.31  0  0  0  0.54  0.98  573

1.293 356.39 19.29  5.48  520.79 15.15 7.64  0  0  0  0.73  1.34  573

1.294 356.71 19.11  5.21  521.01 15.14 7.5   0  0  0  0.72  1.26  573

1.295 356.88 19.34  5     520.23 15.65 7.51  0  0  0  0.74  1.32  573

 1.3  464.31 5.86   0.98  450.28 4.75  1.48  0  0  0  0     0     558

1.301 464.34 5.51   0.95  450.96 4.44  1.4   0  0  0  0     0     558

1.302 464.4  5.3    0.89  451.33 4.29  1.34  0  0  0  0     0     558

 1.31 729.92 19.44  14.91 573.97 8.61  5.84  0  0  0  1.33  3.92  598

1.311 732.03 18.97  12.73 574.3  9.59  5.39  0  0  0  1.33  3.2   598

1.312 734.97 18.44  9.73  574.21 11.17 4.8   0  0  0  1.38  2.34  598

 2.95 739.15 36.11  8.06  541.11 27.87 6.24  0  0  0  0     0.76  558

2.951 741.68 32.19  5.28  547.22 26.59 6.11  0  0  0  0     0.87  558

2.952 742.94 33.5   4.18  543.89 28.65 5.3   0  0  0  0     0.62  558];
```

end

%   X-CO(cm3/min) (CO conversion experimental)--

XCOx=DATA_end (:,7);

%PCO(psi) at the end of the reactor bed---

 PCO_end=DATA_end(:,2);

%PMethanol(psi) at the end of the reactor bed---

PM_end=DATA_end(:,3);

%PCO2(psi) at the end of the reactor bed--

PCO2_end=DATA_end(:,4);

%PH2(psi) at the end of the reactor bed--

PH2_end=DATA_end(:,5);

%PH2O(psi) at the end of the reactor bed--

PH2O_end=DATA_end(:,6);

%PHA(psi) at the end of the reactor bed--

PHA_end=DATA_end(:,11);

%PHC(psi) at the end of the reactor bed--

PHC_end=DATA_end(:,12);

%Reaction Temperature--

Rxn_Temp =DATA_end(:,13);

% total reaction pressure input--

Pt=   PCO_end   +   PM_end + PH2_end   +   PH2O_end   +   PCO2_end;   %total

pressure=p(CO)+P(CH3OH)+P(H2)+P(H2O)+P(CO2) (psi)

%PCO(psi) at the beginning of the reactor bed (PCO0)---

PCO0= PCO_end + PM_end + PCO2_end;

%PCO(psi) which changes during numerical integration(PCOi)------------------------------

PCOi= PCO0;

%Pmethanol(psi) at the beginning of the reactor bed (PM0)--------------------------------

PM0= DATA_end(:,8);

%Pmethanol(psi) which changes during numerical integration(PMi)------------------------

PMi = PM0;

%PH2O(psi) at the beginning of the reactor bed (PH2O0)--------------------------------------

PH2O0= DATA_end(:,10);

%PH2O(psi) which changes during numerical integration(PH2Oi)--------------------------

PH2Oi = PH2O0

%PCO2(psi) at the beginning of the reactor bed (PCO20)--------------------------------------

 PCO20= DATA_end(:,9);

%PH2(psi) at the beginning of the reactor bed (PH20)--

 PH20 = Pt-PCO0;

%PH2(psi) which changes during numerical integration--

 PH2i = PH20

%Initial partial pressure conditions for ODE to be integrated numerically

DATA_initial=[PM0];

%Residence time (T) or (t) which is the range of numerical integration---------------------

T = [0 DATA_end(:,1)'];

t = T;

% The upper and lower limit for each parameters--

lb=[0   1E4   0   -8E4];   % lower band for k for 285C

ub=[1E-2 8E4   1E-2 -1E3];   % Upper band for k for 285C

% inital guess for parameters--

k0=[3.05E-10   1E4   3.54E-4   -9.63E3];

% calculating the sum of residuals (S) and estimating the parameters by Simplex method

```
options=optimset('display',  'iter','LargeScale',  'off','MaxIter',  1000,  'MaxFunEvals',  3000,
'TolFun', 10-6, 'TolX', 10^-6);   % default Tol X = 1E-4

[k,S] = fminsearchbnd(@OBJECTIVE170C4JUN10, k0,lb,ub, options);

tspan=T;

[row,column] = size(DATA_initial);

[k0_row,k0_column] = size(k0);

YM = zeros(row,column);

Y1 = zeros(row,column);

for i=1:row

[t,Y1]=ode45('ODE170C4JUN10',tspan,DATA_initial(i,:),[],k,i);

YM(i,:)=Y1(i+1,:);

end
```

%Methanol calculated partial pressure leaving the reactor----------------------------------

```
PM_end_calc= real(abs(YM(:,1)))';
```

%CO calculated partial pressure leaving the reactor--

```
PCO_end_calc= PCO0' - PM_end_calc;
```

%Start calculating pressure error--

```
 P_error=zeros(row,1);

for i=1:row

P_error(i) = PCO_end_calc(i) + PM_end_calc(i);

P_error(i) = PCO0(i) - P_error(i);

end;
```

%calculating CO conversion--

```matlab
[Xrow Xcolumn]=size(XCOx);

XCO=zeros(Xrow,Xcolumn);

for i=1:Xrow

XCO(i,1)=(PM_end_calc(1,i))/(PCO_end_calc(1,i)+PM_end_calc(1,i))*100;

end;
```

%Calculating sum of resdiual for each experiment separately in the main file-------------

```matlab
%note we have this part in the Objective function as well

%SS is different from S. S is the sum of S(i)s.

SS=zeros(Xrow,Xcolumn);

for i=1:Xrow

SS(i)=1*((PM_end_calc(i)-PM_end(i))).^2;

end;
```

C%alculating P-value for XCO, PCH3OH and PCO2 for all experiments-----------------

```matlab
PCOxc  = zeros(Xrow,Xcolumn+1);     %PCO experimental in 1st column and XCO model
```
calculated in 2nd column

```matlab
PMxc   = zeros(Xrow,Xcolumn+1);     %PCH3OH experimental in 1st column and PCH3OH
```
model calculated in 2nd column

```matlab
for i=1:Xrow

PCOxc (i,1) = PCO_end(i);

PCOxc (i,2) = PCO_end_calc(i);

PMxc (i,1) = PM_end(i);

PMxc (i,2) = PM_end_calc(i);

end;
```

```matlab
[P_value_CO,   table_CO,  stat_CO] = anova1(PCOxc);

[P_value_CH3OH, table_M,   stat_M ] = anova1(PMxc);
```

%calculating standard deviation --

```matlab
 y1r=zeros(row,column);

for i=1:row

  [t,Y1]  = ode45('ODE170C4JUN10',tspan,DATA_initial(i,:),[],[k(1)+h k(2) k(3) k(4)],i);

  y1r(i,:)= Y1(i+1,:);

end

 y2r=zeros(row,column);

for i=1:row

  [t,Y1]=ode45('ODE170C4JUN10',tspan,DATA_initial(i,:),[],[k(1) k(2)+h k(3) k(4)],i);

  y2r(i,:)=Y1(i+1,:);

end

 y3r=zeros(row,column);

for i=1:row

  [t,Y1]=ode45('ODE170C4JUN10',tspan,DATA_initial(i,:),[],[k(1) k(2) k(3)+h k(4)],i);

  y3r(i,:)=Y1(i+1,:);

end

 y4r=zeros(row,column);

for i=1:row

  [t,Y1]=ode45('ODE170C4JUN10',tspan,DATA_initial(i,:),[],[k(1) k(2) k(3) k(4)+h],i);

  y4r(i,:)=Y1(i+1,:);

end
```

```
y1l=zeros(row,column);

for i=1:row

 [t,Y1]=ode45('ODE170C4JUN10',tspan,DATA_initial(i,:),[],[k(1) k(2) k(3) k(4)],i);

 y1l(i,:)=Y1(i+1,:);

end

 df1dk1=[(y1r(:,1)-y1l(:,1))/h];

df1dk2=[(y2r(:,1)-y1l(:,1))/h];

df1dk3=[(y3r(:,1)-y1l(:,1))/h];

df1dk4=[(y4r(:,1)-y1l(:,1))/h];

Jac1=[df1dk1 df1dk2 df1dk3 df1dk4];
```

% degree of freedom = No of dependent variables*No of data points - No of parameters

```
        DF       =    (column+1)      *     row       -    k0_column;

 SE=sqrt(S/DF);

 Astar=Jac1'*Jac1;

Astarinv=inv(Astar);

std_error=SE*sqrt(diag(Astarinv));

 alpha=0.05;

tval=tinv(1-alpha,DF);

m=length(PM_end);

 pin=k0(:);

n=length(pin);

 wt=ones(length(PM_end),1);

wt=wt(:);
```

```matlab
 vernum= sscanf(version,'%f');

 if vernum(1) >= 4,

  Q=sparse(1:m,1:m,(0*wt+1)./(wt.^2));  % save memory

  Qinv=inv(Q);

else

  Qinv=diag(wt.*wt);

  Q=diag((0*wt+1)./(wt.^2));

end;

 jtgjinv=inv(Jac1'*Qinv*Jac1);

 resid=PM_end-PM_end_calc';                          %un-weighted residuals

covr=resid'*Qinv*resid*Q/(m-n);           %covariance of residuals

Vy=1/(1-n/m)*covr;  % Eq. 7-13-22, Bard        %covariance of the data

% calculation of the covariance matrix for the estimated parameters-----------------------

covp=jtgjinv*Jac1'*Qinv*Vy*Qinv*Jac1*jtgjinv;

disp ('Covariance of estimated parameters')

disp (covp)

% calculation of the correlation matrix for the estimated parameters-----------------------

 d=sqrt(abs(diag(covp)));

corp=covp./(d*d');   %corp= correlation matrix for parameters

disp(' Correlation matrix of parameters estimated')

disp(corp)

% display final results----------------------------------------------------------------------------

disp('----------------------------------------------------------------------------------------------------')
```

```
disp('k value(+-)standard deviation          Reaction T (C)        Sum of residuals        P
value for P(CH3OH)')

disp('----------------------------------------------------------------------------------------------------')

fprintf('%.2E(+-)%.2E                %.0f                %.0f                %.2f\n', k(1),
std_error(1),Temp, S, P_value_CH3OH);

fprintf('%.2E(+-)%.2E                %.0f                %.0f                %.2f\n', k(2),
std_error(2),Temp, S, P_value_CH3OH);

fprintf('%.2E(+-)%.2E                %.0f                %.0f                %.2f\n', k(3),
std_error(3),Temp, S, P_value_CH3OH);

fprintf('%.2E(+-)%.2E                %.0f                %.0f                %.2f\n', k(4),
std_error(4),Temp, S, P_value_CH3OH);

disp('----------------------------------------------------------------------------------------------------')
```

%   figure(1)

```
  subplot(3,4,1),plot(PCO_end,PCO_end_calc,'d'), hold, line ([300,800], [300,800]);

title('(P(CO) experimental vs P(CO) calculated)')

xlabel('Experimental Partial Pressure, psi')

ylabel('Calculated Partial Pressure, psi')
```

 % figure(2)

```
 subplot(3,4,2), plot(PM_end,PM_end_calc,'d'), hold, line ([0,40], [0,40]);

title('(P(CH3OH) experimental vs P(CH3OH) calculated)')

xlabel('Experimental Partial Pressure, psi')

ylabel('Calculated Partial Pressure, psi')
```

 % figure(4)

```matlab
subplot(3,4,4), plot(XCOx,XCO,'o'), hold, line ([0,40], [0,40]);

title('(X(CO) experimental vs X(CO) calculated)')

xlabel('Experimental CO conversion, %')

ylabel('Calculated CO conversion, %')

   % figure(5)

subplot(3,4,5), plot(XCOx,SS,'o')

title('(X(CO) experimental vs sum of residual)')

xlabel('Experimental CO conversion, %')

ylabel('sum of residual')

   % figure(6)

subplot(3,4,6), plot(PCO_end,SS,'o')

title('(P(CO) experimental vs sum of residual)')

xlabel('Experimental Partial Pressure, psi')

ylabel('sum of residual')

   % figure(7)

subplot(3,4,7), plot(PM_end,SS,'o')

title('(P(CH3OH) experimental vs sum of residual)')

xlabel('Experimental Partial Pressure, psi')

ylabel('sum of residual')

   % figure(8)

subplot(3,4,8), plot(PCO2_end,SS,'o')

title('(P(CO2) experimental vs sum of residual)')

xlabel('Experimental Partial Pressure, psi')
```

```matlab
ylabel('sum of residual')

  % figure(9)

subplot(3,4,9), plot(PH2O_end,SS,'o')

title('(P(H2O) experimental vs sum of residual)')

xlabel('Experimental Partial Pressure, psi')

ylabel('sum of residual')

  % figure(10)

subplot(3,4,10), plot(PHA_end,SS,'o')

title('(P(C1+OH) experimental vs sum of residual)')

xlabel('Experimental Partial Pressure, psi')

ylabel('sum of residual')

  % figure(11)

subplot(3,4,11), plot(PHC_end,SS,'o')

title('(P(Hydrocarbon) experimental vs sum of residual)')

xlabel('Experimental Partial Pressure, psi')

ylabel('sum of residual')

%calc_result = [PCO_end_calc(1,:)'  PM_end_calc(1,:)' XCO];

disp('-------------------------------------------------------------------------------------------------------
------------------------------------------------------------------------------------------------')

fprintf('Reaction Temeprature ( C ) = %.0f\n', Temp);

disp('-------------------------------------------------------------------------------------------------------
------------------------------------------------------------------------------------------------')
```

222

```
disp(' PH2O_exp(t)        PCO2_exp(t)        PCO_calc(t)        PCO_exp(t)        PM_calc(t)
PM_exp(t)        XCO-calc        XCO-exp        Sum of Residual        PHA_exp
PHC_exp')
disp('  (psi)            (psi)            (psi)            (psi)            (psi)            (psi)            (%)
(%)        (PM_clac(t)-PM_exp(t))^2    (psi)        (psi)')
disp('-----------------------------------------------------------------------------------------------------
-------------------------------------------------------------------------------------------')
for i = 1:m
fprintf('    %6.2f            %6.2f            %6.2f            %6.2f            %6.2f            %6.2f
%6.2f            %6.2f                    %6.2f            %6.2f            %6.2f\n',
PH2O_end(i),PCO2_end(i),PCO_end_calc(i),PCO_end(i),PM_end_calc(i),PM_end(i),XCO(i
),XCOx(i),SS(i),PHA_end(i),PHC_end(i)) % %f=non scientific veiw, %E scientific view
end
disp('-----------------------------------------------------------------------------------------------------
-------------------------------------------------------------------------------------------')
fprintf('
Sum of residual= %6.2f\n', S);
```

M.4 Objective function M-file

```
function OBJ=OBJECTIVE170C4JUN10(x,T)

%global PCO2i PH2i PH2Oi Pt PCOi PMi PCO0 PM0 PH20 PH2O0 dt iteration
DATA_initial XCOx

global PCO2i PH2i PH2Oi Pt PCOi PMi PCO0 PM0 PH20 PH2O0 dt iteration DATA_initial
XCOx T PCO_end PM_end PCO2_end PH2_end PH2O_end Rxn_Temp

%---------------------------------------------------------------------------------------------

[row,column]=size(DATA_initial);

Y=zeros(row,column);

Y1=zeros(row,column);

for i=1:row

[t,Y1]=ode45('ODE170C4JUN10',T,PM0(i,:),[],x,i);

end

% Methanol fugacity calculation--------------------------------------------------------------

PM_end_calc  = real(abs(Y(:,1)));

%Objective  function calculation------------------------------------------------------------

OBJ=sum((1*(PM_end_calc-PM_end)).^2);

% CO fugacity calculation (not used for following objective function!)------------------------

PCO_end_calc = PCO0-PM_end_calc;

%calculating the CO conversion(not used for following objective function!)-------------------

[Xrow Xcolumn]=size(XCOx);

XCO=zeros(Xrow,Xcolumn);
```

```
for i=1:Xrow

XCO(i,1)=(PM_end_calc(i,1))/(PCO_end_calc(i,1)+PM_end_calc(i,1))*100;

end;
```

M.5 Ordinary differential equation M-file

```
function dy = ODE170C4JUN10(t,y,flag,p,i)

 global PCO2i PH2i PH2Oi Pt PCOi PMi PCO0 PM0 PH20 PH2O0 dt Temp Rxn_Temp
```

% reaction 1 = CO + 2H2 → CH3OH

%p is the matrix consisted of k values (unknown parameters for reaction 1)---------------

```
k1=p(1);

k2=p(2);

k3=p(3);

k4=p(4);
```

%Equilibrium constant value for reaction 1--

```
if    Rxn_Temp(i) == 558

keq1=5.18*10^-4;%equilibrium constant for r(1) at 285C

elseif Rxn_Temp(i) == 573

keq1=2.96*10^-4; %equilibrium constant for r(1) at 300C

elseif Rxn_Temp(i) == 598

keq1=1.23*10^-4; %equilibrium constant for r(1) at 325C

end
```

% Add reversible term to reaction 1--

%If reaction 1 is reversible (r = 1). If reaction are not reversible(r=0).

```
c1 = 1;

if c1 == 1

f1=1-((14.7^2)*y(1)/(keq1*PCOi(i)*(PH2i(i)^2)));
```

else

f1=1;

end

% LH rate for reaction 1--

r=zeros(1,1);

r(1)=real(((k1*exp(-k2/(8.314*Rxn_Temp(i)))*(PH2i(i)^1.5)*(PCOi(i)))/(1+(k3*exp(-

k4/(8.314*Rxn_Temp(i)))*PCOi(i)))^2*f1));

%defining detla t (dt) at each numerical integration step--

dt = t-dt;

%finding PH2 at each numerical integration step--

PH2i(i)=PH20(i)-2*(y(1)-PM0(i));

%finding PCO at each numerical integration step--

PCOi(i)=PCO0(i)-(y(1)-PM0(i));

%modifying the detla t (dt) at each numerical integration step--------------------------------

dt=t;

%finding Ptotal at each numerical integration step--

Pt_calc=real(PH2i(i)+PCOi(i)+y(1));

%Ordinary differential equation based on reaction 1 LH model-----------------------------

Rg=1.205E-3;   %universal gas constant (psi.m3.K-1.mol-1)

Tstp=293;   %temperature at standard condition (K)

density=1E6;   %catalyst density (g.m-3)

dy(1)=Rg*Tstp*density*r(1);   %dp(Methanol)/dt(psi.sec-1)

Appendix N   Ensuring plug flow condition in the laboratory reactor

To ensure plug flow operation in laboratory reactor three criteria should be stratified. To investigate theses criteria, following steps were followed. Note that the nomenclature for all the used parameters in this section is given in Table 70.

- Viscosity and density of the syngas at reaction condition was calculated using Aspen plus software.

- Superficial fluid velocity was calculated suing the following formula:

$$V = \frac{F_T}{A} \tag{E18}$$

- Reynolds number based on catalyst diameter was calculated using the following formula:

$$Re_p = \frac{\rho d_{catalyst} V}{\mu} \tag{E19}$$

- Syngas Peclet number was calculated using the experimental equation for gas phase operation as shown in the following equation:

$$Pe = 0.087 Re_p^{0.23} \left(\frac{L}{d_{catalyst}}\right) \tag{E20}$$

- First criterion for investigating plug flow condition was calculated using the following formula:

$$Pe > Pe_{min} \text{ in which } Pe_{min} = 8 \, n \, \ln(\frac{1}{1-X_{CO}}) \tag{E21}$$

- Second criterion for investigating plug flow condition was calculated using the following formula:

$$\frac{L}{d_{catalyst}} > (\frac{L}{d_{catalyst}})_{min} \text{ in which } (\frac{L}{d_{catalyst}})_{min} = 92 Re^{-0.23} \ln\left(\frac{1}{1-X_{CO}}\right) \tag{E22}$$

- Third criterion for investigating plug flow condition was calculated using the following formula:

$$\frac{d_{tube}}{d_{catalyst}} > 10 \tag{E23}$$

The summary of plug flow calculation was shown in Table 70. Based on the calculated results the three criteria are met.

Table 70 Plug flow condition calculation for experiment number 6 (Table 18)

Parameter name	Parameter definition	Value	Unit
d_{tube}	inner diameter of the reactor	0.005	m
μ	fluid density (calculated by Aspen Plus)	27340.0	$g.m^{-3}$
F_T	total Volumetric flow rate at reaction pressure	4.28	cm^3min^{-1}
A	reactor Cross sectional area	1.96E-05	m^2
V	linear flow velocity	3.63E-03	ms^{-1}
$d_{catalyst}$	catalyst diameter	2.76E-04	m
ρ	fluid viscosity (calculated by Aspen Plus)	2.65E-02	$gm^{-1}s^{-1}$
Re_p	Rynolds number based on particle diameter	1.03	-
L	the length of the reactor bed	0.10	m
n	methanol reaction order	1.00	-
Pe	Syngas Peclet number based on particle diameter	30.81	-
Pe_{min}	Minimum Peclet number allowed to ensure plug flow condition	0.06	-
X_{CO}	CO conversion measured in the catalyst testing	0.01	-
$(L/ d_{catalyst})_{min}$	Minimum ratio allowed to ensure plug flow condition	0.66	-
$L/ d_{catalyst}$		351	-
$d_{tube}/d_{catalyst}$		18	-

Appendix O   Ensuring no internal mass transfer limitation

To make sure the oxygenate synthesis reactions were not controlled by the syngas internal mass transfer rate (mass transfer rate of syngas from catalyst surface into the catalyst pores), the following steps were followed. Note that the nomenclature for all the used parameters in this section is given in Table 71.

- Make the following assumption:

  1. Since methanol was the dominant product, therefore, the rate of methanol formation from syngas was used for the present calculation

  2. The reaction was assumed differential and 1st order to simplify the internal mass transfer calculations

  3. The catalyst particles were assumed to be spherical.

- Effective Knudson diffusivity was calculated using the following formulas:

$$D_K = 48.5 d_{pore} \left(\frac{T}{M_{syngas}}\right)^{0.5} \tag{E24}$$

$$D_{K-effective} = \frac{D_K \varepsilon \sigma}{\tau} \tag{E25}$$

- Effective binary CO/H_2 diffusivity was calculated using the following formulas:

$$D_{CO/H_2} = \frac{0.001858 \times 10^{-4} T^{3/4} \sqrt{\frac{M(CO)+M(H2)}{M(CO) \times M(H2)}}}{P \sigma_{CO/H2} \Omega} \tag{E26}$$

$$D_{CO/H_2-effective} = \frac{D_{CO/H2} \varepsilon \sigma}{\tau} \tag{E27}$$

- Effective diffusivity was calculated using the following formula:

$$D_{effective} = \left(\frac{1}{D_{CO/H2-effective}} + \frac{1}{D_{K-effective}}\right)^{-1} \tag{E28}$$

- Thiele modulus was calculated using the following formaula:

$$\varphi = \sqrt{\frac{r_{CH3OH}S_{BET}\rho_p r_p^2}{D_{effective}C_{CO-s}}} \qquad \text{(E29)}$$

- Internal effectiveness factor was calculated using the following formaula:

$$\eta = \frac{3}{\varphi}(\varphi\coth(\varphi) - 1) \qquad \text{in which } \eta \approx 1 \qquad \text{(E30)}$$

The summary of internal mass transfer calculation was shown in Table 71. Based on the calculated results, $\eta = 1$, which indicated that methanol reaction is not diffusion limited and is surface reaction limited.

Table 71 Internal mass transfer calculation for experiment number 6 (Table 18)

Parameter name	Parameter definition	Value	Unit
SA_{BET}	Catalyst BET surface area	44	$m^2.g^{-1}$
T	reaction temperature	573	K
P	reaction pressure	88.77	atm
dpore	catalyst pore diameter	2.08E-08	m
M(CO)	CO molecular weight	28	$g.mol^{-1}$
$M(H_2)$	H_2 molecular weight	2	$g.mol^{-1}$
M_{syngas}	Syngas molecular weight	15	$g.mol^{-1}$
τ	Tortosity	3	-
ε	catalyst porosity	0.4	-
σ	constriction factor	0.8	-
ρ_p	particle density	1.00E+06	$g.m^{-3}$
r_p	catalyst particle radius	1.34E-04	m
Ω	collision integral	0.78	-
σ_{H2-CO}	force constant of Lennard Jones potential function	3.26	
r_{CH3OH}	rate of methanol formation	9.52E-09	$mol.s^{-1}.m^{-2}$
C_{CO-s}	CO inlet concentration at catalyst surface	939.45	$mol.m^{-3}$
D_K	Knudson diffusivity	6.24E-06	$m^2.s^{-2}$
$D_{K-effective}$	effective Knudson diffusivity	6.65E-07	$m^2.s^{-2}$
$D_{CO/H2}$	binary diffusivity of CO-H_2	5.06E-06	$m^2.s^{-2}$
$D_{CO/H2-effective}$	effective binary diffusivity of CO-H_2	5.40E-07	$m^2.s^{-2}$
$D_{effective}$	combined bulk and Knudson diffusivity	2.98E-07	$m^2.s^{-2}$
φ	Thiele modulus	0.01	-
η	internal effectiveness factor	1.00	-

Appendix P   Ensuring no external mass transfer limitation

To make sure the oxygenate synthesis reactions were not controlled by the syngas external mass transfer rate (mass transfer rate of syngas from bulk fluid into the catalyst pores), the following steps were followed. Note that the nomenclature for all the used parameters in this section is given in Table 72.

- Modified Reynolds number based on particle diameter was calculated using the following formula:

$$Re_{p-modifed} = \frac{Re_p}{1-\varepsilon} \quad (Re_p \text{ was calculated in Appendix N}) \tag{E31}$$

- Schmidt number was calculated using the following formula:

$$Sc = \frac{\mu}{\rho D_{effective}} \tag{E32}$$

- Modified Sherwood number was calculated using the following formulas:

$$Sh = Re_{p-modifed}^{1/2} Sc^{1/3} \tag{E33}$$

$$Sh_{modified} = \frac{Sh(1-\varepsilon)}{\varepsilon} \tag{E34}$$

- Syngas mass transfer coefficient was calculated using the following formula:

$$k_c = \frac{Sh_{modified} D_{effective}}{d_p} \tag{E35}$$

- The Mears criterion was calculated using the following formula:

$$\theta = \frac{-r_{CO}\rho_{catalyst} r_{catalyst} n}{k_c C_{CO0}} \text{ in which } \theta < 0.15 \tag{E36}$$

The summary of external mass transfer calculation was shown in Table 72. Based on the calculated results, $\theta < 0.15$, which indicated that the syngas mass transfer from the bulk gas phase to the catalyst surface can be neglected.

Table 72 External mass transfer calculation for experiment number 6 (Table 18)

Parameter	Parameter definition	Value	Unit
Re_p	Rynolds number based on particle diameter (calculated in Appendix N)	1.03	-
ε	catalyst porosity	0.40	-
$Re_{p\text{-modified}}$	modified Reynolds number	1.72E+00	-
$D_{effective}$	combined bulk and Knudson diffusivity	2.98E-07	$m^2.s^{-1}$
Sc	Schmidt number	3.25E+00	-
Sh	Sherwood number	1.94	-
$Sh_{modified}$	modified Sherwood number	2.92	-
k_c	syngas mass transfer coefficient	3.15E-03	$m.s^{-1}$
r_{CO}	rate of CO consumption per catalyst weight	-4.19E-07	$mol.s^{-1}.g^{-1}$
$C_{CO\text{-}s}$	CO concentration at the catalyst surface	939.45	$mol.m^{-3}$
$r_{catalyst}$	radius of catalyst particle	1.38E-04	m
$\rho_{catalyst}$	catalyst density	1.00E-06	$g.m^{-3}$
n	reaction order	1.00	-
θ	Mears criterion	1.95E-17	-

Appendix Q   Ensuring isothermal reaction condition

To make sure that the reactor is running isothermally, the following steps were followed. Note that the nomenclature for all the used parameters in this section is given in Table 73.

- Modified Reynolds number ($Re_{p-modifed}$)was calculated (calculation was shown in Appendix P)

- Thermal diffusivity was calculated using the the following formula:

$$D_{thermal} = \frac{kthermal}{\rho Cp} \qquad (E37)$$

Note $k_{thermal}$, ρ and C_p were calculated using Asepn Plus software.

- Syngas Prantel number was calculated using the following formula:

$$Pr = \frac{v}{D_{thermal}} \qquad (E38)$$

- Syngas Nusselt number was calculated using the following empirical equation:

$$Nu = \frac{1-\epsilon}{\epsilon}\left(0.5Re_{p-modifed}^{\frac{1}{2}} + 0.2Re_{p-modifed}^{\frac{3}{2}}\right)Pr^{1/3} \qquad (E39)$$

- Syngas heat transfer coefficient was calculated using the following formula:

$$h = \frac{K_{thermal}Nu}{d_{catalyst}} \qquad (E40)$$

- Since methanol was the dominant oxygenate which was obtained from syngas reaction, therefore, heat of reaction for methanol synthesis from syngas (ΔH_{CH_3OH}) was calculated using Aspen Plus software.

- Methanol activation energy (E_{CH_3OH}) was obtained from LH_2 parameter estimation (gained from section 4.3.2.5)

- The inter-phase isothermal criterion (β_1) was calculated using the following formula:

$$\beta_1 = \frac{-\Delta H_{CH_3OH}\,(-r_{CO})\rho_{catalyst}r_{catalyst}E_{CH_3OH}}{hT^2R_g} \text{ in which } \beta_1 < 0.15 \tag{E41}$$

- The inter-reactor isothermal criterion (β_2) was calculated using the following formula:

$$\beta_2 = \frac{-\Delta H_{CH_3OH}\,(-r'_{CO})(r_{catalyst})^2E_{CH_3OH}}{k_{thermal}T_{wall}^2R_g} \text{ in which } \beta_2 < 0.20 \tag{E42}$$

The summary of isothermal criterion calculation was shown in Table 73. Based on the calculated results, $\beta_2 < 0.15$ and $\beta_2 < 0.20$, which indicated that the isothermal assumption in the plug flow reactor is valid.

Table 73 Isothermal criterion calculation for experiment number 6 (Table 18)

Parameter	Parameter definition	Value	Unit
$Re_{p\text{-modified}}$	modified Reynolds number	1.72E+00	-
$k_{thermal}$	syngas thermal conductivity	1.35E-01	$J.m^{-1}.K^{-1}.s^{-1}$
ρ	syngas density	27340.00	$g.m^{-3}$
C_p	syngas heat capacity	2011.744	$J.kg^{-1}.K^{-1}$
$D_{thermal}$	syngas thermal diffusivity	2.46E-06	$m^2.s^{-1}$
T	reaction temperature	573	K
T_{wall}	reactor wall temperature	553	K
μ	syngas viscosity	2.65E-02	$g.m^{-1}.s^{-1}$
ν	syngas kinematic viscosity	9.69E-07	$m^2.s^{-1}$
Pr	syngas Prantel number	0.39	-
ε	catalyst porosity	0.40	-
Nu	Syngas Nusselt number	1.04	-
dcatalyst	Diameter of catalyst particle	0.000276	m
h	Syngas heat transfer coefficient	508.75	$J.m^{-2}.s^{-1}.K^{-1}$
E_{CH_3OH}	CH_3OH activation energy	8.64E+04	$J.mol^{-1}$
R_g	gas universal constant	8.314	$J.mol^{-1}.K^{-1}$
$r_{catalyst}$	radius of catalyst particle	1.38E-04	m
$r_{reactor}$	reactor radius	0.0025	m
r_{CO}	rate of CO consumption per catalyst weight	-4.19E-07	$mol.s^{-1}.g^{-1}$
r'_{CO}	rate of CO consumption per reactor volume	-4.19E-01	$mol.s^{-1}.m^{-3}$
$\rho_{catalyst}$	catalyst density	1.00E-06	$g.m^{-3}$
ΔH_{CH_3OH}	CH_3OH heat of reaction (calculated by Aspen Plus)	-90589.69	$J.mol^{-1}$
β_1	inter-phase isothermal criterion	3.26E-16	-
β_2	inter-reactor isothermal criterion	5.96E-02	-